HAL
open science

Search for a charged Higgs boson with the ATLAS detector : from theory to experiment

Carole Weydert

To cite this version:

Carole Weydert. Search for a charged Higgs boson with the ATLAS detector : from theory to experiment. High Energy Physics - Experiment [hep-ex]. Université de Grenoble, 2011. English. NNT : 2011GRENY030 . tel-00629349

HAL Id: tel-00629349

https://theses.hal.science/tel-00629349v1

Submitted on 5 Oct 2011

HAL is a multi-disciplinary open access archive for the deposit and dissemination of scientific research documents, whether they are published or not. The documents may come from teaching and research institutions in France or abroad, or from public or private research centers.

L'archive ouverte pluridisciplinaire **HAL**, est destinée au dépôt et à la diffusion de documents scientifiques de niveau recherche, publiés ou non, émanant des établissements d'enseignement et de recherche français ou étrangers, des laboratoires publics ou privés.

Fonds National de la Recherche Luxembourg

UNIVERSITÉ DE GRENOBLE

THÈSE

Pour obtenir le grade de

DOCTEUR DE L'UNIVERSITÉ DE GRENOBLE

Spécialité : **Physique Subatomique et Astroparticules**

Arrêté ministériel : 7 août 2006

Présentée par

Carole Weydert

Thèse dirigée par **Michael Klasen** et
codirigée par **Benoît Clément**

préparée au sein du **Laboratoire de Physique Subatomique et de Cosmologie**
dans **l'École Doctorale de Physique de Grenoble**

Recherche d'un boson de Higgs chargé avec le détecteur ATLAS : de la théorie à l'expérience

Thèse soutenue publiquement le **5 septembre 2011**
devant le jury composé de :

Mr, Gérard Sajot
Prof., Grenoble, Président
Mr, Arnulf Quadt
Prof. Dr. , Goettingen, Rapporteur
Mr, Fabio Maltoni
Prof., Louvain, Rapporteur
Mr., François Le Diberder
Prof, Paris, Examinateur
Mr, Michael Klasen
Prof., Grenoble, Directeur de thèse
Mr, Benoît Clément
Mcu.,Grenoble, Co-Directeur de thèse

Acknowledgements

Über die weite graue Fläche des Himmels glitt ein Schlittschuhläufer dahin, kopfunter, mit wehendem Wollschal. Er konnte das, denn der Himmel war zugefroren. Mit tropfenden Nasen und offenen Mündern sah die Menschenmenge von der Erde aus zu, zeigte nach ihm hinauf und applaudierte bisweilen, wenn ihm ein besonders schwieriger (natürlich umgekehrter) Sprung gelungen war. Er lief in weiten Bögen und Schleifen, immer wieder die gleichen Figuren, bis sich die Spur seines Laufs in den Himmel gekratzt hatte. Jetzt zeigte es sich, dass es Buchstaben waren, eine dringende Botschaft vielleicht. Dann glitt er davon und verschwand fern hinter dem Horizont. Die Menschenmenge starrte zum Himmel hinauf, aber keiner kannte das Alphabet, keiner konnte die Schrift entziffern. Langsam verschwand die Spur, und der Himmel war wieder nur eine weite graue Fläche. Die Leute gingen nach Hause und hatten bald den ganzen Vorfall vergessen. Jeder hat schliesslich seine eigenen Sorgen, und ausserdem: Wer weiss, ob die Botschaft wirklich so wichtig war.
Michael Ende, "Der Spiegel im Spiegel-Ein Labyrinth"

My thanks go to my supervisors Michael Klasen and Benoît Clément, who've accepted to guide me through this joint theoretical and experimental thesis, with constant encouragement. Thank you for your confidence and support.

I am grateful to my referees Fabio Maltoni and Arnulf Quadt, as well as the other members of my jury, for their careful examination of the manuscript and their presence at the defense. Many thanks to the FNR, which has provided the funding for the publication of this document.

I would also like to express my gratitude to my collaborators through all these years: Karol Kovarik, Tilman Plehn, Eric Laenen and Paolo Nason, with a special dedication to Chris White, for those everlasting checks on the finite virtual part. On the experimental side, I'm indebted to Michael Duehrssen and the ATLAS control room crew.

Je remercie les groupes Théorie et ATLAS du LPSC, en particulier Julien Donini cobureau à thé, compagnon de saucisson de secours d'analyse tardive; Toto, d'être venu à la rescousse après l'attaque du chargeur d'ipod, un peu, et surtout pour le chocolat chaud quand ca n'allait pas; Manu, de m'avoir sauvée lors de la semaine de secourisme.

Merci à la nitescente et farfassue Lauranne, experte en pognologie, légèrement anatidaephobe sur les bords, pour les moultes années de péripatéticianisme, et pour m'avoir appris le mot *potron-minet*. Dans ce contexte, merci[1] également à Florence, Laurence et Richard, pour le club de lecture. Merci à Elsa de m'avoir permis d'explorer le métier d'enseignant et d'avoir gardé, contrairement à moi, les nerfs calmes lors du manque de césium radioactif. Merci à Grégoire, avec qui les 8 heures de TP du vendredi semblaient moins longues. Merci à Pierre Salati, qui a mis tant de coeur et de passion dans ses cours. Merci au docteur Romain Glodt, qui, jadis, répara mes jambes, et pas si jadis que cela, me donna une pîqure de motivation sous forme de pîqure de cortisone. Merci à *Ruthless Ruth*, ma kinné, qui m'aida à mettre mes idées en place en mettant mon dos en place; qui m'aida à mettre le doigt sur les parties qui n'allaient pas en mettant le doigt sur les muscles qui n'allaient pas. Souvent, elle insista plus fortement que moi. Je ne lui en tiens pas rigueur.

I would also like to address my thanks to the people from the CERN Summer Student Program: Ibon, Willy, Claudio, Davide, Gabi, Francesco, Lutz, ... Each time I went back to CERN, all those amazing memories came back, and that was one of the reasons I loved so much being there.

En vrac, non-pas qu'ils soient moins importants, mais il faut bien en finir un jour, merci à Henry Weyer, Jean-Pierre Engel, Roger Strub, Jean-Marc Richard, Aurélien Barrau, Arnaud Lucotte, Benjamin Fuks, Jérémy Andrea et Björn Herrmann.

Merci à toute ma famille et les amis, présents le grand jour mais également les petits: Boma, Mami, Papi, Cinzia, Greg, Christiane, Pippo, Marie-Paule, Guy, Françine, Léon, Marthe, Roger, Françoise, Chloé, Pascal, Marie[2] et Gaby.

Finalement, le plus grand merci revient à mes parents ainsi qu'à Claude, en l'absence desquels cette thèse n'aurait pu se faire.

[1] En français dans le texte.
[2] Merci à Marie pour les pillules de grenouilles séchées.

Contents

Acknowledgements **i**

Introduction **1**

1 The Standard Model of particle physics **5**
1.1 Basic principles 5
1.2 Mass generation in the Standard Model and beyond 7
1.2.1 The Standard Model scalar sector 7
1.2.2 The 2 Higgs Doublet Model 12
1.2.3 Current charged Higgs boson searches 18
1.3 The top quark 20
1.3.1 Historic review 20
1.3.2 Production at the Tevatron and at the LHC 23

2 From hadronic to partonic collisions **27**
2.1 The strong coupling constant 28
2.2 Parton distribution functions 32
2.2.1 Measuring structure functions and cross sections 32
2.2.2 Constructing PDFs with global fits 37
2.3 The mass mess 47
2.3.1 The pole mass 47
2.3.2 Short distance mass schemes 49

3 NLO partonic cross section calculation **51**
3.1 Partonic cross sections 52
3.2 Virtual corrections 54
3.2.1 Regularisation methods 54
3.2.2 Relevant integrals for loop calculations 56
3.2.3 Virtual contributions for tH^- production 62
3.2.4 Renormalisation 66
3.2.5 Counterterms for tH^- production 70
3.2.6 Renormalised virtual contributions for tH^- production 71
3.3 Real corrections 73
3.4 Catani-Seymour dipole subtraction 76
3.5 High and low charged Higgs mass: diagram removal 82

4 Event generator implementation **85**
4.1 Monte Carlo event generators . . . 85
4.1.1 The parton shower . . . 86
4.1.2 Multiple purpose generators . . . 91
4.1.3 Matrix element generators . . . 91
4.1.4 Charged Higgs specific programs . . . 93
4.1.5 Coupling a NLO event generator to a parton shower . . . 94
4.2 MC@NLO . . . 95
4.2.1 MC@NLO coupled to Herwig . . . 95
4.2.2 Comparison of tH^- NLO versus NLO+PS production . . . 96
4.2.3 Systematic uncertainty studies . . . 97
4.3 POWHEG . . . 100
4.3.1 POWHEG coupled to an arbitrary parton shower . . . 100
4.3.2 Code structure . . . 101
4.3.3 Comparison of tH^- NLO versus NLO+PS production . . . 104
4.4 Conclusion . . . 106

5 Startup of the Large Hadron Collider **107**
5.1 The LHC . . . 107
5.2 Taking Control of ATLAS . . . 109
5.2.1 The Inner Detector . . . 110
5.2.2 The calorimetry . . . 111
5.2.3 The muon spectrometer . . . 113
5.2.4 LUCID and ALFA . . . 114
5.2.5 ATLAS as a whole . . . 115
5.2.6 The Root Controller . . . 117
5.3 The Trigger and Data Acquisition Concept . . . 118
5.4 Event simulation and reconstruction . . . 121
5.4.1 Simulation chain . . . 121
5.4.2 Event reconstruction . . . 122
5.4.3 Fast vs Full Simulation . . . 123

6 The 2010 pp physics run **127**
6.1 Data taking periods and consequences . . . 127
6.1.1 Data taking periods . . . 127
6.1.2 Consequences on the charged Higgs boson analysis . . . 129
6.2 Semileptonic electroweak single top production . . . 130
6.3 Relevant objects for the semileptonic Wt analysis . . . 131
6.3.1 Electrons . . . 131
6.3.2 Muons . . . 134
6.3.3 Jets . . . 135
6.3.4 Missing transverse energy . . . 140
6.4 Data and MC samples . . . 140
6.4.1 Data samples . . . 140

6.4.2 MC simulation samples 141

7 Wt analysis in the semileptonic channel **143**
7.1 Preselection and background estimates 143
7.1.1 Preselection 143
7.1.2 Background estimations 146
7.2 Cut-based analysis 150
7.2.1 Final selection 150
7.2.2 Event yields 152
7.3 Systematic uncertainties 152
7.3.1 The PDF systematic uncertainty 152
7.3.2 Other sources of systematic uncertainties 155
7.4 Statistical analysis 157
7.4.1 Semileptonic channels 157
7.4.2 Combination with the dileptonic channels 160
7.5 Conclusion 161

Conclusion **162**

A Borel summation **165**

B Formulas for the Catani Seymour Dipole Subtraction **167**
B.1 Splitting functions for the real dipole contributions 167
B.2 **P** and **K** colour charge operators 169
B.2.1 General expressions 169
B.2.2 tH^- specific expressions 171

C Basic set of divergent scalar integrals **175**

D Combining W+jets samples by Heavy Flavour Overlap Removal **177**

E Preselection event yield **183**

F Tables of systematic uncertainties **187**

Bibliography **191**

Ein Vorwort ist für ein Buch so wichtig und so hübsch wie der Vorgarten für ein Haus. Natürlich gibt es auch Häuser ohne Vorgärtchen und Bücher ohne Vorwörtchen, Verzeihung, ohne Vorwort. Aber mit einem Vorgarten, nein, mit einem Vorwort sind mir die Bücher lieber. Ich bin nicht dafür, dass die Besucher gleich mit der Tür ins Haus fallen. Es ist weder für die Besucher gut, noch fürs Haus. Und für die Tür auch nicht.

Erich Kästner, *"Als ich ein kleiner Junge war"*

Introduction

This thesis is intended as a bridge between the two highly specialised domains of phenomenology and experimental particle physics. The first part describes in detail a next-to-leading-order (NLO) cross section calculation done *by hand*. Fully automated tools for various parts of such calculations have become available nowadays and one can obtain in a few clicks all the virtual diagrams, their reduction to the basic set of scalar integrals, the real emission diagrams, and the subtraction terms. The actual size of the different terms to be calculated and the difficulty in double–checking them makes the emergence and use of these automated tools self-explanatory. We have, however, used none of these things, relying on the fact that *"An expert is a man who has made all the mistakes, which can be made, in a very narrow field."*[3]. Although the methods used for the calculation are well-known to specialists, the aim of this document is to give as much detail and be as plain as possible, in order to gather the experimentalist's interest and retain it to the end, while, at the same time, put theorists into confidence that they'll continue reading through the detector and analysis chapters. We present the calculation of the NLO quantum chromodynamic corrections for charged Higgs boson production in association with a top quark at the LHC, using a special kind of subtraction method. Building an independent NLO code enabled us to cross–check the implemented version of MC@NLO [1], and a few studies have been made which focus on different contributions to the theoretical uncertainty attached to the NLO calculation. The actual implementation was performed for another NLO event generator, POWHEG [2]. Considering the small production cross section of $H^{\pm}t$ production[4], an analysis of this channel using the 35 pb^{-1} of data collected with the ATLAS [3] detector in 2010 from the pp collisions of the LHC, makes no sense, and we switch to a very similar SM channel, namely Wt production. We set-up a dedicated analysis for semileptonic Wt and focus on the evaluation of the PDF systematic uncertainty, following the PDF4LHC recommendation. The electroweak single top production cross section via Wt at the Tevatron is so low that it hasn't been observed until today, so we are able to set the world's first limit on its production cross section and include the most important systematic uncertainties in our analysis.

[3] Quote attributed to Niels Bohr.

[4] Through this document, you will find charged Higgs production referenced as $H^{\pm}t$ in the experimental parts, since this is what we are looking for, and as tH^{-} in the theoretical part, for consistency issues on the presented diagrams.

Chapter 1 gives a brief account of our current understanding of the building blocks of matter by introducing the Standard Model of Particle Physics through its basic principles. Special focus is put on mass generation via the Higgs mechanism. But since the Higgs boson has not yet been observed, the exact structure of the Standard Model scalar sector remains unknown and there is still some room for speculation. We present a possible extension with the two Higgs doublet model, for which there are three neural Higgs bosons and two charged ones. We review current direct and indirect searches of these charged Higgs bosons. Since an important property of Higgs particles is their coupling to other particles proportional to their mass, the top quark plays a very important role in connection with Higgs searches. Therefore, we review its historical discovery and comment on its production at hadron colliders, as well as studies on its general properties.

Keeping in mind that we want to deal with hadron colliders, we explain the evolution of the strong coupling constant in Chapter 2. We'll see that, if we are at high enough energies, the quantities we are interested in may be developed into a perturbative expansion with respect to the coupling. This allows to go from hadronic to partonic cross sections via the use of parton distribution functions (PDF). We list the general philosophy of gaining knowledge on the hadron structure and present the different experiments dedicated to assemble hadronic data. This information is gathered by various collaborations, and we present their parametrisations and fitting techniques, along with their quantification of their results' uncertainties. The special treatment of heavy quark flavours is introduced and leads us to a few general remarks on the concept of mass in particle physics, with special focus again on the top quark.

Chapter 3 concentrates on the partonic cross section calculation. The complexity of NLO calculations is presented, while keeping in mind that, in order to be useful for data comparisons, the process needs to be implemented into an event generator. NLO calculations involve different contributions, which all have to be calculated: the virtual and real contributions, as well as a method to combine them. The virtual emission, or loop, diagrams, need dedicated integral calculations, and the general formalism is introduced. The regularisation procedure makes the divergencies explicit and it becomes clear that there are two different types of poles, stemming from the low and high energy limits in the integral. The high energy divergencies are removed through renormalisation. The real emission diagrams are another contribution which has to be calculated and exhibit low-energy and collinear divergencies. But since the final state phase space of both the virtual and the real contribution are not the same, they cannot be added in a straightforward fashion. The Catani-Seymour subtraction formalism [4, 5] will provide the necessary bridge. It is in this point where the novelty of our work comes in, since we compute $H^{\pm}t$ production with this new subtraction formalism and build an independent NLO code which gives the NLO hadronic cross section. Finally, the case where the charged Higgs boson mass is lower than the top quark is investigated and a method to separate NLO $H^{\pm}t$ production from $t\bar{t}$ is presented. We have now at our disposal enough elements to help for checks and do an implementation into an MC event

generator ourselves.

In Chapter 4 we detail the different aspects of Monte Carlo event generators, with special focus on steps after the hard scattering. The general concept of partons showers is explained, along with the hadronisation process and underlying event. We introduce a list of the most frequently used generators, divided according to multipurpose or matrix element generators. This small section is concluded by a rapid review of charged Higgs specific codes. The general way of coupling a NLO matrix element calculation to a parton shower is explained and we concentrate on two specific codes: MC@NLO and POWHEG. The MC@NLO coupling to the parton shower Herwig is presented. We use our independent NLO calculation to check the MC@NLO implementation, which is strongly based on the previously available Wt process. A few studies are presented which address the issue of systematic uncertainty evaluation. These are contributions from the difference of handling the NLO interference of $H^{\pm}t$ with $t\bar{t}$ in the diagram removal and diagram subtraction scheme. A second study focuses on the influence of the PDF fit input bottom mass on the hadronic cross section. Also, a comparison between the four- and five-flavour-scheme calculation, i.e. using either massive or massless b quarks in the kinematics of the calculation, is presented. Finally, we perform the implementation of NLO $H^{\pm}t$ production in POWHEG. After explaining how POWHEG may be coupled to any parton shower, we detail the $H^{\pm}t$ code structure and show plots of kinematically relevant variables obtained with POWHEG. At this point, we can go no further on the theoretical side and need real data to compare our predictions with.

In Chapter 5, we begin our journey from large to small scales with the Large Hadron Collider and its entire acceleration chain. We will zoom in on one of the multiple purpose detectors situated on a crossing point of the 27 km long ring where protons circulate in two opposite beams. The ATLAS detector is a collection of several sub-detectors, each dedicated to a specific task. The detector and its operation are presented from the run control shifter's point of view. The data trigger and acquisition chain are presented. We finally describe the simulation and reconstruction chain in Athena [6], the general computing framework of the ATLAS collaboration. At this point, we briefly mention the difference between the fast and full simulation, whose comparison has been part of the service task performed during this thesis.

The focus of Chapter 6 lies on the amount of data collected during the 2010 proton-proton collisions by the ATLAS detector. After describing the different periods of data taking and the associated collected luminosity, we comment on the consequences this low amount has on an eventual $H^{\pm}t$ analysis. We explain our need to change our physics focus on a process which is, from the NLO point of view but also from the detector signature, very similar to our original process, namely Wt production. Since this will be an important background for charged Higgs production, it needs to be studied and thoroughly understood. After detailing the relevant objects included in the Wt signature, we turn to the needed Monte Carlo events samples for the signal and its major backgrounds.

In Chapter 7, we finalise our project by performing the Wt analysis in the semileptonic channel. We put a very first limit on its production cross section, by ultimately combining our results with the dilepton channels. The study is completed using all sources of systematic uncertainties. We extend our comments particularly for uncertainties due to the use of parton distribution functions, which were computed by our group. The knowledge of the extraction of parton distribution related systematics, as well as the evaluation of different systematics for $H^{\pm}t$, which have their analogue for Wt, have proven extremely useful in that context.

The starting point is a question.
Outside theology and fantastic literature, few can doubt that the main features of our universe are its dearth of meaning and lack of discernible purpose. And yet, with bewildering optimism, we continue to assemble whatever scraps of information we can gather in scrolls and books and computer chips, on shelf after library shelf, whether material, virtual or otherwise, pathetically intent on lending the world a semblance of sense and order, while knowing perfectly well that, however much we'd like to believe the contrary, our pursuits are sadly doomed to failure. Why then do we do it? Though I knew from the start that the question would most likely remain unanswered, the quest seemed worthwhile for its own sake. This book is the story of that quest.

Alberto Manguel, Foreword to *"The library at night"*

1 The Standard Model of particle physics

1.1 Basic principles

Before plunging into the heart of matter, we briefly recall the very basic principles on which the modern mathematical description of Nature is build. E. Zeidler summarises them as follows [7]

- The infinitesimal principle of Newton and Leibniz states that the laws of Nature are to become simple on an infinitesimal level of space and time.
- The principle of least action asserts that physical processes develop in such an optimal way that their action is extremal, and these processes are governed by ordinary or partial differential equations, the Euler-Lagrange equations.
- Einstein's principle of special relativity brings to attention that physics does not depend on our choice of inertial system.
- Einstein's principle of general relativity states that physics does not depend on the observer's local space-time coordinates.
- Noether's symmetry principle states that symmetries of the action functional imply conservation laws for the corresponding Euler-Lagrange equations.
- The gauge principle and Levi-Civita's parallel transport link the fundamental forces to underlying symmetries of the action functional.
- Planck's quantisation principle asserts that Nature jumps.

- Dirac's unitarity principle states invariance of quantum mechanics under unitary transformations.

The infinitesimal principle and the principle of least action are at the very core of our understanding and describe how we are to find the mathematical laws. But they remain on a classical level. The concepts of special and general relativity give a whole new framework as to how the mathematics behind our ideas are to look like, and put an emphasis on the concept of symmetry via the geometrisation of physical laws. The notion of symmetry becomes even more important with Noether and the gauge principle and it is now central to our current description of the building blocks of matter. Finally, Planck's quantisation principle and Dirac's unitarity principle bring us to the desired small scales, where quantum mechanics takes over.

The first success of a unifying procedure for physical laws can be traced back to the end of the 19th century with Maxwell's theory of electromagnetism, which combined for the fist time the laws of electricity and the magnetic interactions. Both phenomena appeared now as inseparable parts of a more general interaction. The emergence of quantum mechanics, however, rendered the picture more complicated. There was need of a theoretical framework which could translate these conceptual developments into the new quantitative calculation scheme. Very early in the 1930s, quantum electrodynamics emerged as the theory describing the electromagnetic interactions of electrons and photons, and it had the desired features: it was quantised and relativistically invariant. The attempt of unifying the known forces took another step forward in the 1960s when Glashow, Salam and Weinberg elaborated the electroweak theory. Only a few years later, it was realised that even the strong force could be put into a gauge theoretical formulation. This lead up to the modern formulation of the Standard Model (SM) of particle physics, for which the major discoveries of the early twentieth century, quantum mechanics and special and general relativity, are the foundations. The global Poincaré symmetry, which consists of the familiar translational symmetry, rotational symmetry and the inertial reference frame invariance central to the theory of special relativity, is postulated for all relativistic quantum field theories. Then, three different internal symmetries, the local $SU(3)_C \times SU(2)_L \times U(1)_Y$ gauge symmetries, give rise to the three fundamental interactions. Today we know of a total of four fundamental interactions between elementary particles: the gravitational, the electromagnetic, the weak and the strong interaction. Gravity set aside, the description of the elementary particles and their interactions is done via quantised, relativistic, locally interacting fields. The link between the structure of conserved charges and the symmetry groups of the fields is of paramount importance. In the formalism of gauge theories, electromagnetic interactions result from an $U(1)$ symmetry, weak interactions between left-handed fermions from an $SU(2)$ symmetry and strong interactions from an $SU(3)$ symmetry. Since these symmetries do not act on space-time coordinates, they are called internal symmetries. The construction of the Standard Model proceeds following the modern method of constructing most field theories, which consists in first postulating a set of symmetries of the system, and then writing down the most general renormalisable Lagrangian from

its field content that conserves these symmetries. The fermionic particle content of the SM as well as their quantum numbers, which dictate how the particle behaves under a certain symmetry, are listed in Tab. 1.1. The fields of the interacting particles are obtained from the fermion fields by imposing local gauge invariance.

Table 1.1: The fermion fields of the SM and their gauge quantum numbers. T and T_3 are the total weak-isospin and its third component, and Q is the electric charge.

				$SU(3)_C$	$SU(2)_L$	$U(1)_Y$	T	T_3	Q
$Q_L^i =$	$\begin{pmatrix} u_L \\ d_L \end{pmatrix}$	$\begin{pmatrix} c_L \\ s_L \end{pmatrix}$	$\begin{pmatrix} t_L \\ b_L \end{pmatrix}$	3	2	1/6	1/2	$+1/2$ $-1/2$	$+2/3$ $-1/3$
$u_R^i =$	u_R	c_R	t_R	3	1	2/3	0	0	$+2/3$
$d_R^i =$	d_R	s_R	b_R	3	1	$-1/3$	0	0	$-1/3$
$L_L^i =$	$\begin{pmatrix} \nu_{eL} \\ e_L \end{pmatrix}$	$\begin{pmatrix} \nu_{\mu L} \\ \mu_L \end{pmatrix}$	$\begin{pmatrix} \nu_{\tau L} \\ \tau_L \end{pmatrix}$	1	2	$-1/2$	1/2	$+1/2$ $-1/2$	0 -1
$e_R^i =$	e_R	μ_R	τ_R	1	1	-1	0	0	-1
$\nu_R^i =$	ν_R^e	ν_R^μ	ν_R^τ	0	0	0	0	0	0

In the SM, all vector bosons are massless. While this is true for the gluon and the photon, it does not apply to the electroweak W and Z bosons, whose masses have been measured to be $m_W = 80.399 \pm 0.023$ GeV and 91.1876 ± 0.0021 GeV [8]. Also, fermions are observed to be massive, but since the $SU(2)_L$ symmetry couples differently to left and right spinors, these mass terms are forbidden in the Lagrangian. This means that the SM as such is incomplete, and has to be altered to account for this observation. In the 1960s, the Higgs mechanism came as an attempt to complete the SM picture and the hunt for the Higgs boson has been going on ever since.

1.2 Mass generation in the Standard Model and beyond

1.2.1 The Standard Model scalar sector

Experimentally, the weak bosons are massive. Disregarding the fact that we cannot introduce directly a mass term in the Lagrangian without breaking gauge invariance, we can try to see what happens if we try to use massive bosons in calculations by brute force.

1.2.1.1 W scattering

Assuming for the moment that we found a way to incorporate vector boson masses into the Lagrangian in a gauge-invariant way, we can take a look at the scattering of

longitudinally polarised W bosons [9, 10, 11]

$$W^+(p_+) + W^-(p_-) \to W^+(k_+) + W^-(k_-), \tag{1.1}$$

which are the leading terms at high energies for WW scattering.

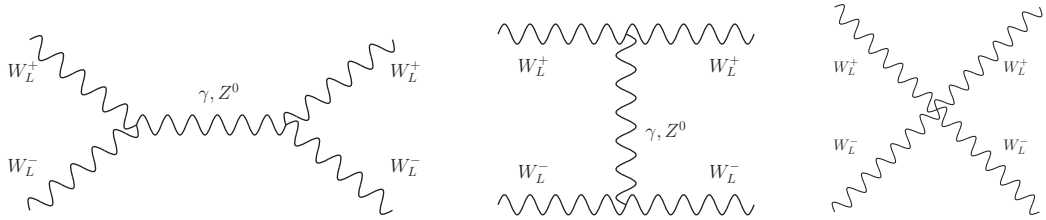

Figure 1.1: The two W_L scattering diagrams in the s- and t-channel contributing to the amplitude $\mathcal{A}_1$ and the 4-vector boson vertex for amplitude $\mathcal{A}_2$.

The contributing diagrams of this purely conceptual process, since we do not have a W boson collider, are shown in Fig. 1.1. The kinematics in the centre of mass reference frame are given by

$$p_\pm = (E, 0, 0, \pm p) \text{ for incoming and} \tag{1.2}$$
$$k_\pm = (E, 0, \pm p \sin\theta, \pm\cos\theta) \text{ for outgoing bosons,} \tag{1.3}$$

with $E^2 - p^2 = m_W^2$ and where θ is the scattering angle in the centre of mass reference frame. The Mandelstam variables are given by

$$s = (p_+ + p_-)^2 \tag{1.4}$$
$$t = (p_+ - k_+)^2. \tag{1.5}$$

Since we only consider scattering of longitudinal polarisations, they are given by

$$\epsilon_L(p\pm) = \Big(p/m_W, 0, 0, \pm E/m_W\Big), \tag{1.6}$$
$$\epsilon_L(k\pm) = \Big(p/m_W, 0, \pm E\sin\theta/m_W, \pm E\cos\theta/m_W\Big). \tag{1.7}$$

They are normalised using $\epsilon^2 = -1$ and respect the Lorentz condition $\epsilon(\vec{q}) \cdot \vec{q} = 0$. We can now take a look at the high energy behaviour. Summing the amplitudes of both the s- and the t-channel scattering of photon and Z-boson exchange, and keeping only the dominant terms in p^2/m_W^2, we have

$$\mathcal{A}_1 = g_W^2 \Big[\frac{p^4}{m_W^4}(3 - 6\cos\theta - \cos^2\theta) + \frac{p^2}{m_W^2}\Big(\frac{9}{2} - \frac{11}{2}\cos\theta - 2\cos^2\theta\Big)\Big]. \tag{1.8}$$

The dominant terms for the four-boson vertex are

$$\mathcal{A}_2 = g_W^2 \Big[\frac{p^4}{m_W^4}(-3 + 6\cos\theta + \cos^2\theta) + \frac{p^2}{m_W^2}\Big(-4 + 6\cos\theta + 2\cos^2\theta\Big)\Big]. \tag{1.9}$$

Adding both terms together cancels out the p^4/m_W^4 term. However, the term $p^2/m_W^2 = s/m_W^2$ is still present and grows indefinitely with the centre of mass energy, which is unacceptable. This shows that the SM as such is incomplete and needs a UV regulator for longitudinal W boson scattering. This situation has an antecedent in quantum chromodynamics (QCD), the theory of strong interactions. In QCD, pions can be described as Goldstone bosons associated to $SU(2)_L \times SU(2)_R/SU(2)_V$, where the pion-pion scattering amplitude is given by

$$\mathcal{A}(s,t,u) = \frac{s}{f_\pi^2}, \tag{1.10}$$

with $f_\pi = 93$ MeV. This leads to a unitarity bound of $\sqrt{s} \approx 4\sqrt{\pi} f_\pi = 660$ MeV, meaning that this calculation is only valid up to this scale. At that point, another mechanism has to take over to regularise the scattering amplitude. This is exactly what the ρ meson with its mass of $m_\rho = 770$ MeV does. And it turns out that the Higgs boson plays exactly that role for the SM W boson scattering issue.

1.2.1.2 The Higgs mechanism

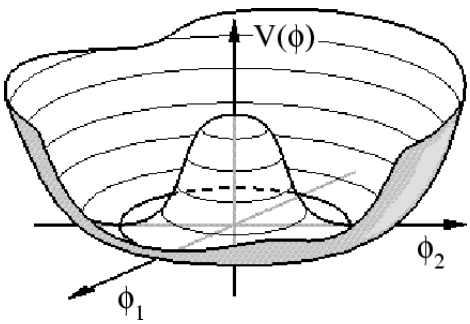

Figure 1.2: The characteristic mexican hat Higgs potential.

In order to confer a mass term to the three vector bosons $W^\pm$ and Z in a proper way, which is needed for the non-abelian SM, the Higgs mechanism is introduced [12, 13]. Mass terms in the Lagrangian are generated from the kinetic energy term of a scalar doublet field that undergoes spontaneous symmetry breaking. The choice of a scalar doublet is motivated via our need for three degrees of freedom to become the three masses. The fourth boson, the photon, should remain massless. The simplest choice is to add a $SU(2)$ doublet of complex scalar fields

$$\Phi = \begin{pmatrix} \phi^+ \\ \phi^0 \end{pmatrix}, \tag{1.11}$$

with hypercharge $Y_\phi = +1$, so that the scalar Lagrangian reads

$$\mathcal{L}_s = \left(D^\mu \Phi\right)^\dagger \left(D_\mu \Phi\right) - V(\Phi). \tag{1.12}$$

The covariant derivative is given by

$$D_\mu = \partial_\mu - i g_2 \frac{\tau}{2} W_\mu^a - i g_1 \frac{1}{2} B_\mu, \tag{1.13}$$

where W^μ and B^μ are the gauge fields with couplings g_2 and g_1 related to the Weinberg angle $\cos\theta_W = g_2/(g_2^2 + g_1^2)^{1/2}$. The potential

$$V(\Phi) = \mu^2 \Phi^\dagger \Phi + \lambda \left(\Phi^\dagger \Phi\right)^2 \tag{1.14}$$

has a minimum, which is not located at $\phi = 0$ if $\mu^2 < 0$, as shown on Fig. 1.2. In this case, the neutral component[1] of Φ will develop a vacuum expectation value (vev)

$$\langle\Phi\rangle_0 = \langle 0|\Phi|0\rangle = \frac{1}{\sqrt{2}}\begin{pmatrix}0\\ v\end{pmatrix}, \tag{1.15}$$

where

$$v = \sqrt{-\frac{\mu^2}{\lambda}}. \tag{1.16}$$

We now develop Φ into four fields, one of them being the Higgs bosons H, around the minimum at first order

$$\Phi(x) = \begin{pmatrix}\theta_2 + i\theta_1\\ \frac{v+H}{\sqrt{2}} - i\theta_3\end{pmatrix} = \exp\Big(\frac{i\theta_a(x)\tau^a(x)}{v}\Big)\frac{1}{\sqrt{2}}\big(v + H(x)\big), \tag{1.17}$$

and perform a rotation via the following gauge transformation

$$\Phi(x) \to \exp\Big(\frac{-i\theta_a(x)\tau^a(x)}{v}\Big)\Phi(x) = \frac{1}{\sqrt{2}}\big(v + H(x)\big). \tag{1.18}$$

We rewrite the fields W^a_μ and B_μ in terms of the vector bosons $W^\pm_\mu, Z_\mu$ and the photon A_μ using

$$W^\pm_\mu \frac{1}{\sqrt{2}}(W^1_\mu \mp W^2_\mu), Z_\mu = \frac{g_2 W^3_\mu - g_1 B_\mu}{\sqrt{g_1^2 + g_2^2}}, A_\mu = \frac{g_2 W^3_\mu + g_1 B_\mu}{\sqrt{g_1^2 + g_2^2}}, \tag{1.19}$$

and expand the first term of the scalar Lagrangian, Eq. (1.12). The terms bilinear in the new fields are identified as mass terms

$$M_W^2 W^+_\mu W^{-\mu} + \frac{1}{2}M_Z^2 Z_\mu Z^\mu + \frac{1}{2}M_A^2 A_\mu A^\mu, \tag{1.20}$$

for which the masses are given by

$$M_W = \frac{v g_2}{2}, M_Z = \frac{v\sqrt{g_1^2 + g_2^2}}{2} \text{ and } M_A = 0. \tag{1.21}$$

Thus, we managed to introduce a mass term for the experimentally massive vector bosons and keep a massless photon by spontaneously breaking the $SU(2)_L \times U(1)_Y$ symmetry down to $U(1)_Q$. The three Goldstone bosons have been reabsorbed by the W and Z bosons.

If we now return to the W scattering problem, we need to add additional contributions due to Higgs exchange, as depicted in Fig. 1.3.

[1] It cannot be the charged component, since we want to preserve the $U(1)$ symmetry of QED.

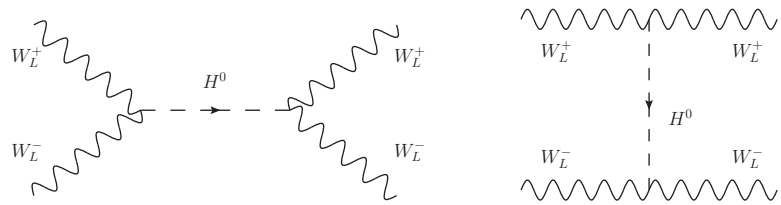

Figure 1.3: The two W_L scattering diagrams contributing to the $\mathcal{A}_H$ amplitude via Higgs boson exchange in the s- and t-channel.

Adding the amplitudes where a Higgs boson exchange occurs in the s- and in the t-channel, we get

$$\mathcal{A}_H = g_W^2 \Big[\frac{p^2}{m_W^2} \Big(-\frac{1}{2} - \frac{1}{2} \cos\theta \Big) - \frac{m_H^2}{4m_W^2} \Big(\frac{s}{s - m_H^2} + \frac{t}{t - m_H^2} \Big) \Big]. \tag{1.22}$$

By summing this amplitude with the ones calculated in Eq. (1.8) and (1.9), the high-energy behaviour of the scattering amplitude becomes well-defined:

$$\mathcal{A}_{1+2+H} = -\frac{g_W^2 m_H^2}{4m_W^2} \Big(\frac{s}{s - m_H^2} + \frac{t}{t - m_H^2} \Big). \tag{1.23}$$

The Higgs mechanism has thus enabled us to confer masses to the electroweak bosons. A second interesting feature of the Higgs mechanism is that it may also be used to generate mass terms for fermions. Also in this case, the couplings of the Higgs boson to the particles are proportional to the masses and are free parameters of the theory.

A unitarity bound using the optical theorem places an upper limit on the Higgs boson mass around 700 GeV. If this limit is exceeded, weak interactions become strong and perturbative calculations are not valid anymore. This implies that studying W boson scattering at hadron colliders in the high energy regime should either reveal a novel behaviour of the electroweak force or the Higgs boson should somehow be seen[2].

The Higgs mechanism has been introduced out of a necessity of a UV moderator of electroweak interactions, but is only the simplest of an important quantity of possibilities that have been proposed over the years, like little Higgs [14], Composite Higgs [15] or higgsless models [16], to name only a few. Since the Higgs boson is intimately linked to the masses of the elementary particles, it is very tempting to think that the Higgs is somehow responsible for these masses. However, up to now all the masses are free parameters of the theory which can only be determined from experiment and cannot be deduced from first principles. Certainly the missing connection between gauge theories and gravity still hides something.

[2]It is also important to note that only a scalar exchange may cancel the growing amplitude in this straightforward way. A vector exchange would already have to be much more fine-tuned to achieve cancellation.

Since the existence of the Higgs particle as the last cornerstone of the SM has not yet been confirmed by experiment, the exact structure of the SM scalar sector is still up to speculation. We shall investigate the simplest extension of the sector we just presented, the 2 Higgs Doublet Model (2HDM), which is obtained via the addition of a second scalar doublet. Models with Higgs doublets and singlets possess the property of conserving, up to finite radiative corrections, the ratio of the W mass and the Z boson mass multiplied with the cosine of the Weinberg angle θ_W

$$\rho = \frac{m_W}{m_Z cos\theta_W} = 1. \tag{1.24}$$

1.2.2 The 2 Higgs Doublet Model

The problem with the Higgs particles as it was just presented, other than its non-observation so far, is that its mass is not stable when quantum corrections are included. Indeed, its mass m_H^2 receives enormous quantum corrections via virtual effects from every massive particle in the theory, giving huge corrections Δm_H^2, which have to be cancelled somehow. A possible way out would be the physicist's favourite trick [17]: *The systematic cancellation of the dangerous contributions to Δm_H^2 can only be brought about by the type of conspiracy that is better known to physicists as a symmetry.*

1.2.2.1 Supersymmetry as a motivation for a type II 2HDM

Poincaré symmetry is realised in Nature, but one can ask the question if it is possible to extend the Poincaré group with internal symmetries. The first answer came in 1967 by Coleman and Mandula via their *no-go theorem* [18], proving that any Lie group which contains both the Poincaré group $\mathcal{P}$ and an internal symmetry group $\mathcal{G}$ must be a trivial direct product $\mathcal{P} \times \mathcal{G}$. Since this means that the generators commute, nothing interesting happens. There is however a possibility to bypass the no-go theorem. In 1975, Haag, Lopuszanski and Sohnius [19] were able to extend the Coleman-Madula theorem by allowing not only commuting, but also anti-commuting generators. They proved that not only is there a non-trivial extension of the Poincaré algebra, but it is also unique, and called it superalgebra. What is now called the Minimal Supersymmetric Standard Model (MSSM), is the minimal extension to the Standard Model that realises supersymmetry. Due to its structure, supersymmetry turns fermionic into bosonic states and in the supersymmetric extension of the SM each of the known fundamental particles has a superpartner with spin differing by half a unit. The single-particle states of a supersymmetric theory fall into irreducible representations of the superalgebra, called supermultiplets. Each supermultiplet contains an equal number of fermionic and bosonic degrees of freedom. It turns out that only one supermultiplet for the Higgs to reside in is not enough. Two main reasons can be brought forth. The first is that were there only one, the electroweak gauge symmetry would suffer a gauge anomaly. The conditions for cancellation of gauge anomalies include that

$$Tr\left[T_3^2 Y\right] = Tr\left[Y^3\right] = 0, \tag{1.25}$$

where T_3 and Y are the third component of the weak isospin and weak hypercharge, so that the electric charge is given by

$$Q = T_3 + Y/2. \tag{1.26}$$

This is the case in the SM for the known quarks and leptons. In supersymmetry, a fermionic partner of a Higgs chiral supermultiplet must be a weak isodoublet with weak hypercharge $Y = +1$ or -1. If there's only one case, such a fermion will contribute to a non-zero contribution to the traces and spoil the anomaly cancellation. This may be fixed if there are two Higgs supermultiplets, one with hypercharge (+1) and the other with (-1), so that the total contribution to the anomaly traces from the two fermionic members of the Higgs chiral supermultiplets vanishes. The second argument for two Higgs doublets is that the structure of supersymmetric theories imposes a particular Yukawa coupling. Only a $Y = +1$ Higgs chiral supermultiplet can be coupled to charge $(+2/3)$ up-type quarks and only a $Y = -1$ Higgs can gives masses to charge $(-1/3)$ down-type quarks and charged leptons.

The 2HDM is the most straightforward extension of the SM scalar sector. People are interested mostly in its type II version, since this is the one fitting in supersymmetry, but is is important to keep in mind that the 2HDM can be constructed without any reference to supersymmetry. In that case however one can relax assumptions and a plethora of different 2HDM types can be constructed. The general 2HDM extensions are classified according to their Yukawa structure, the hermicity of the Yukawa matrices and the way the bosonic sector behaves under CP transformations. In the type I 2HDM, only one Higgs doublet is responsible for the gauge and fermion mass generation, while the second doublet is only aware of this via mixing. The 2HDM type II has natural flavour conservation. Its phenomenology is similar to that of type I, although in this case the couplings to the SM particles occur not only through mixing but also through the Yukawa structure. Finally, there also exist type III, IV and even V models, each with their advantages and disadvantages. Although very interesting from the model building vantage point, we will not list the different versions but focus on type II. A thorough review can be found in [20].

1.2.2.2 The general 2HDM

The most general potential V for two identical doublets Φ_1 and Φ_2 with hypercharge $Y = 1$ is given by [21]

$$\begin{aligned} V = m_{11}^2 \Phi_1^\dagger \Phi_1 + m_{22}^2 \Phi_2^\dagger \Phi_2 - \left[m_{12}^2 \Phi_1^\dagger \Phi_2 + \text{h.c.} \right] + \frac{\lambda_1}{2} \left(\Phi_1^\dagger \Phi_1 \right)^2 + \frac{\lambda_2}{2} \left(\Phi_2^\dagger \Phi_2 \right)^2 \\ + \lambda_3 \left(\Phi_1^\dagger \Phi_1 \right) \left(\Phi_2^\dagger \Phi_2 \right) + \lambda_4 \left(\Phi_1^\dagger \Phi_2 \right) \left(\Phi_2^\dagger \Phi_1 \right) \\ + \left\{ \frac{\lambda_5}{2} \left(\Phi_1^\dagger \Phi_2 \right)^2 + \left[\lambda_6 \left(\Phi_1^\dagger \Phi_1 \right) + \lambda_7 \left(\Phi_2^\dagger \Phi_2 \right) \right] \left(\Phi_1^\dagger \Phi 2 \right) + \text{h.c.} \right\}. \end{aligned} \tag{1.27}$$

Since complex phases may be present in the parameters $\lambda_{5,6,7}$ and m_{12}^2, the most general model has 14 free parameters. If however it is restricted to cases without CP-violation, all the parameters become real and the number of free parameters shrinks down to 10. Electroweak symmetry breaking requires at least one negative eigenvalue in the scalar mass matrix and at the minimum, m_{11}^2 and m_{22}^2 can be eliminated in favour of the vevs of the scalar fields $\langle\Phi_i\rangle = v_i/\sqrt{2}$. The overall scale is given by $v^2 = v_1^2+v_2^2 = (246\text{ GeV})^2$. The 2HDM is invariant under unitarity transformations and a basis in the doublet space is chosen by specifying the ratio of the two vevs, defining the parameter

$$\tan\beta = v_2/v_1. \tag{1.28}$$

1.2.2.3 The Higgs potential of the MSSM

If the 2HDM is to describe the Higgs sector of the MSSM, further restrictions on the parameters are [22]

$$\lambda_1 = \lambda_2 = \frac{g_2^2+g_1^2}{4} \qquad \lambda_3 = \frac{g_2^2-g_1^2}{4} \qquad \lambda_4 = -\frac{g_2^2}{2} \tag{1.29}$$

$$\lambda_5 = \lambda_6 = \lambda_7 = 0 \qquad m_{12}^2 = m_A^2\cos\beta\sin\beta. \tag{1.30}$$

To break the electroweak symmetry in the MSSM, the two doublets of complex scalar fields have to be of opposite hypercharge

$$H_1 = \begin{pmatrix} H_1^0 \\ H_1^- \end{pmatrix} \text{ with } Y_{H_1} = -1 \quad , \quad H_2 = \begin{pmatrix} H_2^+ \\ H_2^0 \end{pmatrix} \text{ with } Y_{H_2} = +1. \tag{1.31}$$

The scalar potential involving the Higgs fields is given by

$$\begin{aligned} V_H &= (|\mu|^2+m_{H_1}^2)|H_1|^2 + (|\mu|^2+m_{H_2}^2)|H_2|^2 - \mu B\epsilon_{ij}(H_1^iH_2^j + \text{h.c.}) \\ &\quad + \frac{g_2^2+g_1^2}{8}(|H_1|^2-|H_2|^2)^2 + \frac{1}{2}g_2^2|H_1^\dagger H_2|^2, \end{aligned} \tag{1.32}$$

where μ is a mass parameter. Expanding the Higgs fields in terms of their charged and neutral components and defining the mass squared terms

$$\overline{m}_1^2 = |\mu|^2+m_{H_1}^2\,,\ \ \overline{m}_2^2 = |\mu|^2+m_{H_2}^2\,,\ \ \overline{m}_3^2 = B\mu \tag{1.33}$$

we obtain

$$\begin{aligned} V_H &= \overline{m}_1^2(|H_1^0|^2+|H_1^-|^2) + \overline{m}_2^2(|H_2^0|^2+|H_2^+|^2) - \overline{m}_3^2(H_1^-H_2^+ - H_1^0H_2^0 + \text{h.c.}) \\ &\quad + \frac{g_2^2+g_1^2}{8}(|H_1^0|^2+|H_1^-|^2-|H_2^0|^2-|H_2^+|^2)^2 + \frac{g_2^2}{2}|H_1^{-*}H_1^0 + H_2^{0*}H_2^+|^2 \end{aligned} \tag{1.34}$$

Just as in the SM Higgs mechanism, we require that the minimum of the potential V_H breaks the $\mathrm{SU(2)_L}\times\mathrm{U_Y}$ group while preserving the electromagnetic symmetry $\mathrm{U(1)_Q}$. At the minimum of the potential $V_H^{\min}$, the vev of the field H_1^- can be chosen equal to zero, $\langle H_1^-\rangle$=0, because of SU(2) symmetry, and at $\partial V/\partial H_1^-$=0, we also have $\langle H_2^+\rangle$=0.

There is therefore no breaking in the charged directions and the QED symmetry is preserved.

The neutral components of the two Higgs fields develop vevs

$$\langle H_1^0 \rangle = \frac{v_1}{\sqrt{2}} \text{ and } \quad \langle H_2^0 \rangle = \frac{v_2}{\sqrt{2}} \tag{1.35}$$

Minimising the scalar potential at the electroweak minimum, $\partial V_H / \partial H_1^0 = \partial V_H / \partial H_2^0 = 0$, and using the relation

$$(v_1^2 + v_2)^2 = v^2 = \frac{4M_Z^2}{g_2^2 + g_1^2} = (246 \text{ GeV})^2, \tag{1.36}$$

we obtain:

$$B\mu = \frac{(m_{H_1}^2 - m_{H_2}^2)\tan 2\beta + M_Z^2 \sin 2\beta}{2} \mu^2 = \frac{m_{H_2}^2 \sin^2\beta - m_{H_1}^2 \cos^2\beta}{\cos 2\beta} - \frac{M_Z^2}{2}.$$

These relations show explicitly that if m_{H_1} and m_{H_2} are known together with $\tan\beta$, the values of B and μ^2 are fixed while the sign of μ stays undetermined.

To obtain the Higgs physical fields and their masses, the two doublet complex scalar fields H_1 and H_2 are developed around the minimum into real and imaginary parts

$$H_1 = (H_1^0, H_1^-) = \frac{1}{\sqrt{2}} \left(v_1 + H_1^0 + iP_1^0 \ , \ H_1^- \right)$$
$$H_2 = (H_2^+, H_2^0) = \frac{1}{\sqrt{2}} \left(H_2^+ \ , \ v_2 + H_2^0 + iP_2^0 \right), \tag{1.37}$$

where the real parts correspond to the CP-even Higgs bosons and the imaginary parts corresponds to the CP-odd Higgs and the Goldstone bosons. We can now diagonalise the mass matrices evaluated at the minimum

$$\mathcal{M}_{ij}^2 = \frac{1}{2} \frac{\partial^2 V_H}{\partial H_i \partial H_j} \bigg|_{\langle H_1^0 \rangle = v_1/\sqrt{2}, \langle H_2^0 \rangle = v_2/\sqrt{2}, \langle H_{1,2}^\pm \rangle = 0} . \tag{1.38}$$

One eigenvalue of the mass matrix is zero and corresponds to the Goldstone boson mass, while the other corresponds to the pseudoscalar Higgs mass and is given by

$$M_A^2 = -\bar{m}_3^2 (\tan\beta + \cot\beta) = -\frac{2\bar{m}_3^2}{\sin 2\beta} \tag{1.39}$$

The mixing angle which gives the physical fields β

$$\begin{pmatrix} G^0 \\ A \end{pmatrix} = \begin{pmatrix} \cos\beta & \sin\beta \\ -\sin\beta & \cos\beta \end{pmatrix} \begin{pmatrix} P_1^0 \\ P_2^0 \end{pmatrix} \tag{1.40}$$

and in case of the charged Higgs boson, the charged fields are obtained with the same rotation matrix

$$\begin{pmatrix} G^{\pm} \\ H^{\pm} \end{pmatrix} = \begin{pmatrix} \cos\beta & \sin\beta \\ -\sin\beta & \cos\beta \end{pmatrix} \begin{pmatrix} H_1^{\pm} \\ H_2^{\pm} \end{pmatrix}. \tag{1.41}$$

The charged Higgs boson mass is related to the W boson mass via

$$M_{H^{\pm}}^2 = M_A^2 + M_W^2. \tag{1.42}$$

The CP–even Higgs case boson masses are given by

$$M_{h,H}^2 = \frac{1}{2}\left[M_A^2 + M_Z^2 \mp \sqrt{(M_A^2 + M_Z^2)^2 - 4M_A^2 M_Z^2 \cos^2 2\beta}\right]. \tag{1.43}$$

The physical CP–even Higgs bosons are obtained from

$$\begin{pmatrix} H \\ h \end{pmatrix} = \begin{pmatrix} \cos\alpha & \sin\alpha \\ -\sin\alpha & \cos\alpha \end{pmatrix} \begin{pmatrix} H_1^0 \\ H_2^0 \end{pmatrix}, \tag{1.44}$$

where the mixing angle α is given by

$$\cos 2\alpha = -\cos 2\beta \, \frac{M_A^2 - M_Z^2}{M_H^2 - M_h^2}\ , \ \sin 2\alpha = -\sin 2\beta \, \frac{M_H^2 + M_h^2}{M_H^2 - M_h^2}. \tag{1.45}$$

Thus, the supersymmetric structure of the theory has imposed very strong constraints on the Higgs spectrum. Out of the six parameters which describe the MSSM Higgs sector, $M_h, M_H, M_A, M_{H^{\pm}}, \beta$ and α, only two parameters, are free parameters at the tree–level. In addition, a strong hierarchy is imposed on the mass spectrum, which reads at tree-level

$$M_H > \max(M_A, M_Z), \tag{1.46}$$

$$M_{H^{\pm}} > M_W \text{ and} \tag{1.47}$$

$$M_h \leq \min(M_A, M_Z) \cdot |\cos 2\beta| \leq M_Z \tag{1.48}$$

The Higgs boson couplings to the gauge bosons are obtained from the kinetic terms of the fields H_1 and H_2 in the Lagrangian

$$\mathcal{L}_{\text{kin.}} = (D^{\mu} H_1)^{\dagger}(D_{\mu} H_1) + (D^{\mu} H_2)^{\dagger}(D_{\mu} H_2), \tag{1.49}$$

and the Yukawa Lagrangian with the notation of the first fermion family is

$$\mathcal{L}_{\text{Yuk}} = -\lambda_u[\bar{u} P_L u H_2^0 - \bar{u} P_L d H_2^+] - \lambda_d[\bar{d} P_L d H_1^0 - \bar{d} P_L u H_1^-] + (\text{h.c.}). \tag{1.50}$$

The fermion masses are generated when the neutral components of the Higgs fields acquire their vevs and they are related to the Yukawa couplings by

$$\lambda_u = \frac{\sqrt{2} m_u}{v_2} = \frac{\sqrt{2} m_u}{v \sin\beta} \quad \text{and} \quad \lambda_d = \frac{\sqrt{2} m_d}{v_1} = \frac{\sqrt{2} m_d}{v \cos\beta}. \tag{1.51}$$

Expressing the fields H_1 and H_2 in terms of the physical fields, one obtains the Yukawa Lagrangian in terms of the fermion masses

$$\begin{aligned}\mathcal{L}_{\rm Yuk} &= -\frac{g_2 m_u}{2M_W \sin\beta}\left[\bar{u}u(H\sin\alpha + h\cos\alpha) - i\bar{u}\gamma_5 u\, A\cos\beta\right] \\ &\quad -\frac{g_2 m_d}{2M_W \cos\beta}\left[\bar{d}d(H\cos\alpha - h\sin\alpha) - i\bar{d}\gamma_5 d\, A\sin\beta\right] \\ &\quad +\frac{g_2}{2\sqrt{2}M_W}V_{ud}\left\{H^+\bar{u}[m_d\tan\beta(1+\gamma_5) + m_u\cot\beta(1-\gamma_5)]d + \text{h.c.}\right\} \quad (1.52)\end{aligned}$$

with V_{ud} the CKM matrix element which is present in the case of quarks. The additional interactions involving the neutral and charged Goldstone bosons G^0 and $G^\pm$ can be obtained from the previous equation by replacing A and $H^\pm$ by G^0 and $G^\pm$ and setting $\cot\beta = 1$ and $\tan\beta = -1$. The MSSM Higgs boson couplings to fermions are given by

$$\begin{aligned}G_{huu} &= i\frac{m_u}{v}\frac{\cos\alpha}{\sin\beta}\,, \quad G_{Huu} = i\frac{m_u}{v}\frac{\sin\alpha}{\sin\beta}\,, \quad G_{Auu} = \frac{m_u}{v}\cot\beta\,\gamma_5 \\ G_{hdd} &= -i\frac{m_d}{v}\frac{\sin\alpha}{\cos\beta}\,, \quad G_{Hdd} = i\frac{m_d}{v}\frac{\cos\alpha}{\cos\beta}\,, \quad G_{Add} = \frac{m_d}{v}\tan\beta\,\gamma_5 \\ G_{H^+\bar{u}d} &= -\frac{i}{\sqrt{2}v}V_{ud}^*[m_d\tan\beta(1+\gamma_5) + m_u\cot\beta(1-\gamma_5)] \\ G_{H^-u\bar{d}} &= -\frac{i}{\sqrt{2}v}V_{ud}[m_d\tan\beta(1-\gamma_5) + m_u\cot\beta(1+\gamma_5)] \quad (1.53)\end{aligned}$$

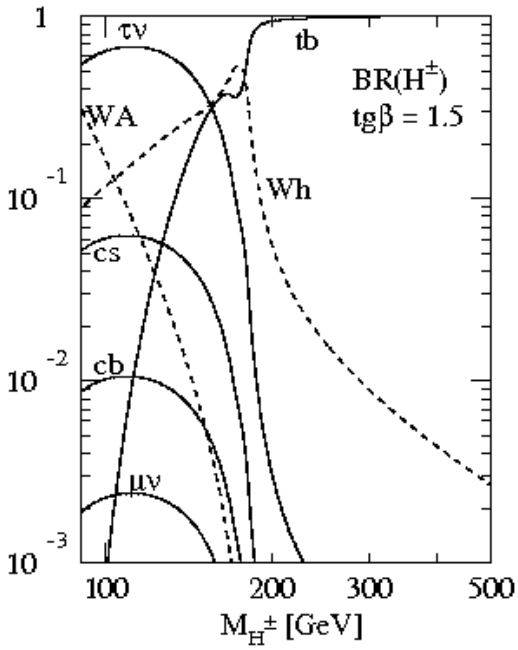

Figure 1.4: Branching ratios of the charged Higgs boson as a function of its mass $m_{H^\pm}$. [23].

Thus, for $\tan\beta > 1$, the couplings of the charged Higgs bosons $H^\pm$ are enhanced to isospin down–type fermions, while the couplings to up–type fermions are suppressed. So for large values of $\tan\beta$, the couplings to b quarks, $\propto m_b\tan\beta$, become very strong while those to the top quark, $\propto m_t/\tan\beta$, become rather weak.

The resulting branching ratios of the charged Higgs boson at $\tan\beta = 1.5$ are shown in Fig. 1.4 as a function of the boson mass. They imply that searches for light charged Higgs bosons, i.e. with masses lower than the top quark mass, will focus on $\tau\nu$ and cs decays, whereas heavy charged Higgs bosons searches will have to be performed in the tb channel.

1.2.3 Current charged Higgs boson searches

Current mass limits on the charged Higgs boson come from two distinct sources: direct charged Higgs boson searches are mainly performed at hadron colliders, the Tevatron and the LHC, whereas B factories provide limits on charged Higgs bosons through indirect searches.

1.2.3.1 Direct searches

The covered mass range for charged Higgs boson searches at the Tevatron is currently 60-300 GeV. Direct searches for mass resonances are performed as well as indirect searches in the form of deviations from SM branching ratios. The decay modes of the charged Higgs are dependent on its mass; if this is below the top and b quark mass $m_{H^\pm} < m_t + m_b$, the analysis focuses on $H^\pm \to \tau\nu_\tau, cs, A^0W^\pm, h^0W^\pm$ and $H^\pm \to t^*b \to W^\pm\bar{b}b$ final states. If however the charged Higgs boson is heavier, i.e. respecting $m_{H^\pm} > m_t + m_b$, then the most important decay is $H^\pm \to tb$. The most recent publications from D0 (including the D0 ratio method [24], the global fit method [25] and the high mass search [26]) as well as those from CDF (direct search [27]) show no evidence of a charged Higgs below 300 GeV, irrespective of the value of $\tan\beta$.

1.2.3.2 Indirect searches

For the moment, the indirect searches at b quark factories give the most stringent constraints on the charged Higgs boson parameters. The search channels distinguish between the leptonic, semileptonic and the inclusive radiative decay of B hadrons.

- **Leptonic decay mode**

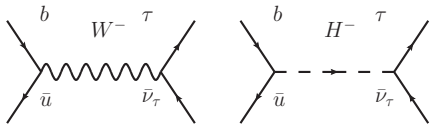

Figure 1.5: Feynman diagrams for the leptonic decay mode.

In the SM, the $B \to \tau\nu_\tau$ decay occurs via W boson mediation only, as shown with the diagram on the left of Fig. 1.5. In general, the B meson decay branching fraction BF into $l^+\nu_l$ is given by its SM value times an additional factor r_H, which encodes an eventual charged Higgs contribution, on the right in Fig. 1.5,

$$BF(B \to l^+\nu_l) = BF(B \to l^+\nu_l)_{SM} \times r_H. \tag{1.54}$$

For a type II 2HDM, r_H depends on the B meson and charged Higgs boson mass and $\tan\beta$ via

$$r_H = \left(1 - \frac{m_B^2 \tan^2\beta}{m_{H^\pm}}\right)^2. \tag{1.55}$$

Measurements from the Belle (in blue) and Babar (in green) collaborations with hadronic tags (in light colours) and semileptonic tags (in dark colours), summarised in Fig. 1.6(a), give the average value (in red) $\left[1.64 \pm 0.34\right] \times 10^{-4}$ [28], and an r_H coefficient of $r_H = 1.37 \pm 0.39$ compatible with unity. This translates into an excluded region for the $\tan\beta/m_{H^\pm}$ ratio, see Fig. 1.6(b), leading to the exclusion of the orange regions in the $(m_{H^\pm}, \tan\beta)$ plane, as depicted in Fig. 1.9.

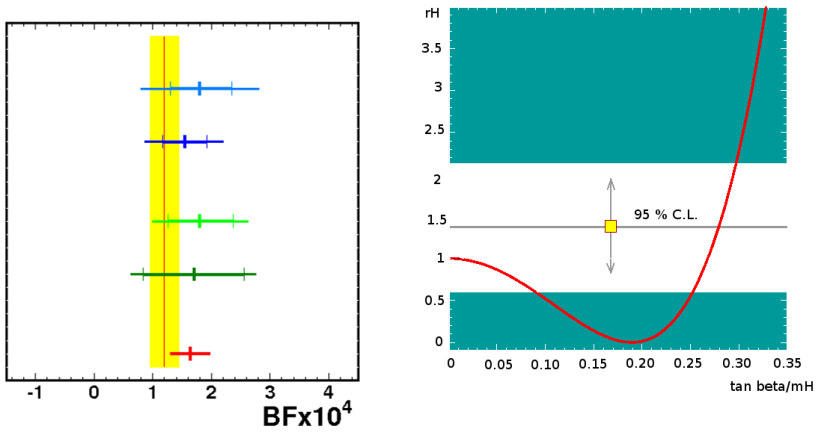

(a) (b)

Figure 1.6: BF measurements for the leptonic $B \to \tau\nu_\tau$ decay and inferred r_H values as a function of $\tan\beta/m_{H^\pm}$, together with the exclusion bands.

- **Semileptonic mode** The exchange of a charged Higgs boson may also alter the BFs for $B \to D^{(*)}\tau\nu_\tau$ decay. The observed BFs in the different channels exclude

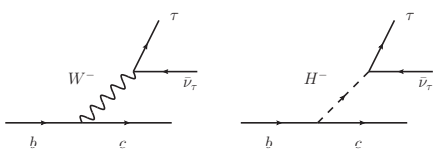

(a) (b)

Figure 1.7: SM (figure (a)) and charged Higgs exchange (figure (b)) Feynman diagrams for the semileptonic mode $B \to D^{(*)}\tau\nu_\tau$.

another region in the $(m_{H^\pm}, \tan\beta)$-plane, which is quite complementary to the one obtained via the $B \to \tau\nu$ decay, as it covers the leftover gap (in green) in Fig. 1.9.

- **Inclusive radiative decay** Charged Higgs boson exchange alters the BF for the $B \to X_s\gamma$ decay, shown in Fig. 1.8, placing a bound on the charged Higgs boson mass $m_{H^\pm} > 295$ GeV at 95 % C.L., independently of the value of $\tan\beta$, (in red) in Fig. 1.9.

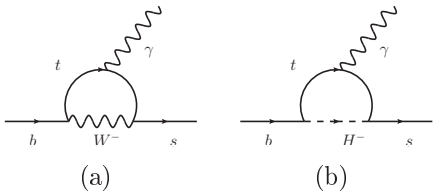

Figure 1.8: Feynman diagrams for the inclusive radiative decay.

The results for the three decay channels are compatible with the SM expectation values within their error bands, but the measured values are systematically higher than the predictions, which might be an indication of new physics and needs further investigation.

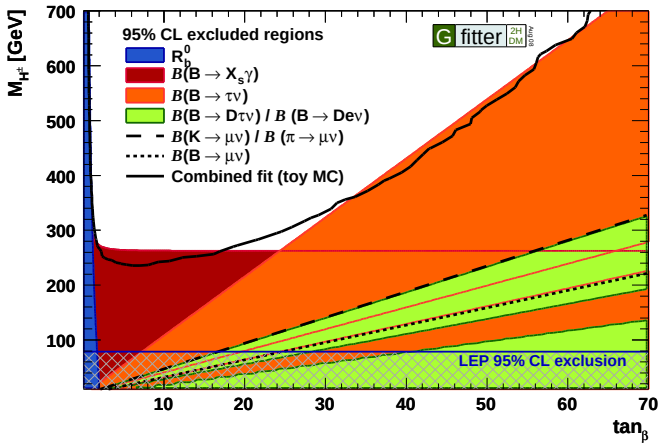

Figure 1.9: Excluded regions in the $m_{H^\pm}, \tan\beta$ plane due to B physics observables [29]

1.3 The top quark

1.3.1 Historic review

The quest for the top quark was triggered in 1977 by the discovery of the bottom quark at the Fermi National Accelerator Laboratory (Fermilab)[30]. To understand what the situation was at that particular moment, we need to go back to the year 1974. At that time, an unexpected, short-lived, massive resonance was found: the J/Ψ, a $c\bar{c}$ bound state. This didn't just prolong the ever-growing list of quarks as the fourth member, but was an essential confirmation of the unified theory of electroweak interactions, freshly developed at that point [31]. The GIM-mechanism states that quarks have to exist in pairs, and thus the c quark came to complete the doublet for the s quark. In 1975, the discovery of the τ, a third type of charged lepton, was a clear indication for a third generation of fundamental particles. This third copy of charged lepton came in

handy, since Kobayashi and Maskawa had just worked on CP violation in kaon decay and needed three quark pairs for their theory to be renormalisable. Now physicists turned to look for the third generation quarks. The first of them, the bottom quark, showed up in 1977 as a $b\bar{b}$-bound state, called the Υ resonance. This meant that the quest for its doublet partner had begun.

The way leading up to the actual discovery of the top quark was long and tortuous, and lasted for 14 years. A lot of initial searches were unsuccessful, forcing particle physicists to consider two options. Either the SM had to be rejected as a viable theory or the bottom quark was somehow a weak interaction singlet. This last statement was definitely ruled out at DESY in 1984 with the measurement of the forward-backward asymmetry in $e^+e^- \to b\bar{b}$ collisions [32]. If the $b\bar{b}$ production proceeded only via photon exchange, no asymmetry would be observed; the b quark would be produced in the positron direction as often as the electron direction. If however the b is part of an electroweak doublet, weak interaction is interfering with electromagnetic production. Since weak interactions were known to violate some fundamental symmetries, as parity for example in this case, there had to be a substantial forward-backward asymmetry. The expected value, computed assuming the validity of the SM, was about 25 % and would be zero for an isospin singlet. The outcome of the measurement gave $22.5 \pm 6.5\%$, confirming the status of the b quark as a member of an electroweak doublet. Since the doublet partner is also mandatory to leave the theory anomaly-free, the search for the top quark could and should be continued.

Top mass estimates relying on a natural progression in the mass scale of the different quarks pointed to a value of about 15 GeV. This meant that it could be observed at the running e^+e^- colliders, as for example at PETRA at DESY at the end of the 1970s. As nothing showed up in the data analysis, the top mass limit was pushed up to 23 GeV. The 1980s saw the limit go further up to 30 GeV with the TRISTAN collider in Japan, and finally SLC at SLAC and LEP observed no Z decay into $t\bar{t}$, so that a top with a mass lower than 45 GeV was ruled out. The search would have to be continued at hadron colliders.

The W and Z bosons were discovered at the proton-antiproton collider $Sp\bar{p}s$ at CERN, with a centre of mass energy of 450 GeV. In 1985 the UA1 collaboration found 12 candidate events in the leptonic channel whereas the expected background was 1.6 events, from hadrons misidentified as electrons. Since a 40 GeV top would produce 10 events, first papers were published assuming a top with a mass ranging between 30 and 50 GeV. This momentum was stopped just short of claiming a discovery. A more thorough analysis on a larger data sample with improved background models (particularly concerning $Wq\bar{q}$ production) showed that there was no 40 GeV top quark and, in 1988, the mass limit was at 44 GeV.

The advent of the Tevatron, a proton-antiproton collider at Fermilab with centre of mass energy of 900 GeV, started the competition between the american CDF and eu-

ropean UA2 collaborations. The years 1988 and 1989, known as *The Race for the Top*, have been a period filled with rumours swinging to and fro. The UA2 exclusion of a top with a mass lower than 69 GeV put an end to the frenzy, since this was the highest limit attainable at the $Sp\bar{p}s$. Another problem seemed to be dawning: if the top mass were higher than 85 GeV, the top would decay into a real W and a b, thus altering completely the $e\nu$, resp. $\mu\nu$ mass distribution, which would then be indistinguishable from W production! A way out of the conundrum was finally found with the presence of two additional b jets in the $t\bar{t}$ events, which would help increase the signal over background ratio. These analyses placed the mass at 91 GeV.

The first estimation for the top quark mass came not from direct observation at colliders, but through electroweak precision measurements. Computation of the so-called T-parameter predicted a top mass between $145 < m_t < 185$ GeV.

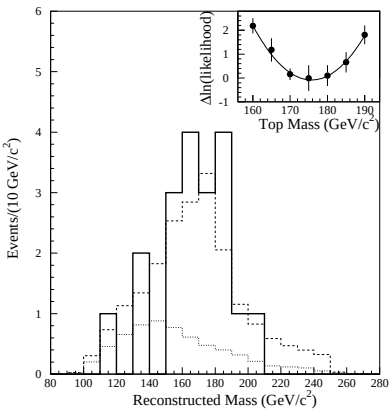

Figure 1.10: Reconstructed top mass distribution.

First observations were finally reported in 1994 [33] with the CDF detector, and its discovery was claimed by both experiments located at the Tevatron collider in 1995 [34, 35]. Fig. 1.10 shows the reconstructed mass distribution for events with an identified b quark and at least four additional jets (solid histogram). Also shown are the background shape (dotted histogram) and the sum of background and $t\bar{t}$ Monte Carlo estimation for a top quark mass $M_{top} = 175$ GeV/c^2 (dashed histogram), with the background constrained to the calculated value, $6.9^{+2.5}_{-1.9}$ events. The inset on the right shows the likelihood fit used to infer the top mass. Due to its large mass compared to the other five quarks, the top plays a special role since it has a very short lifetime compared to the hadronisation time, which can be defined as the time the colour field needs to cover the distance R_{had} which separates two adjacent partons. Considering this to be of the order of a few femtometers, hadronisation time is of the order $\tau_{had} = R_{had}/c$, i.e. $10^{-23}s$. If one considers top decay purely into Wb, the top quark has a width of about 1.5 GeV using a top mass of 173 GeV. This means that its lifetime is given by $\tau_{top} = h/(2\pi)\Gamma^{-1} = 5 \times 10^{-25}s$, indicating that the top quarks decays before even hadronising. As a consequence, there shouldn't be any top-antitop bound states, and no spin-depolarisation by chromomagnetic interactions occurs, allowing studies of spin dependence of the top's decay products. This riddance of the usual complications associated with the strong interaction and the large top mass make this quark an extremely interesting probe.

From then till the present day, the Tevatron has gathered information on various top quark properties such as its mass, decay width and charge. Besides pair production,

single top production via the s- and t-channel have also been observed two years ago by both experiments [36, 37]. Until 2010, the Tevatron has been the only machine allowing the direct of the heaviest member of the SM and its properties. However, many of those have either not been tested or are less known. With the start of the LHC, a second source of information has now become available to study the subject in depth.

1.3.2 Production at the Tevatron and at the LHC

At hadron colliders, top quark production occurs in what is separated into two different modes, because the event topology and thus research strategy will differ. The first possibility is to produce top quarks in pairs, as shown on Fig. 1.11, with a production cross section of ≈7 pb at the Tevatron[3] and 160 pb at the LHC with the current setup[4], or even more than 800 pb at 14 TeV. How exatly such a cross section can be measured at a hadron collider will be presented in detail in Chapter 7. The influence of the collider type and maximum centre of mass energy on the production proportions is best seen in the following comparison.

Considering a scattering of particles into two final state particles a and b, the phase space integration places a limit on the Mandelstam variable s of the hard process. The integration starts with the value which permits to produce the two final state particles at rest, i.e. the energy that has to be made available is the mass energy

$$s_{min} = x_1 x_2 s_H = 4\left(\frac{m_a + m_b}{2}\right)^2, \tag{1.56}$$

where x_1 and x_2 are the momentum fractions of the incoming partons. Considering $t\bar{t}-$production, $m_a = m_b = m_t$, under the assumption that both incoming partons carry the same fraction $x_1 = x_2 = x$, we get a rough idea of the mean value of x contributing to the production

$$< x >= \frac{2m_t}{\sqrt{s_H}}. \tag{1.57}$$

We see that the higher the collider energy, the smaller the values of x can be. For the Tevatron RunII ($\sqrt{s}$ = 1.96 TeV) the mean x value is around 2×10^{-1}, while for the current LHC collisions ($\sqrt{s}$ = 7 TeV) deeper values around 5×10^{-2} are probed, and even half of this could be attained if the design centre of mass energy of 14 TeV is some day reached. Of course our assumption that both momentum fractions are the same is not true in general, but if one value goes up, the other is permitted to go even further down. Since PDFs are dominated at low x by the gluon, all gluon fusion processes will be enhanced at the LHC with respect to the Tevatron.

[3]The NLO cross section is $\sigma_{t\bar{t}} = 6.7 \pm 10\%$ pb for $p\bar{p}$ collisions at $\sqrt{s} = 1.96$ TeV for $m_t = 175$ GeV [38].
[4]The approximated NNLO cross section is $\sigma_{t\bar{t}} = 164.57 + 11.45 - 15.78$ pb for pp collisions at $\sqrt{s} =$ 7 TeV for $m_t = 172.5$ GeV [39].

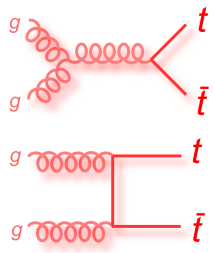

Figure 1.11: The $t\bar{t}$ production diagrams [40].

Since the Tevatron is a proton-antiproton collider, at 19.6 TeV for Run II, $t\bar{t}$ production occurs via $q\bar{q}$ initial states in 85 % and gg in the remaining 15 %. The fact that the LHC is a proton-proton collider which may attain the higher center of mass energy of 14 TeV radically alters the proportions of $t\bar{t}$ production to 10 % in the $q\bar{q}$ and 90 % in the gg channel [38]. In $t\bar{t}$ events both tops will decay into a W boson accompanied by a b quark. The different research channels are classified in relation to the decay products of the W : *dileptonic* refers to both Ws decaying into a lepton and a neutrino, *semi-leptonic* points to events in which one W decays into a lepton plus a neutrino and the other into quarks and *fully hadronic* specifies that both W bosons decay into quarks.

The second category of top production processes is single top production, which can be further separated into t-channel, Wt associated production and s-channel, as shown in Fig. 1.12.

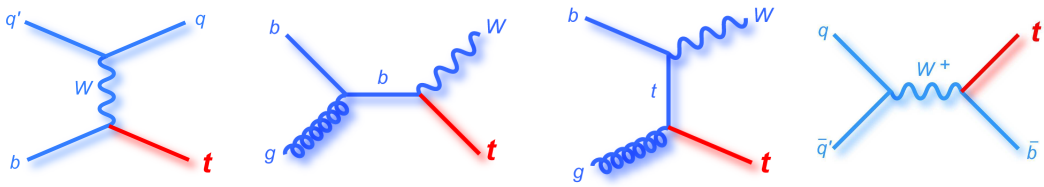

Figure 1.12: Single top production diagrams: the t-channel, the electroweak and the s-channel [40].

The production hierarchy is the same at the LHC and the Tevatron. Single top production at the Tevatron occurs with a cross section of 250 pb in the t-channel, 60 pb via Wt and 10 pb in the s-channel [38]. The evolution of the $t\bar{t}$ cross section at the LHC, including lepton and acceptance cuts of the ATLAS detector, can be seen in Fig. 1.13.

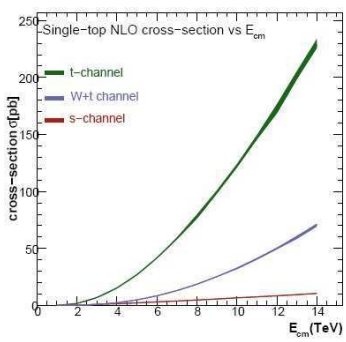

Figure 1.13: Comparison between the three single top production mechanisms. The NLO cross sections are shown as a function of the LHC center of mass energy [41].

Tevatron results The most recent results on the $t\bar{t}$ production cross section from CDF are summarised in Fig. 1.14(a). The recent cross section measurements for single top can be seen in Fig. 1.14(b).

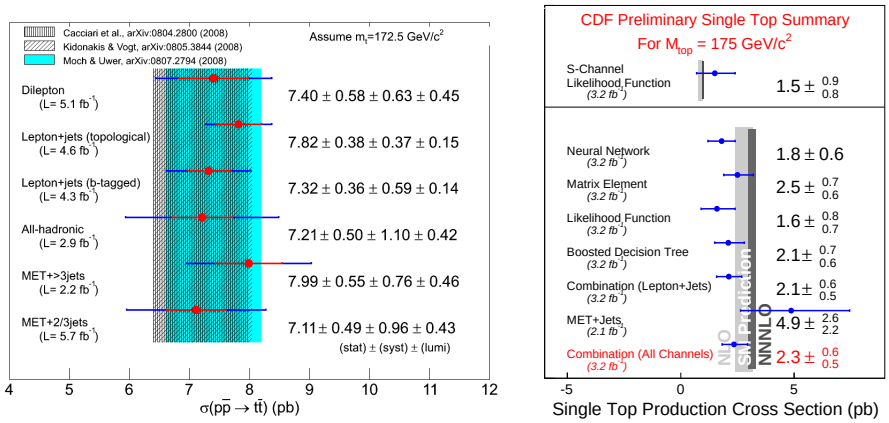

(a) Top pair production (b) Single Top production

Figure 1.14: Recent top production cross sections at the Tevatron.

From these production modes, top quark properties can be studied. The top mass has been extracted from data with two main techniques. The first is the templates method, which relies on the construction of templates that depend on the top mass. These templates are then fitted to the data. CDF has analysed 4.8 fb^{-1} of their data with this technique and obtains a top mass $m_t = 171.9 \pm 1.1(\text{stat.JES}) \pm 0.9(\text{syst.})$ GeV [42]. The second mass determination relies on the Matrix Element (ME) technique, in which a per-event probability $P(x, m_t)$ is calculated, where x denotes the final state parton momenta. This probability is obtained via a leading order matrix element calculation. Finally, the likelihood of the product of the probabilities is minimised, yielding the measured $t\bar{t}$ cross section. The D0 collaboration mass result is $m_t = 173.7 \pm 1.3(\text{stat. JES}) \pm 1.4(\text{syst.})$ GeV using 3.6 fb^{-1} of data [43], and the CDF collaboration has analysed 4.8 fb^{-1} and published a mass of $m_t = 172.8 \pm 0.9(\text{stat. JES}) \pm 0.8(\text{syst.})$ GeV [44]. The most precise result on the top mass comes from the latest CDF and DO combination [45]. Additional comments about the top mass measurements will be made in Section 2.3.1.

The SM states that the mass of a particle and its corresponding antiparticle should be the same. D0 has performed a study on the mass difference between top and antitop using the ME method, with a modified probability term $P(x, m_t, m_{\bar{t}})$, using 1 fb^{-1} and finds a resulting mass difference of $m_t - m_{\bar{t}} = 3.8 \pm 3.7$ GeV [46], compatible with the SM. This measure is still dominated by statistical uncertainties and will become very interesting once more data is available and at the LHC. The top width Γ_t is also under study by the CDF collaboration, which has analysed 4.3 fb^{-1} of data with the template method and this time fitted the width. They obtain a range of $0.4 < \Gamma_t < 4.4$ GeV at 68 % CL, and an upper limit of $\Gamma_t < 7.5$ GeV at 95 % CL [47]. The top charge has been

confirmed to be (2/3), in opposition to the (-4/3) predicted in exotic models [48, 49], and spin correlations have also been studied [50, 51].

LHC results After the first successful LHC run in 2010 and a total amount of about 35 pb^{-1} of collected data, the ATLAS and CMS collaborations have started seeing top quarks.

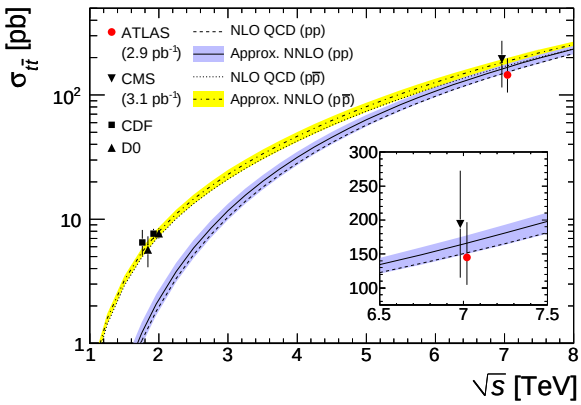

Figure 1.15: Production cross section of $t\bar{t}$ at the LHC and at the Tevatron compared to higher-order calculations.

The measurements of $t\bar{t}$ cross sections [52] at hadron colliders is summarised in Fig. 1.15. The inclusive top quark pair production cross section obtained with ATLAS by combining the semileptonic and dilepton final state analyses is $\sigma_{t\bar{t}} = 180 \pm 9$ (stat.) $\pm$ 15 (syst.) $\pm$ 6 (lumi.) pb [53]. Current preliminary results with 35 pb^{-1} indicate that single top production in the t-channel is almost at evidence level, and a first limit on Wt production has been set. This will be detailed in the second part of this thesis.

The LHC resumed 7 TeV collisions in March 2011, promising a tremendous amount of data for further investigation in 2011. Ongoing analyses in ATLAS are performed using 150 pb^{-1} of data and at total of 700 to 1000 pb^{-1} should be available this summer. Beyond the scope of production cross section and mass measurements, subjects which will be investigated are:

- the top quark charge [54],
- top spin correlations and W polarisation [55],
- anomalous Wtb vertex couplings [56],
- rare top quark decays and FCNC [57], and
- $t\bar{t}$ resonances [58].

History teaches us one thing: discovering new particles at unprecedented energies certainly is a very exciting quest, but the major effort should go into understanding thoroughly the backgrounds. For processes such as charged Higgs boson production, this backgrounds are SM events. Especially in the startup phase of the LHC which we are in now, it is important to focus on understanding the output of the detector an rediscover the SM properly, before even thinking about looking for deviations from it.

Ponder Stibbons was one of those unfortunate people cursed with the belief that if only he found out enough things about the universe it would all, somehow, make sense. The goal is the Theory of Everything, but Ponder would settle for the Theory of Something and, late at night, when Hex appeared to be sulking, he despaired of even a Theory of Anything.

Terry Pratchett, *"The last continent"*

2

From hadronic to partonic collisions

In the previous Chapter we briefly introduced the evolution of particle physics up to it's modern formulation, the Standard Model, and saw a possible extension of the SM scalar sector. In order to shed some light on a remaining dark corner, our aim is now to calculate charged Higgs boson production at colliders as precisely as possible, so as to have a reliable reference for comparisons to real collider data. The current Chapter reviews the main tools and formalisms which will be needed.

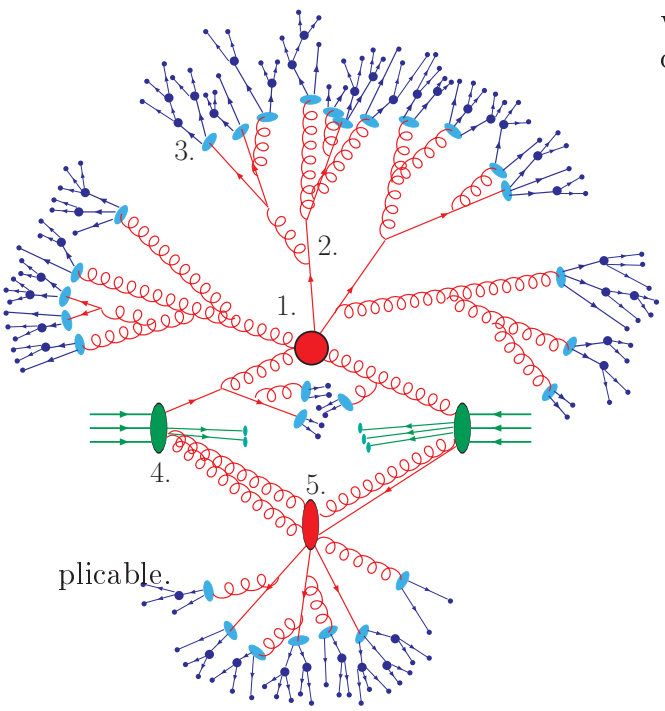

Figure 2.1: Schematic hadronic collision.

Fig. 2.1 sketches the main steps involved in the simulation of a hadronic collision.

1. Partons from the incoming hadron beams interact at high energies and produce many different particles, according to their production cross sections. This is the hard scattering.

2. The energetic coloured particles emit a plethora of radiated gluons and quarks, until the low energy limit is reached and perturbation theory is no more ap-

3. We then enter the domain of hadronisation where only effective models tuned on data are available at the moment.

4. The same is true for other low energy physics phenomena involved, as the distribution of the momentum sharing inside the hadron among the different partons or the beam remnant, for example.

5. It is possible that more than one hard scatter occurs in a hadron-hadron collision, and these multiple interactions render the event structure even more complex.

2.1 The strong coupling constant

In general, the parameters contained in the Lagrangian of a theory do not have a fixed value but may evolve with the energy of the considered process. For hadronic collisions, it is therefore important to know the evolution of the strong coupling constant, and see in which domain perturbative calculations are valid. The decrease of the strong coupling constant as a function of the energy Q can be seen in Fig. 2.2. This is very different from the electromagnetic force, who shows the exact opposite behaviour. In QED, there's only one charge, the electric charge e, and the electromagnetic coupling constant increases with the photon probe scale Q. The photon itself is not charged under $U(1)$.

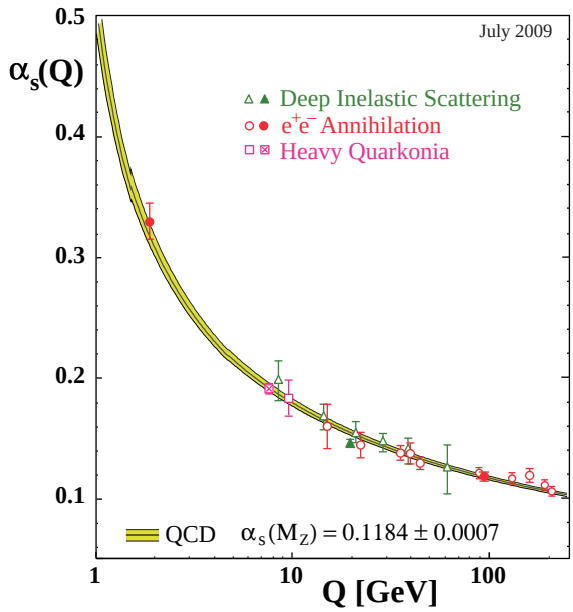

Figure 2.2: Evolution of the strong coupling constant with the energy. The straight line is calculated in perturbative QCD, the dots are measurements by various experiments. [59]

The physical reason for this behaviour is the screening effect. If the energy Q is small, it can only resolve large structures and the photon sees the central charge shielded by vacuum polarisation, like depicted on the left in Fig. 2.3. This reduces the effective charge seen by the photon probe. In terms of Feynman diagrams, these contributions arise from a virtual electron-positron exchange, as shown on the right of Fig. 2.3.

In QCD, the situation is somewhat different, since there are three different colour charges, R, G and B. If we take a B charge for example, the same shielding effect

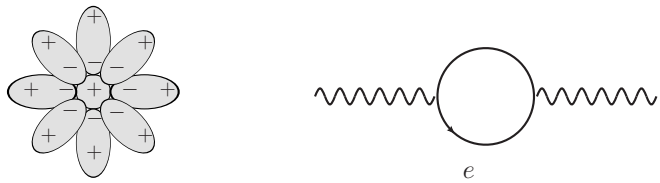

Figure 2.3: Vaccum polarization due to lepton exchange.

as in QED takes place, as shown on Fig. 2.4. This has an analogue Feynman graph representation, where now the gluon materialises for a short time into a quark-antiquark pair and gives a positive contribution to the coupling evolution.

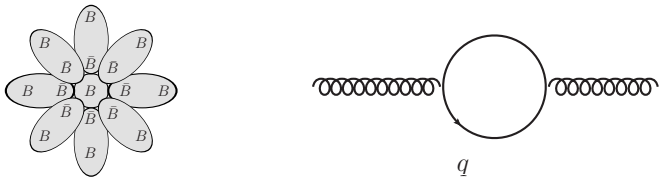

Figure 2.4: Vaccum polarisation correction due to quark exchange.

The difference with respect to QED is that in QCD the force carriers are also charged under $SU(3)$ and may alter the central charge. For example, a B quark may change into a R quark via gluon emission, as shown on the left in Fig. 2.5. We have to take into account the additional Feynman graph in which the gluon emits and reabsorbs another gluon.

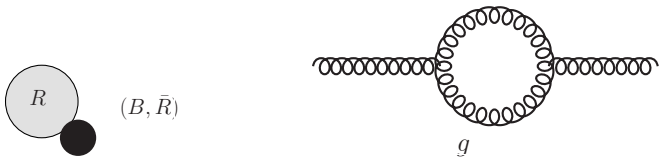

Figure 2.5: Vaccum polarization correction due to gluon exchange.

This contribution is negative and outweighs the positive one if the number of active[1] quarks is $N_f < 17$, as is the case for the SM.

So the coupling strength depends on the energy of the considered process. The dependence of the strong coupling with respect to the scale is logarithmic and is given by the renormalisation group equation (RGE)

$$Q^2 \frac{\partial \alpha_s(Q^2)}{\partial Q^2} = \beta\big(\alpha_s(Q^2)\big), \tag{2.1}$$

[1]By active quark, one means quarks which masses M_Q can be neglected with respect to the considered energy Q.

where the β function encodes the Feynman graph contributions we just reviewed. If the considered energy is high enough, the coupling becomes small and allows for a perturbative treatment of the quantities involved. Currently, the β function can be calculated up to the fourth order [59], but we will truncate the series at the first coefficient, since this is enough to support the argumentation.

$$\beta\big(\alpha_s(Q^2)\big) = -\beta_0\alpha_s^2(Q^2) + \mathcal{O}(\alpha_s^3) \tag{2.2}$$

$$= -\Big(\frac{33-2N_f}{12\pi}\Big)\alpha_s^2(Q^2) + \mathcal{O}(\alpha_s^3). \tag{2.3}$$

The number of active quark flavours at the energy scale Q is given by N_f. The $N_f < 17$ quoted previously comes from the requirement of the leading order term of the beta function β_0 to be positive.

The solution of the truncated differential Eq. (2.1) is given by

$$\alpha_s(Q^2) = \frac{\alpha_s(\mu^2)}{1+\alpha_s(\mu^2)\beta_0 \ln\frac{Q^2}{\mu^2}}. \tag{2.4}$$

This enables us to calculate the value of the coupling at a scale Q, if we have as reference a measured value of α_s at another scale μ. Another feature of QCD can be seen through this evolution, namely asymptotic freedom. Assuming β_0 to be positive, the coupling constant will indeed tend asymptotically to zero for very large scales. This means that if we consider processes taking place at high energies, not only will the coupling be small enough to allow a perturbative expansion of the considered quantities, but coloured particles can be treated as free from the point of view of the strong interaction. As Q decreases, the strong coupling constant grows, until it hits a singularity for

$$\lim_{Q\to\Lambda_{QCD}} \alpha_s(Q) = \infty. \tag{2.5}$$

The exact value of Λ_{QCD} depends on the perturbative expansion of the β function which has been used, but it generally is of the order of 1 GeV. A coupling of order one means that the perturbative formalism cannot be applied anymore and energy scales roughly below 1 GeV are therefore regarded as the nonperturbative region where confinement sets in.

The convergence problem of the pQCD series We have just mentioned that if the coupling is small enough, quantities of interest may be developed into a perturbative series. However, due to long-distance, non-perturbative effects, this series is not convergent. If we compute a physical quantity in terms of the small coupling

$$f(\alpha_s) \approx \sum_{n=0}^{\infty} f_n \alpha_s^n, \tag{2.6}$$

the coefficients f_n exhibit a factorial growth with respect to their order. Only in a free theory, where $\alpha_s = 0$, the series becomes a simple Taylor expansion. For $(\alpha_s \to 0)$

however, the series can at best be asymptotic to $f(\alpha_s)$, but does not uniquely define $f(\alpha_s)$. Now one may wonder what the meaning of perturbation theory may be when it does not converge. But asymptotic convergence is not totally unsatisfactory, because if α_s is sufficiently small, the difference between $f(\alpha_s)$ and and another expression $g(\alpha_s)$ may be numerically small and perturbation theory may give a well-approximated answer.

Factorisation The evolution of the coupling constant defines two regimes, one for which perturbative QCD (pCQD) is valid, an one in which we have to model non-perturbative effects. Those two regimes can be clearly separated in virtue of the the factorisation theorem. The hadronic cross section for two incoming hadrons with momenta $p_{1,2}$ can be computed by using the factorisation formula [60]

$$\sigma(p_1, p_2; Q) = \sum_{a,b} \int dx_1 dx_2 f_a f_b \hat{\sigma}_{ab} + \mathcal{O}((\Lambda_{QCD}/Q)^p), \tag{2.7}$$

where the parton distribution functions (PDFs) $f_a = f_{a/h_1}(x_1, Q^2)$ encode the probability of finding a parton a in hadron h_1 with momentum fraction x_1 at scale Q. The term $\hat{\sigma}_{ab} = \hat{\sigma}_{ab}(x_1 p_1, x_2 p_2; Q; \alpha_s(Q))$ stands for the partonic cross section and $\mathcal{O}((\Lambda_{QCD}/Q)^p)$ encodes non-perturbative contributions such as hadronisation effects, multiparton interactions and contributions from the underlying event. The PDFs $f_{a/h(x,Q^2)}$ at a fixed scale Q are not computable in perturbation theory but their scale dependence can be controlled perturbatively via the Dokshitzer-Gribov-Lipatov-Altarelli-Parisi (DGLAP) equations [61, 62, 63]. The structure of the right-hand side of Eq. (2.7), i.e. the sharing out in terms of perturbative process-dependent partonic cross sections and non-perturbative process-independent PDFs is subject to some degree of arbitrariness, called factorisation-scheme dependence. Since physical quantities cannot dependent on the unphysical factorisation scales, perturbative corrections beyond leading order of the partonic cross section are factorisation-scheme dependent, in order to compensate for the corresponding dependence in the PDFs. If the perturbative series of the partonic cross section and the PDFs is truncated, this compensation is not exact and the theoretical prediction will be tainted with uncertainties. The renormalisation scale μ_R is the scale at which the strong coupling is evaluated. The factorisation scale on the other hand separates the nonperturbative effects in the PDFs from the perturbative interactions in the partonic cross section. It is common use to take $\mu_R = \mu_F = Q$, since on physical grounds these scales have to be of the same order as Q, but their values cannot be unambiguously fixed. If the quantities that enter Eq. (2.7) are calculated at the n-th order in perturbation theory, the final result exhibits a residual μ_F, μ_R-dependence of the $(n+1)$-th order, reflecting the absence of the missing higher-order terms. Varying those scales estimates the theoretical uncertainty caused by the truncation of the perturbative series. This is generally done to give an error band on the theoretical predictions.

2.2 Parton distribution functions

We will now take a look at the first ingredient we need which cannot be calculated from first principles but needs experimental input: the parton distribution functions. There are several methods which allow insight into the structure of hadrons. We will mainly concentrate on deep inelastic scattering. This section is intended only as a brief glance over a subject which fills quantity of excellent textbooks and dedicated reviews [9, 64]. But it is important to keep in mind that different sets of PDFs currently exist, each may implement theoretical quantities at different levels of precision. There are also differences in the considered input data, the ad-hoc parametrisations and the fitting method, resulting in different albeit complementary uncertainties. Since this has a notable impact on predicted cross sections as well as the data analysis we will carry on later, it is important to investigate where these uncertainties come from.

2.2.1 Measuring structure functions and cross sections

Deep Inelastic scattering (DIS)

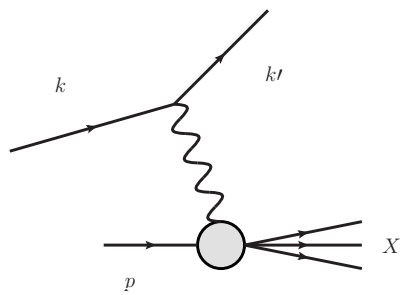

Figure 2.6: DIS of a lepton probe on a hadron.

The parton model is based on the idea that a hadron can be described as a collection of independent partons with small transverse momentum. In DIS, a lepton scatters off a parton via vector boson exchange, as displayed in Fig. 2.6.

The characteristic kinematical variables of DIS are

- the momentum transfer
$$Q^2 = -q^2 = -(k - k')^2, \tag{2.8}$$
where $k(k')$ is the momentum of the incoming (outgoing) lepton,
- the Bjorken scaling variable
$$x = \frac{Q^2}{2p \cdot q}, \tag{2.9}$$
where p is the hadron momentum,
- and the energy fraction y which the lepton has lost in the scattering process, given in the nucleon rest frame
$$y = \frac{q \cdot p}{k \cdot p}. \tag{2.10}$$

The momentum transfer Q can be seen as the magnifying power of the lepton probe, since it allows resolve distances of the order of $d \approx \frac{hc}{2\pi Q} \approx \frac{0.2}{Q}$ fm, where Q is to be given in GeV.

Depending on the nature of the lepton probe, different interactions come into play which are sensitive to different constituents of the hadron. For charged current interactions (CC), where a W boson is exchanged, the probe which scatters on the free nucleon N can either be a lepton $lN \to lX$ or a neutrino $\nu N \to lX$. X is any kind of hadron system. If the exchanged particle is a virtual photon γ or a Z boson, it is a neutral current (NC) interaction $lN \to lX$. If the lepton probe is a positron, the exchanged W has positive charge and the cross section is sensitive to down-type quarks and up-type antiquarks. At leading order, the differential cross-sections can be written in terms of structure functions F^i

$$\frac{d^2\sigma^i}{dxdy} = \frac{4\pi\alpha^2}{xyQ^2}\eta^i\Big[\Big(1 - y - \frac{x^2y^2M^2}{Q^2}\Big)F_2^i + y^2xF_1^i \mp \Big(y - \frac{y^2}{2}\Big)xF_3^i\Big], \tag{2.11}$$

where M is the mass of the nucleon, and i can be either CC or NC. The minus sign is valid if the incoming lepton is a positron or an antineutrino, a plus sign stands for incoming electrons or neutrinos. For unpolarised electron/positron beams, $\eta^{NC} = 1$ and $\eta^{CC} = (1 \pm \lambda)^2 \frac{1}{2}\Big(\frac{G_F M_W^2}{4\pi\alpha}\frac{Q^2}{Q^2+M_W^2}\Big)^2$, where the sign is given by the electron charge and λ is its helicity. The CC and NC cross sections tend to the same behaviour at high energy, exhibiting the unification of weak and electromagnetic interaction, which can be observed in Fig. 2.7. For low Q^2 values photon exchange dominates and thus the NC cross section is several orders of magnitude larger than the CC, whose contribution is dampened due to the W boson propagator.

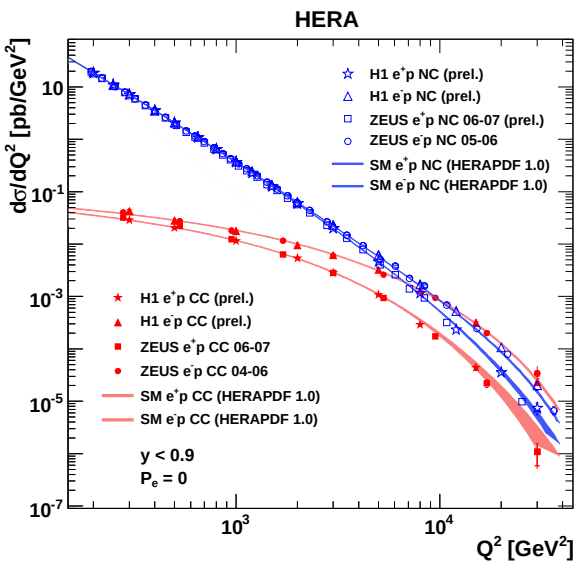

Figure 2.7: Differential CC and NC inclusive cross sections as a function of Q^2, measured at HERA [65].

The structure functions are not calculable in pQCD. At lowest order, they can be given directly in terms of nonperturbative PDFs f, as F_2 for example:

$$F_2(x, Q^2) = x \sum_q e_q^2 f_{q/p}(x), \tag{2.12}$$

where e_q is the electric charge of quark q. What is observed in general is that in the Bjorken limit, i.e. for $(Q^2, \nu) \to \infty$ and fixed x, the structure functions obey an approximate scaling law, depending only on the dimensionless variable x

$$F_i(x, Q^2) \to F_i(x). \tag{2.13}$$

This Bjorken scaling indicates that the probe is scattered-off from point-like constituents. If this wasn't the case, the structure functions would exhibit a dependence on the ratio Q/λ, where $1/\lambda$ would be the characteristic length of the constituents' size. QCD, however, violates Bjorken scaling trough power-corrections which induce logarithms of Q^2. Since the parton transverse momentum inside the hadron is not restricted to be small, but can eventually get large via gluon emission with probability proportional to $\alpha_s dk_T^2/k_T^2$, in which the integral extends to the kinematic limit $k_T^2 \approx Q^2$, these types of emissions can give rise to terms proportional to $\alpha_s \ln Q^2$ which break scaling. These violations are a particular property of renormalisable gauge theories involving point-like interactions between fermions and vector bosons. Thus, taking into account higher-order contributions, the structure function F_2 now reads

$$F_2(x, Q^2) = x \sum_{q\bar{q}} e_q^2 \Big[q_0(x) + \frac{\alpha_s}{2\pi} \int_x^1 \frac{dz}{z} q_0(x) \Big(P(x/z) \ln \frac{Q^2}{\kappa^2} + C(x/z) \Big) + \cdots \Big]. \tag{2.14}$$

where the structure functions F_i parametrise the structure of the target as seen by the virtual probe at scale Q via the bare PDFs $q_0 = f$. Here we are exactly in the same situation as with the strong renormalisation coupling, which we will detail in section, namely that $q_0(x)$ can be seen as an unmeasurable, bare distribution into which the collinear singularities can be absorbed at some scale μ. The functions P are the Altarelli-Parisi splitting functions and give the probability of a particle to disintegrate further. Their exact expressions will be used in the dipole formalism later on and can be found in App. B. The C terms are the coefficient functions. The structure function F cannot be calculated from first principles in pQCD since it receives contributions from long-distance effects, but it can be measured in structure function data. Of course, as we will see in the chapter about renormalisation, some arbitrariness exists as to how the finite contributions are treated during the renormalisation procedure and the outcoming PDFs are renormalisation-scheme dependent. The higher-order terms involve the splitting functions, which favour collinear emissions. Thus the majority of the emissions which modify a parton's momentum are collinear and it is then natural to see these emissions as a modification to the structure of the proton, rather than including it in the coefficient function of the parton's interaction with the vector boson coming from the probe. It is this separation which is somewhat arbitrary and is given by the factorisation scale μ_F.

Emissions above the scale μ_F are included in the coefficient functions, below μ_F they are considered as being part of the PDFs. Since Eq. (2.14) must be independent of the arbitrary scale μ^2, we can establish a renormalisation group equation for the evolution of the structure functions. This will lead to DGLAP evolution equations for the PDFs with respect to Q^2. They can be written as a matrix system

$$t\frac{\partial}{\partial t}\begin{pmatrix} q_i(x,t) \\ g(x,t) \end{pmatrix} = \frac{\alpha_s(t)}{2\pi}\sum_{q_j,\bar{q}_j}\int_x^1 \frac{dz}{z}\begin{pmatrix} P_{q_iq_j}(x/z,\alpha_s(t)) & P_{q_ig}(x/z,\alpha_s(t)) \\ P_{gq_j}(x/z,\alpha_s(t)) & P_{gg}(x/z,\alpha_s(t) \end{pmatrix}\begin{pmatrix} q_j(z,t) \\ g(z,t) \end{pmatrix} \tag{2.15}$$

where $t = \ln Q^2$ and $g = f_g, q_i = f_{q_i}$ are the PDFs for the gluon and i-flavoured quark.

DIS experiments are used to extract physical quantities like cross sections or structure functions, from which one can then infer parton distributions, depending on the perturbation series and the factorisation schemes. The PDFs are thus effective quantities and can be used for predictions if the same theoretical scheme and order of perturbation is used.

Main DIS experiments The HERA accelerator (Hadron-Electron Ring Accelerator) at DESY in Hamburg has collided protons with electrons or positrons during 15 years and operations have stopped in 2007. The centre of mass energy of the collisions was 318 GeV. A large quantity of useful data on the hadron structure has been obtained, which are used in most PDF fits. The main experiments located on the accelerator were H1 and ZEUS. Although the accelerator itself has been shut down, both collaborations recently published combined results in order to reduce the impact of systematic errors [65].
The BCDMS (Bologna-CERN-Dubna-Munich-Saclay) was a fixed-target experiment at CERN where muons were scattered on hydrogen and deuterium atoms.
The CCFR (Chicago-Columbia-Fermilab-Rochester) collaboration collected data from two fixed-target runs at Fermilab, Chicago, in 1985 (experiment E744) and 1987-88 (experiment E770).

Additional processes DIS experiments are not the only possibility to gain access to the hadron constituents. In particular, DIS data are insufficient to determine accurately some aspects of PDFs, such as the flavour composition of the quark-antiquark sea or the gluon distribution at large x. The DIS method can only indirectly determine the gluon distribution, since the exchanged boson is only interacting with quarks at LO, i.e. it probes valence quarks at large x and sea quarks at low x, and infers the gluon distribution from them via the DGLAP equations. An alternative method would be to use gluon-induced processes, as the measurements of jets or heavy meson production rates. This can be done at NLO in DIS, or using hadron-hardon collision data (in inclusive jet production).

Further insight in the proton structure can also be gained via Drell-Yan processes, in which high-mass lepton pairs are produced from electroweak boson decay in hadron-hadron collisions. The first observed Drell-Yan processes were electron-positron or

muon-antimuon pairs from virtual photons, but since then the available energy in colliders has increased and Drell-Yan data now includes contributions from W and Z boson production. The main advantage of Drell-Yan processes are the colourless final states, which has allowed to use it as a test for hadron-hadron collisions of the factorisation approach used before in DIS.

Direct photon production in hadron-hadron collisions are used to constrain the gluon distribution in the hadron at medium and large x, because they occur via QCD Compton scattering $gq \to q\gamma$ and annihilation processes $q\bar{q} \to \gamma g$ at order $\alpha_s \alpha_{em}$. The experimental advantage is that the energy resolution of photons is more precise than for jets. A photon deposits all its energy in the electromagnetic calorimeter, whereas jets are complex objects, extending over both the electromagnetic and the hadronic calorimeter, and undergo fragmentation and hadronisation. The major drawbacks of this channel are the relative low production frequency with respect to QCD jets, and the background from misidentified pions.

Nowadays, one can classify experiments loosely into two categories, depending on their relation to the PDFs. The first category are experiments whose main goal is the study of the hadron structure, las the two experiments at HERA or fixed target. The input data is obtained at low scales Q^2 and used to fashion PDFs. The second category are the PDF users, mostly the Tevatron and the LHC. They need the PDFs as input, PDFs which have been evolved perturbatively up to the much higher Q^2 scale, and produce general physics results. Of course, they will also allow the direct study of the hadrons at those high Q^2 scales, but that is not their primary objective. The gap in energy scales between and the accessible x range at the two categories is illustrated in Fig. 2.8.

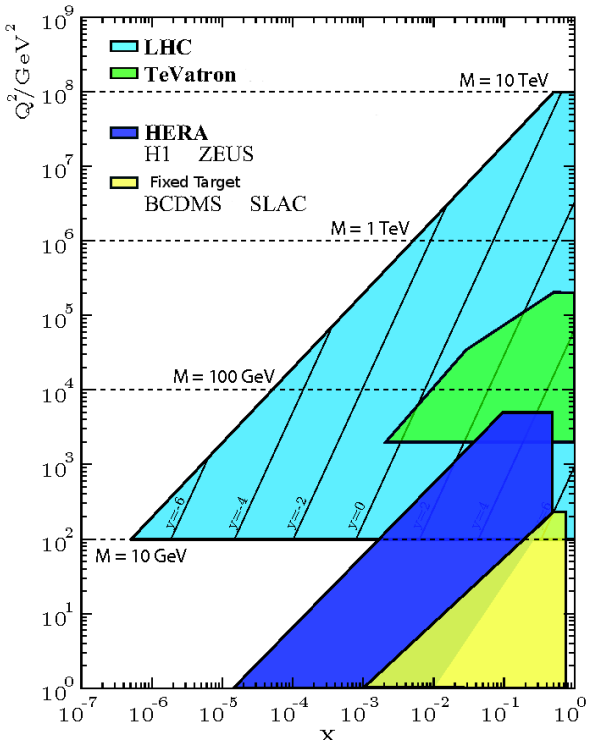

Figure 2.8: Range in x and Q for different collider and DIS experiments [66].

2.2.2 Constructing PDFs with global fits

Our knowledge of the structure of hadrons is not static, but consists of an active field where new data sets become available over time and statistical treatments of global fits evolve. Thus, the various PDF collaborations publish new PDFs on a regular basis, and on average a new PDF set becomes available once a year. In the following section, we will detail the general concepts of the PDF construction and briefly glance at the most commonly used PDF sets, both in the theoretical and experimental community. While for generator codes it is simpler to update production cross section values with the newest PDF set, this is almost impossible to do for experimental Monte Carlo samples, since the whole production and approval chain is long and tedious. We will concentrate on CTEQ, in particular CTEQ 6 and CTEQ 10, MSTW2008 and NNPDF. They globally rely on the same input data sets and the small differences are outlined in their respective paragraphs. There's some tradeoff between the size of the input data sets and their consistency with sets from other experiments, which we will see clearly for the latest CTEQ PDFs. A larger difference exists between (CTEQ, MSTW) and NNPDF, since the first two rely on a Hessian approach for the fit while the latter makes use of Monte Carlo pseudo-data replicas.

Global fit Parton distribution functions are obtained from a global analysis using a best-fit method on parametrised, somewhat *ad hoc* functionals, by selecting the global minimum of a χ^2 function. A global fit of N_e data points D_i from experiment e to their theoretical values T_i given by the parametrisation, not including correlated errors, is performed with the following χ^2 function

$$\chi_0^2 = \sum_e \sum_{i=1}^{N_e} \frac{(D_i - T_i)^2}{\sigma_i'^2}, \tag{2.16}$$

where the first sum is to be taken over all experiments and the second over all data points from each experiment, and where the error σ_i' is composed of the statistical error σ_i and the point-to-point systematic error Σ_i, added in quadrature $\sigma_i'^2 = \sigma_i^2 + \Sigma_i^2$. This is the simplest way to look for optimal global fits but has only limited use in assessing the uncertainties of the fit. If correlated errors are present between different types of data, one could use the covariance matrix or, equivalently, an extended χ^2 function. The collaborations have been facing some practical problems due to the large number of data points and instabilities in the inversion of the covariance matrix and have therefore been forced to devise an alternative method.

The fit determines the optimal value of the parameters in the parametrisation. To assess the uncertainty on these values, error set PDFs are constructed by shifting the value for each parameter with a certain tolerance T, as depicted in Fig. 2.9.

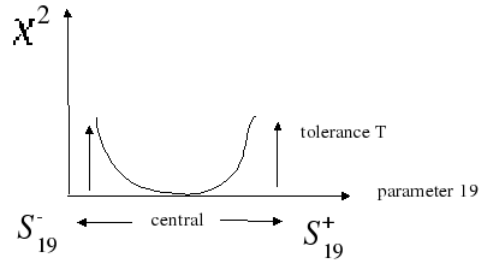

Figure 2.9: Example of the construction of an error set for some parameter. The central value is given by the minimum of the χ^2 fitting function. Error sets are constructed by shifting to the left as well as to the right, since the χ^2 function might in some cases be asymmetric.

Treatment of heavy quarks Various schemes for the treatment of heavy quarks exist in global parton analyses. The simplest evolving procedure is by treating all quarks as massless, but to turn on the distributions at the appropriate transition points, i.e. when the scale reaches the quark mass $Q^2 = m_q^2$. This implies that we assume that the heavy-quark distributions evolve according to the splitting functions for massless quarks. This is motivated by the observation that the massive quarks behave as massless partons at high scales, corresponding exactly to the approximation we are doing in the calculation of the partonic cross section, where we put the masses of the incoming quarks to zero. In the MSTW2008 framework, this is referred to the zero-mass variable flavour number scheme (ZM-VFNS), which is a somewhat misleading name because there actually is a mass dependence included in the boundary conditions for the evolution. The parton distributions are related to each other perturbatively in the different quark number regimes through[2]

$$f_j^{n+1}(\mu_F^2) = \sum_k A_{jk}(\mu_F^2/m_q^2) \otimes f_k^n(\mu_F^2) \tag{2.17}$$

when the number of active quarks is increased from n to $n+1$ and the scale has been fixed at the factorisation scale $Q^2 = \mu_F^2$. The perturbative matrix elements $A_{jk}(\mu_F^2/m_q^2)$ contain logarithms of the form $\ln(\mu_F^2/m_q^2)$ and are known up to $\mathcal{O}(\alpha_s^2)$, resp.$\mathcal{O}(\alpha_s^3)$. Exactly how many quarks are switched on as we pass by their transition point is indicated in the second part of the scheme name. If only the light flavours are kept in the parton distributions, it is the 3-flavour scheme (3FS). Likewise, including the charm quark is included in the evolution above $Q^2 = m_c^2$ generates 4-flavour PDFs in the 4-flavour scheme. The global MSTW parton analysis includes also the b-quark distribution above $Q^2 = m_b^2$, but not the t-quark above $Q^2 = m_t^2$. This is the set we are going to work with for charged Higgs boson production, and it is a 5-flavour set of PDFs in a 5FS. However, since the ZM-VFNS is well suited for energy scales way above the the mass threshold and ignores corrections of the order of $\mathcal{O}(m_q^2/Q^2)$ to the coefficient functions,

[2] The symbol $\otimes$ is shorthand for $f \otimes g \equiv \int_x^1 \frac{dx'}{x'} f(x') g\left(\frac{x}{x'}\right)$.

it is not appropriate for low scale studies where $Q^2 \approx m_q^2$. But this region is exactly where the PDF input data comes from. We have seen that there exist two approaches in which the treatment of heavy flavour is relatively simple, namely the 3FS or fixed flavour scheme at low scale $Q^2 \lesssim m_c^2$, and the ZM-VFNS at higher scales $Q^2 >> m_q^2$. For parton analysis we need a scheme, called general mass variable flavour number scheme (GM-VFNS), which smoothly connects these two different regions.

The bottom quark PDF The bottom PDFs is generated dynamically through the DGLAP equations from the gluon distribution for scales larger than the bottom input mass $Q^2 > m_b^2$. Due to the large uncertainty on the gluon distribution and the fact that different collaborations use different b masses m_b, the resulting bottom PDF can be quite different, as is shown on Fig. 2.10(a). Since charged Higgs production is strongly dependent on the bottom and gluon PDFs, it is important to assess these uncertainties. The bottom mass uncertainty can be evaluated using dedicated PDFs, in which m_b has been varied. Since the point at which the bottom PDF is turned on and since flavour PDFs are linked to each other through sum rules, this affects all PDFs in the global fit. The standard bottom quark PDF for different PDF collaborations can be seen in Fig. 2.10(a), whereas Fig. 2.10(b) compares the variable mass-PDFs from MSTW2008.

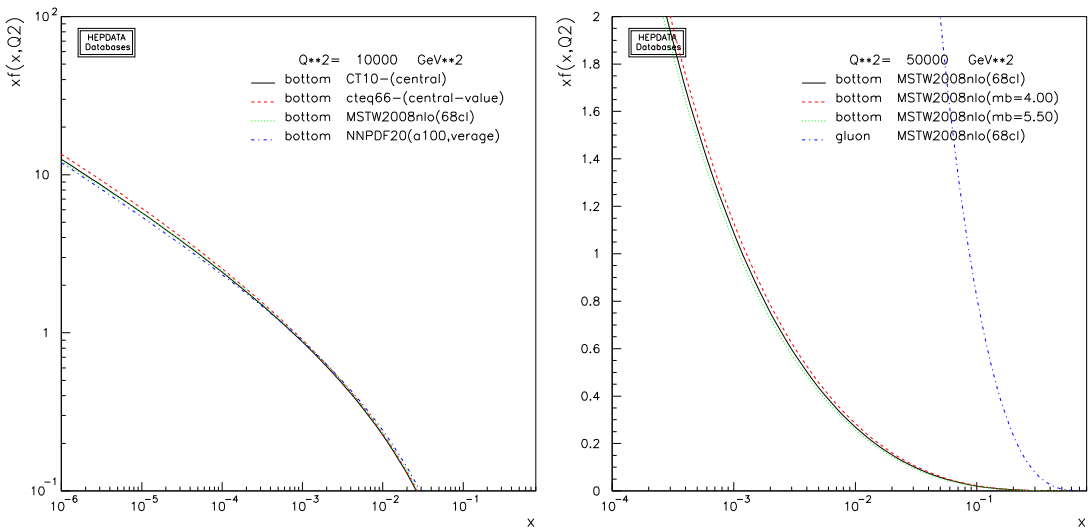

(a) Bottom quark PDF from different collaborations

(b) MSTW2008 Bottom PDF

Figure 2.10: Different bottom quark PDFs.

2.2.2.1 MSTW2008

The Martin, Stirling, Thorne and Watt PDF sets from 2008 [67], called MSTW2008, incorporate leading order, next-to-leading order and next-to-next-to-leading order PDFs and also include various sets for heavy flavour quarks.

The new data sets that have become available are either entirely new types of data, or others which supersede existing sets by improving the precision or extending the kinematic range, or both. Tab. 2.1 lists the main processes which are included in the fit, along with their dominant partonic subprocess, the primary partons which are probed and the x-range constrained by this data.

Table 2.1: The tree main groups of processes included in the current global PDF analysis: fixed-target experiments, HERA and the Tevatron.

Process	Subprocess	Partons	x range
$\ell^\pm \{p,n\} \to \ell^\pm X$	$\gamma^* q \to q$	$q, \bar{q}, g$	$x \gtrsim 0.01$
$\ell^\pm n/p \to \ell^\pm X$	$\gamma^* d/u \to d/u$	d/u	$x \gtrsim 0.01$
$pp \to \mu^+\mu^- X$	$u\bar{u}, d\bar{d} \to \gamma^*$	$\bar{q}$	$0.015 \lesssim x \lesssim 0.35$
$pn/pp \to \mu^+\mu^- X$	$(u\bar{d})/(u\bar{u}) \to \gamma^*$	$\bar{d}/\bar{u}$	$0.015 \lesssim x \lesssim 0.35$
$\nu(\bar{\nu})\, N \to \mu^-(\mu^+)\, X$	$W^* q \to q'$	$q, \bar{q}$	$0.01 \lesssim x \lesssim 0.5$
$\nu\, N \to \mu^-\mu^+ X$	$W^* s \to c$	s	$0.01 \lesssim x \lesssim 0.2$
$\bar{\nu}\, N \to \mu^+\mu^- X$	$W^* \bar{s} \to \bar{c}$	$\bar{s}$	$0.01 \lesssim x \lesssim 0.2$
$e^\pm p \to e^\pm X$	$\gamma^* q \to q$	$g, q, \bar{q}$	$0.0001 \lesssim x \lesssim 0.1$
$e^+ p \to \bar{\nu} X$	$W^+ \{d,s\} \to \{u,c\}$	d, s	$x \gtrsim 0.01$
$e^\pm p \to e^\pm c\bar{c} X$	$\gamma^* c \to c$, $\gamma^* g \to c\bar{c}$	c, g	$0.0001 \lesssim x \lesssim 0.01$
$e^\pm p \to \text{jet} + X$	$\gamma^* g \to q\bar{q}$	g	$0.01 \lesssim x \lesssim 0.1$
$p\bar{p} \to \text{jet} + X$	$gg, qg, qq \to 2j$	g, q	$0.01 \lesssim x \lesssim 0.5$
$p\bar{p} \to (W^\pm \to \ell^\pm\nu)\, X$	$ud \to W, \bar{u}\bar{d} \to W$	$u, d, \bar{u}, \bar{d}$	$x \gtrsim 0.05$
$p\bar{p} \to (Z \to \ell^+\ell^-)\, X$	$uu, dd \to Z$	d	$x \gtrsim 0.05$

The MSTW2008 parameterisation of the parton distributions at the input scale $Q_0^2 = 1\ \text{GeV}^2$ is given by

$$xu_v(x,Q_0^2) = A_u\, x^{\eta_1}(1-x)^{\eta_2}(1+\epsilon_u\sqrt{x}+\gamma_u\, x), \tag{2.18}$$

$$xd_v(x,Q_0^2) = A_d\, x^{\eta_3}(1-x)^{\eta_4}(1+\epsilon_d\sqrt{x}+\gamma_d\, x), \tag{2.19}$$

$$xS(x,Q_0^2) = A_S\, x^{\delta_S}(1-x)^{\eta_S}(1+\epsilon_S\sqrt{x}+\gamma_S\, x), \tag{2.20}$$

$$x\Delta(x,Q_0^2) = A_\Delta\, x^{\eta_\Delta}(1-x)^{\eta_S+2}(1+\gamma_\Delta\, x+\delta_\Delta\, x^2), \tag{2.21}$$

$$xg(x,Q_0^2) = A_g\, x^{\delta_g}(1-x)^{\eta_g}(1+\epsilon_g\sqrt{x}+\gamma_g\, x) + A_{g'}\, x^{\delta_{g'}}(1-x)^{\eta_{g'}}, \tag{2.22}$$

$$x(s+\bar{s})(x,Q_0^2) = A_+\, x^{\delta_S}\,(1-x)^{\eta_+}(1+\epsilon_S\sqrt{x}+\gamma_S\, x), \tag{2.23}$$

$$x(s-\bar{s})(x,Q_0^2) = A_-\, x^{\delta_-}(1-x)^{\eta_-}(1-x/x_0), \tag{2.24}$$

where $\Delta \equiv \bar{d}-\bar{u}$, $q_v \equiv q-\bar{q}$, and where the light quark sea contribution is defined as

$$S \equiv 2(\bar{u}+\bar{d})+s+\bar{s}. \tag{2.25}$$

The input PDFs listed in Eqs. (2.18)–(2.24) are subject to three constraints from number sum rules:

$$\int_0^1 \mathrm{d}x\; u_v(x,Q_0^2) = 2, \qquad \int_0^1 \mathrm{d}x\; d_v(x,Q_0^2) = 1, \qquad \int_0^1 \mathrm{d}x\; s_v(x,Q_0^2) = 0, \tag{2.26}$$

together with the momentum sum rule:

$$\int_0^1 \mathrm{d}x\, x \left[u_v(x,Q_0^2) + d_v(x,Q_0^2) + S(x,Q_0^2) + g(x,Q_0^2)\right] = 1. \tag{2.27}$$

These four constraints are used to determine A_g, A_u, A_d and x_0 in terms of the other parameters. There are therefore potentially $34 - 4 = 30$ free PDF parameters in the fit, including α_S. The resulting PDFs for various scales Q^2 and the low x region can be seen in Fig. 2.11. As we go to lower and lower values of momentum fraction x, the

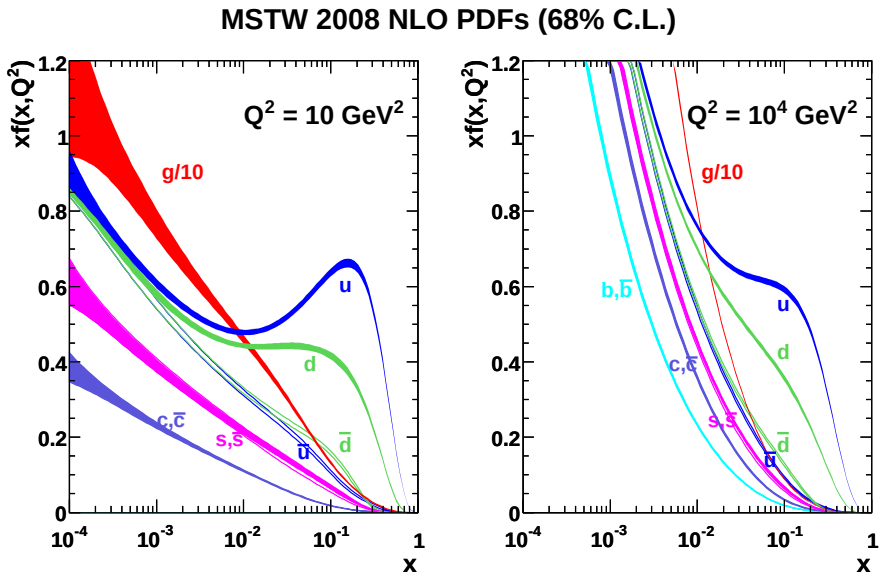

Figure 2.11: NLO PDF distributions for two different scales Q.

gluon distribution rapidly becomes the dominant component. Also, it can be seen that there is no bottom quark pdf at low scale Q, since this is only switched on above the bottom mass threshold.

The uncertainty on a quantity X_0, computed with the PDFs, is evaluated using the up and down error sets $S_i^{\pm}$ by recalculating $X(S_i^{\pm})$. The resulting uncertainty ΔX is given by the asymmetric Hessian method

$$\Delta^+ X = \sqrt{\sum_{i=1}^{20} \max\Big(X(S_i^+) - X_0, 0\Big)^2} \tag{2.28}$$

$$\Delta^- X = \sqrt{\sum_{i=1}^{20} \max\Big(X_0 - X(S_i^-), 0\Big)^2}, \tag{2.29}$$

where S_0 is the central value PDF.

2.2.2.2 CTEQ 6, 6.6 and 10

The most commonly used PDF set for single top analysis studies at the LHC is CTEQ 6 [68]. The data used in the CTEQ 5 fit (fixed-target DIS from BCDMS, NMC, CCFR, Drell-Yann of E605, CDF W-lepton asymmetry and CDF inclusive jets) is supplemented by

- greater precision data and expanded x and Q range for
  - neutral current DIS structure function measurements of H1 and ZEUS,
  - inclusive jet cross section measurements of D0,
- an updated E866 measurement of the Drell-Yann deuteron/proton ratio,
- a reanalysed F_2 measurement of CCFR.

The extensive and precise DIS data from fixed-target and HERA experiments constitute the backbone of the CTEQ parton distribution analysis. The nonperturbative input to the global analysis are PDFs specified in parametrised form at a fixed low-energy scale $Q_0 = 1.3$ GeV. The exact form of the functional and the exact value of Q_0 are not crucial, the parametrisation just has to be flexible enough to accommodate all the available data at the level of accuracy of the data. After some testing, the functional form of the input valence quark PDFs f which has been retained is

$$xf(x, Q_0) = A_0 x^{A_1}(1-x)^{A_2} \exp(A_3 x)(1 + x \exp(A_4))^{A_5}, \tag{2.30}$$

where A_i are the parameters determined from the fit. Independent parameters are used for the parton flavour combinations $u_v \equiv u - \bar{u}, d_v \equiv d - \bar{d}, g$ and $\bar{u} + \bar{d}$. An assumption on intrinsic strangeness at Q_0 is made by imposing

$$s = \bar{s} = 0.2(\bar{u} + \bar{d}), \tag{2.31}$$

and in order to distinguish $\bar{u}$ and $\bar{d}$, their ratio is fitted using

$$\bar{d}(x, Q_0)/\bar{u}(x, Q_0) = A_0 x^{A_1}(1-x)^{A_2} + (1 + A_3 x)(1-x)^{A_4}. \tag{2.32}$$

The poles of the functional (2.30) at $x = 0$ and $x = 1$ reflect the singularities associated with Regge behaviour at small x and the quark counting rules at large x and the ratio of linear polynomials describes the intermediate region in a smooth fashion. The general parametrisation encapsulates some versatility in the sense that, for some flavours, it has more freedom than currently needed, so that not all the parameters are constrained by data. When this occurs, the parameters concerned are kept fixed during the fit. The collaboration is positive that this may rapidly change once more data becomes available. In total, 20 free shape parameters are used the model the CTEQ PDFs at Q_0 and the resulting parametrisations constitute the standard set of PDFs. The value of the strong coupling constant is fixed by $\alpha_S(M_z) = 0.118$ and the charm and bottom masses (fixed at $m_c = 1.3$ GeV and $m_b = 4.5$ GeV) enter only through the scale at which the heavy

quark flavours are switched on in the evolution kernels of the PDFs.

The CTEQ 6 PDFs were constructed by using a novel fit, taking into account correlations between systematic errors. The modified χ^2 function in presence of K sources of correlated errors, reads

$$\chi^2 = \sum_e \Big\{ \sum_{i=1}^{N_e} \frac{(D_i - T_i)^2}{\alpha_i^2} - \sum_{k,k'}^{K_e} B_k (A^{-1})_{kk'} B_{k'} \Big\}, \tag{2.33}$$

where the error α_i is now given by the statistical error and the uncorrelated systematic erroru_i added in quadrature $\alpha_i^2 = \sigma_i^2 + u_i^2$, and where B is a k-sized vector and A is a $K_e \times K_e$ matrix given by

$$B_k = \sum_{i=1}^{N_e} \frac{\beta_{ki}(D_i - T_i)}{\alpha_i^2}, \tag{2.34}$$

$$A_{kk'} = \delta_{kk'} + \sum_{i=1}^{N_e} \frac{\beta_{k'i}\beta_{ki}}{\alpha_i^2} \tag{2.35}$$

and $\beta_{1i}, \cdots, \beta_{Ki}$ are the standard deviations from the K sources of correlated systematic errors.

In the **CTEQ 6.6** PDF set the general mass variable number scheme has been adopted, in contrast to earlier versions which were using the zero mass scheme. There is also a change in the strange distribution, which is now parametrised by

$$s(x, \mu_0) = A_0 x^{A_1} (1 - x)^{A_2} P(x), \tag{2.36}$$

where $P(x)$ is a smooth function used in all sets to ensure that the ratio R_s stays in reasonable range.

The **CTEQ 10** PDF sets include new data sets as well as several improvements to the global fitting procedure. Now included in the fit is the HERA-1 combined data set on $e^{\pm}p$ DIS from H1 and ZEUS which replaces eleven original independent sets for which the correlations between systematic errors were neglected. Since many systematic factors are common to both experiments, the combined data set has a reduced total systematic uncertainty. The fit now also includes the Run-II inclusive jet data and the Z boson rapidity distribution from CDF and DO, as well as the Run-II W lepton asymmetry, on which we will comment shortly later on.

For all previous CTEQ fits, some data sets[3] were assigned weights larger than one to force good fits to these sets, especially during the procedure defining the eigenvector PDF sets which delimit the uncertainty. Now, apart from the special treatment of the

[3]Typically, those sets with a small number of points.

W lepton asymmetry data, all input data sets are on equal footage with weight equal to unity, and an extra contribution the the χ^2 function guarantees the quality of the fit to each data set.
Also, a more flexible PDF parametrisation for some parton flavours (d, s and g) has been adopted to reduce parametrisation dependence. This results in a global increase in the uncertainty in the s and g distributions, particularly affecting charged Higgs production. The functional form of input PDFs for valence u and d quarks s is slightly altered with respect to the CTEQ 6 version 2.30 and reads

$$q_v(x, Q_0) = q(x, Q_0) - \bar{q}(x, Q_0) = a_0 x^{a_1}(1-x)^{a_2} \exp(a_3 x + a_4 x^2 + a_5\sqrt{x}). \tag{2.37}$$

Whereas $a_5 = 0$ in CTEQ 6.6, a_5 is left as a free parameter now to have a more flexible $d(x)$ at large x.
Concerning the gluon PDF $g(x)$, $a_5 = 0$ still holds, but Eq. (2.37) is now proportional to an additional factor $\exp(-a_6 x^{-a_7})$ for extra freedom at small x, where the currently available data provides little constraint. Again, the input parameters of the strong coupling constant and the quark masses are fixed at $\alpha_s(M_z) = 0.118$ and $m_c = 1.3$ GeV and $m_b = 4.75$ GeV. DIS and VBP processes are consistently treated at NLO accuracy, as well as the inclusive jets and W lepton asymmetry. The global CTEQ 10 fit has 26 free parameters, and thus 52 eigenvector sets for uncertainty studies.

A comment is on order about the the Run-II W lepton asymmetry. At the Tevatron, the major W boson production channel in the $p\bar{p}$ collisions is by the annihilation of u and d quarks of the proton with $\bar{d}$ and $\bar{u}$ quark from the antiproton. Since u-type quarks carry on average more momentum than d-type quarks, the propagation of the produced W is not isotropic. Positively charged W bosons will tend to follow the incoming proton's direction, whereas the negatively charged W bosons will tend to follow the antiproton's direction, producing a charge asymmetry in the rapidity distribution of the produced W bosons. The asymmetry in the rapidity distribution of the charged lepton from W boson decay in $p\bar{p}$-collisions is given by

$$A_l(y_l) = \frac{d\sigma^+/dy_l - d\sigma^-/dy_l}{d\sigma^+/dy_l + d\sigma^-/dy_l} \tag{2.38}$$

where $d\sigma^\pm/dy_l = d\sigma(p\bar{p} \to (W^\pm \to l^\pm \nu_l)X)/dy_l$. The semileptonic decay gives rise to an experimental problem, since the longitudinal momentum of the neutrino cannot be measured. Thus, the W boson rapidity is inferred from the lepton rapidity, but since the $V - A$ coupling structure of the decay vertex gives rise to an opposite charge asymmetry effect, the W rapidity is somewhat diluted and statistically large data samples are needed to assess its impact.
The interest for this quantity arose in the late 80s, when its measurement in $p\bar{p}$-collisions was proposed to resolve a controversy between constraints on the down versus up quark distribution ratio $d(x, Q)/u(x, Q)$ obtained in DIS experiments on hydrogen and deuterium targets. Since several theoretical and experimental issues limit the accuracy of the ratio measurement by DIS experiments, the CDF result permitted to go further.

The asymmetry observed by CDF was in agreement with PDFs from fits to the BCDMS and NMC data and conflicted with those based on the EMC data, and the controversy was assumed to be resolved in favour of the BCDMS and NMC experiments. Since then, all three data sets (BCDMS, NMC and CDF) have been intensively used in PDF fits as a self-consistent input. Recently, however, the high-luminosity Run-II from D0 has put the controversy back on the table. Since the data are precise and run into disagreement with some previous data sets as well as exhibit some tension among themselves, the high-luminosity Run-II W lepton asymmetry data set from D0 plays a special role in the CTEQ 10 global fit. Two different PDF fits have been performed

- CT10: without the D0 data on A_l,
- CT10W: in which the D0 A_l data have been moderately emphasised in the fit by increasing the χ^2 weights to ensure reasonable agreements.

The behaviour of the global fit function in the neighbourhood of the minimum in the PDF parameter space is again given in $2N_p$ sets of eigenvector PDFs, where N_p is the number of parameters in the fit. For each parameter i, there are 2 corresponding eigenvector sets $S_i^{\pm}$, depending on whether the shift has been performed to the left or the the right side of the minimum, with a tolerance of $T = 10$. The eigenvector sets are obtained by an iterative procedure of diagonalisation of the Hessian matrix. The final uncertainty on a quantity X is given by the symmetric Hessian method

$$\Delta X = \frac{1}{2}\sqrt{\sum_{i=1}^{N_p}(X(S_i^+) - X(S_i^-))^2}. \tag{2.39}$$

2.2.2.3 NNPDF

The NNPDF collaboration [69] has also developed PDF sets by using very similar input data sets as those already mentioned for other collaborations. The input data, whose x and Q extend can be seen in Fig. 2.12, includes the updated HERA-I set, Drell-Yann production in fixed-target experiments (E605, E866 deuteron/proton ratio, but not the deuteron E866 data which showed low compatibility with other data sets), collider inclusive jet production and the D0 and CDF Z boson rapidity distributions. The CDF W boson asymmetry is taken into account only with the low luminosity data, which is known to be compatible with the other data sets.

The novelty of the NNPDFs is not so much the large set of data they are fitted to, rather the new methodology which was developed especially for that purpose. The NNPDF methodology starts by generating a large sample, of the order of 1000, of Monte Carlo replicas N_{rep} of the original experimental data. Consistent error propagation is handled by the Monte Carlo sampling of the probability distributions given by the data. The N_{rep} artificial replicas are generated following a multi-gaussian distribution, centred on each data point and whose variance is given by the experimental uncertainty. The minimisation of the χ^2 function is done using neural network techniques by training of a set of PDF parametrisations on each of the replicas. The optimisation is stopped

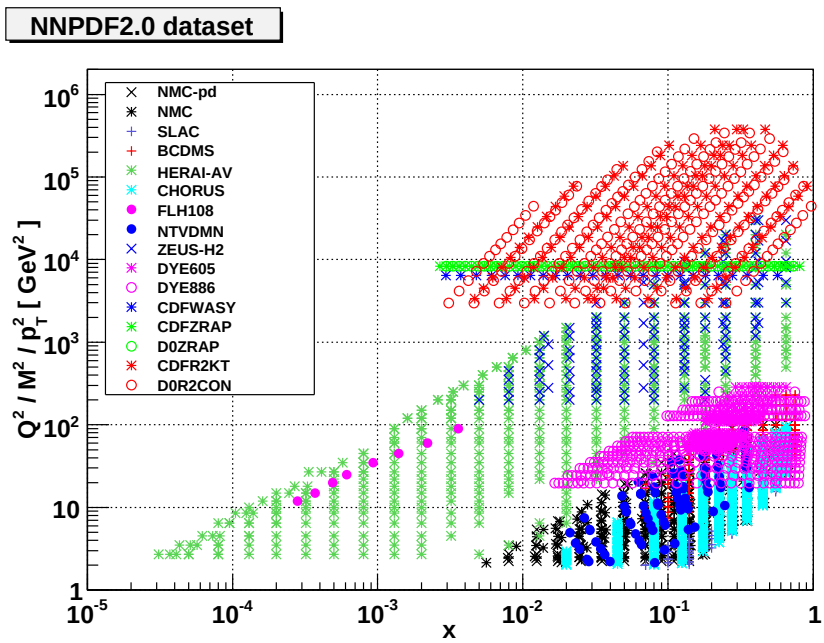

Figure 2.12: Input data for the NNPDF 2.0 data set, displayed in the $(x, Q^2/(M^2 p_T^2))$ plane.

dynamically to avoid overtraining, as the PDF sets should reflect the general underlying laws but not be sensible to the statistical noise. Estimators are then applied to the PDFs to assess their statistical consistency. The central value PDFs S^0 are given by the average of the N_{rep} replicas

$$S_0 =< S >= \frac{1}{N_{rep}} \sum_{i=1}^{N_{rep}} S_i. \tag{2.40}$$

The resulting PDFs have been compared to CTEQ6 and CT10. The most noticeable difference is for the small x gluon distribution, which shows significantly larger uncertainties in NNPDF that CTEQ6, but comparable to MSTW2008, which includes an extra parameter to describe the low x gluon region. A recent update of the PDFs, called NNPDF 2.1 [70], includes now heavy quark mass effects, as was done for the MSTW2008 sets. The deep-inelastic charm structure function data has been added to the input data sets. The update also includes now PDF fitted with varying charm and bottom masses, permitting important uncertainty studies, especially for Higgs boson and single top production. 3- and 4-flavour scheme PDFs are also part of the latest package.
A set of 100 replicas is available to assess the PDF uncertainties. The uncertainty on an observable X is then given by one standard deviation

$$\Delta^+ X = \Delta^- X = \sigma = \sqrt{\frac{1}{N_{rep}-1} \sum_{i}^{N_{rep}} = \Big(X_i - X_0\Big)^2}. \tag{2.41}$$

2.3 The mass mess

The special treatment of the bottom quark in the PDF modelisation leads us to a more general problem on the concept of mass in quantum field theory. As experiments thrive hard to extract physical observables from their data, the notion of mass seems to lose its original clear meaning. In classical physics, the concept of mass has an absolute meaning, be it for the inertial m_i or the gravitational mass m_g and it is an experimental fact that both coincide $m_i = m_g$. In special relativity, it stands for the rest/on-shell mass as the norm of the four-momentum $p^2 = m^2$ and is a scalar in the tensor sense of Lorentz transformation.
In quantum field theory however, particles are described by field-valued operators made from creation and annihilation operators and the Lagrangian operators are constructed using the correspondence principle. The poles in the propagators can correspond to the classical particle poles, if the on-shell renormalisation scheme is applied. UV divergences from quantum corrections have to be removed by renormalisation, because the fields, couplings and parameters, such as the masses, in the classical action are bare quantities and have, before renormalisation, no physical meaning.

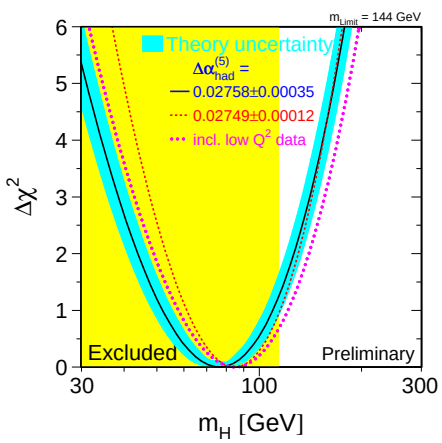

Figure 2.13: Electroweak fit as a function of the SM Higgs boson mass [71].

But different mass definitions exist, depending on what exact quantity one subtracts in the particle self-energy. They are all related through a perturbative series, but some are more suited than others, depending on which process one is interested. A good scheme choice gives systematically and not accidentally a good convergence. This point is particularly crucial for the top mass. For example, the sensitivity of the electroweak fit, displayed on Fig. 2.13 on the input top mass is such that a 2 GeV alteration in the top input mass results in a 15 % change in the favoured Higgs mass m_H.

2.3.1 The pole mass

Since quarks cannot be observed as free particles, the concept of quark mass becomes somewhat different and the use of the pole mass may cause problems [72]. A special formalism has been developed in order to address such questions: the Heavy Quark Effective Theory (HQET) [73]. In this formalism, it has been shown that no precise definition of the pole mass can be established in a full theory which incorporates non-

perturbative effects. This results from the presence of an infrared renormalon generating a factorial divergence in the higher order corrections of the strong coupling α_s. Incorporating the running coupling constant in the pole mass M_Q, the difference between the pole mass and the scale dependent mass $m_Q(\mu_0)$

$$M_Q - m_Q(\mu_0) = \frac{8\pi}{3}\int_{|\vec{k}|<\mu_0}\frac{d^3k}{(2\pi)^3}\frac{\alpha_s(\vec{k}^2)}{\vec{k}^2}. \tag{2.42}$$

Using the the strong coupling series

$$\alpha_s(\vec{k}^2) = \frac{\alpha_s(\mu_0^2)}{1-\Big(b\alpha_s(\mu_0^2)/(4\pi)\Big)\ln(\mu_0^2/\vec{k}^2)} = \alpha_s(\mu_0^2)\sum_{n=0}^{\infty}\Big(\frac{b\alpha_s(\mu_0^2)}{4\pi}\ln\frac{\mu_0^2}{\vec{k}^2}\Big)^n, \tag{2.43}$$

and performing the change of variables $x = k/\mu_0$, the mass difference 2.42 can be written as

$$M_Q - m_Q(\mu_0^2) = \frac{8\pi}{3}\int_0^1\frac{\mu_0^3 dx^3}{(2\pi)^3}\frac{\alpha_s(\mu_0^2)}{(x\mu_0)^2}\sum_{n=0}^{\infty}\Big(\frac{b\alpha_s(\mu_0^2)}{4\pi}\ln\frac{1}{x^2}\Big)^n \tag{2.44}$$

$$= \frac{4\alpha_s(\mu_0^2)}{3\pi}\mu_0\sum_{n=0}^{\infty}C_n\Big(\frac{b\alpha_s(\mu_0^2)}{4\pi}\Big)^n, \tag{2.45}$$

with

$$C_n = \int_0^1 dx\Big(\ln\frac{1}{x^2}\Big)^n. \tag{2.46}$$

The integrals in the C_n coefficients can be repeatedly integrated by parts, and since the part in between brackets always tends to 0, we have

$$C_n = \Big[x\Big(\ln\frac{1}{x^2}\Big)^n\Big]_0^1 + 2n\int_0^1 dx\Big(\ln\frac{1}{x^2}\Big)^{n-1} \tag{2.47}$$

$$= (2n)\times(2(n-1))\times(2(n-2))\cdots\int_0^1 dx \tag{2.48}$$

$$= 2^n n!. \tag{2.49}$$

This means that when higher order effects are taken into account the self-energy exhibits a renormalon-like behaviour in the low-energy regime

$$\sum(m_t) \approx m_t\sum_n \alpha_S^{n+1}(2\beta_0)^n n! \tag{2.50}$$

where β_0 is the first coefficient of the $\beta-$function. So the linear sensitivity to infrared momenta leads to factorially growing coefficients in pQCD. This non-perturbative ambiguity is an issue relevant for heavy quarks because it results in an uncertainty of order $\Delta m \approx \Lambda_{QCD}$ on the heavy quark mass. Since QCD becomes non-perturbative in the low energy regime, these long-distance effect besmirch the perturbative calculations and

leftover uncertainties due to these effects cannot be gotten rid of. This becomes somewhat problematic at the moment, since experiments at the Tevatron, and some day at the LHC, have been able to bring down their uncertainty limits on the measured top mass to the theoretical limit of the mass definition. So even if we measure the top mass as precisely as possible, we still don't know exactly what we measure.

Although the pole mass is probably the easiest to grasp conceptually, it is not appropriate in all situations and may lead to artificially large corrections in higher order terms. In experiments where heavy quark masses need to be known with uncertainties below $\mathcal{O}(1)$ GeV, short-distance mass schemes [74, 75] must be used, as is already done in Quarkonium and B-physics.

2.3.2 Short distance mass schemes

The $\overline{MS}$ mass, which will be detailed in Section 3.2.4, is relevant in processes in which the top quarks are off-shell and energetic. Logarithms of the form $\ln(\mu^2/m_t^2)$ are resummed in the running of $m_t(\mu)$, thus eliminating potentially large contributions when the renormalisation scale is chosen of the order of the hard scattering scale Q and if $Q >> m_t$. The $\bar{M}S$ mass is not suited however for $t\bar{t}$ production at threshold, since it exhibits a strong dependence on the top quark velocity v due to terms of the form $(\alpha_S/v)^k$ which are enhanced when v tends to 0. The generic form of a short-distance mass scheme is [76]

$$m^{sd}(R) = m^{\text{pole}} - R\Big(a_1\frac{\alpha_s}{4\pi} + a_2\Big(\frac{\alpha_s}{4\pi}\Big)^2 + \cdots\Big). \tag{2.51}$$

where the a_i coefficients are chosen so that the renormalon is removed, and the scale R is of the order of the momentum scale relevant for the process. The MSbar mass is thus a short-distance mass with $R = \bar{m}(\mu)$ and $a_1 = 16/3 + 4\ln\mu^2/m^2$.

Attempts [77] are ongoing to define a short-distance top mass which could in principle be determined with an accuracy better than Λ_{QCD}, by establishing a factorisation formula in terms of jets and soft components in the framework of Soft Collinear Effective theories (SCET), valid in the $Q >> m_t >> \Gamma_t >> \Lambda_{QCD}$ regime. Other mass definitions for heavy quarks have been proposed over the years. Threshold masses, like the 1S- or the potential-subtracted mass, are useful for heavy quarks close to their mass-shell, as in quarkonium bound states for example. Also, jet masses have been defined in collider physics, where the scale is of the order of the quark's decay width $R \sim \Gamma_Q$. This is useful for single quark resonances, where heavy quarks are very close to their mass-shell.

If we think about top mass reconstruction at hadron colliders, where the decay products form jets and those are summed $m_t^2 = \sum p_i^2$, the measured quantity does not exist a priori and is defined only through the experimental prescription. So the question one has to address is how does the reconstructed top mass relate to the simulated MC mass? In the pole mass scheme the quantum corrections down to 0 momentum are

kept in the perturbative calculation. In the MC however, the perturbative contributions in the PS are switched off by the shower cut-off. This means that the MC mass will have no renormalon problem, but it won't certainly be the pole mass. The MC mass is thus in principle a short-distance mass. but it is difficult to identify it clearly with a standard mass concept with leading order shower elements implemented, since it depends on the structure of the perturbative part and on the interplay of perturbative and non-perturbative parts in the MC. And since the standard Tevatron analyses, such as the template or the matrix-methods, are driven by MC PS generators such as Herwig and Pythia, this is clearly an issue. In those programs, top decays are matched to their exact tree level $t \to bWg$, but virtual corrections are only included in the soft/collinear limit via the Sudakov form factor. There also remains an uncertainty due to the colour flow and hadronisation models. In principle, higher-order corrections are available even for top decays, but these are often too inclusive to be used by the experiments in a straightforward fashion, as results are expressed in terms of the b quark energy fraction in the top rest frame, and this is a very difficult observable to measure. Another work [78] has recently become available, recomputing several quantities relying on top decays at next-to-leading order using the pole mass but no comparison to data has yet been performed.

"... yes, here, a mistake, a stupid mistake of four hundred and ten lire in an addition." At the bottom of the page the total is ringed in red pen. "And nobody realized, only I know about it, and you're the first person I've told: keep it to yourself and don't forget! And then, even if you did go round telling people, you're only a boy and nobody would believe you... But now you know that everything's wrong. Over all these years, you know what that mistake of four hundred and ten lire has become? Billions! Billions! The calculating machines and electronic brains and whatnot can grind out numbers all they like. The mistake is right at the core, beneath all their numbers, and it's growing bigger and bigger and bigger!"

Italo Calvino, *"Numbers in the Dark"*

3

NLO partonic cross section calculation

We have seen that the factorisation theorem allows to separate a hadronic collision into non-perturbative and perturbative terms by the use of parton distribution functions and we can now concentrate on the partonic cross section. The calculations of higher order terms in the perturbation series become more and more complex as the order increases. Currently Next-to-Leading Order (NLO) processes for the most important production channels have been implemented in Monte Carlo event generator codes. The NLO term gives not only a more precise evaluation of the cross section, i.e. changes the normalisation factor, but may also alter the shape of various distributions. Another improvement over the Born approximation is the reduced sensitivity to unphysical scales. For charged Higgs boson production in association with a top quark, this calculation has already been performed several years ago [79, 80], but in a fashion which does not allow a straightforward Monte Carlo implementation. Therefore, we have recomputed the calculation as a cross-check and used a different formalism. The different ingredients of a NLO calculation, which will be presented in this Chapter, are:

1. the leading order (LO), also called Born or tree level, process,
2. the NLO contributions, which are split into two categories:
   - the virtual contributions, which contain divergencies from the high energy as well as the low energy regime. High energy poles are regularised and then renormalised, while low energy poles are kept to be cancelled later on,
   - and the real emission contributions, which also contain divergencies from the low energy spectrum,
3. a method to cancel the divergencies between the virtual and real contributions.

3.1 Partonic cross sections

Particles are described through Green's functions. The practical meaning of Green's functions is that if we know the solution of a given differential equation in one specific set of parameters, then we can have access to it in all the possible configurations. They are not necessarily physical observables by themselves, but can be linked to cross sections. The scattering matrix, or simply S-matrix, relates incoming particles with momentum eigenstates to outgoing particles with momentum eigenstates, and can be derived from Green's functions via reduction formulas. It can be decomposed as an identity matrix an a transition matrix $\mathcal{T}$,

$$\mathcal{S} = I + i\mathcal{T}, \tag{3.1}$$

where the transition matrix contains a momentum-conservation delta-function as well as the matrix element or Feynman amplitude $\mathcal{M}$:

$$\mathcal{T}\Big[(p_a, p_b) \to (p_1, \cdots, p_n)\Big] = \\ - i(2\pi)^4\delta^4\Big[(p_a + p_b) - (p_1 + \cdots + p_n)\Big]\mathcal{M}\Big[(p_a, p_b) \to (p_1, \cdots, p_n)\Big]. \tag{3.2}$$

The squared matrix elements are related to the partonic cross section σ via the integration over the differential phase space dPS_n for n final state particles

$$\sigma\Big[(p_a, p_b) \to (p_1, \cdots, p_n)\Big] = \int \frac{dPS_n}{\mathcal{F}} \frac{1}{C_i S_i} |\mathcal{M}\Big[(p_a, p_b) \to (p_1, \cdots, p_n)\Big]|^2, \tag{3.3}$$

where the coefficient $1/(C_i S_i)$ averages over the initial state colours and spins and $\mathcal{M}$ is the matrix element. The flux factor for two massless incoming particles is given by $\mathcal{F} = 2s$, and dPS_n contains now the momentum conservation constraint

$$dPS_n = \prod_{i=1}^{n} \Big(\frac{d^3 p_i}{2\omega_i (2\pi)^3}\Big) N_i (2\pi)^4 \delta^4\Big[(p_a + p_b) - (p_1 + \cdots + p_n)\Big] \tag{3.4}$$

The amplitudes can be expanded in a perturbative series in the strong coupling g_s

$$|\mathcal{M}((p_a, p_b) \to (p_1, \cdots, p_n))|^2 = |g_s \mathcal{M}_B + g_s^2 \mathcal{M}_R + g_s^3 \mathcal{M}_V + \cdots|^2 \tag{3.5}$$

Matrix elements with one additional coupling with respect to the Born diagram $\mathcal{M}_B$ are called real emission corrections $\mathcal{M}_R$ and those including an additional g_s^2 factor are the virtual corrections $\mathcal{M}_V$. By squaring the matrix elements, the series can now be expanded with respect to $\alpha_s = g_s^2/(4\pi)$:

$$\sigma^{(NLO)} = \alpha_s \sigma^{LO} + \alpha_s^2 \sigma^{NLO} + \mathcal{O}(\alpha_s^3), \tag{3.6}$$

in which the Leading Order (LO)/Born term consists of $\mathcal{M}_B \mathcal{M}_B^*$. The Next-to-Leading-Order (NLO) terms are the sum of the virtual and the real contributions,

$$\sigma^{NLO} = \sigma^V + \sigma^R, \tag{3.7}$$

where the virtual part is proportional to $2Re(\mathcal{M}_V \mathcal{M}_B^*)$ and the real part to $Re(\mathcal{M}_R \mathcal{M}_R^*)$.

Leading order tH^- production At tree level and in the 5-flavour scheme with active bottom (b) quarks as well as gluons (g) in protons and anti-protons, the production of charged Higgs bosons (H^-) in association with top quarks (t) occurs at hadron colliders via the process

$$b(p_1) + g(p_2) \to H^-(k_1) + t(k_2) \tag{3.8}$$

through the s- and t-channel diagrams ($\mathcal{S}$ and $\mathcal{T}$) shown in Fig. 3.1. The massive top quark is represented by a double line, whereas the bottom quark is treated as massless and represented by a single line.

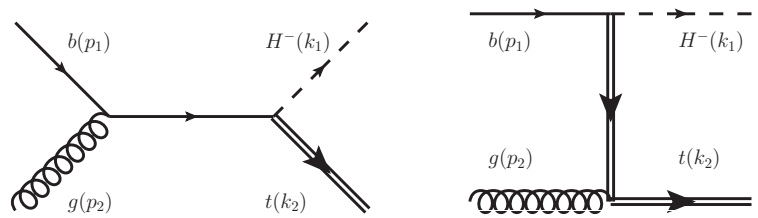

(a) S-channel (b) T-channel

Figure 3.1: Tree-level diagrams for the associated production of charged Higgs bosons and top quarks at hadron colliders.

The associated Mandelstam variables are

$$s = (p_1 + p_2)^2 = (k_1 + k_2)^2, \tag{3.9}$$
$$t = (p_2 - k_2)^2 = (k_1 - p_1)^2, \tag{3.10}$$
$$u = (p_2 - k_1)^2 = (k_2 - p_1)^2, \tag{3.11}$$

and one of them can be replaced using

$$s + t + u = m_t^2 + m_H^2. \tag{3.12}$$

Since the incoming particles are a gluon and a quark, averaging over the spins gives a factor $S_g S_q = 4$ and the colour averages are $C_q = N_C = 3$ and $C_g = N_C^2 - 1$. The LO amplitude squared contribution is given by

$$|\mathcal{M}_B|^2 = SS^* + ST^* + TS^* + TT^* = SS^* + 2ST^* + TT^*, \tag{3.13}$$

or, in terms of the Mandelstam variables,

$$|\mathcal{M}_B|^2 = 4\sqrt{2}\alpha_s(A^2 + B^2)G_F\pi C_F N_C \frac{1}{s(m_t^2 - t)^2} \times$$
$$\Big[2m_H^4(m_t^2 - t) + 2m_H^2\Big(t(s+t) - m_t^4\Big) + (m_t^2 - s - t)\Big(m_t^4 - sm_t^2 + t(s+t)\Big)\Big], \tag{3.14}$$

where $A = m_t/\tan\beta$ and $B = m_b \tan\beta$. The 2-particle final state phase space can be written as

$$dPS_2 = \frac{dt}{8\pi s} \tag{3.15}$$

with integration limits

$$t_{max/min} = m_t^2 + m_{H^-}^2 - s \pm \sqrt{(s - m_t^2 - m_{H^-}^2)^2 - 4m_{H^-}^2 m_t^2}. \tag{3.16}$$

3.2 Virtual corrections

In this Section, we concentrate on virtual diagrams and the different associated divergencies. The calculation of loop diagrams involves complicated integrations and a general approach is introduced, which ultimately leads to a set of useful analytic relations. After applying these to the virtual diagrams for tH^- production, we turn to the concept of renormalisation in order to remove some of the bothering poles.

Virtual diagrams are characterised by the presence of an additional particle which is emitted and then reabsorbed by particles contained in the Born diagram. As an example, think of a quark emitting and reabsorbing a gluon, as shown in Fig. 3.2. According to quantum mechanics, the shorter the time of the emission, the higher the energy of the emitted gluon. It also works the other way around, the gluon can have very low energy and live quite long. As every case has to be taken into account we must to integrate over the unconstrained momentum q. Since the momentum integration runs from zero to infinity, these boundary values can cause divergences. If they occur for the low-energy limit ($E \to 0$), they are called infrared (IR) divergencies. If however the other integration end at high energies ($E \to \infty$) diverges, the integral contains an ultraviolet (UV) pole. The first step of virtual calculations thus consists in taking control of these poles by regularising the integrals.

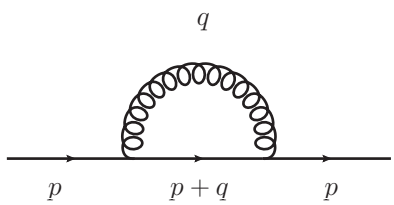

Figure 3.2: Quark with four momentum p emitting and reabsorbing a gluon with an unconstrained momentum q.

3.2.1 Regularisation methods

Over the years, different regularisation methods have been developed. As the problem arises at the high-energy as well as the low-energy limit, the most intuitive method is to cut the integral off at a scale Λ before the problem arises. Early calculations in QED have been performed using this **cut-off regularisation** [81]. However, since this is only applied on the energy-coordinate, the result is not Lorentz-invariant nor gauge invariant anymore. An alternative method is the **Pauli-Villars regularisation** [82], in which one introduces auxiliary fields with large mass in order to achieve convergence of the integrals. The use of a Pauli-Villars regulator conserves translation and Lorentz invariance, and gauge invariance is preserved in QED. Massless Yang-Mills theories such as QCD can also be consistently treated by this method. If, however, one is interested in massive Yang-Mills theories, like the Weinberg-Salam theory for example, the Pauli-Villars regularisation method does not conserve gauge invariance anymore. Other methods worth mentioning are the **analytical regularisation** [83], **the higher covariant derivative method** and the **zeta-function method**. A method which has become very popular and which will be used in this calculation is **dimensional regularisation**, where the space-time dimension $D = 4 - 2\epsilon$ is kept different from 4 via

the parameter ϵ, supposed to be small. The idea behind dimensional regularisation can be illustrated by a very simple example. The integration of the term $1/r^2$ depends on the dimension of the integration measure. Changing it converts the UV pole to an IR pole or makes the integral convergent altogether, as shown in Tab. 3.1.

Table 3.1: Integration example with altering integration measure.

	UV	IR
$\int_0^\infty \frac{d^3r}{r^2}$	Divergent	Convergent
$\int_0^\infty \frac{d^2r}{r^2}$	Divergent	Divergent
$\int_0^\infty \frac{dr}{r^2}$	Convergent	Divergent

Depending on the sign of ϵ, we will deal with different divergencies: ultraviolet divergencies for positive values and infrared divergencies when ϵ is negative, thus allowing us to handle both types of poles with the same regularisation method. Simple poles can now be collected as $1/\epsilon-$terms, double poles will appear as $1/\epsilon^2-$terms.

Dimensional regularisation Dimensional regularisation has been introduced in 1972 by G. 't Hooft and M. Veltman to show that, contrary the the Fermi model, the electroweak Standard Model is renormalisable. The advantage of this method over others is that properties such as gauge invariance and unitarity are preserved. All objects are continuated from 4 to D dimensions. The integral measure now reads

$$\int \frac{d^4k}{(2\pi)^4} \to \int \frac{d^Dk}{(2\pi)^D}, \tag{3.17}$$

and the change in dimension of the integral and the coupling constant is compensated by a multiplication with

$$(2\pi\mu)^{4-D}, \tag{3.18}$$

where μ is the renormalisation scale and has the dimension of a mass. All four-momenta become

$$p^\mu = (p^0, p^1, p^2, p^3) \to (p^0, p^1. \cdots, p^{D-1}). \tag{3.19}$$

and the metric tensor contraction now yields

$$g^\mu_\mu = 4 \to g^\mu_\mu = D. \tag{3.20}$$

The Dirac algebra is also extended to D dimensions, and the anticommutation relations of the Dirac matrices obey

$$\left\{\gamma^\mu, \gamma^\nu\right\} = 2g^{\mu\nu}1_D, \tag{3.21}$$

where 1_D is the identity matrix in D dimensions. We have

$$\gamma^\mu\gamma_\mu = D, \tag{3.22}$$
$$\gamma^\alpha\gamma^\mu\gamma_\alpha = (2-D)\gamma^\mu, \tag{3.23}$$
$$\gamma^\alpha\gamma^\mu\gamma^\nu\gamma_\alpha = 4g^{\mu\nu} - (4-D)\gamma^\mu\gamma^\nu, \tag{3.24}$$
$$\gamma^\alpha\gamma^\mu\gamma^\nu\gamma^\sigma\gamma_\alpha = -2\gamma^\sigma\gamma^\nu\gamma^\mu + (4-D)\gamma^\mu\gamma^\nu\gamma^\sigma. \tag{3.25}$$

This will be particularly important in trace calculations, since it leads to ϵ-dependent terms, which need to be kept, since they produce finite terms when multiplied with a pole. The definition of γ_5 cannot be given straight away. For $D = 4$, the Dirac matrix γ_5 is defined as

$$\gamma_5 = \frac{-i}{4!}\epsilon_{\mu\nu\rho\sigma}\gamma_\mu\gamma_\nu\gamma_\rho\gamma_\sigma, \tag{3.26}$$

where $\epsilon_{\mu\nu\rho\sigma}$ is the totally antisymmetric tensor. This is a purely 4-dimensional object which cannot be self-consistently continuated to D dimensions. For practical purposes, one defines an object which satisfies the anticommutation relation $\{\gamma_5, \gamma^\mu\} = 0$. In theories with anomalies[1], the treatment is therefore different and is done via the dimensional reduction scheme.

3.2.2 Relevant integrals for loop calculations

Generic integral

We will now investigate a very useful general integral to aid us in loop calculations. In the simplest case we have to deal with integrals of the type

$$\mathcal{I}_n(A) = \int d^D q \frac{1}{\left(q^2 - A + i\varepsilon\right)^n}. \tag{3.27}$$

Depending on the particles involved, more complicated expressions can occur, but which can be related to this generic integral $\mathcal{I}_n(A)$. It is therefore convenient to evaluate it once and for all. The poles of the function being integrated are located at

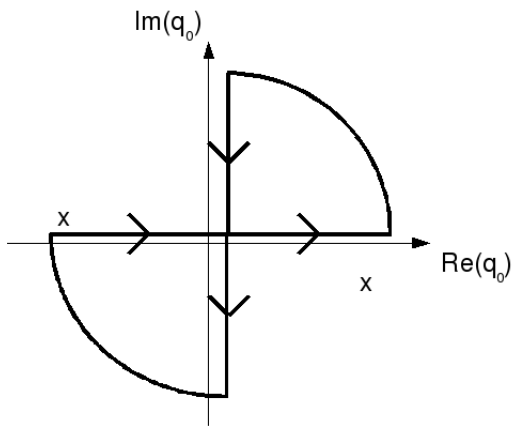

Figure 3.3: Integration contour

$$\begin{aligned} & q^2 - A + i\varepsilon = 0 \\ \Leftrightarrow\ & q_0^2 - \vec{q}^2 - A + i\varepsilon = 0 \\ \Leftrightarrow\ & q_0 = \pm\sqrt{\vec{q}^2 + A - i\varepsilon} \end{aligned} \tag{3.28}$$

These are the usual poles of the propagator and have nothing to do with IR or UV poles. Those will only show up later. We may now choose an integration contour along the real and the imaginary axis, as depicted in Fig. 3.3 and use the Cauchy therorem.

[1] The symmetry of the Lagrangian is classical and there is no guarantee whatsoever that the symmetry also hold on a quantum level. The case for which the classical symmetry of the Lagrangian does not survive the process of quantisation is called an anomaly. If the anomalies do not cancel then the gauge theory cannot be renormalised.

The area defined by the contour $\mathcal{C}$ does not contain any poles and thus

$$\int_{\mathcal{C}} dq_0 \int d^{D-1}q(q^2 - A + i\varepsilon)^{-n} = 0. \tag{3.29}$$

Integrating along both arcs does not give a contributions and what is left is

$$\int_{-\infty}^{\infty} dq_0 \int d^{D-1}q(q^2 - A + i\varepsilon)^{-n} = \int_{-i\infty}^{i\infty} dq_0 \int d^{D-1}q(q^2 - A + i\varepsilon)^{-n}. \tag{3.30}$$

We now perform a Wick rotation exclusively on the energy coordinate and define a new variable q_E, which allows us use a Euclidian metric

$$q_0 = iq_{E,0}, q_k = q_{E,k}, \tag{3.31}$$

giving

$$q^2 = -q_E^2. \tag{3.32}$$

Rewriting the integral using our new coordinate system yields

$$\mathcal{I}_n(A) = i \int d^D q_E (-1)^n (q_E^2 + A - i\varepsilon)^{-n}. \tag{3.33}$$

If we switch to polar coordinates to perform the integration we can write

$$\int d^D q_E = \int d\Omega_D \int_0^{\infty} dq_E q_E^{D-1} = \int d\Omega_D \int_0^{\infty} dq_E^2 \frac{(q_E^2)^{D/2-1}}{2}, \tag{3.34}$$

where Ω_D is the D-dimensional space angle

$$\Omega_D = \frac{2\pi^{D/2}}{\Gamma(D/2),} \tag{3.35}$$

and Γ is Euler's Gamma function[2]

Now $\mathcal{I}_n(A)$ yields

$$\mathcal{I}_n(A) = i(-1)^n \frac{\pi^{D/2}}{\Gamma(D/2)} \int_0^{\infty} dq_E^2 \frac{(q_E^2)^{D/2-1}}{2} (q_E^2 + A - i\varepsilon)^{-n}. \tag{3.36}$$

With the change of variable

$$y = \frac{A - i\varepsilon}{q_E^2 + A - i\varepsilon}, \tag{3.37}$$

[2]The Γ function is given by

$$\Gamma(z) = \int_0^{\infty} t^{z-1} e^{-t} dt.$$

A useful property for Taylor series developments around the poles is $\Gamma(z+1) = z\Gamma(z)$.

the integral can be rewritten as

$$\begin{aligned}\mathcal{I}_n(A) &= i(-1)^n \frac{\pi^{D/2}}{\Gamma(D/2)}(A-i\varepsilon)^{D/2-n}\int_0^1 dy(1-y)^{D/2-1}y^{n-D/2-1} \\ &= i(-1)^n \frac{\pi^{D/2}}{\Gamma(D/2)}(A-i\varepsilon)^{D/2-n}\frac{\Gamma(D/2)\Gamma(n-D/2)}{\Gamma(n)},\end{aligned} \tag{3.38}$$

and the final formula yields

$$\boxed{\mathcal{I}_n(A) = i(-1)^n \pi^{D/2}\frac{\Gamma(n-D/2)}{\Gamma(n)}\Big(A-i\varepsilon\Big)^{D/2-n}} \tag{3.39}$$

In this form, it can be seen in Fig. 3.4, that the divergence is caused by the gamma function $\Gamma(n-D/2)$ if $D > 2n$.

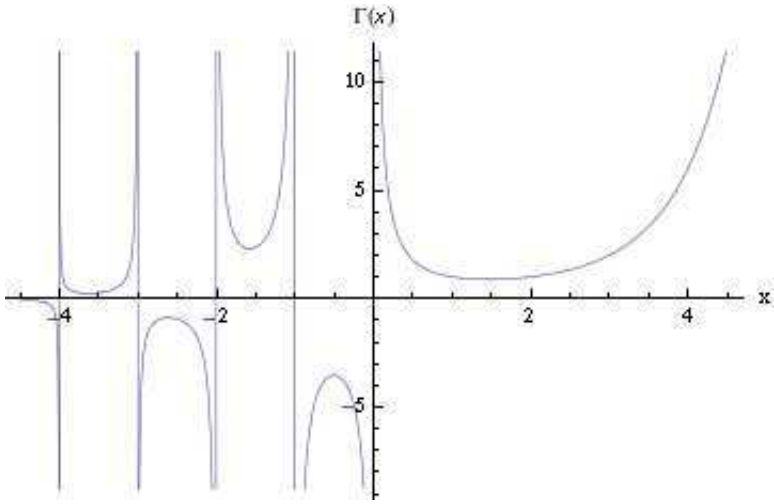

Figure 3.4: The gamma function $\Gamma(x)$ is divergent at the origin and for negative integers.

Thus, these divergencies may appear if n equals one or two, i.e. for virtual contributions with one or two particles in the loop and they correspond to UV-poles. Since integrals with three or more particles in the loop are convergent in the high energy limit, those will be UV-finite. They may, however, still be affected by poles, but this time from the IR regime, as may happen for some special argument set. Now that we have a generic result, our next task will be devoted to link the general formula to concrete examples of loop calculations.

Scalar integrals

The nomenclature of the basic set of scalar integrals is based on the number of particles contained in the loop. This means that contributions which have only one propagator involved in the loop are called an A-type integrals, while integrals with two propagators are noted as B integrals and so forth, as illustrated in Tab. 3.2.

Table 3.2: Nomenclature of the basic set of scalar integrals.

Notation	Type	Name	Diagram
A_0	1-point-function	tadpole	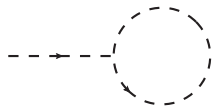
B_0	2-point-function	bubble	
C_0	3-point-function	triangle	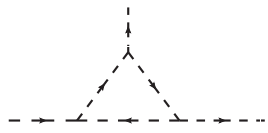
D_0	4-point-function	box	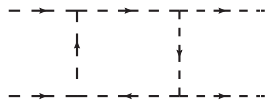

As an example, we will calculate the simplest scalar integral, the tadpole, by relating its expression to the generic form we calculated before

$$A_0(m^2) = \frac{(2\pi\mu)^{4-D}}{i\pi^2}\int d^Dq\frac{1}{q^2-m^2+i\varepsilon} \tag{3.40}$$

$$= \frac{(2\pi\mu)^{4-D}}{i\pi^2}I_1(m^2). \tag{3.41}$$

Replacing its definition, Eq.(3.39) we have

$$A_0(m^2) = -m^2\Big(\frac{m^2}{4\pi\mu^2}\Big)^{(D-4)/2}\Gamma\Big(\frac{2-D}{2}\Big). \tag{3.42}$$

The pole of the scalar integral $A_0(m^2)$ becomes now apparent. It is encoded in the gamma function, which becomes divergent for $D \to 4$. Using

$$\epsilon = \frac{4-D}{2} \tag{3.43}$$

as the gap between the number of dimensions D and 4, the scalar integral becomes

$$A_0(m^2) = -m^2\Big(\frac{m^2}{4\pi\mu^2}\Big)^{-\epsilon}\Gamma\big(\epsilon-1\big). \tag{3.44}$$

To find the final form of $A_0(m^2)$, we expand

$$\Big(\frac{m^2}{4\pi\mu^2}\Big)^{-\epsilon} = \exp\Big[-\epsilon\ln\Big(\frac{m^2}{4\pi\mu^2}\Big)\Big] \tag{3.45}$$

$$= 1-\epsilon\ln\Big(\frac{m^2}{4\pi\mu^2}\Big)+\mathcal{O}(\epsilon^2), \tag{3.46}$$

and by using $\Gamma(x+1) = x\Gamma(x)$ twice, we can rewrite the Gamma function as

$$\Gamma(\epsilon - 1) = \frac{1}{\epsilon(\epsilon-1)}\Gamma(\epsilon+1). \tag{3.47}$$

Using $\frac{1}{1-x} = \sum_{i=0}^{\infty} x^i$ for one term and a Taylor expansion for the Gamma function, we have now

$$\begin{aligned}
\frac{1}{\epsilon(\epsilon-1)}\Gamma(\epsilon+1) &= \frac{1}{\epsilon}(1+\epsilon+\mathcal{O}(\epsilon^2))\big(\Gamma(1)+\Gamma'(1)\epsilon+\mathcal{O}(\epsilon^2)\big) && (3.48)\\
&= -\frac{1}{\epsilon} - \Gamma(1) - \Gamma'(1) + \mathcal{O}(\epsilon) && (3.49)\\
&= -\big(\frac{1}{\epsilon} + 1 - \gamma_E\big) + \mathcal{O}(\epsilon) && (3.50)
\end{aligned}$$

where the first derivative of the gamma function $\Gamma'(1) = -\gamma_E = -0.5772$ is called the Euler-Mascharoni constant. By replacing those expansions we can collect the poles and the constant coefficients

$$\begin{aligned}
A_0(m^2) &= m^2\big(\frac{1}{\epsilon} + 1 - \gamma_E + \mathcal{O}(\epsilon)\big)\big[1 - \epsilon\ln\big(\frac{m^2}{4\pi\mu^2}\big) + \mathcal{O}(\epsilon^2)\big] && (3.51)\\
&= m^2\big[\frac{1}{\epsilon} - \gamma_E + \ln 4\pi - \ln\big(\frac{m^2}{\mu^2}\big) + 1 + \mathcal{O}(\epsilon)\big]. && (3.52)
\end{aligned}$$

As can be seen in this final expression, the $A_0(m^2)$ tadpole is proportional to the mass of the particle in the loop. Thus tadpole contributions are zero for massless particles. Another aspect which has been illustrated through this short example is the origin of the mass logarithm, which depends on the renormalisation scale μ. Additionally, and we see where the factor $-\gamma_E + \ln 4\pi$ comes from, which gets subtracted along with the pole in the $\overline{MS}$ prescription (see below). For convenience, we therefore define

$$\Delta_{UV} = \frac{1}{\epsilon} - \gamma_E + \ln 4\pi. \tag{3.53}$$

Of course, the complexity of the calculation increases once there are more propagators involved. If there are for example two propagators, we will use the following Feynman trick[3] to bring the denominator into the suitable form:

$$\frac{1}{ab} = \int_0^1 \frac{dx}{(a(1-x)+bx)^2}. \tag{3.54}$$

[3] The general formula for the Feynman trick allows us to combine n propagators using

$$\frac{1}{\prod_{i=1,n} a_i} = (n-1)!\int_0^1 dx_1 \int_0^{x_1} dx_2 \cdots \int_0^{x_{n-2}} dx_{n-1} \big[a_1 x_{n-1} + a_2(x_{n-2} - x_{n-1}) + \cdots + a_n(1-x_1)\big]^{-n}.$$

Further complications arise when one or more input values are zero, as some masses for example, as they generate IR poles. A list of the special argument set that is needed for top quark and charged Higgs production are found in App. C. This has been gathered mostly by the more general list from reference [84].

Tensor Reduction

For the moment we have seen integrals in which the unconstrained momentum only appears in the denominator. But depending on the particles involved in the loop, a quark for example, it may also show up in the numerator, leading to a further complication. In

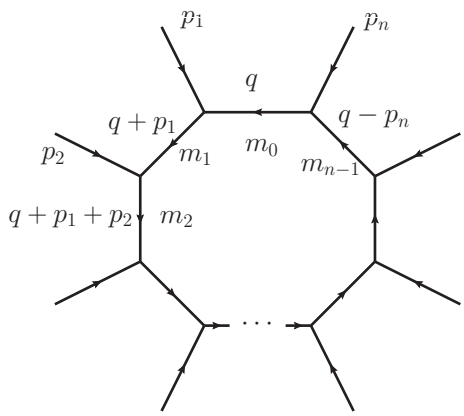

Figure 3.5: General loop with n external particles.

general, if we have n external particles and $(n-1)$ propagators, as shown in figure 3.5, we can have tensor integrals of the form

$$\mathcal{T}_n^{\mu_1\cdots\mu_m}(p_1,\cdots,p_{n-1};m_0,\cdots,m_{n-1}) = \frac{(2\pi\mu)^{4-D}}{i\pi^2}\int d^Dq \frac{q^{\mu_1}\cdots q^{\mu_m}}{(q^2-m_0^2+i\varepsilon)\big((q+p_1)^2-m_1^2+i\varepsilon\big)\cdots\big((q-p_n)^2-m_{n-1}^2+i\varepsilon\big)} \tag{3.55}$$

where q appears in the numerator with μ_m different indices. A way of making use of all the work we did before on the scalar integrals is to use tensor decomposition to the four basic scalar integral A_0, B_0, C_0 and D_0. The disadvantage of this method is that some special kinematic configurations can lead to linear equation systems that are not invertible. But since this was no problem for the calculation of $tH^\pm$ production, we will not detail this further.

As an example for tensor reduction, we will calculate a B class integral with one momentum in the numerator. Again, this is a simple example; the higher the class of the integral and the more momenta involved, the worse it gets. If one propagator introduces a q-dependence in the numerator we have B^μ

$$B^\mu = \frac{(2\pi\mu)^{4-D}}{i\pi^2}\int d^Dq \frac{q^\mu}{(q^2-m_0^2+i\varepsilon)\big[(q+p_1)^2-m_1^2+i\varepsilon\big]}. \tag{3.56}$$

We try to express this in terms of relevant four-momenta. Here, the only tensor available is the momentum p_1. The decomposition of B^μ can thus be written as

$$B^\mu(p_1^2; m_0^2, m_1^2) = p_1^\mu B_1(p_1^2; m_0^2, m_1^2). \tag{3.57}$$

To obtain the expression of B_1, we contract Eq.(3.57) with $p_{1\mu}$

$$p_{1\mu} B^\mu(p_1^2; m_0^2, m_1^2) = \frac{(2\pi\mu)^{4-D}}{i\pi^2} \int d^D q \frac{p_1 \cdot q}{(q^2 - m_0^2 + i\varepsilon)\big[(q+p_1)^2 - m_1^2 + i\varepsilon\big]}, \tag{3.58}$$

and write the scalar product $p_1 \cdot q$ as

$$p_1 \cdot q = \frac{1}{2}\big\{\big[(q+p_1)^2 - m_1^2 + i\varepsilon\big] - (q^2 - m_0^2 + i\varepsilon) - (p_1^2 - m_1^2 + m_0^2)\big\}. \tag{3.59}$$

Inserting this term into Eq.(3.58), we get a set of simpler integrals

$$\begin{aligned} p_1^2 B_1(p_1^2; m_0^2, m_1^2) = \frac{(2\pi\mu)^{4-D}}{i\pi^2} \frac{1}{2} \Big(& \int d^D q \frac{1}{q^2 - m_0^2 + i\varepsilon} - \int d^D q \frac{1}{(q+p_1)^2 - m_1^2 + i\varepsilon} \\ & - (p_1^2 - m_1^2 + m_0^2) \int d^D q \frac{1}{(q^2 - m_0^2 + i\varepsilon)\big[(q+p_1)^2 - m_1^2 + i\varepsilon)\big]} \Big). \end{aligned} \tag{3.60}$$

Finally we can express B_1 using the scalar integrals A_0 and B_0

$$B_1(p_1^2; m_0^2, m_1^2) = \frac{1}{2p_1^2}\Big[A_0(m_0^2) - A_0(m_1^2) - (p_1^2 - m_1^2 + m_0^2) B_0(p_1^2; m_0^2, m_1^2)\Big]. \tag{3.61}$$

Other terms may appear in the calculation, but they can all be decomposed using the basic set of scalar integrals. It should however be noted that different decomposition choices can be made.

3.2.3 Virtual contributions for tH^- production

We can now turn to the relevant virtual contributions for charged Higgs boson production with a top quark. We need to calculate the self-energy contributions for the external gluon, as shown on Figs. 3.6(a) to 3.6(d). The quark loop in diagram 3.6(a) can be massless or massive in case of a top-antitop contribution. If the triple-gluon vertex contribution of diagram 3.6(b) is calculated using the simple polarisation sum, the ghost loop 3.6(c) has to be added to remove the unphysical gluon polarisations. Finally, the tadpole contribution 3.6(d) gives no contribution, since it is proportional to $A_0(0) = 0$. We also have to calculate self-energies for the massless and massive quarks, as shown in Fig. 3.6(e). Bubble contributions are not the same if they occur on external legs or on propagators, since in propagators the particle is off-shell. Thus we have different contributions for the external b quark where $p^2 = p_1^2 = 0$, for the external top quark where $p^2 = p_2^2 = m_t^2$ and for the s- and t-channel propagators where $p^2 = s$ and $p^2 = t$.

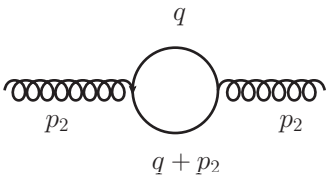

(a) Gluon quark loop contribution.

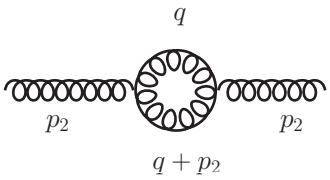

(b) Gluon gluon loop contribution.

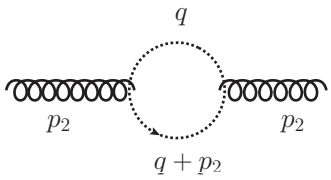

(c) Gluon ghost loop contributions.

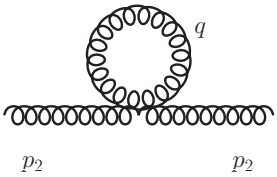

(d) Gluon tadpole contribution.

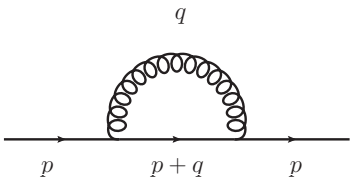

(e) Quark loop contribution.

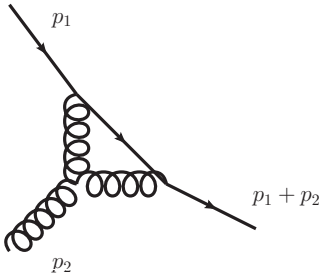

(f) g-b-g loop

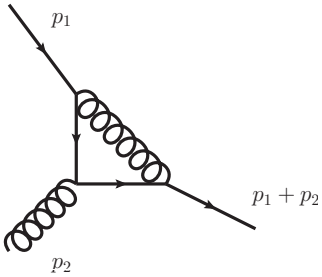

(g) b-g-b loop

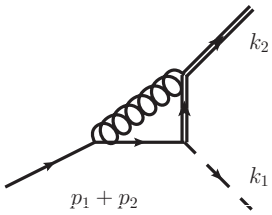

(h) b-g-t loop

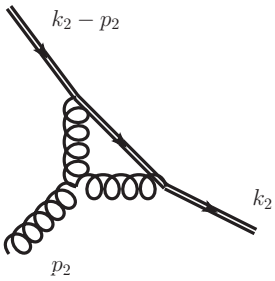

(i) g-t-g loop

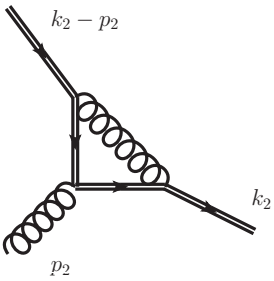

(j) t-g-t loop

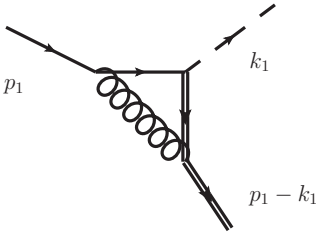

(k) b-g-t loop

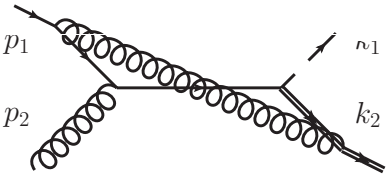

(l) Box contribution

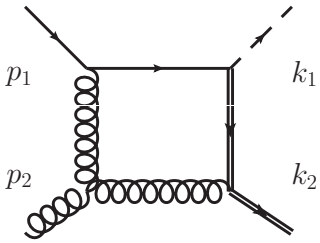

(m) Box contribution

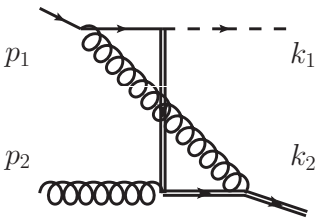

(n) Box contribution

Figure 3.6: Virtual corrections for tH^- production.

There are also several vertex contributions to consider. In the s-channel, a gluon may be exchanged between the two initial state partons, Fig. 3.6(f), or between the incoming b quark and the b propagator, Fig. 3.6(g), or between the propagator and the outgoing top, Fig. 3.6(h). For the t-channel, a gluon might be exchanged between the incoming gluon and the external top, Fig. 3.6(i), between the top propagator and the outgoing top, Fig. 3.6(j), or between the incoming b quark and the top propagator, Fig. 3.6(k).

Box contributions arise from the s-channel Born diagram if the top quark exchanges a gluon with the incoming b quark, Fig. 3.6(l), or the incoming gluon, Fig. 3.6(m). In the t-channel Born diagram, a gluon can be exchanged between the incoming b quark and the top, Fig. 3.6(n), whereas the exchange of a gluon between the incoming b and gluon gives the same contribution as we already constructed via the s-channel, so the total amount of different box contributions adds up to three.

As an application of all we have seen so far, we will calculate the NLO contribution to the bbg-vertex. As was already mentioned, these vertex corrections arise due to the exchange of a virtual gluon between the b propagator with either the incoming b quark or the incoming gluon. Both contributions have to be contracted with the s- and t-channel Born diagrams. A first intermediate step gives the result as a function of the basic scalar integrals

$$\begin{aligned}
2|\mathcal{M}_{V_{bgb}}\mathcal{M}_B|^2 = \frac{16\alpha_S^2\,(A^2+B^2)\,C_F\pi^2}{s\,(m_t^2-t)}\times \\
\Big[2\left(\left(m_t^2-t\right)m_H^2+\left(m_t^2-s-t\right)\left(m_t^2(\epsilon-1)-t\epsilon\right)\right)B_0(0,0,0) \\
+\Big((\epsilon-1)m_H^4-\left((2\epsilon+1)m_t^2-3t+s(\epsilon-1)\right)m_H^2+m_t^4\left(-2\epsilon^2+\epsilon+1\right) \\
-t(s+t)\left(2\epsilon^2+1\right)+m_t^2(2\epsilon+1)(s(\epsilon-1)+t(2\epsilon-1))\Big)B_0(s,0,0)\Big]
\end{aligned} \tag{3.62}$$

for contribution 3.6(g) with the Born s- and t-channel, and

$$\begin{aligned}
2|\mathcal{M}_{V_{gbg}}\mathcal{M}_B|^2 = \frac{16\alpha_S^2\,(A^2+B^2)\,C_F N_C^2\pi^2}{s\,(m_t^2-t)}\times \\
\Big[3\left(m_H^4-\left(m_t^2+s+t\right)m_H^2-m_t^4(\epsilon-1)-t(s+t)(\epsilon-1)+m_t^2(s(\epsilon-1)+t(2\epsilon-1))\right)B_0(0,0,0) \\
-\left(m_H^2-t\right)\left(m_H^2-s-t\right)\epsilon B_0(s,0,0) \\
+s\Big(-m_H^4+\left(2m_t^2+s\right)m_H^2+2m_t^4(\epsilon-1) \\
+t(s+t)(2\epsilon-1)+2m_t^2(s+t-(s+2t)\epsilon)\Big)C_0(0,0,s,0,0,0)\Big]
\end{aligned} \tag{3.63}$$

for contribution 3.6(f) with the Born s- and t-channel. The $\mathcal{O}(\epsilon^3)$ contributions in the trace have been removed since they cannot give rise to finite contributions, as the maximum pole order is 2 for the C_0 scalar function.

After summing both contributions and replacing the scalar integrals, we can give the final result ordered according to the poles

$$2\Big(|\mathcal{M}_{V_{bgb}}\mathcal{M}_B|^2 + |\mathcal{M}_{V_{gbg}}\mathcal{M}_B|^2\Big) = f_{UV}\Delta_{UV} + \frac{f_{IR2}}{\epsilon^2} + \frac{f_{IR}}{\epsilon} + f_0, \tag{3.64}$$

where additional contributions to f_0 may still come from terms $\Delta_{UV}/\epsilon = 1 + \mathcal{O}(\epsilon)$, but we will expand those only after renormalisation, since some terms will drop out.

The coefficient of the UV pole is given by

$$\begin{aligned} f_{UV} = -\frac{\alpha_S^2\,(A^2+B^2)\,C_F}{s\,(m_t^2-t)}\Big(&\big((\epsilon-3)N_C^2-\epsilon+1\big)\,m_H^4 \\ &+\big(\big(3N_C^2-1\big)\,\big(m_t^2+s+t\big)+\big(2m_t^2-N_C^2 s+s-2N_C^2 t\big)\,\epsilon\big)\,m_H^2 \\ &+m_t^4\,\big(3(\epsilon-1)N_C^2-3\epsilon+1\big)+t(s+t)\,\big((4\epsilon-3)N_C^2-2\epsilon+1\big) \\ &-m_t^2\,\big(s\,\big(3(\epsilon-1)N_C^2-3\epsilon+1\big)+t\,\big((6\epsilon-3)N_C^2-4\epsilon+1\big)\big)\Big). \end{aligned} \tag{3.65}$$

The IR double pole coefficient is given by

$$\begin{aligned} f_{IR2} = -\frac{\alpha_S^2\,(A^2+B^2)\,N_C}{2s\,(m_t^2-t)} \\ \big(N_C^2-1\big)\,\big(m_H^4-\big(2m_t^2+s\big)\,m_H^2+2m_t^4-2m_t^2(s+t)+t(s+t)\big)\,, \end{aligned} \tag{3.66}$$

the IR simple pole coefficient is

$$\begin{aligned} f_{IR} = -\frac{\alpha_S^2\,(A^2+B^2)\,(N_C^2-1)}{2N_C s\,(m_t^2-t)} \\ \Big(3N_C^2 m_H^4-\big(\big(3N_C^2-2\big)\,m_t^2+2t+3N_C^2(s+t)\big)\,m_H^2 \\ -2m_t^4+m_t^4 N_C^2+N_C^2 t^2+2m_t^2 s-m_t^2 N_C^2 s+2m_t^2 t+m_t^2 N_C^2 t+N_C^2 st \\ -N_C^2\,\big(m_H^4-\big(2m_t^2+s\big)\,m_H^2+2m_t^4-2m_t^2(s+t)+t(s+t)\big)\log(s/m_t^2)\Big) \end{aligned} \tag{3.67}$$

and the constant term is given by

$$\begin{aligned} f_0 = -\frac{\alpha_S^2\,(A^2+B^2)\,C_F}{2s\,(m_t^2-t)} \\ \Big(N_C^2\,\big(m_H^4-\big(2m_t^2+s\big)\,m_H^2+2m_t^4-2m_t^2(s+t)+t(s+t)\big)\log\left(-\frac{s}{m_t^2}\right)^2 \\ -2\big(-2m_H^4+2\,\big(-m_t^2+s+3t\big)\,m_H^2+3m_t^4 N_C^2+\big(3N_C^2-4\big)\,t(s+t)+m_t^2\,\big(2t-3N_C^2(s+2t)\big) \\ +\big(m_H^4+\big(m_t^2-s-3t\big)\,m_H^2-m_t^4\,\big(2N_C^2+1\big)-\big(2N_C^2-1\big)\,t(s+t)+m_t^2\,\big(2sN_C^2+4tN_C^2+s+t\big)\big) \\ \log\left(\frac{s}{m_t^2}\right)\big)\Big). \end{aligned} \tag{3.68}$$

In order to have a complete result, all the diagrams of Fig. 3.6 have to be calculated in this fashion, and the poles gathered as we just did. Once this is done, the UV poles have to be removed via renormalisation.

3.2.4 Renormalisation

Nowadays the term renormalisation is often straightforwardly associated with quantum field theory, since it received a great deal of attention in this area in the 60s. But this method is largely applied in other domains as well. The basic concept of renormalisation reaches far back, to 1877, where it was applied for the first time by Boussinesq to turbulance diffusivity. Later, more concrete examples were the Weiss theory of ferromagnetism in 1907 and the Debye-Hückel theory of the screened potentials in electrolytes in 1922. Those examples are still classical physics. The process of renormalisation will result in replacing a bare quantity by a renormalised, i.e. an effective quantity, introducing a scale dependence on it.

Electron in an electrolyte Consider a single electron in classical mechanics, with electric charge e. Its potential at a distance r is given by Coulomb's law

$$V(r) = \frac{e}{r}. \tag{3.69}$$

If however this electron is surrounded by others, like in an electrolyte for example, the induced charge is screening the Coulomb potential, which, according to the Debye-Hückel theory, can be expressed as

$$V(r) = \frac{e\exp\left(\frac{r}{l_D}\right)}{r}, \tag{3.70}$$

l_D being the Debye-Hückel length. The screened potential has the same form as the Coulomb potential if we replace the *bare* charge e by the *renormalised* charge $e\exp\left(\frac{r}{l_D}\right)$, which does now depend on the space coordinate r.

Renormalisation in QCD The previous section Section showed that in calculating higher order corrections the different terms that we compute can have infinite values. The ultraviolet divergencies came from the fact that we used inappropriate bare quantities which have no direct relation to observables in an interacting theory. The renormalisation method consists in redefining multiplicativly new parameters by only a finite number of redefinitions and thus eliminate all ultraviolet infinities. It is important to note that renormalisation would have to be carried out in an interacting theory, even if infinities were absent. In that case, physical quantities could be expressed through bare quantities, but it is more convenient anyhow to express them in terms of experimentally measurable quantities.

QCD is a non-abelian gauge theory[4] whose quark fields ψ, with mass m, belong to the fundamental representation of the $SU(3)$ group. The generators T^a generators satisfy

[4] A passage from A. Zee's book "Fearful symmetry" takes us back to the birth of the theory when it was still only a mathematical appealing construct with no link to reality: "When Yang-Mills theory first came out, the community of theoretical physicists agreed that it was indeed beautiful, but no one, not even Yang and Mills, had the foggiest idea what is was good for. Most physicists simply mumbled that it is too bad that we do not live in a non-abelian gauge world, shrugged, and went on with whatever they were doing. "

the Lie algebra

$$\left[T^a, T^b\right] = i f^{abc} T^c, \tag{3.71}$$

where f^{abc} are the structure functions characterising the algebra. Gauge invariance gives rise to the A^a_μ gluon gauge fields, belonging to the adjoint representation. The strong coupling constant between the matter fields ψ and the gauge fields A^a_μ is denoted g_s. The QCD Lagrangian can be decomposed into a free part $\mathcal{L}_0$ and an interaction part $\mathcal{L}_{int}$ [85]

$$\mathcal{L}_{QCD} = \mathcal{L}_0 + \mathcal{L}_{int}. \tag{3.72}$$

The free part reads explicitly

$$\mathcal{L}_0 = -\frac{1}{4}(\partial_\mu A^a_\nu - \partial_\nu A^a_\mu)(\partial^\mu A^{a\nu} - \partial^\nu A^{a\mu}) - \frac{1}{2\alpha}(\partial^\mu A^a_\mu)^2 + i(\partial^\mu \chi^a_1)(\partial_\mu \chi^a_2) + \bar{\psi}^i(i\gamma_\mu \partial_\mu - m)\psi^i, \tag{3.73}$$

where the term proportional to $1/(2\alpha)$ is the gauge-fixing term and χ are the Faddeev-Popov ghost fields. The interaction part is given by four terms, which are the three-gluon, four-gluon, ghost-gluon and quark-gluon interactions

$$\begin{aligned}\mathcal{L}_{int} = &-\frac{g_s}{2} f^{abc}(\partial_\mu A^a_\nu - \partial_\nu A^a_\mu) A^{b\mu} A^{c\nu} - \frac{g_s^2}{4} f^{abe} f^{cde} A^a_\mu A^b_\nu A^{c\mu} A^{d\nu} \\ &- i g_s f^{abc}(\partial^\mu \chi^a_1)\chi^b_2 A^c_\mu + g_s \bar{\psi}^i T^a_{ij} \gamma^\mu \psi^j A^a_\mu.\end{aligned} \tag{3.74}$$

In order to obtain the renormalised Lagrangian, the gluon, quark and ghost bare fields are rescaled by the field-strength renormalisation constants $\mathcal{Z}_i$,

$$A^a_\mu = \sqrt{\mathcal{Z}_A}\, A^a_{r\mu},\ \psi = \sqrt{\mathcal{Z}_\psi}\, \psi_r,\ \chi^a_{1,2} = \sqrt{\mathcal{Z}}_\chi\, \chi^a_{r1,2}, \tag{3.75}$$

and the bare masses and coupling are also expressed as parameter renormalisation constants $\mathcal{Z}_i$ and renormalised quantities

$$g = \mathcal{Z}_g g_r, \alpha = \mathcal{Z}_3 \alpha_r, m = \mathcal{Z}_m m_r. \tag{3.76}$$

The renormalisation constants are expanded in infinite series, each term cancelling the divergence of specific graphs. At one-loop, we only need the first term of the series

$$\mathcal{Z} = 1 + \delta\mathcal{Z}. \tag{3.77}$$

By plugging this into the Lagrangian, Eq.(3.72), we obtain a new Lagrangian

$$\mathcal{L} = \mathcal{L}_{0,r} + \mathcal{L}_{int,r} + \mathcal{L}_C, \tag{3.78}$$

where the original Lagrangian is recovered $\mathcal{L}_{0,r} + \mathcal{L}_{int,r}$, but is this time expressed solely via renormalised parameters. The additional part $\mathcal{L}_C$ gives rise to new contributions. These counterterms have to be added to the calculation as they will ultimately cancel

the ultraviolet divergencies. The counterterm Lagrangian is given by

$$\begin{aligned}\mathcal{L}_C =& -\delta Z_A \frac{1}{4}(\partial_\mu A^a_{r\nu} - \partial_\nu A^a_{r\mu})(\partial^\mu A^{a\nu}_r - \partial^\nu A^{a\mu}_r) + i\delta Z_\chi(\partial^\mu \chi^a_{1r})(\partial_\mu \chi^a_{2r}) \\ &+ \delta Z_\psi \bar{\psi}^i_r (i\gamma^\mu \partial_\mu - m_r)\psi^i_r - Z_\psi \delta Z_m m_r \bar{\psi}^i_r \psi^i_r \\ &- (Z_g Z_A^{3/2} - 1)\frac{g_{sr}}{2} f^{abc}(\partial_\mu A^a_{r\nu} - \partial_\mu A^a_{r\mu})A^{b\mu}_r A^{c\nu}_r - (Z_g^2 Z_A^2 - 1)\frac{g_{sr}^2}{4} f^{abe} f^{cde} A^a_{r\mu} A^b_{r\nu} A^{c\mu}_r A^{d\nu}_r \\ &- i(Z_g Z_\chi Z_A^{1/2} - 1) g_{sr} f^{abc}(\partial^\mu \chi^a_{1r})\chi^b_{2r} A^c_{r\mu} + (Z_g Z_\psi Z_A^{1/2} - 1) g_{sr} \bar{\psi}^i_r T^a_{ij} \gamma^\mu \psi^j_r A^a_{r\mu}.\end{aligned} \tag{3.79}$$

Again, we only keep terms of the first order here, which means that the counterterm for the gluon-quark-quark vertex, for example, will be proportional to

$$\mathcal{Z}_g \mathcal{Z}_\psi \mathcal{Z}_A^{1/2} = 1 + \delta\mathcal{Z}_g + \delta\mathcal{Z}_\psi + 1/2\delta\mathcal{Z}_A + \mathcal{O}(\delta^2). \tag{3.80}$$

Field and mass renormalisation A renormalised field is one whose propagator has the same behaviour near its pole as a free field. The renormalised mass is defined by the position of the pole. The Dyson series for the quark propagator is just

$$\begin{aligned}\tilde{G}^{(2)}_c(p,-p) &= \frac{i}{\not p - m} + \frac{i}{\not p - m} i\Sigma(\not p)\frac{i}{\not p - m} + \frac{i}{\not p - m} i\Sigma(\not p)\frac{i}{\not p - m} i\Sigma(\not p)\frac{i}{\not p - m} + \dots \\ &= \frac{i}{\not p - m}\sum_{k=0}^{\infty}\left(i\Sigma(\not p)\frac{i}{\not p - m}\right)^k \\ &= \frac{i}{\not p - m}\left(1 + \Sigma(\not p)\frac{1}{\not p - m}\right)^{-1} \\ &= \frac{i}{\not p - m + \Sigma(\not p)}\end{aligned} \tag{3.81}$$

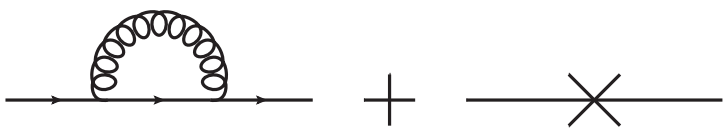

Figure 3.7: Contributions to the quark self energy $\Sigma(\not p)$: emission and reabsorption of a gluon by the quark (left) and counterterm contribution (right).

The renormalised one-particle irreducible self-energy is the sum of the self-energy contribution and the counterterm, Fig. 3.7. It reads

$$\Sigma(\not p) = -\frac{\alpha_s C_F}{4\pi}\Big(\mathcal{B}(p)\not p + \mathcal{A}(p)) + (\partial Z_\psi \not p - (\partial Z_\psi + \partial Z_m)m\Big), \tag{3.82}$$

where $\mathcal{A}$ and $\mathcal{B}$ can be given in terms of scalar integrals

$$\mathcal{A} = m(4 - 2\epsilon)B_0(p^2; m^2, 0) \tag{3.83}$$

and

$$\mathcal{B} = (2-2\epsilon)\Big[B_0(p^2;m^2,0) + B_1(p^2;m^2,0)\Big]. \tag{3.84}$$

We rearrange the terms for later convenience as

$$\Sigma(\not{p}) = \not{p}(\mathcal{B}(p) + \partial Z_\psi) + (\frac{\mathcal{A}(p)}{m} - \partial Z_\psi - \partial Z_m)m \tag{3.85}$$

The mass counterterm ∂Z_m will now be fixed by the pole condition. The residue condition determines the expression for the fermion field counterterm ∂Z_ψ.

Different renormalisation schemes Renormalisation is a method to remove the UV poles in loop calculations via counterterms, so the main focus lies on the UV divergence. But the counterterms may remove more than just the pole. The different renormalisation schemes thus define which finite part is subtracted along with the pole.

When dealing with heavy particles, it is quite common to use the *on-shell scheme*, since it is the most intuitive one. In this scheme, the pole of the propagator is at $p^2 = m^2_{phys}$, where m^2_{phys} is the physical mass of the particle. The condition that the pole occurs for $p^2 = m^2_{phys}$ can be transcribed mathematically as

$$\Big[\tilde{G}^{(2)}_c(p,-p)\Big]^{-1} u(p)|_{p^2=m^2} = 0 \tag{3.86}$$

$$\Leftrightarrow \quad -i(\not{p} - m + \Sigma(\not{p}))u(p)|_{p^2=m^2} = 0 \tag{3.87}$$

$$\Leftrightarrow \quad \Big[(1+\mathcal{B}(\not{p}) + \partial Z_\psi)\not{p} - m(1 - \frac{\mathcal{A}(\not{p})}{m} + \partial Z_\psi + \partial Z_m)\Big]|_{p^2=m^2} = 0 \tag{3.88}$$

Since the particle is on shell, we can use the Dirac equation $\not{p}u(\not{p}) = mu(\not{p})$, giving

$$\partial Z_m = \frac{\partial m^{OS}}{m} = \mathcal{B}(m^2) + m^2\mathcal{A}(m^2), \tag{3.89}$$

which reads explicitly

$$\frac{\partial m^{OS}}{m} = -\frac{\alpha_S}{4\pi}3C_F\Big(\frac{1}{\epsilon} - \gamma_E + \ln 4\pi + \frac{4}{3} + \ln\frac{\mu_R^2}{m^2}\Big). \tag{3.90}$$

This counterterm clearly includes finite parts. Other schemes may now be defined, depending on which finite terms are subtracted.
The MS scheme typically subtracts only the divergence

$$\frac{\partial m^{MS}}{m} = -\frac{\alpha_S}{4\pi}3C_F\Big(\frac{1}{\epsilon}\Big), \tag{3.91}$$

while the $\overline{MS}$ scheme also removes finite geometric terms,

$$\frac{\partial m^{\overline{MS}}}{m} = -\frac{\alpha_S}{4\pi}3C_F\Big(\frac{1}{\epsilon} - \gamma_E + \ln 4\pi\Big). \tag{3.92}$$

3.2.5 Counterterms for tH^- production

The ultraviolet divergencies contained in the virtual cross section $d\sigma^V$ have been made explicit using dimensional regularisation with $D = 4 - 2\epsilon$ dimensions and are cancelled against counterterms originating from multiplicative renormalisation of the parameters in the Lagrangian. In particular, the counterterm for the strong coupling constant $\alpha_S = g_S^2/(4\pi)$,

$$\partial g_S = -\frac{\alpha_S(\mu_R^2)}{8\pi}\Big[\Delta_{UV}\Big(\frac{11}{3}N_C - \frac{2}{3}N_F\Big) - \frac{2}{3}\ln\frac{\mu_R^2}{m_t^2}\Big], \tag{3.93}$$

is computed in the $\overline{MS}$ scheme using massless quarks with $\Delta_{UV} = 1/\epsilon - \gamma_E + \ln 4\pi$, with $N_C = 3$ and $N_F = 6$ being the total numbers of colours and quark flavours, respectively, but decoupling explicitly the heavy top quark with mass m_t from the running of α_S [86]. The top quark mass is renormalised in the on-shell scheme,

$$\frac{\partial m_t^{OS}}{m_t} = -\frac{\alpha_S(\mu_R^2)}{4\pi}3C_F\Big(\Delta_{UV} + \frac{4}{3} + \ln\frac{\mu_R^2}{m_t^2}\Big), \tag{3.94}$$

where $C_F = (N_C^2 - 1)/(2N_C)$. On the other hand, we perform the renormalisation of both the bottom and top Yukawa couplings in the $\overline{MS}$ scheme,

$$\frac{\partial y_{b,t}}{y_{b,t}(\mu_R^2)} = -\frac{\alpha_S(\mu_R^2)}{4\pi}3C_F\Delta_{UV}. \tag{3.95}$$

This enables us to factorise the charged Higgs boson coupling at LO and NLO, making the QCD correction (K) factors independent of the 2HDM and value of $\tan\beta$ under study. The Yukawa couplings in Eq. (3.95) are evaluated at the process energy scale fixed at μ_R using the running quark $\overline{MS}$ masses from an initial scale M_Q

$$m_Q^{\overline{MS}}(\mu_R) = m_Q^{\overline{MS}}(M_Q)\frac{c\Big(\alpha_s(\mu_R)/\pi\Big)}{c\Big(\alpha_s(M_Q)/\pi\Big)} \tag{3.96}$$

, where

$$c(x) = \Big(\frac{23}{6}x\Big)^{12/23}(1 + 1.175x + 1.501x^2) \text{ for } M_b < \mu_R < M_t \tag{3.97}$$

and

$$c(x) = \Big(\frac{7}{2}x\Big)^{4/7}(1 + 1.398x + 1.793x^2) \text{ for } \mu_R > m_t. \tag{3.98}$$

The starting values of the $\overline{MS}$ masses can be obtained from the on-shell masses M_Q through the relation

$$\bar{m}_Q(M_Q) = \frac{M_Q}{1 + \frac{4}{3}\frac{\alpha_S(M_Q)}{\pi} + K_Q\Big(\frac{\alpha_s(M_Q)}{\pi}\Big)^2} \tag{3.99}$$

with $K_b \approx 12.4$ and $K_t \approx 10.9$.

Wave-functions are renormalised in the $\overline{MS}$ scheme

$$\partial Z = -\frac{\alpha_S(\mu_R^2)}{4\pi} 3 C_F \Delta_{UV}. \tag{3.100}$$

Thus, the complete $bbg-$, resp. $ttg-$, vertex counterterm contribution is given by

$$\left[\delta Z_g + \frac{1}{2}\delta Z_A + 2\frac{1}{2}\delta Z_{\psi,b/t}\right] \mathcal{B}_{(D)} = \left[\frac{\alpha_s}{4\pi}\left(N_C + C_F\right)\Delta\right] \mathcal{B}_{(D)}, \tag{3.101}$$

and the $Hbt-$ vertex counterterm reads

$$\left[\frac{1}{2}\delta Z_{\psi,b} + \frac{1}{2}\delta Z_{\psi,t} + \frac{1}{2}\delta y_b + \frac{1}{2}\delta y_t\right] \mathcal{B}_{(D)} = \frac{\alpha_s}{4\pi} C_F \left[4\Delta + \frac{3}{2}\left(\frac{4}{3} - \ln\frac{mt^2}{\mu^2}\right)\right] \mathcal{B}_{(D)} \tag{3.102}$$

where $\mathcal{B}_{(D)}$ is the Born term calculated in D dimensions

$$\mathcal{B}_{(D)} = \frac{1}{SC}|\mathcal{M}_B|^2 = \frac{2\sqrt{2}\alpha_s(A^2+B^2)G_F\pi}{N_C}\frac{1}{s(m_t^2-t)}\Big[\mathcal{M}_0 + \epsilon\mathcal{M}_1\Big], \tag{3.103}$$

with

$$\mathcal{M}_0 = \frac{2m_H^4(m_t^2-t) + 2m_H^2\Big(t(s+t) - m_t^4\Big) + (m_t^2-s-t)\Big(m_t^4 - sm_t^2 + t(s+t)\Big)}{(m_t^2-t)} \tag{3.104}$$

and

$$\mathcal{M}_1 = -(s+t-m_t^2)^2. \tag{3.105}$$

If ($\epsilon \to 0$) we see that Eq. (3.103) indeed reduces to its 4-dimensional expression, Eq. (3.14).

3.2.6 Renormalised virtual contributions for tH^- production

We have just seen that in order to compute a cross section that is UV-finite, we have to calculate all virtual contributions with renormalised quantities rather than bare quantities and add the counterterms. All renormalised contributions for tH^- production are shown in Fig. 3.8, where the blob indicates the loop contributions added to the counterterms.

If we turn our attention back to the vertex correction we calculated earlier, we see that the renormalisation of this vertex is given by the counterterm contribution multiplied with the Born matrix elements

$$\begin{aligned} 2|\mathcal{M}_C\mathcal{M}_B|^2 = &-\frac{\alpha_S^2\left(A^2+B^2\right)C_F N_C}{3s\left(m_t^2-t\right)}\times \\ &\left(m_H^4 - \left(m_t^2+s+t\right)m_H^2 - m_t^4(\epsilon-1) - t(s+t)(\epsilon-1) + m_t^2(s(\epsilon-1)+t(2\epsilon-1))\right) \\ &\left(6(C_F+N_C)\Delta_{UV} + (11N_C - 2N_F)\log\left(\frac{\mu_F^2}{\mu^2}\right) - 2(3N_C+1)\log\left(\frac{\mu^2}{m_t^2}\right)\right) \end{aligned} \tag{3.106}$$

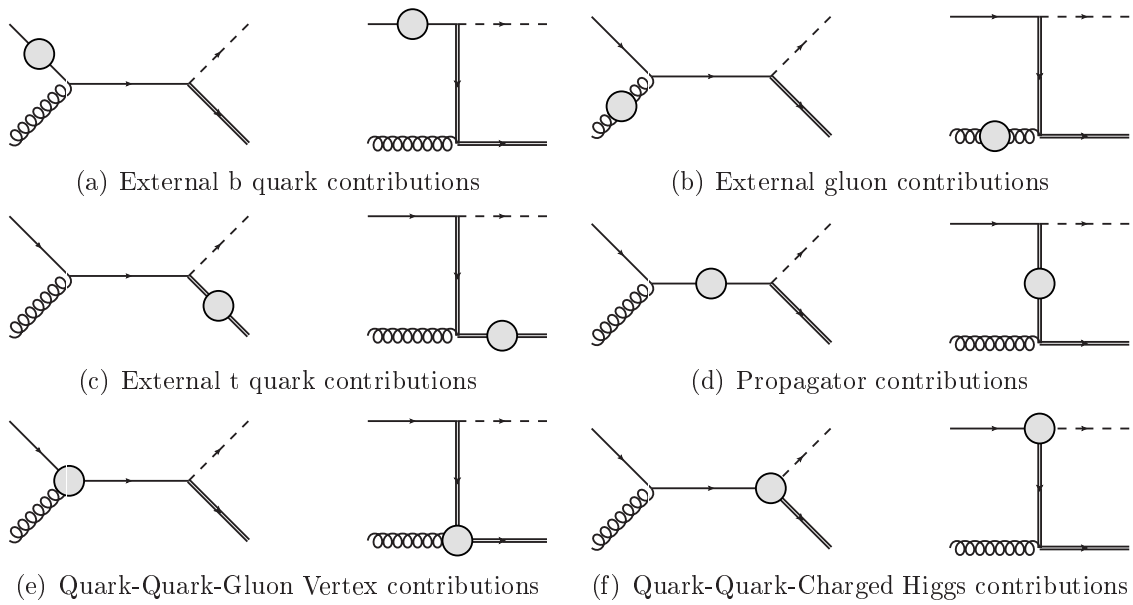

(a) External b quark contributions (b) External gluon contributions

(c) External t quark contributions (d) Propagator contributions

(e) Quark-Quark-Gluon Vertex contributions (f) Quark-Quark-Charged Higgs contributions

Figure 3.8: Virtual renormalised contributions. The grey dot indicates the NLO virtual contributions plus the counterterm.

and the sum of this term with Eq.(3.64) will yield no UV pole anymore but a remaining finite term

$$2\Big(|\mathcal{M}_{\mathcal{V}_{gbg}}\mathcal{M}_B|^2 + |\mathcal{M}_{\mathcal{V}_{bgb}}\mathcal{M}_B|^2 + |\mathcal{M}_C\mathcal{M}_B|^2\Big) = -\frac{\alpha_S^2\,(A^2+B^2)\,(N_C^2-1)}{2N_C s\,(m_t^2-t)}\times$$
$$\Big(\big(N_C^2-1\big)\,m_H^4 + \big(2m_t^2 - N_C^2 s + s - 2N_C^2 t\big)\,m_H^2 - 2m_t^4 + 2m_t^2(s+t) + \big(N_C^2-1\big)\,t(s+t)\Big)\,. \tag{3.107}$$

Independence of the wave function renormalisation When renormalising the QCD Lagrangian, we redefined the parameters such as the masses and the coupling constants, but also the wave functions. Since the final cross section can ultimately only depend on physical quantities, the wave function dependence must drop out. Sketching rapidly what happens, we see that it does indeed. For example, the dependence on the gluon wave-function counterterm is only included in the external gluon leg and the vertex corrections and we see that the leg contribution will be cancelled by the sum of the vertex corrections:

Leg	$-\frac{1}{2}\delta Z_g$ 2 Born
S-Channel vertex	$\frac{1}{2}\delta Z_g$ 2 $(\mathcal{SS}+\mathcal{ST})$
T-Channel vertex	$\frac{1}{2}\delta Z_g$ 2 $(\mathcal{TS}+\mathcal{TT})$
Sum	0

This means that one can avoid calculating all these contributions, since they sum up to zero. It is nevertheless useful to compute the amplitudes including the wavefunction renormalisation to check UV-finitness of the legs and vertices separately.

Remaining IR poles

The renormalised virtual cross section still exhibits some IR poles

$$\sigma_v = \int dPS^{(2)} \Big[\Big(\frac{C_2}{\epsilon^2} + \frac{C_1}{\epsilon} \Big) \mathcal{B}_{(D)} + C_0 \Big], \tag{3.108}$$

where the double and simple poles are given by

$$C_2 = \frac{1}{2N_C} - \frac{3}{2} N_C, \tag{3.109}$$

$$\begin{aligned} C_1 &= \frac{1}{4N_C} \Big(5 - 4 \ln \frac{m_t^2 - u}{m_t^2} \Big) \\ &+ \frac{N_C}{12} \Big(-37 + 12 \ln \frac{s}{m_t^2} + 12 \ln \frac{m_t^2 - t}{m_t^2} \Big) + \frac{1}{3} N_F. \end{aligned} \tag{3.110}$$

The constant term C_0 is too long to quote here, but can be found in the Monte Carlo event generator codes.

3.3 Real corrections

We have just gone through an extended Section concerning virtual contributions, where special calculus techniques were introduced and the renormalisation procedure to be defined. For the next part of the NLO calculation, which are the real emission diagrams, the situation will be completely different. These diagrams allow for a straightforward calculation and may be implemented as such in the code. The divergencies occurring in these contributions will be taken care of by the subtraction formalism.

Real emission diagrams are constructed on one hand from the Born terms in which coloured particles may emit an additional particle, or on the other hand, the tH^- final state may come from different incoming partons altogether. Since the energy involved in the collision is bounded from above, we won't run into UV divergencies in this Section. However, the additionally emitted parton can have an energy tending to 0 or may be emitted collinear to another particle, and this gives rise to IR poles. For illustration purposes, we'll see what happens to a quark emitting a gluon, as in figure 3.9.

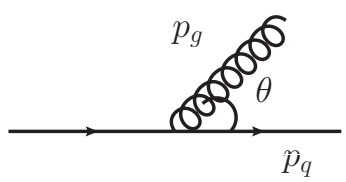

Figure 3.9: Gluon emission by quark.

The denominator of the quark propagator prior to emission reads

$$\mathcal{P} = \frac{1}{(p_q + p_g)^2 - m_q^2} = \frac{1}{2E_g E_q (1 - \beta_q \cos\theta)} \tag{3.111}$$

with $\beta_q = (1 - \frac{m_q^2}{E_q^2})^{1/2}$. E_i is the energy of particle i and θ is the angle between the quark and the gluon. This expression exhibits two singular regions ($\mathcal{P} \to \infty$) which may overlap:

If the energy of the emitted particle tends to zero ($E_g \to 0$), the divergence is called a **soft singularity**. If however the emission angle tends to zero ($\theta_{qg} \to 0$), it is called a **collinear** or **mass singularity**, the second denomination because this only occurs if the quark is massless. The Kinoshita-Lee-Nauenberg (KLN) theorem [87, 88, 89] guarantees that for inclusive quantities these contributions are exactly the same as the IR poles in the virtual term, but with this time a positive prefactor, so that their sum will be finite.

Real emission contributions for tH^- production

The real emission can be grouped into four processes:

- **Process**(a) : $b(p_1) + g(p_2) \to H^-(k_1) + t(k_2) + g(k_3)$
  These contributions, which are shown in Fig. 3.10, arise when coloured particles of the Born s- and t-channel diagrams emit a gluon. The additional gluon can be emitted by either the incoming b quark or gluon, by the outgoing top quark, or by the b or top quark in the propagator.

- **Process** (b) : $g(p_1) + g(p_2) \to tH^-(k_1) + t(k_2) + \bar{b}(k_3)$
  Process (b) can be obtained from (a) by crossing k_3 with $-p_1$, and multiplying the matrix element squared by a factor (-1) to take into account the altered sign of the quark impulse in the spinor sum. The real contributions for two incoming gluons are shown in Fig. 3.11. Since we computed them using the simple polarisation sum for the external gluons, ghost contributions, depicted in Fig. 3.12, have to be added to remove the unphysical polarisation states.

- **Process** (c) : $\bar{q}/q(p_1) + b(p_2) \to H^-(k_1) + t(k_2) + \bar{q}/q(k_3)$
  Diagrams for process (c) are displayed in Fig. 3.13. They require an incoming b quark and another quark or antiquark.

- **Process**(d) : $\bar{q}(p_1) + q(p_2) \to H^-(k_1) + t(k_2) + \bar{b}(k_3)$
  This process describes $q\bar{q}$ annihilation, illustrated in Fig. 3.14, and is convergent for incoming quarks $q = u, d, c$ and s, but interferes with process (c) for incoming b quarks. These contributions are, however, negligible due to the low b-quark distribution function.

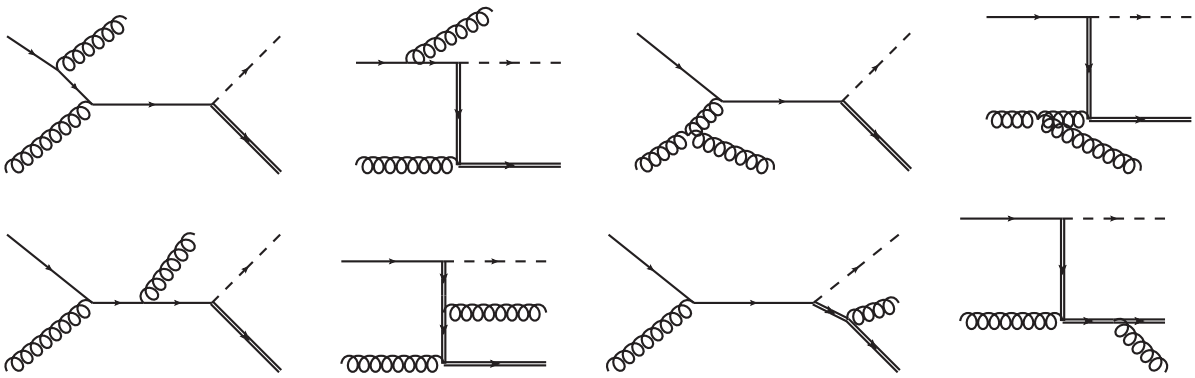

Figure 3.10: Real emission contributions in the gb channel.

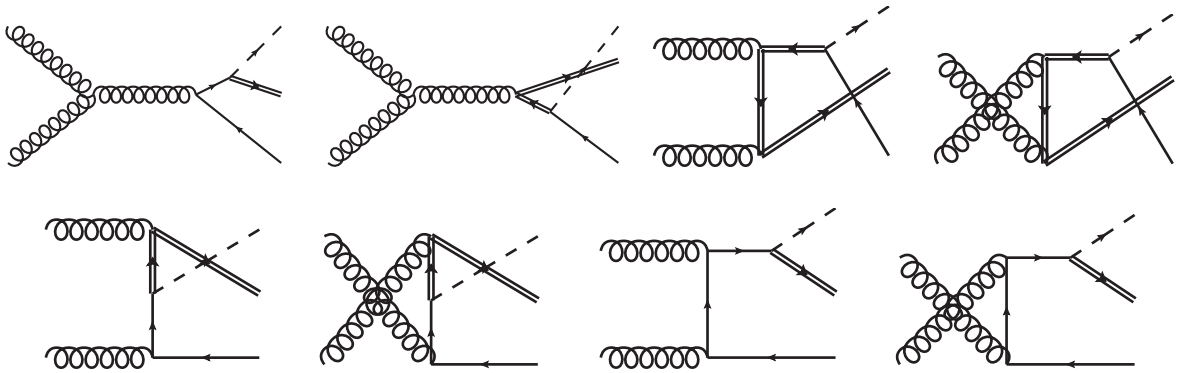

Figure 3.11: Real emission contributions in the gluon-gluon channel.

Figure 3.12: Ghost contributions for the gluon-gluon channel.

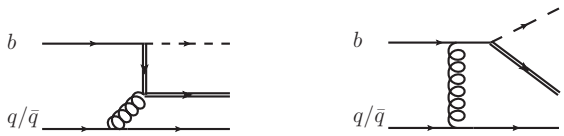

Figure 3.13: $q/\bar{q}b$ initial state processes.

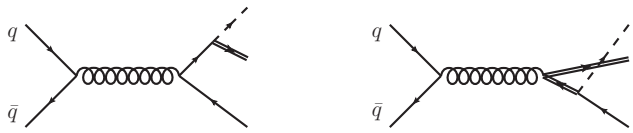

Figure 3.14: $q\bar{q}$ initial state processes.

3.4 Catani-Seymour dipole subtraction

In QCD calculations beyond leading order, analytic calculations are in general impossible for all but the simplest quantities because of the complicated phase space for multi-parton configurations. The use of numerical methods is ubiquitous but far from trivial since virtual and real contributions have a different number of final-state partons and thus have to be integrated separately over different phase space regions. Two different approaches can and have been used to cancel the infrared divergencies that appear at intermediate steps of the NLO calculation, namely phase-space slicing and the subtraction method. In both, only the small part of the calculations which gives rise to these singularities is treated analytically. The feature of a NLO cross section calculation that makes it possible to define a process-independent method is that, in the soft and collinear limit, the real cross section $d\sigma^R$ is given by the process-dependent Born-level cross section $d\sigma^B$ times process-independent singular factors. In that sense, the IR contributions to the real cross section are universal. The additional single-parton phase space describes the two-parton decay and thus contains the kinematical dependence on the degrees of freedom that lead to the IR poles.

The general philosophy of the **phase space slicing method** [90, 91, 92] is to introduce an arbitrary finite cut-off δ, with $\delta \ll 1$, in order cut out the divergent part of the real contribution in such a way that it can be added to the virtual

$$\begin{aligned}
\sigma_{R+V} &= \int_\delta^1 \frac{dx}{x^{1+\epsilon}} M(x) + \int_0^\delta \frac{dx}{x^{1+\epsilon}} M(x) + \frac{1}{\epsilon} M_0 \\
&\approx \int_\delta^1 \frac{dx}{x^{1+\epsilon}} M(x) + \int_0^\delta \frac{dx}{x^{1+\epsilon}} M_0 + \frac{1}{\epsilon} M_0 \\
&= \int_\delta^1 \frac{dx}{x^{1+\epsilon}} M(x) + \frac{1}{\epsilon}\left(1 - \delta^{-\epsilon}\right) M_0 \\
&\approx \int_\delta^1 \frac{dx}{x^{1+\epsilon}} M(x) + M_0 \ln \delta
\end{aligned} \tag{3.112}$$

The KLN theorem guarantees that $M(0) = M_0$. The overall dependence on δ naturally cancels out for $\delta \to 0$. In computer simulations however, the finite accuracy may lead to incomplete cancellations for different regions of phase space. The method's disadvantage is introducing this slicing parameter, which should in principle be sent to zero at the end of the calculation but in practice cannot be chosen too small. This may lead to uncontrolled errors, rendering the slicing method ill-adapted for numerical implementations.

An alternative approach is the **subtraction method** [93, 94, 95], in which a general term is added and subtracted in a suitable form for the real and the virtual poles to be

cancelled

$$\begin{aligned}\sigma_{R+V} &= \int_0^1 \frac{dx}{x^{1+\epsilon}} M(x) - \int_0^1 \frac{dx}{x^{1+\epsilon}} M_0 + \int_0^1 \frac{dx}{x^{1+\epsilon}} M_0 + \frac{1}{\epsilon} M_0 \\ &= \int_0^1 \frac{M(x) - M_0}{x^{1+\epsilon}} dx + \left(-\frac{1}{\epsilon} + \frac{1}{\epsilon}\right) M_0 \\ &\approx \int_0^1 \frac{M(x) - M_0}{x} dx + \mathcal{O}(1) M_0. \end{aligned} \tag{3.113}$$

The advantage of the dipole subtraction method consists in replacing cancellation between integrals by cancellation amongst integrands.

Another issue arises when dealing with massive final state partons. We have seen that QCD radiation off such a parton is infrared finite. It can however lead to sizeable contributions, since some may be proportional to powers of $\ln Q^2/M^2$, where M stands for the parton mass and Q is the scale of the hard scattering process. These contributions are logarithmically enhanced in kinematic regions where $Q \gg M$ and may spoil the numerical convergence of the calculation. This means that special care has been taken with the construction of the dipoles, so that the instabilities that such terms can produced are minimised.

The Catani-Seymour formalism Although MC@NLO and POWHEG use FKS dipoles [94], which are constructed automatically in POWHEG, we have built a standalone NLO code using Catani Seymour dipoles [4, 5], for checking purposes. This implementation will be detailed here. In the Catani-Seymour dipole formalism, the master equation for the NLO cross section can be written as

$$\begin{aligned}\sigma^{NLO}(p_1, p_2; \mu_F^2) &= \sigma^{NLO\{2\}}(p_1, p_2) + \sigma^{NLO\{3\}}(p_1, p_2) \\ &+ \int_0^1 dx \Big[\sigma^{NLO\{2\}}(x; xp_1, p_2; \mu_F^2) + \sigma^{NLO\{2\}}(x; p_1, xp_2; \mu_F^2)\Big]. \end{aligned} \tag{3.114}$$

We will start by introducing the general colour structures needed for $tH^\pm$ production at NLO and then detail the different dipole contributions.

Colour Algebra In this formalism, we denote the colour matrices as $\mathbf{T}_i \cdot \mathbf{T}_j = \mathbf{T}_j \cdot \mathbf{T}_i$ and $\mathbf{T}_i^2 = C_i$, where C_i is the quadratic Casimir operator in the representation of particle i. $C_i = C_F = (N_C^2 - 1)/(2N_C)$ in the fundamental representation and $C_i = C_A = N_C$ in the adjoint representation.
We have

$$\mathbf{T}_{t,b}^2 |t; b, g\rangle = C_F \text{ and} \tag{3.115}$$

$$\mathbf{T}_g^2 |t; b, g\rangle = N_C. \tag{3.116}$$

Since the process we are interested in involves only three partons t, b, g, the color algebra can be performed in closed form and color conservation imposes

$$\sum_{i=t,b,g} \mathbf{T}_i |t; b, g\rangle = 0. \tag{3.117}$$

Using this fact, we can easily derive that

$$\begin{aligned} 0 &= \left(\sum_{i=t,b,g} \mathbf{T}_i\right)^2 |t; b, g\rangle \\ &= \left(\mathbf{T}_t^2 + \mathbf{T}_b^2 + \mathbf{T}_g^2 + 2\,\mathbf{T}_t \cdot \mathbf{T}_b + 2\,\mathbf{T}_t \cdot \mathbf{T}_g + 2\,\mathbf{T}_b \cdot \mathbf{T}_g\right) |t; b, g\rangle \end{aligned} \tag{3.118}$$

and

$$\left(\mathbf{T}_t \cdot \mathbf{T}_b + \mathbf{T}_t \cdot \mathbf{T}_g\right) |t; b, g\rangle = -\mathbf{T}_t^2 |t; b, g\rangle. \tag{3.119}$$

Finally we have

$$2\,\mathbf{T}_b \cdot \mathbf{T}_g |t; b, g\rangle = \left(\mathbf{T}_t^2 - \mathbf{T}_b^2 - \mathbf{T}_g^2\right) |t; b, g\rangle \tag{3.120}$$

$$2\,\mathbf{T}_t \cdot \mathbf{T}_g |t; b, g\rangle = \left(\mathbf{T}_b^2 - \mathbf{T}_t^2 - \mathbf{T}_g^2\right) |t; b, g\rangle \tag{3.121}$$

$$2\,\mathbf{T}_t \cdot \mathbf{T}_b |t; b, g\rangle = \left(\mathbf{T}_g^2 - \mathbf{T}_t^2 - \mathbf{T}_b^2\right) |t; b, g\rangle \tag{3.122}$$

The color structures we need are

$$\mathbf{T}_t \cdot \mathbf{T}_b |t; b, g\rangle = -\left(C_F - \frac{N_C}{2}\right) |t; b, g\rangle = \frac{1}{2N_C} |t; b, g\rangle, \tag{3.123}$$

$$\mathbf{T}_{t/b} \cdot \mathbf{T}_g |t; b, g\rangle = -\frac{N_C}{2} |t; b, g\rangle, \tag{3.124}$$

using the normalisation $T_R = 1/2$.

Virtual dipole contribution In Eq. (3.114), the two-body final-state contribution is given by

$$\begin{aligned} \sigma^{NLO\{2\}}(p_1, p_2) &= \int_2 \left[d\sigma^V(p_1, p_2) + d\sigma^{LO}(p_1, p_2) \otimes \mathbf{I}\right]_{\epsilon=0} \\ &= \int d\Phi^{(2)} \left[2\,\overline{\mathrm{Re}}\left[\mathcal{M}_{1-\mathrm{loop}}\,\mathcal{M}^\dagger_{\mathrm{Born}}\right] + {}_2\langle t; b, g \mid \mathbf{I}(\epsilon) \mid t; b, g\rangle_2\right]_{\epsilon=0} \end{aligned} \tag{3,125}$$

The factor $d\Phi^{(m)(p_a,p_b)}$ regroups the final state phase space, the flux factor and the average over the spin configurations

$$d\Phi^{(m)}(p_a, p_b) = \frac{1}{\mathcal{S}_a \mathcal{S}_b \mathcal{F}} d\phi_m(p_1, ..., p_m; p_a + p_b). \tag{3.126}$$

After the renormalisation of the ultraviolet singularities has been performed as described in the previous section 3.2, the virtual cross section contains only infrared poles. These can be removed by convolving the Born cross section with the subtraction term

$$\mathbf{I}(\epsilon) = \mathbf{I}_2(\epsilon, \mu^2; \{k_2, m_t\}) + \mathbf{I}_b(\epsilon, \mu^2; \{k_2, m_t\}, p_1) + \mathbf{I}_g(\epsilon, \mu^2; \{k_2, m_t\}, p_2) + \mathbf{I}_{bg}(\epsilon, \mu^2; p_1, p_2), \tag{3.127}$$

where in our case $\mathbf{I}_2(\epsilon,\mu^2;\{k_2,m_t\})=0$, since there are no QCD dipoles with a final state emitter and a final state spectator. The dipoles depending on one initial state parton ($a=b,g$) with four-momentum p_i ($i=1,2$) are

$$\begin{aligned}\mathbf{I}_a(\epsilon,\mu^2;\{k_2,m_t\},p_i) &= -\frac{\alpha_s}{2\pi}\frac{(4\pi)^\epsilon}{\Gamma(1-\epsilon)}\left\{\frac{1}{\mathbf{T}_t^2}\mathbf{T}_t\cdot\mathbf{T}_a\left[\mathbf{T}_t^2\left(\frac{\mu^2}{s_{ta}}\right)^\epsilon\left(\mathcal{V}_t(s_{ta},m_t,0;\epsilon)-\frac{\pi^2}{3}\right)\right.\right.\\ &\qquad\left.+\Gamma_t(\mu,m_t;\epsilon)+\gamma_t\ln\frac{\mu^2}{s_{ta}}+\gamma_t+K_t\right]\\ &+\frac{1}{\mathbf{T}_a^2}\mathbf{T}_a\cdot\mathbf{T}_t\left[\mathbf{T}_a^2\left(\frac{\mu^2}{s_{at}}\right)^\epsilon\left(\mathcal{V}_a(s_{at},0,m_t;\epsilon,\kappa)-\frac{\pi^2}{3}\right)+\frac{\gamma_a}{\epsilon}\right.\\ &\qquad\left.\left.+\gamma_a\ln\frac{\mu^2}{s_{at}}+\gamma_a+K_a\right]\right\},\end{aligned}\tag{3.128}$$

where $\mathbf{T}_{a,t}$ denotes the color matrix associated to the emission of a gluon from the parton a or the top quark t, the dimensional regularisation scale μ is identified with the renormalisation scale μ_R, and $s_{ta}=s_{at}=2p_1k_2$. The kernels

$$\mathcal{V}_t(s_{ta},m_t,0;\epsilon) = \mathcal{V}^{(S)}(s_{ta},m_t,0;\epsilon)+\mathcal{V}_t^{(NS)}(s_{ta},m_t,0)\tag{3.129}$$

$$\mathcal{V}_b(s_{bt},0,m_t;\epsilon,2/3) = \mathcal{V}^{(S)}(s_{bt},0,m_t;\epsilon)+\mathcal{V}_b^{(NS)}(s_{bt},0,m_t)\tag{3.130}$$

$$\mathcal{V}_g(s_{gt},0,m_t;\epsilon,2/3) = \mathcal{V}^{(S)}(s_{gt},0,m_t;\epsilon)+\mathcal{V}_g^{(NS)}(s_{gt},0,m_t;2/3)\tag{3.131}$$

consist of the singular terms

$$\begin{aligned}&\mathcal{V}^{(S)}(s_{ta},m_t,0;\epsilon)=\mathcal{V}^{(S)}(s_{at},0,m_t;\epsilon)\\ &\quad=\frac{1}{2\epsilon^2}+\frac{1}{2\epsilon}\ln\frac{m_t^2}{s_{ta}}-\frac{1}{4}\ln^2\frac{m_t^2}{s_{ta}}-\frac{\pi^2}{12}-\frac{1}{2}\ln\frac{m_t^2}{s_{ta}}\ln\frac{s_{ta}}{Q_{ta}^2}-\frac{1}{2}\ln\frac{m_t^2}{Q_{ta}^2}\ln\frac{s_{ta}}{Q_{ta}^2}\end{aligned}\tag{3.132}$$

with $Q_{ta}^2=Q_{at}^2=s_{ta}+m_t^2+m_a^2$ and the non-singular terms

$$\mathcal{V}_t^{(NS)}(s_{ta},m_t,0) = \frac{\gamma_t}{\mathbf{T}_t^2}\ln\frac{s_{ta}}{Q_{ta}^2}+\frac{\pi^2}{6}-\mathrm{Li}_2\left(\frac{s_{ta}}{Q_{ta}^2}\right)-2\ln\frac{s_{ta}}{Q_{ta}^2}-\frac{m_t^2}{s_{ta}}\ln\frac{m_t^2}{Q_{ta}^2},\tag{3.133}$$

$$\begin{aligned}\mathcal{V}_b^{(NS)}(s_{bt},0,m_t) &= \frac{\gamma_b}{\mathbf{T}_b^2}\left[\ln\frac{s_{bt}}{Q_{bt}^2}-2\ln\frac{Q_{bt}-m_t}{Q_{bt}}-2\frac{m_t}{Q_{bt}+m_t}\right]\\ &+\frac{\pi^2}{6}-\mathrm{Li}_2\left(\frac{s_{bt}}{Q_{bt}^2}\right),\end{aligned}\tag{3.134}$$

$$\begin{aligned}\mathcal{V}_g^{(NS)}(s_{gt},0,m_t;2/3) &= \frac{\gamma_g}{\mathbf{T}_g^2}\left[\ln\frac{s_{gt}}{Q_{gt}^2}-2\ln\frac{Q_{gt}-m_t}{Q_{gt}}-2\frac{m_t}{Q_{gt}+m_t}\right]+\frac{\pi^2}{6}-\mathrm{Li}_2\left(\frac{s_{gt}}{Q_{gt}^2}\right)\\ &+\frac{4}{3}\frac{T_R}{N_C}\left[\ln\frac{Q_{gt}-m_t}{Q_{gt}}+\frac{m_t}{Q_{gt}+m_t}-\frac{4}{3}\right].\end{aligned}\tag{3.135}$$

The constant κ is a free parameter, which distributes non-singular contributions between the different terms in Eq. (3.114). The choice $\kappa=2/3$ considerably simplifies the gluon kernel. For massive quarks, one has in addition

$$\Gamma_t(\mu,m_t;\epsilon)=C_F\left(\frac{1}{\epsilon}+\frac{1}{2}\ln\frac{m_t^2}{\mu^2}-2\right),\tag{3.136}$$

while

$$\gamma_q = \frac{3}{2}C_F \quad , \quad \gamma_g = \frac{11}{6}N_C - \frac{2}{3}T_R N_f \tag{3.137}$$

and

$$K_q = \left(\frac{7}{2} - \frac{\pi^2}{6}\right)C_F \quad , \quad K_g = \left(\frac{67}{18} - \frac{\pi^2}{6}\right)N_C - \frac{10}{9}T_R N_f \tag{3.138}$$

with $T_R = 1/2$ and $N_f = 5$ the number of light quark flavours. The last term in Eq. (3.127)

$$\mathbf{I}_{bg}(\epsilon, \mu^2; p_1, p_2) = -\frac{\alpha_s}{2\pi}\frac{(4\pi)^\epsilon}{\Gamma(1-\epsilon)}\left\{\frac{1}{\mathbf{T}_g^2}\mathbf{T}_g\cdot\mathbf{T}_b\left[\left(\frac{\mu^2}{s_{bg}}\right)^\epsilon\left(\frac{\mathbf{T}_g^2}{\epsilon^2} + \frac{\gamma_g}{\epsilon}\right) - \mathbf{T}_g^2\frac{\pi^2}{3} + \gamma_g + K_g\right] + (g \leftrightarrow b)\right\} \tag{3.139}$$

depends on both initial state partons.

Real dipole contributions The second term in Eq. (3.114) concerns the real emission dipoles and is given explicitly by

$$\sigma^{NLO\{3\}}(p_1, p_2) = \int d\Phi^{(3)}\left\{\overline{|\mathcal{M}_{3,ij}(k_1, k_2, k_3; p_1, p_2)|^2} - \sum_{\text{dipoles}} \mathcal{D}(k_1, k_2, k_3; p_1, p_2)\right\} \tag{3.140}$$

includes the spin- and color-averaged squared real emission matrix elements

$$\overline{|\mathcal{M}_{3,ij}(k_1, k_2, k_3; p_1, p_2)|^2} \tag{3.141}$$

with three-particle final states, as detailed in Section 3.3, and the corresponding unintegrated QCD dipoles $\mathcal{D}$, which compensate the integrated dipoles $\mathbf{I}$ in the previous section. Both terms are integrated numerically over the three-particle differential phase space $d\Phi^{(3)}$. The sum over the dipoles in Eq. (3.140) includes initial-state emitters ab with both initial- and final-state spectators c ($\mathcal{D}^{ab,c}$ and $\mathcal{D}_c^{ab}$) and the final-state emitter ab with initial-state spectators c ($\mathcal{D}_{ab}^c$). For the three divergent processes, we have

$$(a) \; : \; \sum_{\text{dipoles}} = \mathcal{D}^{bg,g} + \mathcal{D}^{gg,b} + \mathcal{D}_t^{bg} + \mathcal{D}_t^{gg} + \mathcal{D}_{tg}^b + \mathcal{D}_{tg}^g, \tag{3.142}$$

$$(b) \; : \; \sum_{\text{dipoles}} = \mathcal{D}^{g_1 b,g_2} + \mathcal{D}^{g_2 b,g_1} + \mathcal{D}_t^{g_1 b} + \mathcal{D}_t^{g_2 b}, \quad \text{and} \tag{3.143}$$

$$(c) \; : \; \sum_{\text{dipoles}} = \mathcal{D}^{qq,b} + \mathcal{D}_t^{qq}. \tag{3.144}$$

Denoting by a the original parton before emission, b the spectator, and i the emitted particle, the dipole for initial-state emitters and initial-state spectators is given by

$$\mathcal{D}^{ai,b} = -\frac{1}{2p_a k_i}\frac{1}{x_{i,ab}}\,{}_{2,ab}\langle\tilde{H}, \tilde{t}; \tilde{ai}, b \mid \frac{\mathbf{T}_b\cdot\mathbf{T}_{ai}}{\mathbf{T}_{ai}^2}\mathbf{V}^{ai,b} \mid \tilde{H}, \tilde{t}; \tilde{ai}, b\rangle_{2,ab}, \tag{3.145}$$

where the momentum of the intermediate initial-state parton $\tilde{ai}$ is $\tilde{p}^\mu_{ai} = x_{i,ab}\, p^\mu_a$ with $x_{i,ab} = (p_a p_b - k_i p_a - k_i p_b)/(p_a p_b)$, the momentum p_b is unchanged, and the final-state momenta k_j with $j = 1, 2$ are shifted to

$$\tilde{k}^\mu_j = k^\mu_j - \frac{2k_j \cdot (K + \tilde{K})}{(K + \tilde{K})^2}(K + \tilde{K})^\mu + \frac{2k_j \cdot K}{K^2}\tilde{K}^\mu \tag{3.146}$$

with $K^\mu = p^\mu_a + p^\mu_b - k^\mu_i$ and $\tilde{K}^\mu = \tilde{p}^\mu_{ai} + p^\mu_b$. The necessary splitting functions $\mathbf{V}^{ai,b}$ for $\{ai, b\} = \{qg, g; gg, q; gq, g; qq, q\}$ can be found in App. B.

The dipole for initial-state emitters and a final-state spectator, which is in our case the top quark t, is given by

$$\mathcal{D}^{ai}_t = -\frac{1}{2p_a k_i}\frac{1}{x_{it,a}}\, {}_{2,\tilde{ai}}\langle H, \tilde{t}; \tilde{ai}, b \mid \frac{\mathbf{T}_t \cdot \mathbf{T}_{ai}}{\mathbf{T}^2_{ai}}\mathbf{V}^{ai}_t \mid H, \tilde{t}; \tilde{ai}, b\rangle_{2,\tilde{ai}}, \tag{3.147}$$

where the momentum of the intermediate initial-state parton $\tilde{ai}$ is $\tilde{p}^\mu_{ai} = x_{it,a} p^\mu_a$ with $x_{it,a} = (p_a k_i + p_a p_t - k_i p_t)/(p_a k_i + p_a p_t)$, the momentum p_b is unchanged, and the momentum of the final-state top quark p_t is shifted to $\tilde{p}^\mu_t = k^\mu_i + p^\mu_t - (1 - x_{it,a})p^\mu_a$. Here again, we list the necessary splitting functions $\mathbf{V}^{ai}_t$ for $\{ai, t\} = \{qg, t; gg, t; gq, t; qq, t\}$ in App. B.

Finally, the dipole for final-state emitter (the top quark t) and initial-state spectator a is given by

$$\mathcal{D}^a_{tg} = -\frac{1}{2p_t k_i}\frac{1}{x_{it,a}}\, {}_{2,a}\langle H, \tilde{it}; \tilde{a}, b \mid \frac{\mathbf{T}_a \cdot \mathbf{T}_{it}}{\mathbf{T}^2_{it}}\mathbf{V}^a_{it} \mid H, \tilde{it}; \tilde{a}, b\rangle_{2,a}, \tag{3.148}$$

where the momentum of the initial parton a is shifted to $\tilde{p}^\mu_a = x_{it,a} p^\mu_a$ with $x_{it,a} = (p_a k_i + p_a p_t - k_i p_t)/(p_a k_i + p_a p_t)$, the momentum p_b is unchanged, and the momentum of the intermediate final-state top quark p_t is $\tilde{p}^\mu_{it} = k^\mu_i + p^\mu_t - (1 - x_{it,a})p^\mu_a$. The required splitting function $\mathbf{V}^a_{gt}$ can again be found in App.B.

The last terms in Eq. (3.114) are finite remainders from the cancellation of the ϵ-poles of the initial-state collinear counterterms. Their general expressions read

$$\begin{aligned}\int_0^1 dx\, \sigma^{NLO\{2\}}\left(x; xp_1, p_2; \mu^2_F\right) &= \sum_{a'}\int_0^1 dx \int_2 \left[d\sigma^{LO}_{a'b}\left(xp_1, p_2\right) \otimes \left(\mathbf{K} + \mathbf{P}\right)^{a,a'}(x)\right]_{\epsilon=0} \\ &= \sum_{a'}\int_0^1 dx \int d\Phi^{(2)}(xp_1, p_2)\; {}_{2,a'b}\langle k_1, k_2; xp_1, p_2|\mathbf{K}^{a,a'}(x) + \mathbf{P}^{a,a'}(x; \mu^2_F)|k_1, k_2; xp_1, p_2\rangle_{2,a'b}\end{aligned} \tag{3.149}$$

and similarly for $(a \leftrightarrow b)$ and $(p_1 \leftrightarrow p_2)$. It is important to note that for process (b), both gb and bg Born processes are needed to construct the dipoles. The colour-charge operators $\mathbf{K}$ and $\mathbf{P}$ are explicitly given in App. B.

3.5 High and low charged Higgs mass: diagram removal

All of the previously described calculations are valid in a straightforward fashion for charged Higgs masses higher than the top mass $m_{H^-} > m_t$. If, however, the charged Higgs mass is lower than the top quark mass m_t, the top propagator of some amplitudes can go on-shell, resulting in a drastic increase in the total cross section. This happens for two amplitudes of process (b) on Fig. 3.11 and also for the second amplitude shown in Fig. 3.14 for processes (d). Although this is what happens in Nature, one would prefer having a way to separate at this stage the contributions coming from top anti-top production and its interference with charged Higgs production. We will discuss here only the case of diagram removal (DR) and leave the description of the diagram subtraction scheme and the analysis of both up to a later point.
In DR, the top anti-top production is removed at amplitude level. If we separate the amplitudes of a real process with colliding partons α and β into contributions which proceed through $t\bar{t}$-production, $\mathcal{A}^{t\bar{t}}_{\alpha\beta}$, and those which do not, $\mathcal{A}^{tH^-}_{\alpha\beta}$,

$$\mathcal{A}_{\alpha\beta} = \mathcal{A}^{t\bar{t}}_{\alpha\beta} + \mathcal{A}^{tH^-}_{\alpha\beta}, \tag{3.150}$$

squaring the amplitudes gives rise to three different quantities:

$$\begin{aligned} |\mathcal{A}_{\alpha\beta}|^2 &= |\mathcal{A}^{tH^-}_{\alpha\beta}|^2 + 2\mathcal{R}\big(\mathcal{A}^{tH^-}_{\alpha\beta}\mathcal{A}^{t\bar{t}*}_{\alpha\beta}\big) + |\mathcal{A}^{t\bar{t}}_{\alpha\beta}|^2 && (3.151)\\ &= \mathcal{S}_{\alpha\beta} + \mathcal{I}_{\alpha\beta} + \mathcal{D}_{\alpha\beta}. && (3.152)\end{aligned}$$

The term $\mathcal{D}_{\alpha\beta}$ contains neither collinear nor soft singularities. The interference term $\mathcal{I}_{\alpha\beta}$ contains infrared singularities when only the matrix element squared are considered, but those are integrable when multiplied by the phase space factor. These terms are therefore sometimes referred to as subleading with respect to the ones in $\mathcal{S}_{\alpha\beta}$. So $\mathcal{S}_{\alpha\beta}$ contains all the singularities which have to be regularised via the subtraction formalism. Since diagram removal requires removing $t\bar{t}$ production at the amplitude level, the only element which is kept is $\mathcal{S}_{\alpha\beta}$. This contains all the leading divergencies and the dipoles we used in the $m_{H^-} > m_t$ case are still valid and can be taken over as such.

Removing diagrams from amplitude level causes the loss of gauge invariance. A considerable part of [96] has been dedicated to the analysis of this impact. They considered different gauges for the gluon propagator and found differences of per mille order. One aspect which has not been checked yet in previous papers, but which has drawn our attention, is the impact of the polarisation sum of external gluons.

Consider an amplitude with an external gluon with four-momentum k and polarisation vector ϵ with polarisation λ. The easiest and quickest way of calculating the matrix element squared is to replace the polarisation sum

$$P^{\mu\nu}(k) = \sum_{\lambda=1,2} \epsilon^{\mu}(k,\lambda)\epsilon^{\nu}(k,\lambda) \tag{3.153}$$

by

$$P^{\mu\nu}(k) = -g^{\mu\nu}. \tag{3.154}$$

In doing this, we not only sum over the physical, transverse polarisations of the gluon, but also over non-physical longitudinal ones. Usually we would add ghosts whenever necessary to recover the right sum. In this case, individual matrix element squared terms have no meaning and only their sum is gauge invariant. But since in DR a subset of those diagrams is to be removed, there is no proper way to do this using the simple polarisation sum. Of course the statement for the polarisations

$$\epsilon^{\mu}(k,\lambda)\epsilon_{\mu}(k,\lambda^{'}) = -\delta_{\lambda\lambda'} \tag{3.155}$$

is still valid, and we also have

$$\epsilon \cdot k = 0, \tag{3.156}$$

but unfortunately this fixes the choice for the polarisation vector not completely if $k^2 = 0$ as in our case. These conditions need to be supplemented with an additional statement, introducing a new four-vector η such as

$$\eta \cdot \epsilon = 0. \tag{3.157}$$

This will result in the following expression for the polarisation sum:

$$P^{\mu\nu}(k) = -g^{\mu\nu} - \frac{1}{(k\cdot\eta)^2}\left[\eta^2 k^{\mu}k^{\nu} - k\cdot\eta\,(k^{\mu}\eta^{\nu} + \eta^{\mu}k^{\nu})\right], \tag{3.158}$$

where the sum is now really only over physical polarisations. Usually the η-dependence drops out when calculating a gauge invariant quantity but this will not be our case as we argued earlier. Since in the gg-channel we have to deal with two external gluons with momenta k_a and k_b and polarisation vectors ϵ_a and ϵ_b, we introduce two new four-vectors η_a and η_b and we choose

$$\eta_a = k_b, \tag{3.159}$$

$$\eta_b = k_a, \tag{3.160}$$

in order to respect the aforementioned constraints.

Je sers la science et c'est ma joie!

Disciplus Simplex, *"Léonard"*

4
Event generator implementation

Now that we have at our disposal a complete NLO calculation for tH^- production, we can turn to the integration into Monte Carlo event generators. In a first part, we describe different issues connected to event generators. We then comment on the MC@NLO implementation, for which our NLO code provides a useful check. Additionally, we perform different phenomenological studies using tH^- production in MC@NLO, focusing on aspects which lead to contributions in systematic uncertainty evaluations. In a third part, we describe in detail the implementation of NLO tH^- production in POWHEG and discuss some relevant distributions.

4.1 Monte Carlo event generators

Monte Carlo event generators numerically implement the predictions of cross section calculations. The calculation of the hard scattering often involves very complicated final state phase space integrations, which can no longer be performed analytically, so that specific Monte Carlo integration techniques have been developed to address this issue. Also, comparing experimental data with theoretical predictions is simplified with Monte Carlo codes, because eventual kinematic cuts can be applied trivially. Another advantage of a Monte Carlo simulation is that it allows to simulate, to a certain degree of accuracy, the real experiment and can be used for different tests and estimations as, for example, a check of whether the real experiment would be feasible in a reasonable amount of time. Modern research in particle physics is intimately linked to Monte Carlo estimations, as they intervene in several steps: during the R&D phase to test sub-detector performances, for data analysis in order to estimate the signal and background fraction and optimise their ratio, and to perform statistical tests. We will see that dressing hadronic processes with low energy gluon radiation can also be done by a

Monte Carlo code. Thus, the notion of Monte Carlo is very broad and can have several meanings, depending on which action the attention is focused on.

Fixed-order Monte Carlo codes generate partonic final states according to the exact matrix elements, to a given order in perturbation theory. They provide accurate descriptions of well separated, hard jets, which correspond to parton configurations away from the singular collinear and soft regions. In these regions, large logarithmic enhancements imply the need to use resummed contributions and this can be done via another type of Monte Carlo generators, the all-order event generators. This allows one to switch from the theoretically well defined parton final states to the more realistic hadronic states observed in particle physics detectors. The art lies in the connection of both regimes. Today, there are two major codes for which it is possible to generate events with NLO matrix elements for the hard process and that subsequently passes them over to an all-order Monte Carlo code for showering and hadronisation. These are MC@NLO and POWHEG and will be discussed in more detail in dedicated sections. As we have seen in Fig. 2.1, the structure of a simulated event is as follows: a primary hard process, calculated to some fixed order in pQCD, is handed over to a parton shower, which dresses incoming as well as outgoing partons with additional radiation. The generation of the incoming space-like and the outgoing time-like parton showers is done using modified versions of the DGLAP equations for PDFs and fragmentation functions. These shower developments are still in the perturbative regime. Then, non-perturbative interactions take over and convert the showers into outgoing hadrons, which may also decay. On top of this, the beam remnants have to be taken care of, and secondary interactions may give rise to an underlying event.

Since Monte Carlo generators for hadronic events are based on QCD, one would think that there are in principle only a few basic parameters to be set, as the quark masses for example. But due to the different necessary perturbative and non-perturbative approximations, there are actually many more. The perturbative expansion depends on the renormalisation and factorisation scales, the parton shower needs cut-off scales, not to talk of all the parameters that come with the effective hadronisation and underlying event models. Most of these input parameters are unphysical and are selected by either sticking to the default values, often *guestimates*, or, more realistically, by tuning the different programs to experimental data.

4.1.1 The parton shower

A parton shower Monte Carlo program is used to simulate QCD jets by performing parton branchings in terms of the Sudakov form factor. The cross section of a hard process σ_0, which produces partons of flavour i, can be linked to the cross section $d\sigma$, in which the hard process is accompanied by a parton j with momentum fraction z, by

$$d\sigma \approx \sigma_0 \sum_{\text{partons } j,k} \frac{\alpha_s}{2\pi} \frac{d\theta^2}{\theta^2} P_{i\to jk}(z) dz, \tag{4.1}$$

where P is a set of universal, flavour- and spin-dependent splitting functions. These are valid only in the collinear limit, i.e. for $\theta \to 0$, and they are independent of the exact definition of the z variable, as for example the energy fraction or the light-cone momentum fraction, of parton j with respect to parton i.

This factorisation allows a quite straightforward implementation in a Monte Carlo generator of the showering procedure by iteration: the hard process is used to generate one collinear splitting and then this new final state can be used as input again to do further splittings. This iterative process has to be stopped some time, which brings us to the question of what a final state parton actually is. Since a physical measurement is not able to distinguish between a pair of collinear partons and a single parton with the same total momentum, we have to introduce some resolution criterion and generate only the distributions of the resolvable partons. For example, one can say that two partons are resolvable if their relative transverse momentum is above some cut-off Q_0. So the soft and collinear divergencies are cut off and the total resolvable emission probability is finite.

In the leading-logarithmic picture, a parton shower can be seen as a sequence of $1 \to 2$ branchings, where the mother particle a produces two daughter particles b and c. Then, each daughter is free to branch in its turn, giving ultimately something like a tree-like structure. The kinematics of the branchings are given by two variables Q^2 and z, which often differ from one parton shower program to another. For example, in Pythia, the default algorithm is called *mass-ordered* because it uses the squared effective mass of the branching particle as scale $Q^2 = m_a^2$.[1] A second algorithm uses the transverse momentum as scale variable $Q^2 = p_T^2 = z(1-z)m^2$. The z variable is just the energy and momentum fraction taken by one of the daughters, so that the other one takes $1-z$. In Herwig, the scale association is done via $Q^2 = m^2/(2z(1-z))$.
In this formalism, the differential probability for parton a to undergo a branching is given by

$$d\mathcal{P}_a = \sum_{b,c} \frac{\alpha_s}{2\pi} P_{a\to bc}(z) dt dz, \tag{4.2}$$

where the variable $t = \ln \frac{Q^2}{\Lambda}$ is linked to the energy scale of the process and can be seen as an analogue of a time variable, with which the shower develops. Λ is the scale at which α_s is evaluated, and the splitting kernels for the different possibilities can be found in App. B. Since for final state showers, all virtualities involved are time-like, the maximum allowed virtuality starts at the hard scattering scale and evolves down to the cut-off scale Q_0. So the t parameter controls the development of the shower, and each branching is associated with a fixed value of t. For a given t, the integral of the

[1] The effective branching mass is linked to the cut-off scale Q_0 by $m_g = Q_0/2$ for gluons and $m_q = \sqrt{m_q^2 + Q_0^2/4}$ for quarks.

branching probability over all allowed z values $z \in \left[z_-(t), z_+(t)\right]$ is given by

$$I_{a\to bc}(t) = \int_{z_-(t)}^{z_+(t)} dz \frac{\alpha_s}{2\pi} P_{a\to bc}(z). \tag{4.3}$$

The probability that a branching occurs during a small interval δt is given by $\sum_{b,c} I_{a\to bc}\delta t$ and the probability of no branching is given by one minus this term. If t_0 is the starting value, the probability of no branching between t_0 and t can be derived by taking the limit $\delta t \to 0$

$$P_{\text{no br}}(t_0, t) = \exp\Big(-\int_{t_0}^{t} dt' \sum_{b,c} I_{a\to bc}(t')\Big) = S_a(t). \tag{4.4}$$

This is the Sudakov form factor.

The actual probability that a branching occurs at time t is then given by

$$\frac{dP_a}{dt} = -\frac{dP_{\text{no br}}(t_0, t)}{dt} = \Big(\sum_{b,c} I_{a\to bc}(t)\Big) \exp\Big(-\int_{t_0}^{t} dt' \sum_{b,c} I_{a\to bc}(t')\Big), \tag{4.5}$$

where the first term on the right hand side is the naive branching probability and the second term encodes the suppression due to the conservation of the total probability.

These are the evolution equations which govern the shower development. But there are several ambiguities in the algorithm construction. First, whatever variable we chose for Q^2 and z, it is correct in the collinear limit, but may have different extrapolations away from that limit. Then, as the hard scattering matrix element contains on-shell partons and the PS generates a virtuality for the partons, the energy-momenta have to be shuffled between partons in some way to be conserved, but the collinear approximation gives no specification as to how this has to be done. This means that all the different methods on the market have the same leading collinear logarithmic accuracy but differ in the sub-leading terms that they necessarily introduce. Also, the strong coupling in the shower $\alpha_s(\Lambda)$ is scale dependent. As the scale decreases, the coupling becomes larger and it becomes easier and easier to emit further gluons until at small enough scales the emission probability becomes of order one and phase space fills with soft gluons. This means that we have to impose some cut-off scale $Q_0 \gg \Lambda_{QCD}$ to avoid the large-coupling region. This is not a mere theoretical quantity but has physical relevance since it is affecting observables. The PS is thus not just a purely perturbative description but induces power corrections, usually of the order Q_0/Q, which contribute to the non-perturbative structure of the final state.

The evolution we have just described is a final state evolution. In principle, initial state evolution is very similar. In practice however, this proves to be extremely inefficient. The majority of partons have low energy and virtuality, and it would then be very rare to produce the right kinematics to give the hard process of interest. Therefore, it is more efficient to first select the hard process, and then dress it with additional radiation

using backwards evolution: the probability distribution for a parton of given momentum fraction and value of evolution scale to have come from one at higher momentum and lower scale is generated and this procedure is iterated until the evolution scale reaches the infrared cut-off. Then, the non-perturbative model of the remnant left behind takes over. It is important to note that the classification into initial and final state emission is arbitrary and only the sum of both is physically meaningful to reproduce the underlying quantum mechanical amplitude.

We have seen in the real matrix element calculation that two different configurations lead to divergencies: collinear and soft gluons. It turns out that soft gluon effects can be correctly taken into account by a collinear PS algorithm provided that the opening angle is used as evolution scale. For the mass-ordering algorithm, this is not the case and additional requirements on allowed emissions have to be set. This leads to angular-ordered or coherence-improved PS, like Herwig for example. The p_T-ordered shower however leads to the correct coherence effect without additional constraints. As a consequence of angular-ordering, the first emission is often not the hardest one and his can be troublesome for matching the PS to matrix elements.

A general comment about PS can be made for the very low x regime where logarithms of the momentum fraction at each splitting can be very large and a different resummation technique is needed, as BFKL [97] or CCFM [98] for example. Since it seems very likely that some processes at the LHC will have originated from momentum fractions below the 10^{-4} or event 10^{-5} range, they will thus significantly be affected by them, and alterations to the PSs will have to be made.

Additional aspects

Hadronisation models Since the earliest developments, the term hadronisation has been used with different meanings, always referring to what happens after the PS stage. Nowadays it refers to the model used in an event generator, which performs the transition from the showered coloured partonic final state to the complete colourless hadronic final state. Again, since this is an IR process, the coalescence of gluons and quarks into hadrons happens too late to have any effect on the hard interaction itself and the hadronisation process can be decoupled from the hard scattering. But since this lies in the non-perturbative regime of QCD, only effective models are available. The PS output is a set of coloured partons with low virtuality around the PS-cutoff scale Q_0. Ideally, Q_0 should just be a parameter, and the hadronisation model should also have a parameter Q_0, whose effect would cancel out the PS dependence when both codes are run one after the other. It turns out however that this is not possible since model deficiencies retain this dependence. Thus Q_0 is another parameter to be adjusted with data and whose variation has to be taken into account in systematic uncertainty studies.
A general concept for hadronisation is the local parton-hadron duality, where one supposes that the flow of momentum an quantum numbers at hadron level is dictated by

and follows the underlying parton level. This means that, for example, the flavour of a jet is that of a quark located near the jet axis, a fact which will become very important for physical analyses based on the identification of b jets. There are three main streams in fragmentation modelling: string models, independent fragmentation and cluster formation, although various hybrid implementations also exists.

The principle of string fragmentation is based on the Lund model, in which a quark q and antiquark $\bar{q}$ are connected via a colour string. Under the assumption of linear confinement, the potential energy of the colour field increases linearly as the two particles move away from each other. The potential energy stored in the colour flux tube being stretched increases until a new $q\bar{q}$ pair is generated via quantum tunnelling. This string break up process is iterised until only hadrons which are on their mass-shells remain. Different string breaks are supposed to be causally disconnected. Gluon complicate this picture a bit, they are modelled as kinks in the strings. The general string assignment is not unique but in the leading colour approximation, the leading contributions come from strings stretching between the closest partons having opposite charges. String fragmentation is the default hadronisation model used in Pythia, although other options are also available.

Cluster models start by decaying all gluons non-perturbatively into $q\bar{q}$ pairs [99], and then form an intermediate stage of colour-singlet cluster objects with a characteristic mass scale of a few GeV. The clusters are seen as superpositions of meson resonances which finally decay into hadrons. Herwig's hadronisation model is based on cluster fragmentation.

Underlying soft event In hadron-hadron collisions, typically only one parton from each hadron participates in the hard scattering, leaving behind the rest of the hadron, called beam remnant. The underlying event describes what happens with those beam remnants. Since this is manly low p_T scattering processes, perturbative calculation is not adequate. This is a domain which is still poorly understood, different effective models are available. In Herwig, for example, the remnants are modelled via beam clusters. The colour connection between the beam remnants and the partons which participate in the hard interaction is broken by a forced emission of a soft $q\bar{q}$ pair, and the underlying event is a soft collision between the two beam clusters. The implemented model is based on a modified version of the minimum bias pp-event generator used in the UA5 collaboration. In PYTHIA, different multiple parton interactions are modelled and there are attempts to keep the colour connection. The default version uses Poisson distribution over the threshold scale p_T^{min}, usually around 2 GeV, and switches to a simplified two string model under this threshold.

In the next section, we review the major MC based event generators which are currently used [100]. We divide them according to the structure of their final output, but

with the recent activity on all fronts, these boarders are not fixed, and some programs evolve into another category by adding features to their initial purpose code.

4.1.2 Multiple purpose generators

There are a set of codes, called multiple purpose event generators, which are able to perform one or more steps down to the generation of events. We will only review here three multiple-purpose event generators which automatically combine LO matrix element generation with parton shower dressing and hadronisation to produce complete hadronic final states.

- **PYTHIA** [101] [102] has been developed out of the Lund string model, and this provides the default hadronisation scheme. The code contains a wide range of hard subprocesses at LO and has relatively elaborate models for soft physics. The basic parton cascades use virtuality ordering with colour coherence imposed in the time-like cascades via a veto on opening angles. Many tunes to LEP and Tevatron data exist.

- **HERWIG** [103] places its emphasis on the perturbative description of an event. It uses sophisticated parton showers which build in colour coherence automatically via ordering of suitable evolution variables and includes angular corrections. Hadronisation is done using the cluster model.

- **Sherpa** [104] provides particle production at tree level in the SM and beyond. The complete set of Feynman rules for the MSSM have been implemented, including general mixing matrices for inter-generational squark and slepton mixing. Other available models are the ADD model of Large Extra Dimensions, anomalous gauge couplings, a model with an extended Higgs sector and a version of the 2HDM.

Due to their relatively evolved and much-tested parton shower and hadronisation models, they are often coupled to other Monte Carlo codes which provide the matrix element calculation.

4.1.3 Matrix element generators

Matrix Element (ME) generators provide events based on the computation of tree-level matrix elements with a fixed number of partons in the final state and they generally do not include any form of showering or hadronisation. The output final states thus consist of bare quarks and gluons, which have to be used as input in a dedicated parton shower code. This may however cause problems, because a kinematic configuration with n final state partons can be obtained in different ways, by starting from $n - m$ partons generated by the tree-level matrix element generator and completing them by m extra partons provided by the shower. Different strategies have been devised to deal with this over-counting problem. Usually, the ME generators feature a predefined list of partonic processes. If they provide multi-leg amplitudes, these codes additionally

include powerful phase-space sampling algorithms which have been optimised for the specific process, since they are strongly and irregularly peaked. We will focus on a small set of existing ME generators, most of which are intensively used by the ATLAS collaboration for signal and background process simulations.

- The **AcerMC** [105] event generator is dedicated to the generation of SM background processes in pp collisions at the LHC. The program provides a rather large library of matrix elements and phase space modules to be used for generation of a set of selected processes, as for example Z and W associated with heavy jets production with their decay. Also included are top and single top production, but only incorporating part of the NLO corrections. The matrix elements have been coded by the MadGraph/HELAS package.

- **AlpGEN** [106] is designed for the generation of SM processes in hadronic collisions, with emphasis on final states with large jet multiplicities. It is based on the exact leading order evaluation of partonic matrix elements, with the inclusion of b and t quark masses, as well as t quark and gauge boson decays with helicity correlations.

- The **JIMMY** generator is a library of routines which are meant to be linked with HERWIG. The original version of the JIMMY code [107] focusses on photoproduction.

- **VECBOS** is a LO MC program for inclusive production of a W-boson plus up to four jets or a Z-boson plus up to three jets in hadron collisions. The correlations of the vector boson decay fermions with the rest of the event are built in.

- The **MCFM** [108] program is designed to calculate cross-sections for various femtobarn-level processes at hadron-hadron colliders. For most processes, matrix elements are included at NLO and incorporate full spin correlations. Implemented processes [109] focus on W and Z production with additional jets, diboson production, as well as Higgs production in association with jets and processes concerning heavy quarks, c, b and t, such as single top for example.

There are also automated matrix element generators where the user only has to specify the initial and final state particles for the process he is interested in, and then the program enumerates the different Feynman diagrams which contribute to that process and writes the code to evaluate the matrix elements. These codes typically focus on SM particles and couplings, but some SM extensions are also implemented. Since many packages include phase space sampling routines, they are also able to generate partonic events. The limiting factor for these codes is the user's computing power.

- The **CompHEP** [110] code starts from the level of Feynman rules for a gauge model Lagrangian and calculates the matrix element for any SM or MSSM process defined by the user. It can then generate the Feynman diagrams and present them in a graphical form with a Latex output, or compute the squared Feynman

diagrams symbolically and then numerically calculate LO cross sections and distributions. After numerical computation, unweighted events can be generated along with their colour flow information. It allows for the computation of scattering processes with up to six particles and decay processes with up to seven particles in the final state.

- **MadGraph** [111] allows the generation of amplitudes and events for any process with up to nine external particles in many different models, such as the SM, Higgs effective couplings, MSSM and the general 2HDM. It provides a user-friendly interface for the implementation of model extensions. MadGraph is part of the MadEvent software, where events at the parton, hadron and detector level can be generated directly from a web interface. It has a standalone running mode for creating and testing matrix elements; generation of events corresponding to different processes, such as signal(s) and backgrounds, in the same run; two platforms for data analysis, where events are accessible at the parton, hadron and detector level; and the generation of inclusive multi-jet samples by combining parton-level events with parton showers.

Apart from MCFM, all the presented event generators are using LO matrix elements. The automatisation of NLO processes is under way, there are packages capable of generating virtual contributions, real contributions and dipoles, but the matching is still not at automated level.

4.1.4 Charged Higgs specific programs

The following section briefly summarises tools available concerning charged Higgs bosons [112], which are not primarily focused on event generation.

- **FeynHiggs** [113] concentrates on the MSSM Higgs section and can be used for the calculation of mass spectra, mixings and a lot of other features.

- The **2HDM Calculator** [114] is a relatively new general-purpose calculator for the 2HDM, which allows different parametrisations of the Higgs potential. It features a convenient specification of generic Yukawa sectors, includes the evaluation of decay widths and is able to give theoretical constraints.

- **SuperIso** [115] is a program for general calculations of flavour physics observables. This can be done either in the Standard Model (SM), in the general 2HDM, in the MSSM and next to minimal supersymmetric Standard Model (NMSSM).

- **HiggsBounds** [116] is a computer code which can be used to test theoretical predictions of models with arbitrary Higgs sectors against the exclusion bounds obtained from the Higgs searches at LEP, the Tevatron and the LHC. It needs a selection of Higgs sector predictions as input and then uses the experimental topological cross section limits from the various Higgs searches to determine if this parameter point has been excluded at 95% C.L.

- The **Matchig** [117] package has been available for some years, as a first step of improvement of the LO calculation towards NLO. The strategy is the following: both processes $gb \to tH^-$ and $gg \to tH^-\bar{b}$ are produced with PYTHIA at LO. The user can add them together and use MATCHIG to compute and subtract the double counting term from b-parton densities which have originated from the gluon splitting into $b\bar{b}$-pairs. Although this is already an improvement over taking into account only the LO gb contribution to charged Higgs production, it is not a complete NLO code.

4.1.5 Coupling a NLO event generator to a parton shower

The main difficulty of coupling a NLO calculation with a PS is that of avoiding over-counting, since the PS already incorporates approximate NLO corrections. The general ingredients are

- the Born cross section B,
- the exact virtual and real cross sections V and R,
- the radiation cross section of the PS R^S, which is generally related to the Altarelli-Parisi splitting kernels $P(z)$ via

$$R^S = B\frac{1}{t}\frac{\alpha_s}{2\pi}P(z). \tag{4.6}$$

- and the full phase space Φ, which can be factorised into the Born phase space Φ_B times the phase space relative to the radiation variables of the PS Φ_r^S, according to the reshuffling procedure of the MC which yields Φ from Φ_B and Φ_r^S.

The cross section of the hardest event is calculated according to

$$d\sigma = \underbrace{\bar{B}^S(\Phi_B)d\Phi_B}_{\text{S event}}\underbrace{\left[\Delta_{t_0}^S + \Delta_t^S\frac{R^S(\Phi)}{B(\Phi_B)}d\Phi_r^S\right]}_{\text{MC shower}} + \left[\underbrace{R(\Phi) - R^S(\Phi)}_{\text{H event}}\right]d\Phi, \tag{4.7}$$

where the S- and H-event stands for the soft, resp. hard, event, and MC shower refers to the shower-dependent term. Δ_t^S is the Sudakov form factor and $\bar{B}^S$ stands for

$$\bar{B}^S(\Phi_B) = B(\Phi_B) + \left[V(\Phi_B) + \int R^S(\Phi)d\Phi_r^S\right], \tag{4.8}$$

where the virtual and the real part are infinite, but their sum is finite.

At this point, we can verify that the expansion of $d\sigma$ matches the exact NLO expression from analytic calculations. For this, we develop the Sudakov form factor and also replace Eq.(4.8) in the master expression, Eq.(4.7), and obtain

$$d\sigma = \left[B + V + \int R^S d\Phi_r^S\right]d\Phi_B\left[1 - \int \frac{R^S}{B}d\Phi_r^S + \frac{R^S}{B}d\Phi_r^S\right] + \left[R - R^S\right]d\Phi. \tag{4.9}$$

Now, keeping only terms up to NLO, we are left with

$$\begin{aligned} d\sigma &= \Big[B+V\Big]d\Phi_B + \int R^S d\Phi_B d\Phi_r^S + B d\Phi_B \Big[\frac{R^S}{B} d\Phi_R^S - \int \frac{R^S}{B} d\Phi_r^S\Big] + \Big[R - R^S\Big] d\Phi \\ &= \Big[B+V\Big]d\Phi_B + B d\Phi_B \Big[\frac{R^S}{B} d\Phi_R^S + \int \frac{R^S}{B} d\Phi_r^S - \int \frac{R^S}{B} d\Phi_r^S\Big] + \Big[R - R^S\Big] d\Phi \\ &= \Big[B+V\Big]d\Phi_B + \Big[R - R^S\Big] d\Phi + R^S d\Phi \end{aligned} \tag{4.10}$$

which can finally further be simplified to

$$d\sigma = \Big[B+V\Big]d\Phi_B + R d\Phi \tag{4.11}$$

which is the exact NLO expression. All shower-dependent terms have been cancelled and are no longer present.

There exist several merging approaches. We shall investigate two, MC@NLO and POWHEG, stressing the differences and major advantages of each method.

4.2 MC@NLO

The MC@NLO approach [1] has been the first one to give an acceptable solution to the over-counting issue, by subtracting from the exact NLO cross section the approximation implemented in the PS to which the NLO calculation is matched. Thus this method is dependent on which PS is used. The PS currently coupled to MC@NLO is Herwig, although attempts are ongoing for processes to be matched with Pythia. A side-effect of this method is that generally, the cross section minus the subtraction term need not be positive, and the output event might be affected with a negative weight. This is not a problem for general physics analysis which use distributions of variables, but might become a problem when one uses multivariate methods which are fed one event at a time and often do not accept negatively weighted events.

4.2.1 MC@NLO coupled to Herwig

The MC@NLO output events are infra-red safe observables which have NLO accuracy, collinear emissions are resummed at the leading-logarithmic (LL) level and the double logarithmic region (for soft and collinear gluon emission) is treated correctly by Herwig, since it is based upon an angular-ordered branching.

In MC@NLO, the phase space parametrisation has to be the one of the PS. S- and H-events are computed by MC@NLO, the MC shower event is computed by the PS (usually Herwig) and the differential cross section is given by Eq. (4.7). In particular for MC@NLO, the H-event is computed using the PS approximation in the collinear and soft regions $R^S d\Phi_r = R^{MC} d\Phi_r^{MC}$. So the event generation algorithm goes through the following steps:

- First, it computes the cross sections for $S-$ and $H-$events according to

$$\sigma_S = \int |\bar{B}^S(\Phi_B)| d\Phi_B \text{ and } \sigma_H = \int |R - R^{MC}| d\Phi. \tag{4.12}$$

- Then, it chooses an S- or H-event with a probability proportional to the cross sections σ_S and σ_H.

- If an S-event has been chosen, Born kinematics are generated with probability $|\bar{B}^S(\Phi_B)|$ and they are fed to the PS for subsequent showering, with associated weight ± 1, according to the sign of $\bar{B}^S(\Phi_B)$ which is mostly 1, except for a very narrow region where the virtual contributions are strongest. This is "normal" and has nothing to do with the negative weights problem of MC@NLO.

- If however an H-event has been produced, radiation kinematics are generated with probability $R - R^S$ and they are given over to the PS for further showering, with associated event ± 1, following the sign of $R - R^S$, where it can happen that this term is negative. This is where the negative weights in MC@NLO come from. Another issue connected to this part is that the term $R - R^S$ must be non-singular, i.e. the PS must reproduce exactly the soft and collinear singularities of the real matrix elements, This is in fact not always the case, as some PS are not accurate in the soft limit.

In the following, we will briefly review different aspects of charged Higgs production that have been studied using the MC@NLO implementation.

4.2.2 Comparison of tH^- NLO versus NLO+PS production

The implementation of tH^- in MC@NLO [118] has been largely based on the previously available Wt production [96]. We will discuss here some key variable distributions for LHC collisions at 14 TeV. Input masses are $m_t = 172$ GeV for the top quark and $m_{H^-} = 300$ GeV for the charged Higgs boson. The factorisation and renormalisation scales have been put to $\mu_F = \mu_R = (m_t + m_{H^-})/2$, and the PDFs are the CTEQ5M1. Fig. 4.1 compares the predictions before showering, (pure NLO, in plain), to those after showering with Herwig (NLO+PS, in dashed). The p_T distribution of the pair formed by the charged Higgs boson and the top quark shows the desired evolution: at values of p_T it is tending to zero, the pure NLO result becomes negative due to the virtual contributions. This behaviour is regularised by the PS for which the small value of the Sudakov form factor, i.e. the probability for no additional gluon emission, dampens the distribution at zero. Thus the (NLO+PS) curve starts at zero and then evolves up to the maximum value, before plunging down again at high p_T values.

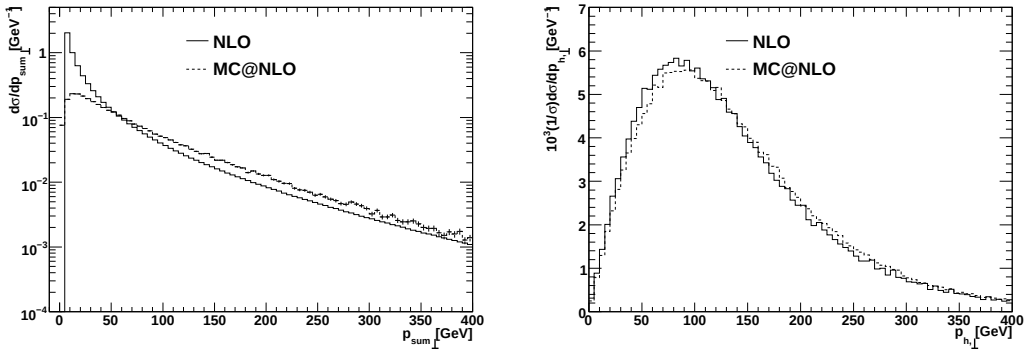

Figure 4.1: Comparison between pure NLO against NLO coupled to the PS Herwig. The left plot shows the p_T distribution of the charged Higgs boson plus top quark, whereas the right plot displays the p_T of only the charged Higgs boson. Parameters are set according to the values quoted in the text.

4.2.3 Systematic uncertainty studies

In this part, we will assess the impact different parameters can have on the tH^- NLO cross section predictions. Their variation can be used to infer systematic uncertainty on the theoretical cross section prediction, which is a vital input for any physics analysis.

4.2.3.1 Dependence on the PDF fit input bottom mass

In this section, we present a study [119] of the dependence of the tH^- production cross section on the bottom mass used in the MSTW2008 PDF fit. Bottom parton densities are based on the splitting of an off-shell gluon into a pair of massive bottoms. While for light-flavour quarks the splitting threshold is of the order of Λ_{QCD} and hence not numerically relevant, for bottoms it is in the range of perturbative QCD. This makes it a relevant input parameter in the computation of bottom parton densities and whose variation has to be accounted for in a systematic uncertainty evaluation. To first approximation, a shift in the bottom mass changes the logarithmic parton densities by

$$\log \frac{M}{m_b} \to \log \frac{M}{m_b + \delta m_b} = \log \frac{M}{m_b} - \log \left(1 + \frac{\delta m_b}{m_b}\right) \simeq \log \frac{M}{m_b} - \frac{\delta m_b}{m_b} \,. \tag{4.13}$$

For well motivated applications of the bottom parton densities in which the kinematic scale is much higher than the bottom mass ($M \gg m_b$), the uncertainty due to the bottom mass becomes increasingly irrelevant. Relative and absolute cross section values for varying input bottom mass PDF sets have been computed and are given in Tab. 4.1.

Table 4.1: Absolute and relative production rates for tH^- production at NLO, varying the input bottom mass in the on-shell scheme. The coupling is fixed by $\tan\beta = 30$, and the renormalisation scale is $\mu = (m_t + m_H)/2$.

	$m_H = 200$ GeV				$m_H = 500$ GeV		$m_H = 800$ GeV	
	7 TeV		14 TeV		14 TeV		14 TeV	
m_b	σ[pb]	$\sigma/\sigma_{4.75}$	σ[pb]	$\sigma/\sigma_{4.75}$	σ[pb]	$\sigma/\sigma_{4.75}$	σ[pb]	$\sigma/\sigma_{4.75}$
4.25	0.1845	1.055	1.279	1.049	0.1168	1.045	0.01989	1.044
4.50	0.1796	1.026	1.248	1.025	0.1142	1.021	0.01945	1.021
4.75	0.1750	1.0	1.219	1.0	0.1118	1.0	0.01905	1.0
5.00	0.1708	0.976	1.192	0.978	0.1096	0.980	0.01868	0.981
5.25	0.1668	0.953	1.166	0.957	0.1074	0.961	0.01832	0.977

4.2.3.2 Diagram removal versus diagram subtraction

As was already seen in Chapter 3, interference between H^-t and $t\bar{t}$ production occurs when $m_{H^-} < m_t$. In this case, diagrams where the H^-t production occurs via $t\bar{t}$ give a larger and larger contribution due to the intermediate top quark propagator going on-shell. This is not permitted by the kinematics of the final state if $m_{H^-} > m_t$. Although this is what happens at quantum level, both processes do interfere, and one needs an artificial separation procedure. This will be an approximation forced by practical purposes only, and it has to be checked whether the separation remains meaningful,i.e. that the interference term remains small, depending on the final state cuts applied to the analysis. Since this problem already arose for Wt production at NLO, two different schemes were proposed: the diagram removal (DR) and diagram subtraction (DS). They were designed in such a way that the difference between them measures the degree of interference between H^-t and $t\bar{t}$ production. This difference may then be used to give an estimate of the systematic uncertainty due to interference effects.
We have seen that DR removes the problematic diagrams at amplitude level, leading to a gauge-dependent calculation. In DS, the NLO H^-t production cross section is modified by a local subtraction term, which removes the contributions of the resonant diagrams in a point-by-point fashion in phase space

$$d\sigma^{DS}_{H^-t} = d\sigma_{H^-t} - d\sigma^{sub}_{H^-t}. \tag{4.14}$$

There are two requirements on the exact form of the subtraction term:

1. If the invariant mass of the $H-b$ subsystem is equal to the top mass, the subtraction term should give exactly the fully exclusive $t\bar{t}$ cross section, with $t \to Hb$, so a to cut-out the resonant region.

2. Away from the resonant region, the subtraction term should fall off rapidly, so as not to alter the H^-t NLO cross section.

This procedure has the advantage of being gauge invariant.
The H^-t production cross section in both the DR and DS scheme as a function of the charged Higgs boson mass can be seen in Fig. 4.2.

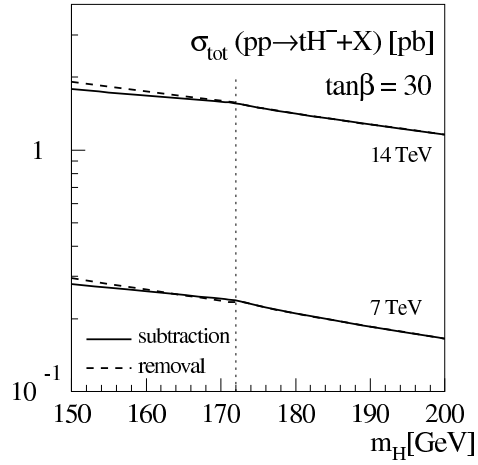

Figure 4.2: Comparison between the DR and DS schemes. [119]

A change in the slope can be observed for the low mass region with respect to the high mass region, both at 7 and 14 TeV. Due to the design of both methods, DS acting on cross section level and DR on amplitude level, the interference term is still present in the DS case but not for DR. Thus the difference between both measures the interference. Since there is not much difference between the DR and DS cross section values, the interference term is small. This might however not be the case in a physical analysis, where cuts on selected event topologies are used. Of course, users have to keep in mind that both evaluation methods present flaws. In particular, the DS result depends on the exact form of the subtraction term, and the DR result is gauge-dependent. The influence of the gauge-dependence from the gluon propagator and of the form of the subtraction term have been investigated and found to be small [96].

4.2.3.3 Four- versus five-flavour-scheme

The NLO calculation of charged Higgs production, which was presented in Chapter 3, was performed using an incoming b quark mass equal to zero. This defines the five-flavour scheme (5FS). Potentially large logarithms $\ln(\mu_{\mathrm{F}}/m_b)$, which arise from the splitting of incoming gluons into nearly collinear $\bar{b}b$ pairs can be summed to all orders in perturbation theory by introducing bottom parton densities. The use of bottom distribution functions is based on the approximation that the outgoing b quark is at small transverse momentum and massless, and the virtual b quark is almost on-shell.
This is however not the only way the calculation can be done. Several PDF collaborations have published sets without b PDFs, to be used for processes with a massive initial state b quark. In the four-flavour scheme (4FS), the b is thus not considered massless anymore. The lowest-order QCD production processes are now gluon–gluon fusion and quark–antiquark annihilation, $gg \to \mathrm{t}b\mathrm{H}^{\pm}$ and $\bar{q}q \to \mathrm{t}b\mathrm{H}^{\pm}$, respectively [120].
To all orders in perturbation theory the four-and five-flavour schemes are identical, but the way of ordering the perturbative expansion is different, and since the series is truncated at NLO, the results do not match exactly at finite order. It is therefore important to compare the numerical results of both schemes. Fig. 4.3 shows that while the 5FS

prediction (in red) has a central value above the 4FS cross section, but both calculations agree within the theoretical error bands. Additionally, one can see that the error bands are larger for the 4FS calculation than for the 5FS. As discussed before, this is due to the explicit presence of the b mass logarithms and was to be expected.

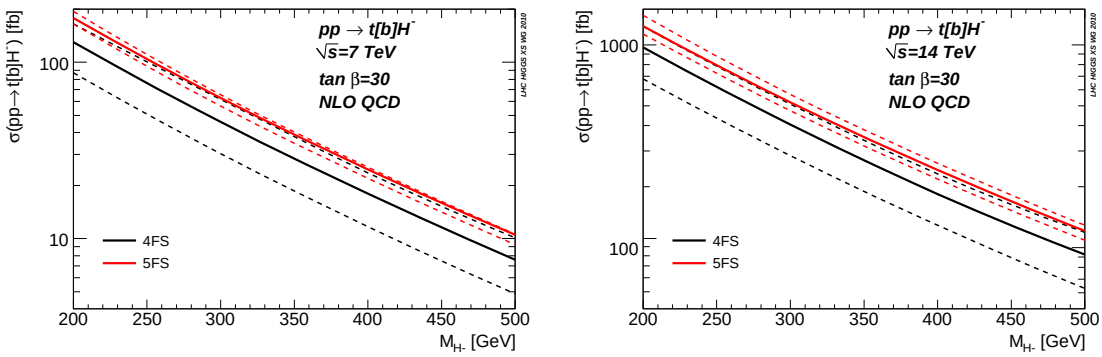

Figure 4.3: Comparison between the 4- and 5-FS cross section predictions at the LHC for 7 and 14 TeV. [121] Error bands are obtained by varying the factorisation and renormalisation scales between $\mu/3 < \mu_0 < 3\mu$, with $\mu_0 = (m_t + m_b + m_H^-)/3$ for the 4FS and $\mu_0 = (m_t + m_H^-)/4$ for the 5FS.

4.3 POWHEG

An alternative to MC@NLO is POWHEG [2], which stands for Positive Weight Hardest Emission Generator. The major improvements over MC@NLO are that this program

- yields only positive-weighted events
- and is PS independent.

Also, the POWHEG-BOX [122, 123] provides a user-friendly structure to add NLO calculations for new processes.

4.3.1 POWHEG coupled to an arbitrary parton shower

The master equation for event generation of the hardest configuration in POWHEG is still Eq. (4.7), but this time the H-event uses not the real emission of the PS but rather

$$R^S d\Phi_r = RF(\Phi), \tag{4.15}$$

where F is a function of the total phase space Φ, respecting

$$0 \leq F(\Phi) \leq 1, \tag{4.16}$$

and where $F(\Phi) \to 1$ in the soft and collinear limit. This means that S-events, H-events and also the MC-shower part are generated by POWHEG. Only then are they passed

to the PS for subsequent showering by imposing no radiation for $t > t_{\text{POWHEG}}$. In this way, the event generation is PS independent, since the hardest emission is always done within POWHEG. Furthermore, since now the quantity

$$R - R^S = R(1 - F(\Phi)) > 0 \tag{4.17}$$

cannot be negative anymore, events generated with POWHEG have positive weights.

4.3.2 Code structure

We will now explain in detail the different parts of the POWHEG tH^- implementation [124]. The recently developed environment of the POWHEG-BOX allows an almost straightforward implementation for NLO calculations, if the following elements are provided:

1. the list of all flavour structures of the Born and the real processes,
2. the Born phase space,
3. the Born squared amplitudes $\mathcal{B}$, the colour correlated ones $\mathcal{B}_{ij}$, spin correlated ones $\mathcal{B}_{\mu\nu}$ and the Born colour structures in the limit of a large number of colours,
4. the real matrix elements squared for all relevant partonic processes, and
5. the finite part $\mathcal{V}_{fin}$ of the virtual corrections

$$\mathcal{V} = \frac{(4\pi)^\epsilon}{\Gamma(1-\epsilon)}\Big(\frac{\mu_R^2}{Q^2}\Big)^\epsilon \frac{\alpha_s}{2\pi}\Big[\Big(\frac{C_2}{\epsilon^2} + \frac{C_1}{\epsilon}\Big)\mathcal{B} + \mathcal{V}_{fin}\Big], \tag{4.18}$$

   where $\mathcal{B}$ is the Born process computed in $D = 4 - 2\epsilon$ dimensions.

For charged Higgs production, all these elements have been presented in Chapter 3, and they have been implemented. In the POWHEG formalism, a process is defined by its particle content and each particle is encoded via the PDG numbering scheme, except for gluons which are assigned the value 0. The order of the final state particles has to be respected: first are listed colourless, then heavy coloured and then massless coloured particles. Thus the Born process becomes

$$(bg \to H^- t) \to [5, 0, -37, 6]\,. \tag{4.19}$$

The POWHEG code structure relevant for tH^- production contains the following Fortran files:

1. **init_couplings.f**
   The init_processes subroutine has to start by defining the index of the first coloured light parton in the final state. In our case, this is the additional jet from the real emission, particle number 5 according to the classification code

$$\text{flst_lightpart} = 5.$$

Then, the possible Born subprocesses are to be referenced. There are two for tH^- production

$$\text{flst_nborn} = 2,$$

with a gluon coming from one hadron and b quark coming from the other one, or vice versa:

$$[5, 0, -37, 6] \text{ and } [0, 5, -37, 6]\,. \tag{4.20}$$

Then, all real emission processes are assigned a number in the list. We have

$$\text{flst_nreal} = 30$$

processes in total. Our list is given in Tab. 4.2 according to the different initial states.

Table 4.2: Process numbers of the different real emissions. Here $q = d, u, s, c$.

Process number	Initial state	Process number	Initial state
1	bg	16-19	$\bar{q}b$
2	gb	20-23	$q\bar{q}$
3	gg	24-27	$\bar{q}q$
4-7	bq	28	$b\bar{b}$
8-11	qb	29	$\bar{b}b$
12-15	$b\bar{q}$	30	bb

2. **Born_phsp.f**
   In the *born_phsp* subroutine, integration variables, named *xborn(i)*, for the Born phase space are generated between zero and one. The hadronic cross section can be linked to the differential partonic cross section $d\hat{\sigma}$ via the integration

$$\sigma = \int_0^1 f_{a/A}\, dx_a \int_0^1 f_{b/B}\, dx_b \int_{t_{min}}^{t_{max}} \frac{d\hat{\sigma}}{dt} dt \tag{4.21}$$

$$= \int_{\tau_{min}}^{\tau_{max}} d\tau \int_{y_{min}}^{y_{max}} dy\; f_{a/A}\; f_{b/B} \int_{t_{min}}^{t_{max}} \frac{d\hat{\sigma}}{dt} dt, \tag{4.22}$$

where $f_{i/I}$ is the PDF of parton i inside hadron I with momentum fraction x_i, and we have performed the change of variables

$$y = ln \frac{x_a}{\sqrt{x_a x_b}} \text{ and } \tau = x_a x_b. \tag{4.23}$$

The integration limits are given in Tab. 4.3.

The Jacobian contribution due to the change of integration variables $xborn(i) \rightarrow (\tau, y, t)$ is

$$\Delta_{jac} = (\tau_{max} - \tau_{min}) \times (y_{max} - y_{min}) \times (t_{max} - t_{min}), \tag{4.24}$$

Table 4.3: Integration limits for the hadronic cross section.

Variable V	V_{min}	V_{max}
τ	$\frac{(m_{H^-}+m_t)^2}{s_H}$	1
y	$\frac{1}{2}\ln\tau$	$-\frac{1}{2}\ln\tau$
t	$\frac{1}{2}(t_1-t_2)$	$\frac{1}{2}(t_1+t_2)$
$t_1 = m_t^2 + m_{H^-}^2 - s,\ t_2 = \sqrt{(s-m_t^2-m_{H^-}^2)^2 - 4m_t^2 m_{H^-}^2}$		

which has to be multiplied with 2π for the integration over the azimuthal angle ϕ, that will be randomly generated by POWHEG. Then the different kinematical variables are built in the centre of mass reference frame and in the lab frame via boosts.

This Fortran file also contains the subroutine *set_fac_ ren_ scales*, where the renormalisation and factorisation scales are to be set. The usual convention is to use

$$\mu_R = \mu_F = \frac{m_t + m_{H^-}}{k}, \tag{4.25}$$

where k is to be varied for uncertainty studies.

3. **Born.f**
   The subroutine *setborn* contains the factors for the colour-correlated Born amplitude. They are given in Section 3.4. In *compborn* the Born matrix element squared is given as well as the spin correlated Born matrix element

$$\mathcal{B}_{\mu\nu} = -\Big(\mathcal{S}_\mu\mathcal{S}_\nu + \mathcal{S}_\mu\mathcal{T}_\nu + \mathcal{T}_\mu\mathcal{S}_\nu + \mathcal{T}_\mu\mathcal{T}_\nu\Big). \tag{4.26}$$

   It is the Born term before summing over the initial gluon polarisations, with normalisation according to

$$\mathcal{B} = -g^{\mu\nu}\mathcal{B}_{\mu\nu}, \tag{4.27}$$

   where $g^{\mu\nu}$ is the metric tensor.

   The running Yukawa couplings are computed according to the discussion in Section 3.2.5. The subroutine *borncolour_ lh* contains the colour flow of the Born term in the large N_C limit, shown in Fig. 4.4.

4. **real_ampsq.f**
   In this subroutine, the real emission matrix element squared results are assigned

Figure 4.4: Colour flow in the Born contribution $[5, 0, -37, 6]$ and for switched incoming partons $[0, 5, -37, 6]$.

to the processes with the process number defined in the *ini_processes* subroutine. They are given by their straightforward calculation with all 5 momenta used. While the different combinations are not independent and a subset of them have to be used for comparison purposes to existing calculations, this is not a problem here.

5. **virtual.f**
   This file contains the finite term of the virtual contributions, as defined in Eq. 4.18. The term is split according to the finite terms stemming from D,C,B functions and leftover parts. General, non-divergent C-functions and Euler dilogarithms are computed using functions contained in the *loopfun.f* file [125].

The POWHEG-Box does not need dipole calculations as input, since they are computed automatically by the code in the FKS formalism. While running, the code produces a *pwhg_checklimits* file in which the ratio of the from the Born information generated dipoles and the real emission processes are given in the soft and collinear limit. This provides a first and useful check of the consistency of the implementation.

4.3.3 Comparison of tH^- NLO versus NLO+PS production

As a consistency check, we show various normalised distributions, which compare the pure NLO calculation (blue line), the POWHEG + Herwig result (red line) and the MC@NLO + Herwig output (black line) for a charged Higgs boson mass of $m_{H^-} = 300$ GeV and $\tan\beta = 30$, and a centre-of-mass energy of the LHC of $\sqrt{S} = 14$ TeV. The left plots of Fig. 4.5 display the transverse momentum distribution of the charged Higgs boson and the top quark. All distributions can be seen to agree within the statistical precision. The same comment applies to the rapidity distributions of the charged Higgs boson and the top quark, shown on the plots on the right in Fig. 4.5.

The normalised distribution of the transverse momentum of the system formed by the top and charged Higgs boson is displayed on the left of Fig. 4.6. The pure NLO curve is negative for the first bin and then reaches very high values. This typical behaviour is seen to be smoothened by the PS for both the POWHEG and the MC@NLO result, which are again in agreement with each other. A resummed calculation would also be similar to the PS behaviour. The plot on the right shows the azimuthal angle between

the top quark and the charged Higgs boson. Again, the PS regularises the behaviour of the NLO calculation at $\phi = \pi$, and the MC@NLO and POWHEG output are consistent with each other.

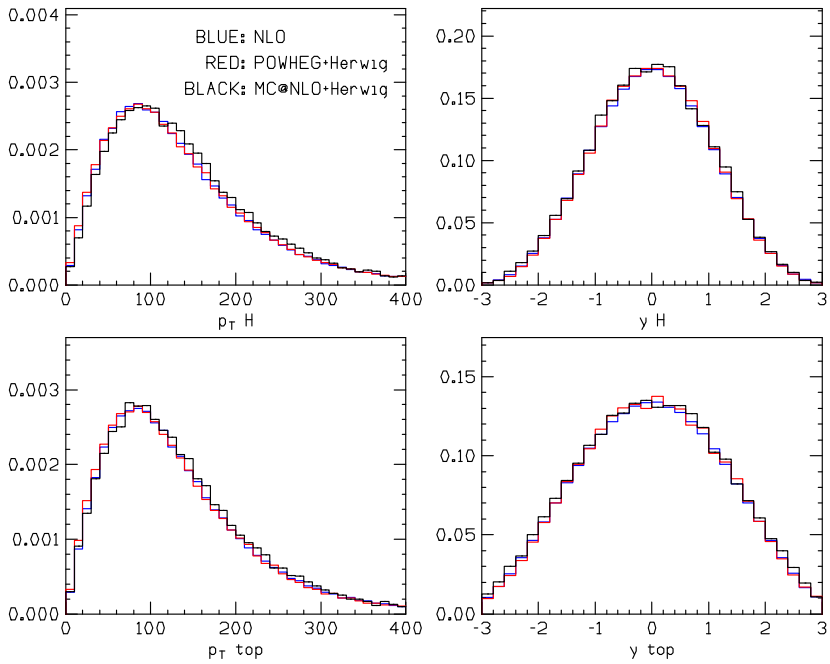

Figure 4.5: Normalised distributions comparing the pure NLO calculation (blue line), the POWHEG + Herwig result (red line) and the MC@NLO + Herwig output (black line) for the charged Higgs and the top quark transverse momentum p_T and rapidity y.

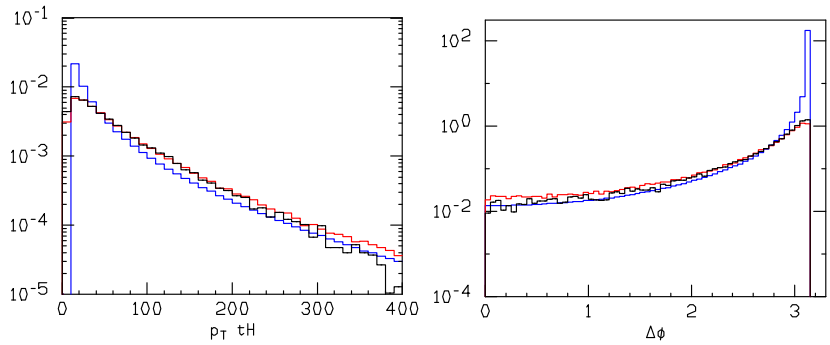

Figure 4.6: Normalised distributions comparing the pure NLO calculation (blue line), the POWHEG + Herwig result (red line) and the MC@NLO + Herwig output (black line) for the pair transverse momentum $p_{T,top+H}$ and the azimuthal angle ϕ between the top quark and the charged Higgs boson.

4.4 Conclusion

These four chapters have lead a long way up to a complete MC implementation of NLO charged Higgs boson production. We have seen that diverse MC codes are based on different assumptions and include unphysical parameters which have to be optimised on data. We have listed a small set of studies, focusing on their effect for systematic uncertainties. Such theoretical error bands are of paramount importance in a comparison to real data. An additional factor, which should not be neglected, is that the complexity of those MC codes implies that they almost inevitably contain bugs. All these reasons imply the necessity to use different MC simulations whenever possible to generate the processes one is interested in. The implementation in MC@NLO along with its counterpart in POWHEG accomplish exactly that goal and both have to be used to evaluate this systematic uncertainty. Although the MC generation can already be used for different phenomenological studies, it is not yet suited for a physical analysis. We still need data to compare our predictions with, and a code which enables us to run the generated events through the detector simulation to be able to compare both on an equal footage.

Comme il est profond, ce mystère de l'Invisible. Nous ne pouvons le sonder avec nos sens misérables, avec nos yeux qui ne savent apercevoir ni le trop petit, ni le trop grand, ni le trop près, ni le trop loin, ni les habitants d'une étoile, ni les habitants d'une goutte d'eau... avec nos oreilles qui nous trompent, car elles nous transmettent les vibrations de l'air en notes sonores. Elles sont des fées qui font ce miracle de changer en bruit ce mouvement et par cette métamorphose donnent naissance à la musique, qui rend chantante l'agitation muette de la nature... avec notre odorat, plus faible que celui du chien... avec notre goût, qui peut à peine discerner l'âge d'un vin! Ah, si nous avions d'autres organes qui accompliraient en notre faveur d'autres miracles, que de choses nous pourrions découvrir encore autour de nous!

Guy de Maupassant, *"Le horla"*

5 Startup of the Large Hadron Collider

In this Chapter we will review the start of operation of the new proton-proton collider installed in the LEP tunnel at the CERN research facility near Geneva. We will also describe the ATLAS detector and see how the event information from *pp* collisions is assembled. In the last section, we detail the software framework of ATLAS and look at event generation in this context. It is the duty of every ATLAS member to perform a certain amount of work useful to the whole collaboration, called service task. We will have a brief glance at the service task performed during this thesis, a work which involved comparing the complete simulation of events in ATLAS to a CPU-optimised version.

5.1 The LHC

The Large Hadron collider (LHC), a 27 km long proton-proton collider, is the last step in the accelerator chain [126] represented in Fig. 5.1. It starts with a duoplasmatron ion source, where electrons form a cathode filament hit gaseous hydrogen atoms, liberating the protons that will eventually end up in the high energy collisions. They are accelerated to 750 keV with a radiofrequence quadrupole. A second acceleration is given by the LINAC where the protons reach 50 MeV and are given over to the booster, pushing them up to 1.4 GeV. Next, several bunch trains are formed in the Proton Synchrotron (PS), i.e. the protons circulate now in groups of 10^{11}, called bunches, with a nominal spacing in between the groups of 25 ns. After reaching 26 GeV in the PS, they are shoot towards the Super Proton Synchrotron (SPS). Warmed up to 450 GeV in the SPS, they are now knocking on the door of the LHC. Proton bunches are then injected stepwise

into the LHC, up to a total of 2808 at nominal luminosity. The 40 MHz design collision rate could theoretically allow up to 3564 bunches, but some holes are to be left in the orbit for the kicker injection magnets.

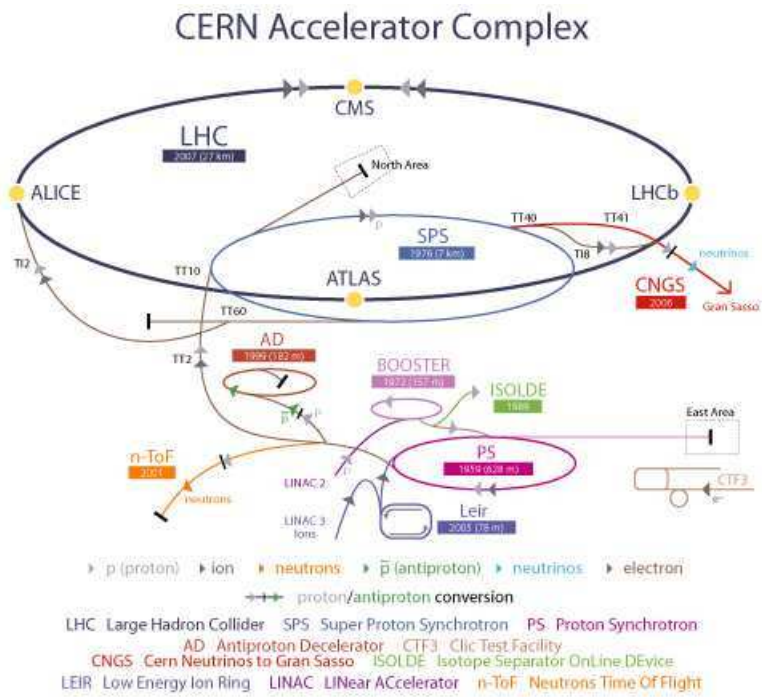

Figure 5.1: The accelerator complex at CERN.

The first successful operation of the LHC was achieved on the 10th of September 2008, where proton beams were circulating in the whole circumference of the accelerator for the first time. No proton-proton collisions were initiated, but experiments could record collision events between beam protons and the low density gas present in the beam vacuum and between protons and beam stop elements. Nine days later, on the 19th of September 2008, about 100 magnets were quenched [127]. The source of the quench was a faulty electrical connection between two dipoles during a ramping test. A resistive zone developed and triggered the quench protection system. In addition to this, an electrical arc punctured the helium enclosure and a large amount of helium escaped into the vacuum system. The valves could not handle the enormous pressure of more than 0.15 MPa and the helium was released into the beam pipes, the neighbouring sectors and finally the tunnel itself. During this sudden pressure release many magnets became misaligned, some were even misplaced by several tens of cm. All operations had to be stopped to allow repairs, the magnetic system had to be warmed up, 14 broken quadrupoles and 39 dipoles had to be brought to the surface for repairs and the beam pipe had to be cleaned on a length of 4 km. New safety systems were installed, above all a new quench protection system with special detectors, better valves and stronger magnet anchoring. During this time, the experiments went trough a long commissioning period with cosmic rays. The LHC finally came back to life the 20th of November

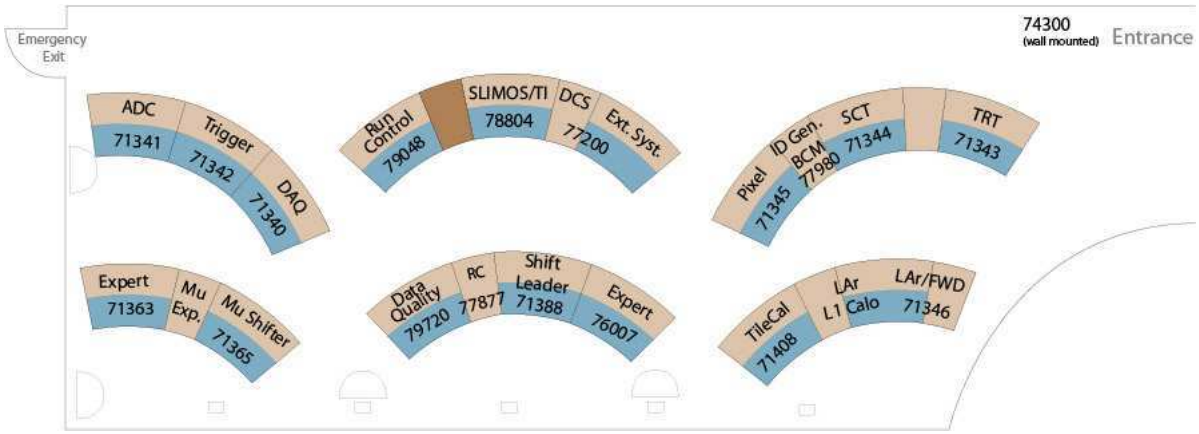

Figure 5.2: The ATLAS control room.

2009 and reported the first collisions three days later at an injection energy of 900 GeV. After a brief shutdown during the winter of 2009, the machine has been running with a reduced centre of mass energy of 3.5 TeV, and finally powered up to 7 TeV in March 2010. It has been working extremely well ever since, progressively rediscovering the SM while grading up in luminosity. The LHC will however still need a relatively long shutdown, evaluated to last approximately one and a half year, to upgrade its magnets with the safety requirements mandatory for 14 TeV collisions at nominal luminosity. This is scheduled to happen in 2012 and 2013.

Among the different experiments located at the LHC, we will zoom in on one of the two multipurpose detectors, the ATLAS (A Toroidal LHC ApparatuS) detector, situated on the accelerator opposite of the CMS (Compact Muon Solenoid) detector.

5.2 Taking Control of ATLAS

The general idea of the ATLAS detector dates back to the year 1992, when the letter of intent was published and proposed *a general purpose pp experiment* [128]. It took on more shape two years later with the Technical Design Proposal [129] and assemblage was accomplished in the beginning of 2008. Now that proton beams are circulating and colliding in the LHC, taking data with the detector requires about twenty people at all time in the Control Room. In this section we will take a walk through the ATLAS Control Room, shown on Fig. 5.2, where the ATLAS sub-detectors are grouped in desks according to their purpose. This is intended to give only a brief overview, since a thorough description can be found in [130] (from 1999) and more recent information (from 2008) is given in [131]. By walking into the ATLAS control room from the entrance on the left, the first desk we encounter on our tour is responsible for the inner detector.

5.2.1 The Inner Detector

When particles are produced in hadronic collisions, the first sub-detector they cross is the Inner Detector (ID). Its purpose is to reconstruct tracks from charged particles and measure interaction vertices. A precise track reconstruction, especially near the interaction point, is mandatory to distinguish particles coming from the primary vertex where the initial pp interaction happened, from eventual displaced vertices coming from b quarks for example. Therefore, the ID combines high-resolution detectors near the interaction point and continuous tracking elements at the outer region. At nominal luminosity, about 1000 particles will be created at the collision point every 25 ns. Given this enormous track density, the momentum and vertex resolution requirements put stringent constraints on the detector technology, imposing fine-granularity detectors such as semiconductor tracking detectors with silicon micro-strip and pixel technology. The ID covers pseudorapidities of $|\eta|$ <2.5, extends 6.2 m in length and 2.1 m in radius. As can be seen on Fig. 5.3, it consists of three independent but complementary sub-detectors:

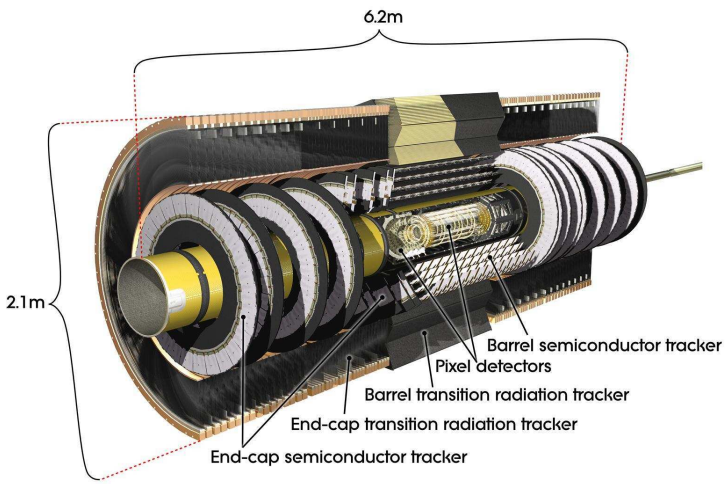

Figure 5.3: The ID is composed of three sub-detectors. Nearest to the interaction point, the pixel detector is composed only of a cylindrical barrel, whereas the SCT and TRT are each made of a barrel and two end-caps.

The **pixel detector** was designed to provide a high-granularity, high precision set of measurements as close as possible to the interaction point. The high-granularity requirement is fulfilled via a total of 140 million detector elements and the implemented system in three layers gives three precision measurements over the full acceptance. In this way, the pixel detector determines the impact parameter resolution, and finds short-lived particles such as B-hadrons or τ leptons.

The **semi-conductor tracker** system covers the $|\eta| < 2.5$ region and is composed of eight layers of silicon micro-strip detectors which perform precision measurements of the charged particle tracks with a resolution of $\approx 200\mu$m. It has a coarser granularity

than the pixel detector because it is further away from the interaction point.

The **transition radiation tracker** allows to discriminate between electrons and pions. It is made up of straw detectors of very small diameter (4 mm) and covers the range within $|\eta| < 2.0$. It provides 36 measurements along a track. The spacial track resolution is less than 0.15 mm for charged particles tracks of $p_T > 0.5$ GeV. The TRT is operated with a gas mixture of 70% xenon, 20 % CO_2 and 10 % CF_4, with a total volume of 3 m^3. The xenon is used to add electron identification capability by detecting transition-radiation photons created in a radiator between the straws. The TRT is operated at room temperature, but the silicon sensors of the other two sub-detectors have to be cooled down to -25°C.

5.2.2 The calorimetry

We continue our tour of the Control Room with the desk behind the ID group: here we are in the Liquid Argon section. The purpose of a calorimeter is to measure the energy deposit and its direction. This is done via a sampling technique, which consists in alternating layers of passive dense material, where the metallic absorber interacts with the incoming particles, and active layers of scintillator, which collect the deposited energy and generate the signal. In ATLAS, the active medium of the calorimeter is liquid argon, because of its excellent performance in terms of energy and position resolution. The passive absorber is lead. By separating the calorimeter in small segments both longitudinally and transversally, the particle track and its identity can be detected. All elements of the ATLAS calorimeter can be seen in Fig. 5.4.

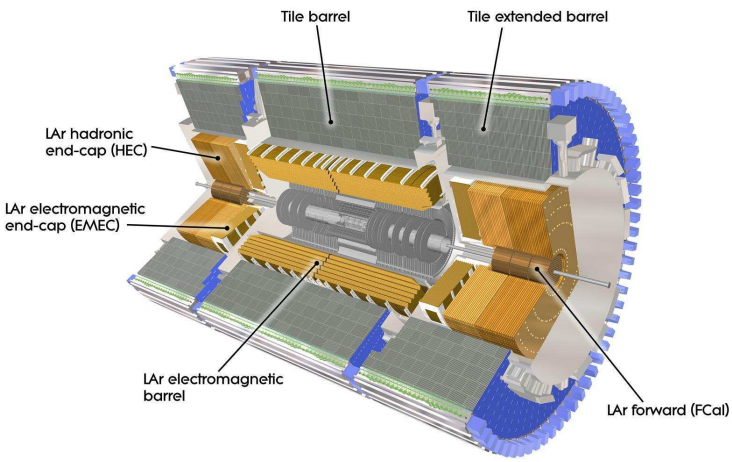

Figure 5.4: The ATLAS calorimetry system.

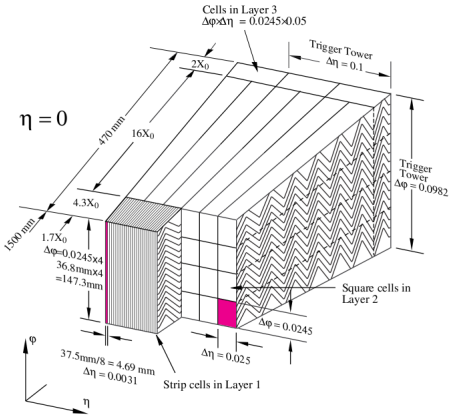

Figure 5.5: The accordion geometry of the ECAL absorber layers.

The electromagnetic calorimeter (ECAL) measures photons and electrons, and is composed a barrel and two end-caps. While travelling through dense matter, highly energetic electrons lose their energy predominantly by bremsstrahlung. For high-energetic photons, the main process is e^+e^- pair production. These two mechanisms combine to produce an electromagnetic (EM) shower. The characteristic amount of traversed matter is called the radiation length X_0, with units $g\ cm^{-2}$. This is the mean distance over which a high-energy electron loses all but $1/e$ of its energy via bremsstrahlung[1]. This is an appropriate length scale for the description of EM cascades and the physical size of EM calorimeters (ECALs) is usually of the order of 15 to 30 X_0, so as to contain the whole shower. The accordion geometry for the ECAL absorber layers, shown in Fig. 5.5 has been retained because it provides naturally a full ϕ coverage without any cracks and leads to a very uniform performance in terms of linearity and resolution as a function of ϕ. Over the region devoted to precision physics ($|\eta| < 2.5$), the ECAL is segmented in three sections in depth. The first layer, composed of fine-grained strips along the η direction, provides an excellent $\gamma - \pi^0$ discrimination. The second layer has a lateran granularity of 0.025×0.025 in (η, ϕ) space. This is where the most of the electromagnetic shower of highly energetic electrons is collected. The third section is the back layer which enables a correction to be made for the tail of highly energetic EM showers. These three layers are complemented by a presampler layer ($|\eta| < 1.8$) placed in front to correct for energy loss in the material before the calorimeter. The transition region between barrel and end-cap in the $1.37 < |\eta| < 1.52$ region has poorer performance due to the large amount of material in front of its first active layer.

Jets begin showering in the ECAL but continue to the hadronic calorimeter (HCAL) parts: the tile barrel and extended barrel, and both end-caps. The HCAL in ATLAS covers the range $|\eta| < 4.9$ with very different techniques. Over the range $|\eta| < 1.7$, the barrel and extended barrel function using iron tiles as scintillating material and iron as absorber. Over the range $1.5 < |\eta| < 4.9$, LAr calorimeters were chosen: the hadronic end-cap calorimeter (HEC) extends to $|\eta|3.2$, while the range $3.1 < |\eta|4.9$ is covered by the high-density forward calorimeter (FCAL), which has longitudinal segmentation in three layers. An important parameter in the design of the hadronic calorimeter is its thickness: it has to provide good containment for hadronic showers and reduce punch-through into the muon system to a minimum. For hadronic calorimeters (HCALs), the equivalent of the radiation length is the nuclear interaction length λ. The total thickness

[1] Here, $e = 2.718$ is the base of the natural logarithm and not the electric charge.

is 11 λ at $\eta = 0$, including about 1.5 λ from the outer support. This is adequate to provide good resolution for high energy jets. Together with the large η-coverage, this will also guarantee a good missing transverse energy measurement, which is important for many physics signatures, as single top for example.

5.2.3 The muon spectrometer

We now leave the LAr desk, pass the central desk where the shift leader overviews the smooth flow of operations, and visit the *muon boys* on the left corner of the ATLAS control room. They look after

- the Monitored Drift Tubes (MDT),
- the Thin Gap Chambers (TGC),
- the Cathode Strip Chambers (CSC) and
- the Resistive Plate Chambers (RPC),

which constitute the ATLAS muon system, displayed in Fig. 5.6. The muon system is composed of two parts: the coarsely grained but fast triggering system and the detection chambers which give an accurate measurement of the muon momenta. The muon spectrometer determines the overall dimensions of the ATLAS detector. The outer barrel chambers are at a radius of about 11 m and the half-length of the barrel toroid coils is 12.5 m. The third layer of the forward muon chambers, which are mounted on the cavern wall, is located at about 23 m away from the beam crossing point.

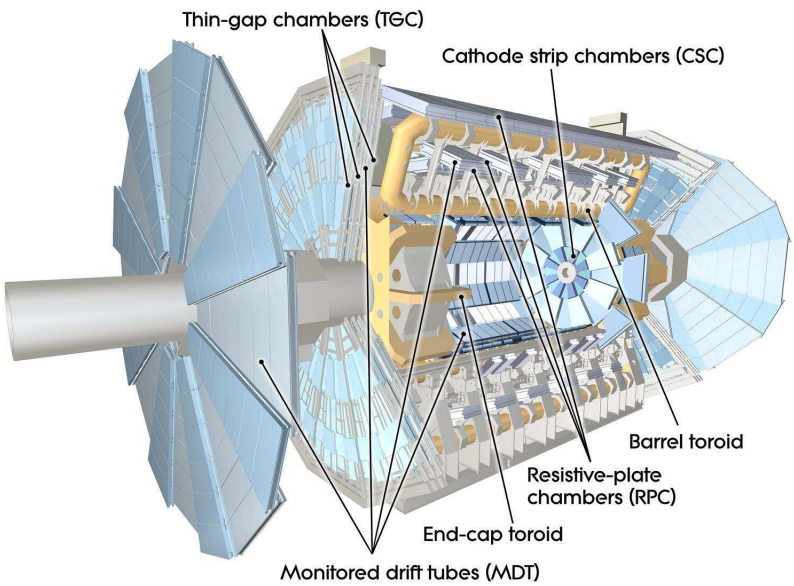

Figure 5.6: The ATLAS Muon spectrometer.

The conceptual layout of the muon spectrometer is based on the magnetic deflection of muon tracks in the large superconducting air-core toroid magnets. Over the range $|\eta| < 1.0$, magnetic bending is provided by the large barrel toroid. For $1.4 < |\eta| < 2.7$, muon tracks are bent by two smaller end-cap magnets inserted into both ends of the barrel toroid. Over $1.0 < |\eta| < 1.4$, usually referred to as the transition region, magnetic deflection is provided by a combination of barrel and end-cap fields. This magnet configuration generates a field that is mostly orthogonal to the muon trajectories, while minimising the degradation of resolution due to multiple scattering.

The tracking system, arranged on three stations around the beam axis, is composed of Monitored Drift Tubes (MDTs) and Cathode Strip Chambers (CSCs). CSCs are multi-wire proportional chambers with cathode planes segmented into strips in the plane orthogonal to the beam axis. The MDTs constrain the muon tracks in the z coordinate with a precision of 35 μm and cover a range of $|\eta| < 2.7$. At larger pseudorapidities and close to the interaction point, the CSCs provide complementary track information in the R coordinate with a precision of 40 μm and in the ϕ direction with a 10 μm precision. Optical alignment systems ensure that the stringent constraints on the mechanical accuracy of the precision chambers are met.

The trigger system, installed in the pseudorapidity range $|\eta| < 2.4$, is composed of Resistive Plate Chambers (RPCs) in the barrel and Thin Gap Chambers (TGCs) in the end-cap regions. Their intrinsic time resolution (1.5 ns for the RPCs and 4 ns for the TGCs) is appropriate for triggering and to identify the bunch crossing.

5.2.4 LUCID and ALFA

LUCID(LUminosity measurement using Cherenkov Integrating Detector) is a detector primarily dedicated to online relative luminosity monitoring by counting Cherenkov photons created by particles from minimum bias events. The detector consists of twenty

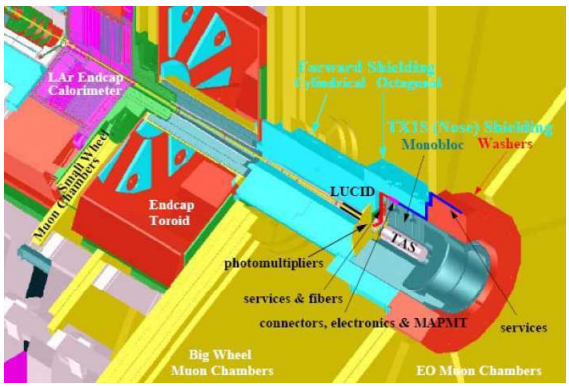

Figure 5.7: LUCID position in the ATLAS detector.

aluminium tubes which surround the beam-pipe and point toward the interaction point,

as shown on Fig. 5.7. The tubes are filled with C_4F_{10} and are kept at a constant pressure of $1.2 - 1.4$ bar, in order to provide a Cherenkov threshold of 2.8 GeV for pions and 10 MeV for electrons. Two detectors are installed, one in each end-cap region of ATLAS, at a distance of 17 m from the interaction point and at 10 cm radial distance from the beam-line. The flat surface of each tube which points back to the interaction point is black to protect against beam background. The quartz window is however sensitive to beam background, beam halo muons in particular.

The second detector dedicated to the luminosity measurement, ALFA (Absolute Luminosity For ATLAS), is located at 240 m from the interaction point on both sides. The luminosity measurement is done with scintillating fibre trackers located inside Roman pots, which approach the beam as close as 1 mm.

5.2.5 ATLAS as a whole

We have assembled piece by piece the ATLAS detector, which can be seen in its full extension on Fig. 5.8.

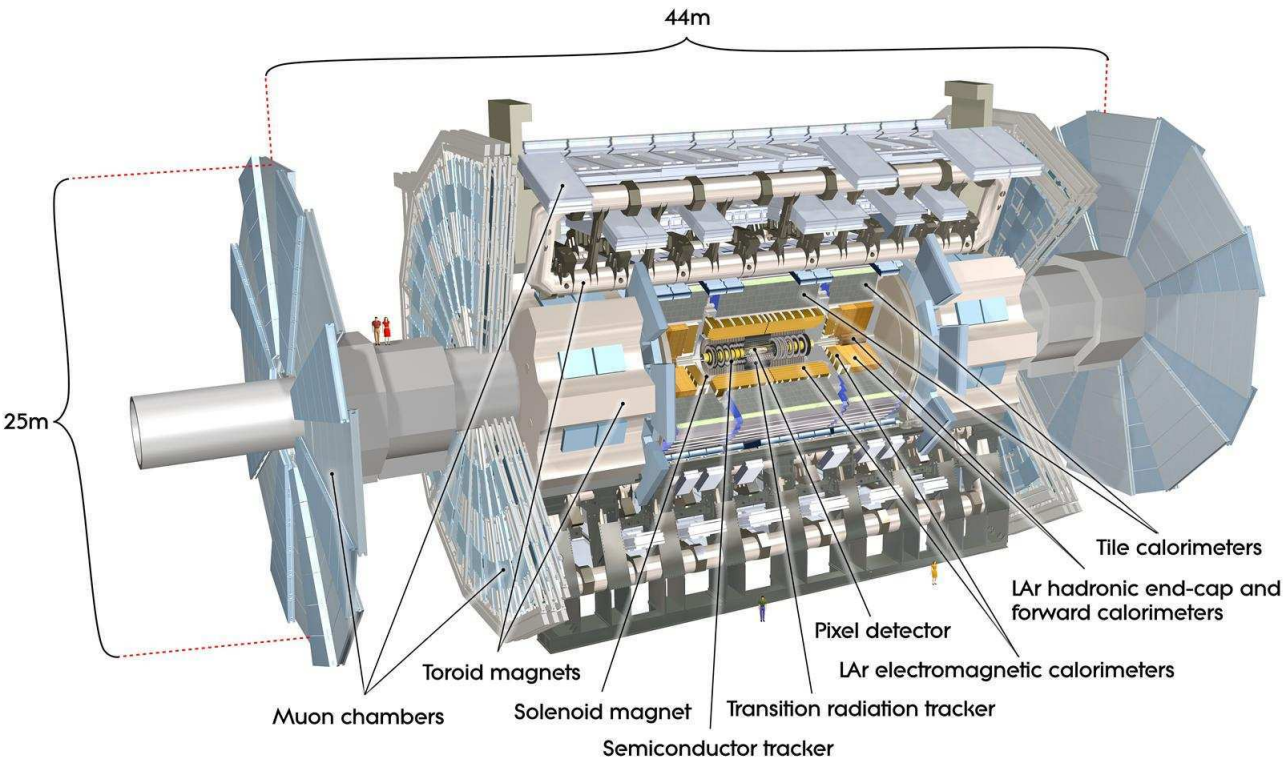

Figure 5.8: The ATLAS detector

The whole detector has a length of 44 m and a diameter of 22 m, for a total weight of 7000 tons. The primary goal of the experiment is to be able to operate at high

Table 5.1: The general performance goals of the ATLAS detector. The units for the energies E and transverse momentum p_T are in GeV.

Detector component	Required resolution	η coverage	
		Measurement	Trigger
ID	$\frac{\sigma_{p_T}}{p_T} = 0.05\%\ p_T \oplus 1\%$	$\pm$ 2.5	
ECAL	$\frac{\sigma_E}{E} = \frac{10\%}{\sqrt{E}} \oplus 0.7\%$	$\pm$ 3.2	$\pm$ 2.5
HCAL Barrel and End-Caps	$\frac{\sigma_E}{E} = \frac{50\%}{\sqrt{E}} \oplus 3\%$	$\pm$ 3.2	$\pm$ 3.2
Forward	$\frac{\sigma_E}{E} = \frac{100\%}{\sqrt{E}} \oplus 10\%$	$3.1 < \lvert\eta\rvert < 4.9$	$3.1 < \lvert\eta\rvert < 4.9$
Muon spectrometer	$\frac{\sigma_{p_T}}{p_T} = 10\%$ at $p_T = 1$ TeV	$\pm$ 2.7	$\pm$ 2.4

luminosity and reconstruct as many signatures as possible. The ATLAS detector as it is now has excellent detection characteristics, listed in Tab. 5.1. The general formula for the energy resolution of the calorimeters [8] is

$$\frac{\sigma_E}{E} = \frac{a}{\sqrt{E}} \oplus b \oplus \frac{c}{E}. \tag{5.1}$$

where the input energies E are given in GeV and the $\oplus$ sign indicates that the terms are added in quadrature. The a coefficient is called the stochastic term and includes statistics-related fluctuations as for example intrinsic shower fluctuations, sampling fluctuations and photoelectron statistics. Also accounted for in this term is the dead material in front of the calorimeter. This coefficient is of order of a few percent for homogenous calorimeters, but is more important, of the order of 10 %, for sampling calorimeters, which is the case here. The b coefficient is the systematic or constant term, which includes effects from the detector non-uniformity, calibration uncertainties and radiation damage to the active medium. This terms can be minimised if radiation-hard material is used and submitted to frequent in situ calibration and monitoring. The c coefficient accounts for electronic noise.

The tracking quality of the ID and the muon spectrometer is indicated via the position resolution

$$\frac{\sigma_{p_T}}{p_T} = \frac{a}{\sqrt{E}} \oplus b. \tag{5.2}$$

These numbers show that the original requirements listed in the ATLAS technical report are met. The high luminosity and bunch crossing frequency at the LHC makes it an extremely challenging experimental environment for the detectors, which need fast and radiation-hard components and electronics, as well as high detector granularity to be able to handle the high particle fluxes and be capable of distinguishing overlapping events. The following points sum up the advantages of the whole detector:

- The ID provides a good charged-particle momentum resolution and reconstruction efficiency in the inner tracker. This is particularly important to distinguish primary from secondary vertices, as required for b-tagging.
- Muons, electrons, photons and jets are the very core of most physics analysis channels. The good electromagnetic calorimetry for electron and photon identification and measurements is complemented by full-coverage hadronic calorimetry for accurate jet and missing transverse energy measurements. Good muon identification and momentum resolution over a wide range of momenta is assured by the whole muon system.
- Missing transverse energy can be reconstructed very precisely, due to a large acceptance in pseudorapidity with almost full azimuthal angle coverage.

5.2.6 The Root Controller

Now that we have put ATLAS together from the hardware point of view, we must do the same for the software. So we come back to the center of the room to the Run Control shifter. His task is to assemble in the Root Controller the sub-detectors which participate in the data taking session, shown on Fig. 5.9, using the ATLAS partition. Partitioning refers to the ability to provide the functionality of the system to use only a subset of the ATLAS detector if necessary. While this is not recommended in the case of a physics fill, it is necessary during intermediate testing stages. Other tasks of the Run Control shifter include setting the prescale keys handed over by the DAQ shifter and the parameters of the run, stop and start the runs and alert the corresponding sub-detector shifter if any error messages disrupt the data taking process.

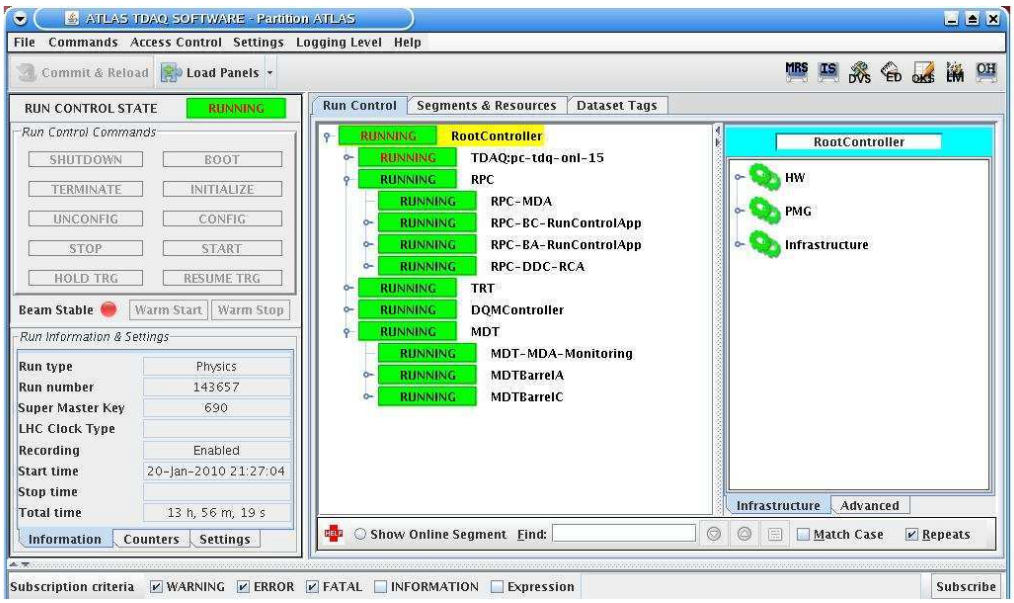

Figure 5.9: Snapshot of the Root Controller software [132].

5.3 The Trigger and Data Acquisition Concept

The last desk we need to visit in the Control Room is responsible for trigger and data acquisition issues. The nominal collision rate of the LHC will be of the order of 40 MHz. Out of all these collisions, only a mere 200 Hz will ultimately be recorded on tape (CASTOR). So the job of the Trigger and Data Acquisition (TDAQ) system is to reduce the bunch-crossing rate to the requested 200 Hz recorded events and transfer the detector read-outs to the mass storage. The challenge lies in the required overall rejection factor of 10^7 against minimum bias events while retaining an excellent efficiency for rare new physics processes. The ATLAS trigger setup is based on three levels of online event selection, as shown in Fig. 5.10. Each trigger level refines the decision made at the previous level and applies, if necessary, additional selection criteria. The level 1 (LVL1) trigger is an inbuilt, hardware trigger. The high level trigger (HLT) is split into two: the level 2 (LVL2) trigger and the event filter (EF).

The LVL1 trigger is responsible for the initial selection based on reduced granularity information from a subset of detectors. High p_T muons are identified using only the trigger chambers, RPCs in the barrel and the TGCs in the end-caps. The calorimeter selections are based on reduced granularity information. Objects searched for by the calorimeter trigger are for example high-p_T electrons and photons, jets and tau leptons decaying into hadrons. They also include large missing and total transverse energy. All those trigger information may be provided for a number of sets of p_T-thresholds, typically six to eight sets per object type. The maximum rate of the LVL1 trigger is 75 kHz. An essential requirement of the LVL1 trigger is to identify the bunch-crossing of interest. Given the short bunch-crossing interval (25 ns at design luminosity), this is

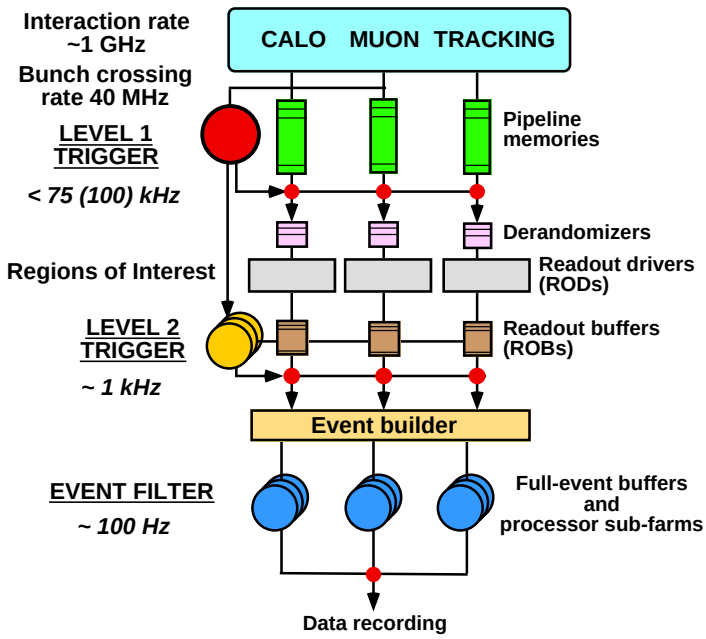

Figure 5.10: The ATLAS trigger scheme.

a non-trivial consideration. For the muon trigger for example, the physical size of the muon spectrometer implies times-of-flight comparable to the bunch-crossing period. For the calorimeter trigger, the challenge lies in the pulse shape of the calorimeter signals, which extend over many bunch-crossings. The LVL1 is composed of the Central Trigger Processor (CTP) and exchanges signals with the detector via the Trigger Timing Control (TTC) system. It sends the signal to either accept or reject the event to all TTC partitions, and gives the ROI information over to the L2 system. The prescale is a number N which is set by the TDAQ shifter and means that 1 out of N events of the given type are accepted.

The HLT is composed of 160 Read-Out System (ROS) PCs. The LVL2 trigger makes use of the region of interest (ROI) information provided by the LVL1. This is composed of position reference (η and ϕ) as well as p_T information of candidate objects, and energy sums (missing E_T vector and scalar E_T value). The LVL2 selectively accesses this information, moving only the data that are required in order to make its decision. It has however access to all of the event data, including full granularity and precision. But thanks to the ROI mechanism, only a small fraction of the event information is needed.

After the LVL2 trigger, the last stage of the online selection is performed by the EF, which employs offline algorithms and even uses the calibration and magnetic field maps. The EF makes its final decision on complete physics events. The ROS passes the event fragments to the Event Builder, which fashions complete events to pass over to the EF. If the event passes the requirements of the EF, the event is copied from the SubFarm Output (SFO) to CASTOR via a python script. Events accepted by the EF are divided

into different streams, according to their trigger signature. This enables a quick access to the data portion which is relevant for the different physics analysis. The streaming structure was elaborated in reference [133] and its composition for the 2010 physics data [134] is given by the following inclusive data streams:

- **Egamma** which contains electron and photon objects,
- **JetTauEtMiss** for jets, tau leptons and missing transverse energy,
- **Muon** for muons and
- **minBias** for minimum bias events.

The streams can be inclusive or exclusive. While an event containing an electron and a jet would be in both the Egamma and JetTauEtMiss streams for the inclusive configuration, it would enter a special overlap stream in the exclusive case.

One of the roles of the run control shifter is to regularly verify that the event reconstruction chain for the triggers is working smoothly. In problematic cases, i.e. if one sub-detector experiences problems, the information flow gets stuck at some point, blocking event recording. The system goes *busy*. The status of the different sub-detector readouts can be seen on the busy panel in Fig. 5.11. In order not to lose precious col-

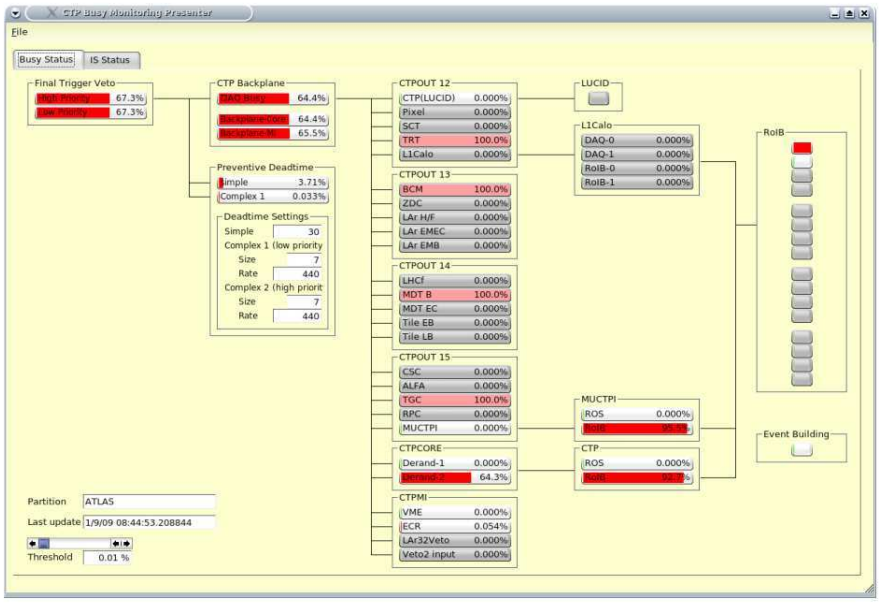

Figure 5.11: The busy panel shows the occupation of the sub-detector read-outs.

lision data, the experts from the sub-detector have to resolve the problem as fast as they can, to restore the optimal data taking configuration. Each data-taking session is identified by a partition name and a run number (typically a few hours long), and

further subdivided into different luminosity blocks (of a few minutes). Two different clocks are used: LHC whenever the beam configuration is not changing (BC1), and the internal one (BCref) whenever LHC is ramping, i.e. accelerating the bunches. The acceleration process alters the beams revolving frequency and this shifting clock could be troublesome for the detector. At those moments the triggers are automatically held by the system. When the beam is dumped during or after the ramp, the whole system has to ramp-down anyway because of the hysteresis-cycle of the magnets.

5.4 Event simulation and reconstruction

The ATHENA [135, 6] control framework is the ATLAS offline software which is used to produce the full chain of simulated events, including the detector response and trigger, and reconstruct simulated or real data in formats defined by the Event Data Model. This section details these different steps.

5.4.1 Simulation chain

The simulation chain in the Athena framework is shown in Fig. 5.12.

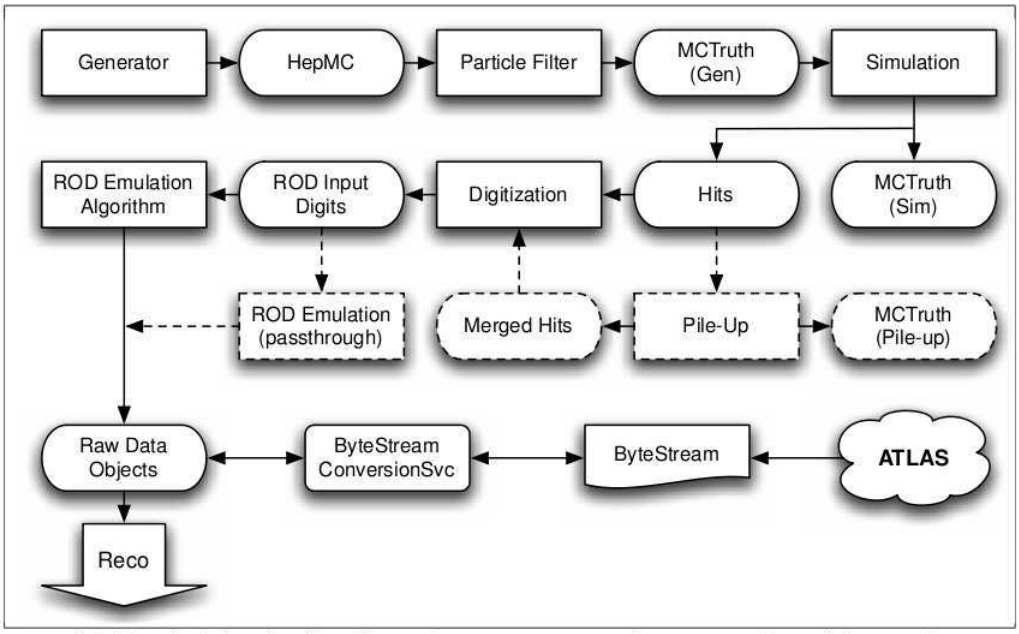

Figure 5.12: Data flow for simulation and collision data. Processing stages are represented by rectangles, rounded rectangles stand for EDM objects. Dashed rectangles are optional.

The different steps of simulated event production are:

- **Event generation** is done using Monte Carlo generators, such as those described in Section 4.1, which have been approved from the collaboration for the selected physics process. The generation is run from inside Athena and the output is converted into a common format by mapping into HepMC.

- The passage of particles through the detector is simulated with the **GEANT4 ATLAS simulation (G4ATLAS)**. Provided functionalities include geometry description, the propagation of particles through the different sub-detectors, the description of materials and the modelling of physics processes. At this stage, it is also possible to simulate pile-up, i.e. the overlaying of signal and background events. As can be seen on Fig. 5.12, this is optional in the simulation processing pipeline. The output of G4ATLAS is in form of hits, which are a record of the interactions of particles in the detector.

- The next stage is **digitisation**. The hits produced either directly by G4ATLAS, or from merged of pile-up events, need now to be translated into the output which would actually be produced by the ATLAS detectors. This conversion is a very detector-specific task since it should simulate the response of the readout electronics. For example, it needs information as the propagation of charges for the tracking detectors and the LAr calorimeter. A package exists for each of the detector subsystems and the design and operating conditions (like magnetic field or voltage) of the detectors can be set using job-option parameters or taken from the condition or detector description database. The final output of the digitisation step are Raw Data Objects (RDOs or RAW) are identical to real detector data, but may also contain truth information from the MC particle generation.

At this point, simulated and real collision data have the exact same form and can be processed with the same algorithms in the reconstruction process.

5.4.2 Event reconstruction

Event reconstruction is done in several stages, where each step contains a subset of the information available in the step before and objects may be formed by combination of different pieces of information. The different file formats and their size are defined in the Event Data Model.

The Event Data Model (EDM) defines a number of successively derived data formats, which begin with either raw or simulated data and evolve through reconstruction into more streamlined event representations, which become more and more suitable for a physical analysis. The different formats are

- The **RAW data** contains the output of the ATLAS detector information coming from the final trigger element, the Event Filter . The average event size is ≈ 1.6 MB.

- The **Event Summary Data (ESD)** consists of both the detector information and the full output of the reconstruction process in object format as tracks (and their hits), calorimeter clusters and cells, combined reconstruction objects etc. The initial nominal size at this stage is about 1 MB/event, but is to decrease as the understanding of the detector improves.

- The **Analysis Object Data (AOD)** is a reduced event representation which contains a subset of the ESD information. It can be seen as a summary of event reconstruction using objects such as electrons, muons, jets, etc. The nominal size is 100 kB/event.

- **The Derived Physics Data (DPD)** are skimmed/slimmed/thinned events derived from AODs and ESDs for specific physics channels. The data is reduced by removing irrelevant containers and by selecting objects and dropping information from those objects. Nominally the event size is about 10 kB on average but there are large variations depending on the different physics channels.

Reprocessing As we have seen, it is a quite long way from RAW collision data to the output format which allows a physical analysis. In addition to this, the detector configuration changes over time, so that the most accurate description needs to be used. Often, collision data will have to be reprocessed approximately two to three months after acquisition using improved calibration and alignment maps, which have been obtained from continued studies of the calibration stream data. This offline calibration process sets the time scale for the reprocessing. In some cases it may be possible to reprocess starting from ESD rather than going back to the RAW data format.

5.4.3 Fast vs Full Simulation

The simulation chain depends on what is used as input. For generated Monte Carlo events, detector simulation is done via GEANT4 using a detailed model of the detector geometry. Each particle is propagated through the detector material, generating hits which are then digitised, reproducing the RAW data coming from ATLAS. But the use of an extremely accurate detector description has one major drawback: it is very CPU time consuming. Simulation can take up to several minutes just for one event, the greatest time fraction being spent on the calorimeter section. Considering the size of samples needed for physics analysis, the current full simulation setup of ATLAS will not be possible for all physics requirements with sufficient statistics. Therefore an alternative has been set up, the fast simulation AtlfastII. The event reconstruction chain for full simulation and fast simulation are shown in Fig. 5.13.

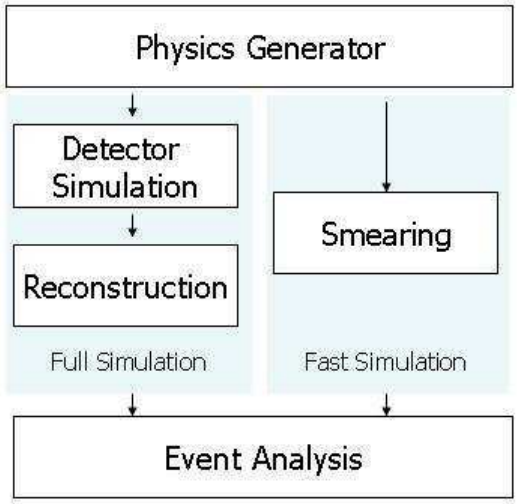

Figure 5.13: Schematic comparison between the fast and full simulation of events.

In AtlfastII, there is the possibility of using fast simulation of either the calorimeter, FastCaloSim [136], or of the inner detector, FATRAS [137]. The gain in CPU time in the fast simulation comes from the use of parametrisations of the raw energy response of the calorimeter, which replace the step by step calculation of the physical processes of particle showers. In the initial stage of Atlfast, photons, charged pions and electrons were simulated with the same parametrisation as photons. This was changed in AtlfastII, where electrons have a parametrisation on their own. All other particles, except neutrinos and muon, use the pion parametrisation. The parametrisation of AtlfastII has been derived from a very early version of the ATLAS full simulation. The energy deposit in the calorimeter layers is based on parametric shape functions and electric noise is added to each calorimetric cell in the final step. Due to this parametric nature in which not all of the shower details and fluctuations are accounted for, it is important to provide a clear check of AtlfastII versus the full simulation. We give here an example of such a consistency check.

A comparison between the full and the fast simulation of *electron gun* events, i.e. events in which an electron was created at the interaction point and goes through the detector, can be seen in Fig. 5.14. Due to the magnetic field in the ID, the electron emits bremsstrahlung and arrives with different energies in the calorimeter in one event from the other. Depending on the fraction of energy arriving in the calorimeter as electrons and as photons, the AtlfastII response has to be consistent with the full simulation. Different control variables are used to test the adequacy of the fast simulation. On the y-axis, we find the energy that has been reconstructed by the algorithm, normalised to its generated value, the truth energy. The first plot shows the reconstruction as a function of the sum of the energy of the photons in the event. For the second plot, we follow the original electron through its bremsstrahlung process and record its energy when reaching the calorimeter. Again, this quantity is normalised with respect to the input

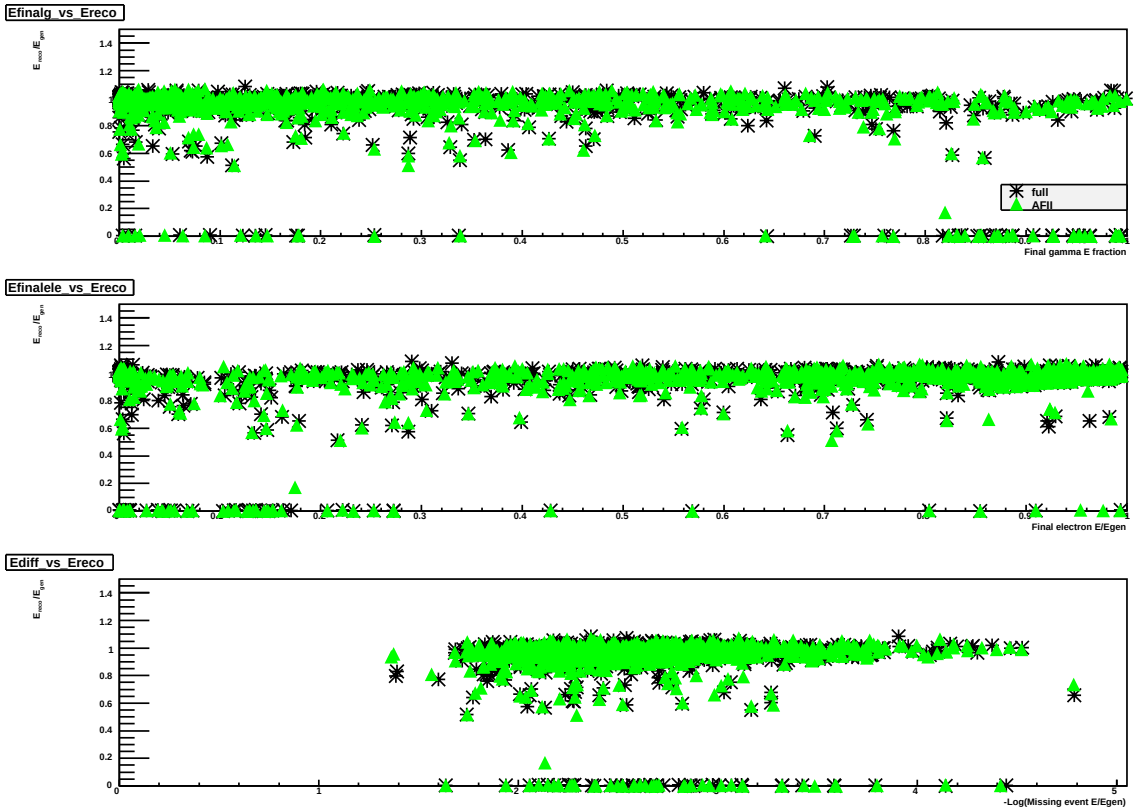

Figure 5.14: Comparisons between the FastCaloSim (in green) and full simulation (in black) for 1000 electron gun events with an energy of 15 GeV shot in the $0.20 < \eta < 0.25$ region.

value. The third plot displays as a function of the missing energy. For each interaction vertex, the mother energy is compared to the energy sum of the daughters, and then this is summed for all interaction vertices in the event. In general, this quantity is small, as it should be. During this investigation, the only relevant problem which came up is for a very small fraction of events which do not get reconstructed the same way in fast and in full simulation. The problem is intuited to lie in the Geant4 simulation, which does not propagate particle information for photons with an energy less than 100 MeV. In order to clarify and solve this issue, a more complex analysis on the Geant4 simulation level is required, which is behind the scope of this service task.

Donald Crowhurst started to contemplate the insoluble mystery of the square root of minus one and before long found himself entering a "dark tunnel" from which he was never to emerge. Most of us, thankfully, are luckier than that.

Jonathan Coe, *"The terrible privacy of Maxwell Sim"*

6 The 2010 pp physics run

The reprocessed data at our disposal for a subsequent analysis has been collected during the 2010 physics run of the LHC. In this Chapter, we review the quantity of available data, and evaluate if an analysis of charged Higgs boson production is feasible. Since this is not be the case, we focus on important backgrounds to $H^{\pm}t$ production, which are mainly $t\bar{t}$ and Wt. Because of the similitude between $H^{\pm}t$ and Wt and because the task force is needed, we concentrate on semileptonic Wt. Therefore, we detail the objects in Wt-like signatures and gather the necessary MC samples for the signal and its backgrounds.

6.1 Data taking periods and consequences

6.1.1 Data taking periods

The 2010 physics run of the LHC with colliding protons at 7 TeV has been an eventful time. A small recapitulation of the data periods and subdivisions with relevant improved collision conditions is listed in Tab. 6.1. The subdivisions will be important in Section 6.4.1, since not the whole data taking period will be used for the analysis. Throughout the different periods, the LHC has constantly been upgrading its run conditions, progressively filling in more and more proton bunches and thus gaining each time an important factor on the delivered luminosity. This rise is best seen in Fig. 6.1. Out of a delivered integrated luminosity of almost 50 pb^{-1}, the ATLAS detector has recorded 45 pb^{-1}, but only 35 pb^{-1} pass the several data quality requirements. These events have been reprocessed and can be used for physics analysis.

Table 6.1: The 2010 data periods and subdivision with their collected luminosity and comments on the major changes [138]. The amplitude function β^*, dictated by the LHC machine, needs to be minimised to obtain maximum luminosity. The design value is $\beta^* = 55$ cm.

Period	Subperiod	Comment	$\mathcal{L}$ (nb^{-1})
A	–	Unsqueezed stable beam data ($\beta^* = 10$ m), typical beam spot width is $(50-60)^2$ μm^2.	0.4
B	B1-B2	First squeezed stable beams ($\beta^* = 2$ m), typical beam spot width is $(20-30)^2$ μm^2.	9
C	C1-C2	–	9.5
D	D1-D6	Nominal LHC bunches ($\approx 0.9 \times 10^{11}$p/bunch), pileup now significant: about 1.3 interactions per crossing (was <0.15 before).	320
E	E1-E7	Brand new trigger menu: previous data were taken with the **InitialBeams**, now taken with the **Physics** menu.	978
F	F1-F2	36 colliding bunches in ATLAS	1980
G	G1-G6	Bunch trains with 150 ns spacing from LHC.	9070
H	H1-H2	233 colliding bunches in ATLAS.	9300
I	I1-I2	295 colliding bunches in ATLAS.	23000

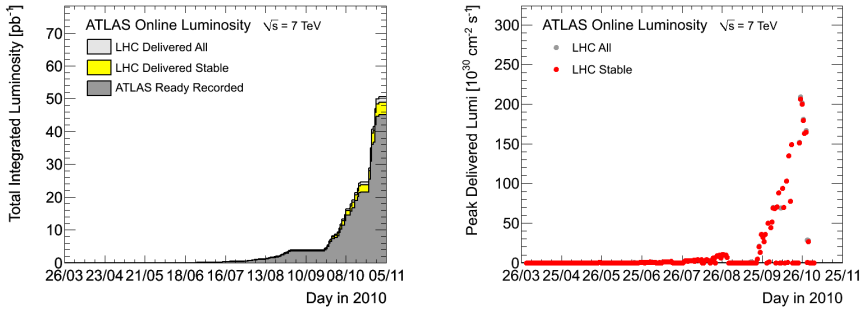

Figure 6.1: Integrated (on the left) and peak (on the right) luminosity delivered by the LHC and recorded by the ATLAS detector in 2010.

6.1.2 Consequences on the charged Higgs boson analysis

In the previous chapters, we have been preparing the very first step of the analysis of a novel physics channel at hadron colliders by calculating a production process at NLO and implementing it in Monte Carlo event generators. While charged Higgs studies have been performed at the Tevatron for quite some time now, the prospect of the LHC startup, with its design centre of mass energy of 14 TeV and nominal luminosity of 10^{34} cm^{-2}s^{-1}, promised to quickly overrun the Tevatron findings. But things went another way, and it is still not clear if the expected 14 TeV can be reached in the coming years. The delay in the physics program due to the various shutdown periods and the reduced energy of 7 TeV puts things in another perspective for charged Higgs production. Charged Higgs production cross sections range up to at most a picobarn for best case scenarios. Considering selection efficiencies of those topologically very complicated events, a charged Higgs analysis simply makes no sense at this point. The thing to do beforehand is to clearly identify the possible backgrounds to charged Higgs production from the SM and be sure to understand them thoroughly. In Fig. 6.2, the major SM backgrounds to $H^{\pm}t$ production, $t\bar{t}$ and Wt, are classified according to their resemblance to $H^{\pm}t$ as a function of the different number of b quarks in the signature.

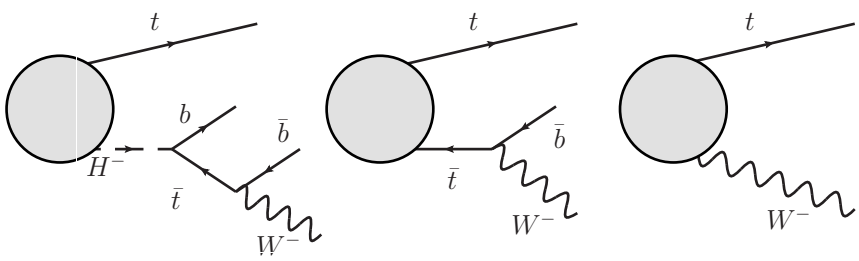

Figure 6.2: At LO, these final state signatures differ only in the number of b quarks: $H^{\pm}t$ production (left) has an additional b quark with respect to $t\bar{t}$ production (centre), which again has one b quark more than Wt production (right).

Assuming an acceptable mistag rate, current algorithms identifying b jets in ATLAS have on average a 50 % tagging efficiency, which means that one out of two b quarks will not be identified. Since the SM process cross sections are noticeably higher than $H^{\pm}t$ production, whatever analysis selection is devised for $H^{\pm}t$, it will suffer from SM top production contamination via either $t\bar{t}$ or Wt. In the presented diagram, the charged Higgs boson decays into a top and a b quark. Other relevant search channels will be the decay to $\tau\nu$ and $c\bar{s}$, which are even more similar to Wt production. Due to its large mass, the τ lepton decays in the detector, leaving a jet-like signature and a charged Higgs boson $c\bar{s}$ decay will resemble a W decay into light jets with a shifted dijet mass. It is therefore mandatory to study and understand the SM backgrounds. The Wt production is especially challenging, since it has not yet been observed. We may still gain from the experience gathered in Chapter 3, since at NLO, Wt and $H^{\pm}t$ production are very similar. Also, they involve the same problematic interference with $t\bar{t}$, and diagram removal and diagram subtraction MC samples will be needed.

6.2 Semileptonic electroweak single top production

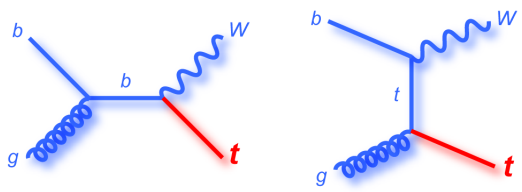

Figure 6.3: Feynman diagrams for LO electroweak single top production in the s- and t-channel.

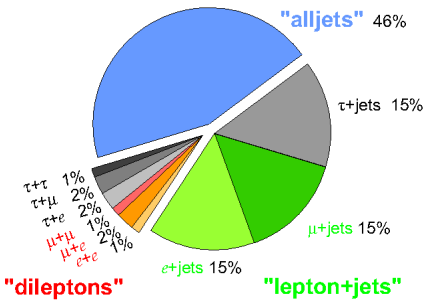

Figure 6.4: Relative fractions for events containing two W bosons, classified according to their decay type.

Electroweak single top diagrams, shown in Fig. 6.3, are very similar to $H^{\pm}t$ production and are obtained by replacing the charged Higgs boson by a W boson in the s- and t-channel. Since the production cross section at the Tevatron is too low to allow for a physical analysis of Wt events, this process has not yet been observed, nor is there any measured limit on its cross section. The process will be enhanced at the LHC, where it has a NLO production cross section of $\sigma_{Wt}^{LHC} = 14.6$ pb at 7 TeV, since it comes from gluon and b parton distribution functions. Also, a major part of the NLO contribution comes from gluon-gluon fusion. Since the branching

of $t \to Wb$ is almost 100 %, Wt events contain two on-shell W bosons and their signatures in the detector can be classified according to their decay. The branching ratios for W boson decay are listed in Tab. 6.2, and the resulting proportions for the different channels are displayed in Fig. 6.4.

The final state of semileptonic Wt is $l\nu_l\ b\ qq'$. This translates into a detector signature of a lepton and missing transverse energy to account for the neutrino, a jet which is identified as coming from a b flavoured quark and two additional jets. All these objects now have to be identified through their interactions in the different sub-detectors of ATLAS.

Table 6.2: Decay modes of the W^+ boson in the SM. The different branching ratios are given in percent [8].

W^+ decay	branching ratios in %
$e^+\nu_e$	10.75 ± 0.13
$\mu^+\nu_\mu$	10.57 ± 0.15
$\tau^+\nu_\tau$	11.25 ± 0.20
$\bar{q}q'$	67.60 ± 0.27

6.3 Relevant objects for the semileptonic Wt analysis

We have left the last Chapter at the description of simulated events and have stopped short after the Geant 4 detector simulation step. After digitisation, events are in the same form as real events in data and we have to reconstruct physical objects from the simulated or real readout of the sub-detectors. The reconstructed event objects are stored in dedicated rootfile containers [139]. The top group collects the global object definitions from the different performance groups, and these are taken over by the single top group, sometimes with slight modifications. Since we are in a relatively early phase of running and will be analysing the first data, with no prior experience of the detector and its output, the analysis concentrates on the simplest objects of interest for the top signature, i.e. electrons, muons, jets and missing transverse energy. We do not consider top quark decay into taus, since they form complex jet-like structures in the detector which have to be studied further.

6.3.1 Electrons

Definition The standard electron reconstruction algorithm is based on energy deposits detected in the ECAL, called clusters, which are associated to tracks of charged particles reconstructed in the ID. The electron reconstruction starts on a seed of energy greater than 2.5 GeV with a sliding- window algorithm in the middle layer of the ECAL, where most of the energy of high-energetic electrons is deposited. The size of this window has been optimised to 3×5 cells. Then, a matching track to the cluster is searched for.

Three cuts for the reconstructed electron quality are defined, depending on the signal efficiency and jet rejection requirements [140]:

- The **loose** cut corresponds to simple shower shape cuts in the middle layer and very loose matching criteria between the reconstructed track and the calorimetric cluster.
- The **medium** cut uses additional information from the first ECAL layer and the track quality cuts are similar to standard requirements.
- The **tight** cut has tighter track-matching criteria and cuts on the energy-to-momentum ratio. Further electron isolation may also be required.

For the single top analysis, the electrons are required to pass even more stringent quality constraints. Additionally to those quality cuts, they must have a $p_T > 20$ GeV and the electromagnetic cluster position has to lie within $|\eta_{\text{clus}}| < 2.47$. Electrons which lie in the calorimeter barrel-endcap overlap region, $1.37 < |\eta_{\text{clus}}| < 1.52$, are rejected, since in this region there is only limited calorimeter instrumentation.

Background contamination With all the activity in the detector, it may happen that the object reconstructed as an electron was not an electron at all in the first place. Fake electrons can come from cases where a jet has a low energy deposit in the HCAL and is reconstructed via the electron algorithm. A second possibility is that the electron which was reconstructed comes from a heavy-flavour decay, and so it would belong to the jet structure. Photon conversions constitutes a third important background. In order to suppress contributions from these sources, the reconstructed electron is required to show little calorimeter activity and only few tracks in an (η-ϕ) cone surrounding it. To this purpose, two isolation variables are employed, a calorimeter isolation variable `Etcone30` and a track isolation variable `Ptcone30`. Isolated electrons are then defined by imposing `Etcone30`$/p_T < 0.15$ and `Ptcone30`$/\ p_T < 0.15$.

MC to data corrections Electron identification efficiencies for well-isolated electrons have been obtained on data using the tag-and-probe method. This method is applied on a clean dielectron sample from W and Z to e^+e^- decays. In each event, the electron with the best reconstruction criteria is defined to be the tag. Another electron is searched for, constituting the probe, with this time less stringent isolation criteria, so that the tag and probe ensemble give a reconstructed mass in the electroweak boson peak region. The discrepancy between MC and data is quantified via correction factors, called scale factors. These studies have shown that the scale factors depend on the η and the p_T of the electron and therefore the scale factors are provided in eight bins of η and six bins of p_T. They differ slightly from the top group standard due to the tighter isolation requirement used in this analysis. They were approved by the ATLAS egamma group.

Calibration and resolution

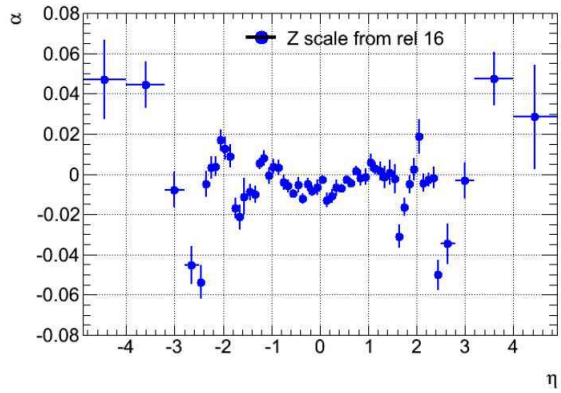

Figure 6.5: The α correction factor applied to the electron energy scale as a function of η.

Corrective factors on the energy scale have been determined in 50 η bins for central and 8 bins for forward electrons, by constraining the dielectron invariant mass distribution to the Z lineshape in $Z \to ee$ events from the 2010 data [141]. The corrected energy E' is obtained by

$$E' = \frac{E}{1+\alpha}, \tag{6.1}$$

where α is shown as a function of η in Fig. 6.5.

Since MC events do not reproduce the electron resolution found in data, a smearing procedure has to be applied to the MC samples via the `EnergyRescalerTool`. The discrepancy is attributed to the constant term C in the resolution parametrisation

$$\frac{\sigma}{E} = \frac{S}{\sqrt{E}} \oplus C, \tag{6.2}$$

since the low energy domain is dominated by the sampling term S and J/ψ distributions are correctly reproduced. The constant term has been measured to be $1.1\% \pm 0.1(stat.) \pm 0.2(syst.)$ for electrons in the barrel. Fig.6.6 shows the dielectron invariant mass distribution in the J/ψ and Z boson mass peak region after calibration and smearing.

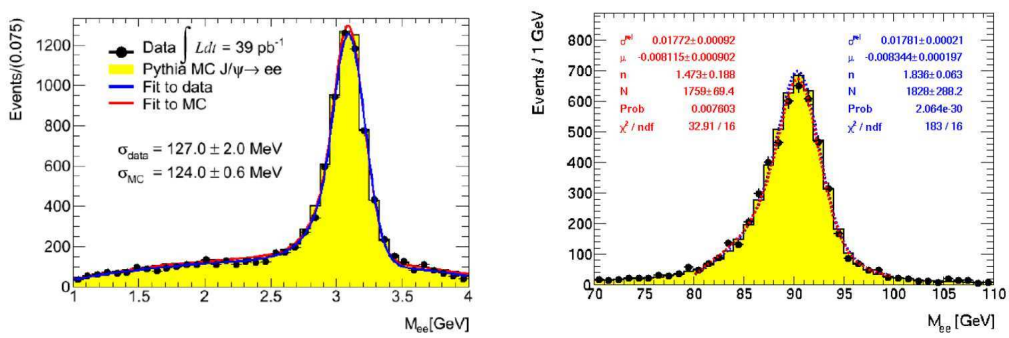

(a) (b)

Figure 6.6: The J/ψ (figure (a)) and Z boson (figure (b)) mass peak regions for $Z \to ee$ events in the barrel after calibration and smearing.

6.3.2 Muons

Definition Muon candidates are reconstructed by matching the muon spectrometer (MS) hits with the inner detector (ID) tracks, using the complete track information of both detectors and accounting for material effects of the ATLAS detector structure. Muons with transverse momenta between 3 GeV and 3 TeV can be reconstructed using three different strategies:

- In the **stand-alone** mode, only information from the MS is used.
- The **combined** method uses ID and MS track combination.
- The **segment tag** uses information from the ID and the inner station of the MS.

The final candidates are required to have a transverse momentum greater than 20 GeV and to be in the pseudo-rapidity region of $|\eta| < 2.5$.

Background contamination The muon fake rate is by no means as important as the electron. It can nevertheless happen that, as was also the case for electrons, a muon is reconstructed which stems from the decay of a heavy flavour quark. Again, the muon should then be part of the reconstructed jet. Therefore, an isolation criterion is applied. The transverse energy in a cone of $R = 0.3$ around the muon direction is required to be less than 4 GeV. In addition, the scalar sum of the transverse momenta of any additional tracks inside a cone of $R = 0.3$ around the muon must be less than 4 GeV. An overlap removal between jets and muons is applied, removing any muon whose momentum direction is within a $\Delta R < 0.4$ cone of a jet with $p_{\mathrm{T}} > 20$ GeV.

MC to data corrections The muon identification efficiencies have been measured in a dimuon data sample at the Z boson mass peak and scale factors have been derived in 10 bins in η and ϕ. The scale factor is of order unity for most bins with an uncertainty of around 4%.

Calibration and resolution

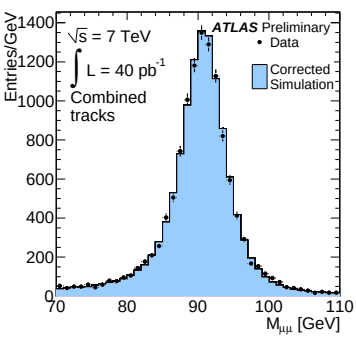

Figure 6.7: Di-muon invariant mass comparison in the Z boson mass range between collision data and MC simulation for combined (MS+ID) tracks.

A recent study on $Z \to ee$ events in 7 TeV collisions [142] gives the combined (CB) muon momentum measurement, determined by the relative weights of the ID and the MS. The corrected muon p'_T is given as a function of its original p_T via

$$p'_T(CB) = p_T(CB)\left[1 + \frac{\frac{\Delta_{MS}}{\sigma^2_{MS}} + \frac{\Delta_{ID}}{\sigma^2_{ID}}}{\frac{1}{\sigma^2_{MS}} + \frac{1}{\sigma^2_{ID}}}\right], \tag{6.3}$$

where $\Delta_{MS,ID}$ is the correction to the simulated MS or ID p_T and $\sigma_{MS,ID}$ are the

values for the resolution at that p_T. An example of a combined muon p_T resolution curve in the barrel is given in Fig. 6.8. The comparison between data and MC after correction of the simulated muon p_T is shown in Fig. 6.7. The distributions are integrated over the full range of η.

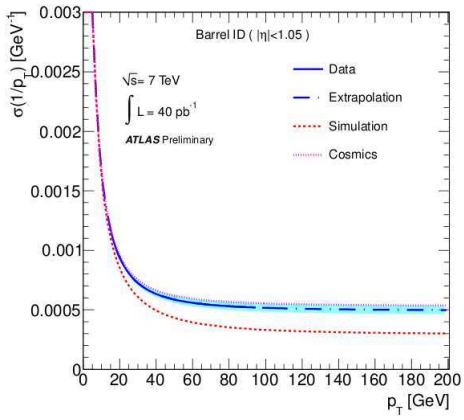

Figure 6.8: Muon resolution p_T of tracks in the ID in the $|\eta| < 1.05$ range shown for the collision data (blue solid line) and their extrapolation (blue dashed line). The results from cosmic ray muons is superposed (light red dashed line) and the uncorrected MC simulation is shown (red dashed line).

6.3.3 Jets

Definition The final topology of an outgoing parton is a group of collinear bundles of partons in which the energy of the initial particle is contained. This is more commonly referred to as a jet. So, a jet is not a fundamental object defined by theory, but rather an effective description of what is seen in the detector and it is therefore mandatory to specify which jet reconstruction algorithm has been used. The jet algorithm, i.e., the way the individual tracks are grouped together, has to satisfy certain properties so as to be acceptable both the theoretically and experimentally. Since one wants to match pQCD calculations at different orders to different jet topologies, we have to be sure that the jet algorithm is well-defined, and this is only true for collinear and infrared safe algorithms. This means that if in a partonic configuration we replace a parton by a set of collinear and soft partons with the same total momentum, the algorithm should reproduce the same result. The hadronisation procedure is seen to preserve the jet structure, and the distribution of the total momentum of the jet's constituents can approximately be derived by pQCD calculations of partons with the same total momentum. In ATLAS, jets are reconstructed using the infrared safe anti-k_T algorithm [143] with a width parameter 0.4. The inputs of the jet finding algorithm are topoclusters constructed by the clustering algorithm. The jets then need to be calibrated from the raw electromagnetic scale using a Monte Carlo based correction factor, which on average brings the measured jet p_T to the particle level in the simulations. Jets are

required to have a $p_T > 25\,\text{GeV}$ and $|\eta_{\text{det}}| < 5.0$, where the jet is defined at EM+JES scale.

Background contamination For a very small fraction of events with pathological noise bursts in the calorimeter, it may happen that jets are incorrectly reconstructed from a few noisy cells. These events are removed with special cleaning cuts if the jet p_T is > 10 GeV. Jet structures overlapping with identified electron candidates within a cone of $\Delta R < 0.2$ are removed from the list of jets, as the jet and the electron are very likely to correspond the same physics object.

Jet Energy Scale (JES) Calibration Hadronic showers are by no means as regular as EM showers. In addition, an important fraction of the partons initial energy is not measured because it is either used in the fragmentation process or escapes the calorimeter in form of neutrinos or muons. Therefore, an electron e and a pion π of the same energy detected in the calorimeter will have different reconstructed energies. Thus jets are measured at the EM scale, which accounts correctly for the energy deposit in the calorimeter by EM showers, but not hadronic showers. This implies that the jet energy evaluation has to be carried out via correction factors. Low signal densities in the calorimeter cell indicate a hadronic signal and a correction factor will have to be applied, while this is not the case for high signal densities which are generated by EM showers. The hadronic JES is on average restored via data-derived correction and calibration constants, obtained by comparing the reconstructed jet kinematics to the ones of the truth level jet in MC simulations. The JES calibration is then validated with in situ techniques.

The calibration scheme applied in ATLAS for the 2010 data is called `EM+JES`. It applies jet-by-jet corrections as a function of the jet's energy and η location. It proceeds in three steps:

1. The average additional energy due to pile-up is subtracted from the measured energy in the calorimeters. The correction constants for this procedure have been extracted from an in situ measurement.

2. The jet position is corrected. The jet axis points now to the interaction vertex.

3. The JES factors are applied. This jet calibration, based on the H1 method, is done by application of cell signal weighting. All calorimeter cells with four-momenta $(E_i, \vec{p}_i)$, where $E_i = |\vec{p}_i|$ of the tower or cluster jets are summed with weighting functions w to give the reconstructed jet four-momentum

$$(E_{\text{reco}}, \vec{p}^{\,\text{jet}}_{\text{reco}}) = \Big(\sum_i^{\text{cells}} w(\rho_i, \vec{X}_i) E_i, \sum_i^{\text{cells}} w(\rho_i, \vec{X}_i)\vec{p}_i\Big). \tag{6.4}$$

   The weights w depend on the signal density $\rho_i = E_i/V$, where V is the volume of the considered cell, and on the module and layer identifiers encoded in $\vec{X}_i$.

Since the startup of the LHC, constant progress is being achieved on the JES measurement and its systematic uncertainty [144]. The validation using tracks [145] and finer effects such as the influence of other close tracks [146] have been studied. A recent analysis [147] evaluated the JES correction using the 7 TeV data collected in 2010. The average jet energy scale correction is shown as a function of calibrated jet transverse momentum p_T for three jet η intervals in Fig. 6.9.

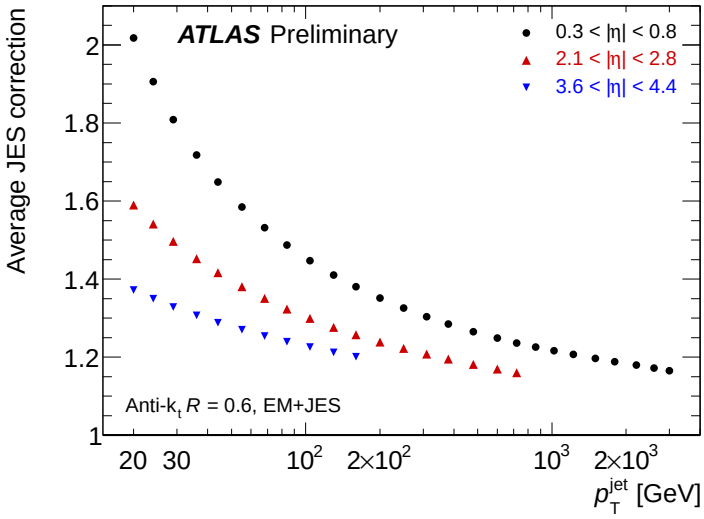

Figure 6.9: Average jet energy scale correction as a function of the calibrated jet transverse momentum p_T for three representative η-intervals.

B jets One of the most important selection criterion of events containing top quarks is the identification of jets stemming from b quarks. This is done by taking advantage of several of b quark jet properties which allow to distinguish them from jets which contain only light quarks. These features are:

- **Hard fragmentation.** The b hadron retains about 70% of the original b quark momentum.
- **Large b hadron mass.** The invariant mass of b hadrons is usually greater than 5 GeV, enabling their decay products to have a large transverse momentum with respect the jet axis. Separation from light jets may then be done by measuring the greater opening angle of the decay products.
- **Long lifetime.** The feature which is most used in b-tagging algorithms is the relatively long lifetime of hadrons containing a b quark, which is of the order of 1.5 ps. This means that a b hadron in a jet will have a significant flight path length, on average about 3 mm in the transverse plane, before decaying. A first discriminating variable can be constructed using the tracks' impact parameter. The transverse impact parameter d_0 is the distance of closest approach of a track

to the primary vertex point, in the r, ϕ projection. The longitudinal impact parameter z_0 is the z coordinate of the track at the point of closest approach in r, ϕ. Since tracks reconstructed from b hadron decay products tend to have rather large impact parameters, they can be distinguished from tracks stemming from the primary vertex. The second, more demanding option is to reconstruct explicitly the displaced vertex. These two approaches, using the impact parameters of tracks or reconstructing the secondary vertex, are referred to as spatial b-tagging.

- **Semileptonic decay.** The semi-leptonic decays of b hadrons can be used by tagging the lepton in the jet. Also in this case, the reconstructed tracks of the jet cross in a displaced, secondary vertex.

Based on those properties, there exist several b-tagging algorithms at the moment, all more or less refined.

- **Impact Parameter (IP) algorithms.** Methods using the IP are `JetProb` and `TrackCounting` $IPxD$, where $x = 1, 2, 3$ is the number of dimensions. They were studied with the first 15 nb^{-1} of data. The `JetProb` algorithm starts by computing the probability of a track to come from the primary vertex, based on the signed transverse impact parameter. It then combines the probabilities of all tracks belonging to the jet to give a jet probability ranging between zero and one. Jets from light quarks have a flat distribution, whereas b jets peak at zero.
  The `TrackCounting` algorithm requires at least two good quality tracks with a signed transverse impact parameter significance above a given threshold. It uses the significance distributions of b and light jets to calculate a jet weight via a likelihood approach.

- **Secondary vertex taggers.** These tagging methods reconstruct the secondary vertex from tracks associated with the jet. The `SV0` tagger gives a jet weight from a likelihood ratio based on distributions like the vertex mass and the energy fraction. It has been studied with 3 pb^{-1} in [148]. The `JetFitter` algorithm uses a Kalman filter approach[1] to fit the b decay chain.

- **Soft lepton taggers.** The soft muon tagger uses a one-dimensional likelihood ratio of the muon relative transverse momentum $p_{T,rel}$ to give a jet weight. Another, simplified version, is already used for early data analysis. The soft electron algorithm is a more sophisticated likelihood ratio combining input variables from the ID and the calorimeter.

The tagger used for the single top analysis is `SV0` [149], where within a given jet, the two-track vertices that are significantly displaced from the primary vertex are reconstructed. Those that are consistent with K_S^0 or Λ^0 decays, $\gamma \to e^+e^-$ conversions, or material interactions are removed.

[1] The Kalman filter algorithm can be used to obtain the optimal parameters in either track or jet reconstruction, by progressively removing either hits or tracks with large contributions to the χ^2 function.

A secondary vertex fit is performed on the remaining tracks, iteratively removing the track with the highest contribution to the χ^2 until an acceptable χ^2 is obtained. The weight is the three dimensional signed decay length significance, $L/\sigma(L)$, of the secondary vertex position with respect to the primary vertex. The sign is given by the sign of the projection of the decay length vector on the jet axis, i.e. it is positive if tracks cross the jet axis after the primary vertex, as shown on Fig. 6.10. The jet axis can be determined accurately from the calorimeter information. On Fig. 6.11, the different signed decay length significance distributions for data as well as MC b, c and light jets in an inclusive jet sample can be seen.

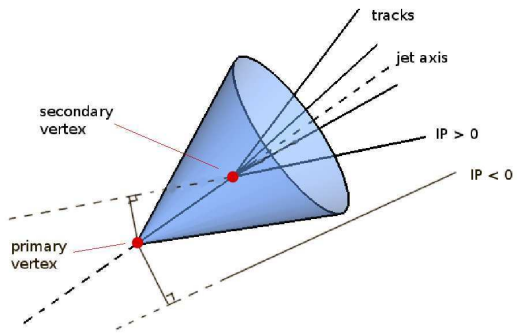

Figure 6.10: The jet cone starts from the primary vertex and is centred on the jet axis. Tracks belonging to the secondary vertex have a positively signed IP.

In the single top analysis, the `SV0` tagger weight cut is applied at 5.85, which corresponds to a b-tagging efficiency of 50% and a light quark jet rejection factor of 271[2]. This working point has been derived from $t\bar{t}$ MC simulations. The performance of the `SV0` tagger was evaluated in [150] and further details about the measurement of the b-tagging efficiencies and mistag rates can be found in [151].

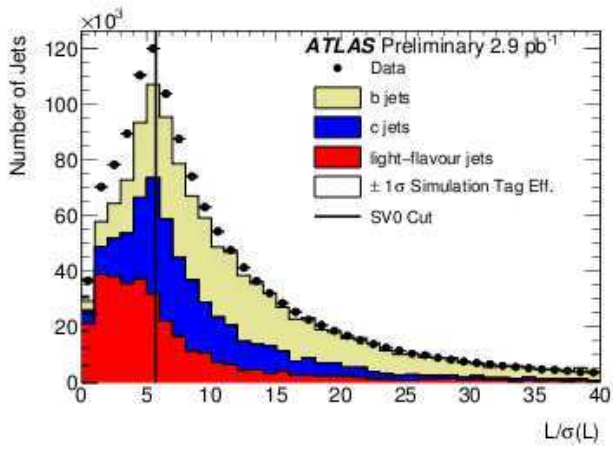

Figure 6.11: The signed decay length significance for the `SV0` b-tagging algorithm in data (points) and simulation (stacked histogram) for an inclusive jet sample. The vertical line is a possible cut at 5.72 for b-tagging. [148]

[2]The rejection factor R means that $1/R$ light jets will pass the cut, so that $R = 271$ translates into a mistag rate of about 0.4 %.

6.3.4 Missing transverse energy

Since single top event signatures include a neutrino from the W boson decay, the signature in the detector is missing transverse energy that the escaping neutrino took away. But missing transverse energy can also come from other effects. If for example a fraction of the particle energy is badly reconstructed, due to a non instrumented region or miscalibrated part, this will lead to the mismeasurement of the true E_{T} of the final interacting objects. The missing transverse energy is calculated as the vector sum over all calorimeter energy clusters in the event, and is further refined by applying object level corrections for the contributions which arise from identified photons, leptons and jets.

6.4 Data and MC samples

The last step we need to take before the actual analysis is assemble the portion of the 2010 collected data relevant for Wt production. Also, we gather the MC samples for the signal and all possible backgrounds. The ATLAS geometry tag for data and MC events is `ATLAS-GEO-16-00-00` and the reconstruction software version is `16.0.3.3.3`.

6.4.1 Data samples

The data samples used in this analysis are those of periods E4 to I, defined in Tab. 6.1. The very first data from runs A to E3 have not been used due to a problem with the muon trigger timing, but those periods have only negligible integrated luminosity, as has already been shown on Fig. 6.1.

Single Top trigger signatures Wt-like events are selected via the unprescaled single electron and muon triggers in the muon trigger, Egamma and JetTauEmiss trigger streams. For single top events in the **electron channel**, the trigger requirement consists of one high p_T electron. At L1 an electromagnetic deposit with $E_T > 10$ GeV is required, and the HLT has full information on the whole granularity of the calorimeter and the tracking. The calorimeter cluster is matched to a track and the trigger electron object is required to have a energy deposit $E_T > 15$ GeV where the energy is measured at the EM scale. The single muon trigger requires at L1 a muon chamber track with a 10 GeV threshold, matched by a reconstructed muon in the precision chambers at the EF level, this time with a 13 GeV threshold.
In order to be accepted, events have to be part of the Good Run List, i.e. they occurred during a period in which there were stable beams in the accelerator and the parts of the detector and the trigger system were working. The total number of events corresponds to an integrated luminosity of 35.3 pb^{-1}. They have undergone the event reconstruction process described in Section 5.4 and the final analysis was performed on top group specific DPDs in root trees.

6.4.2 MC simulation samples

The major backgrounds to the semileptonic single top Wt signature are in great part related to the b-tagging issues. A signature with one additional b quark which can be missed is $t\bar{t}$ production. Then, since the signature is mainly a W and jets, W+jets is also an important background. Events might also get picked up from purely QCD like multijet production. Also taken into account are Z plus jets and diboson production, and s- and t- channel single top production. Signal and background processes have been simulated using different Monte Carlo event generators and a complete list is given in Tab. 6.3, along with their hadronic production cross section and the number of generated events.

For the single top quark and $t\bar{t}$ samples, generation has been done with MC@NLO coupled to Herwig for the parton showering and hadronisation of events, using CTEQ6.6 as PDFs. Renormalisation and factorisation scales have been set at the top quark mass $\mu_R = \mu_F = m_t$.

W+jet events are the dominant background after $t\bar{t}$ production. All W+jets Monte Carlo samples, have been generated at LO with ALPGEN, coupled to Herwig for showering and the normalisation is done via K-factors, following the NNLO recommendation [152]. Different jet multiplicities and flavours have been generated. As the history of the top quark discovery has shown, understanding the W+jets background is extremely important. Since the different multiplicities are generated individually, special care has to be taken in combining the different ALPGEN samples, since radiation from one multiplicity may migrate the event into another multiplicity bin. The various flavour samples are combined using the MLM matching procedure implemented in ALPGEN. The different flavour samples are then combined with the heavy flavour overlap removal tool specific to the ATLAS analysis [153, 154]. In this method, the removal criterion is the distance ΔR between two heavy-flavour quarks. Additional details on this issue can be found in App. D.

The Z+jet samples have been generated at LO with ALPGEN, again combined with Herwig for the parton showering and normalised to NNLO K-factors [152].

Dibosons in which one of the bosons decays leptonically are also a background contribution to Wt production and the different channels are WW, WZ and ZZ production. They have been simulated with Herwig at LO and normalised to the NLO cross section values of MCFM.

Table 6.3: MC signal and background samples used in the Wt analysis.

	Cross-section [pb]	Generator	Generated Events
Wt all decays	14.58	MC@NLO+Herwig	200,000
t-channel (lepton+jets)	7.15	MC@NLO+Herwig	200,000
s-channel (lepton+jets)	0.468	MC@NLO+Herwig	10,000
$t\bar{t}$ no fully hadronic	89.02	MC@NLO+Herwig	1,000,000
$W \to \ell\nu$ + 0 parton	8,400	ALPGEN+Herwig	1,306,000
$W \to \ell\nu$ + 1 partons	1,580	ALPGEN+Herwig	552,000
$W \to \ell\nu$ + 2 partons	460	ALPGEN+Herwig	188,000
$W \to \ell\nu$ + 3 partons	123	ALPGEN+Herwig	50,000
$W \to \ell\nu$ + 4 partons	31	ALPGEN+Herwig	12,990
$W \to \ell\nu$ + 5 partons	8.5	ALPGEN+Herwig	3,500
$W \to \ell\nu + b\bar{b}$ + 0 parton	55.6	ALPGEN+Herwig	182,000
$W \to \ell\nu + b\bar{b}$ + 1 partons	41.1	ALPGEN+Herwig	67,000
$W \to \ell\nu + b\bar{b}$ + 2 partons	20.4	ALPGEN+Herwig	33,000
$W \to \ell\nu + b\bar{b}$ + 3 partons	7.7	ALPGEN+Herwig	13,000
$W \to \ell\nu + c\bar{c}$ + 0 parton	155.6	ALPGEN+Herwig	255,000
$W \to \ell\nu + c\bar{c}$ + 1 partons	125.9	ALPGEN+Herwig	206,000
$W \to \ell\nu + c\bar{c}$ + 2 partons	63.1	ALPGEN+Herwig	103,000
$W \to \ell\nu + c\bar{c}$ + 3 partons	20.6	ALPGEN+Herwig	34,000
$W \to \ell\nu + c$ + 0 parton	526.2	ALPGEN+Herwig	742,780
$W \to \ell\nu + c$ + 1 partons	195.3	ALPGEN+Herwig	290,000
$W \to \ell\nu + c$ + 2 partons	51.8	ALPGEN+Herwig	84,900
$W \to \ell\nu + c$ + 3 partons	12.1	ALPGEN+Herwig	20,000
$W \to \ell\nu + c$ + 4 partons	2.8	ALPGEN+Herwig	5,000
$Z \to \ell\ell$ + 0 parton	807.5	ALPGEN+Herwig	304,000
$Z \to \ell\ell$ + 1 partons	162.6	ALPGEN+Herwig	63,000
$Z \to \ell\ell$ + 2 partons	49.2	ALPGEN+Herwig	19,000
$Z \to \ell\ell$ + 3 partons	13.7	ALPGEN+Herwig	5,500
$Z \to \ell\ell$ + 4 partons	3.3	ALPGEN+Herwig	1,500
$Z \to \ell\ell$ + 5 partons	1.0	ALPGEN+Herwig	500
WW	17.9	Herwig	250,000
WZ	5.4	Herwig	250,000
ZZ	1.2	Herwig	250,000

Now it's full night, clear, moonless and filled with stars, which are not eternal as was once thought, which are not where we think they are. If they were sounds, they would be echoes, of something that happened millions of years ago: a word made of numbers. Echoes of light, shining out of the midst of nothing.
It's old light, and there's not much of it. But it's enough to see by.

Margaret Atwood, *"Cat's eye"*

7

Wt analysis in the semileptonic channel

This Chapter is dedicated to the semileptonic Wt analysis in the 2010 LHC collision data. Our effort has been focused on the final analysis strategy, described in Section 7.2 and the elaboration of the PDF systematic uncertainties, given in Section 7.3.1. Additional details to the analysis can be found in the internal note [155].

7.1 Preselection and background estimates

We have seen that Monte Carlo simulation contains several input parameters which have to be adjusted to data and some processes are not modelled well enough to permit a stand-alone contribution to the analysis. This means that for a large class of processes, the most reliable estimation of background shapes and/or normalisation is obtained through data driven methods. If the Monte Carlo distributions are taken over and are normalised with data, one speaks of scale factors to adjust the normalisation. In this section, we will define the general preselection for single top events and the specific Wt selection. We will also detail the modelisaiton of the different background processes.

7.1.1 Preselection

The single top group has defined a preselection for all single top like events, which filters samples from data and MC that have a single top signature. The preselection is applied on all events from the good-run list from the top group, where events with badly reconstructed jets have been taken out. Equally rejected are events with no primary vertex reconstructed from at least five tracks. Then tight selection cuts are applied in

order to isolate the single top signal. For the semi-leptonic single top channel, events are required to have exactly one lepton, either electron or muon, with p_T greater than 20 GeV and missing transverse energy superior to 25 GeV to account for the leptonic decay of a W boson. In addition to this, events must have at least two jets with p_T greater than 25 GeV. This defines the **pretag** sample. The **tag** sample is a subset of the pretag sample which contains events where exactly one of the jets is b-tagged. Due to the difficulty of modelling correctly the huge QCD multijet background at the LHC, a dedicated multijet veto is constructed.

QCD multijet rejection QCD multijet events have a production cross section several times that of Wt and may create a fake electron signal. The single top preselection picks up these events when a jet deposits a high fraction of its energy in the electromagnetic calorimeter and gets misidentified as an isolated electron. Typical candidates for fake electrons are π^0 in jets, which loose their energy mainly via photons. It might also be that electrons are reconstructed from events with non-prompt electrons, from the decay of a b-quark for example, which appear isolated. This is very difficult to model via a Monte Carlo generator. But in this case, one can exploit the kinematic properties of those events by looking at the missing transverse energy E_T^{miss} and the transverse mass $M_{T,W}$ defined by the (lepton, E_T^{miss})-system

$$M_{T,W} = \sqrt{2p_{T,l}E_T^{\text{miss}}(1 - \cos(\phi_l - \phi_{E_T^{\text{miss}}}))}. \tag{7.1}$$

The principle relies on the simulation of real W bosons, depicted in Fig. 7.1(a), which can be modelled very accurately. Those are then subtracted in the real data distributions shown on Fig. 7.1(b). Then, by supposing that this removes the real W boson contribution in the data distribution, all that is left are the fake electrons, Fig. 7.1(c). Now that we know where they are, we can cut them out. This is done via a triangular cut in the $(E_T^{\text{mis}}, M_{T,W})$ plane, also called QCD multijet veto. As can bee seen on Fig. 7.1, the white line removes the majority of the fake electrons, which are concentrated in the low E_T^{miss} and low $M_{T,W}$ region. The applied triangular cut is given by

$$M_{T,W} > 60 - E_T^{\text{miss}}. \tag{7.2}$$

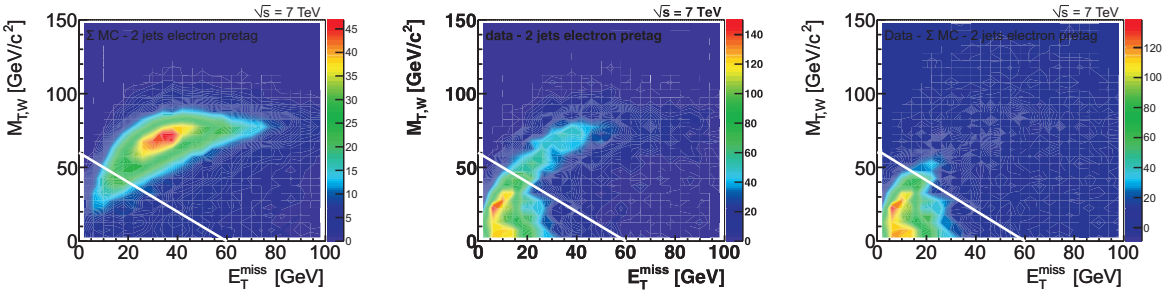

(a) (b) (c)

Figure 7.1: Scatter plots of the W boson transverse mass M_T (W) versus the missing transverse energy E_T^{miss} in the electron + 2 jets dataset. Figure (a) are the simulated W+jets events, figure (b) the observed distribution in data, and figure (c) shows the distribution for the fake electrons obtained by taking the difference between the observed distribution and the expectation for W+jets events.

Data cut flow The number of data events and the fraction of Wt signal which pass the selection cuts is given in Tab. 7.1 in form of a cut flow. The initial numbers are those contained in the trigger streams Egamma, Muon and JetTauEtMiss, which were defined in Section 5.3. The sample composition after all the preselection cuts are given according to jet multiplicities in Tab. 7.2.

Table 7.1: Event count in data after each of the preselection cuts and signal acceptance for the Wt signal samples. The MC@NLO event weights (+1 or -1) are included, but no other event weights. The lepton line also includes all event cleaning cuts. Each row includes all cuts of the previous row, except for the last row which does not include a 2-jet cut.

Cut	data		Wt	
	μ	e	μ	e
Initial events	1.1308e+07	1.98788e+07	504	504
Exactly one lepton	286017	202570	68	52
Missing E_T	164753	107151	58	43
Trigger	158866	106253	47	43
Triangle cut	153608	102614	45	40
Exactly two jets	5591	4112	13	12
Exactly three jets	1521	1212	15	14

Table 7.2: Event count in data after preselection cuts.

data set	1-jet	2-jets	3-jets	≥4-jets
pretag e	13566	4112	1212	667
pretag μ	19508	5591	1521	820
pretag total	33074	9703	2733	1487
tag e	185	163	141	179
tag μ	251	265	170	203
tag total	436	428	311	382

7.1.2 Background estimations

7.1.2.1 QCD multijets

After applying the mutlijet veto cut, the pretag sample still contains contributions from purely QCD events and these have to be modelled correctly in shape and normalisation. The shapes of the kinematical distributions are constructed using an QCD enriched sample orthogonal to the signal sample. This is obtained by applying all of the selection criteria, except for the lepton identification requirement, which has been inverted. In the muon sample, the muon is still required to pass all muon ID cuts but it has to fail the muon isolation requirement. The normalisation is done using the matrix method, which is a data driven technique for estimating the number of fake leptons in a sample. One defines two event selections, which differ only on the lepton quality criteria. The *tight* selection now refers to the same criterion used in the analysis. The *loose* selection relaxes the lepton selection criterion, so that the tight sample is a subset of the loose sample. For the loose muon, the hit and isolation requirements are relaxed. A linear system of two equations can be written and by solving it, the method gives the number of fake leptons passing the tight requirement. The event yields for the QCD muon channel obtained via the matrix method are listed in Tab. 7.3 according to the jet structure of the event.

Table 7.3: Event yields of the QCD-multijet background in the muon+jets channel for different jet bins of pretag and tagged events using the matrix method.

	Pretagged events		Tagged events	
Jet bin	QCD	QCD fraction	QCD	QCD fraction
1-jet	583 ± 88	3.0%	22 ± 4	8.8%
2-jet	314 ± 30	5.6%	42 ± 5	15.9%
3-jet	154 ± 15	10.2%	22 ± 4	13.3%
≥4-jet	69 ± 9	8.4%	13 ± 3	6.4%

The situation is somewhat different for the **electron+jets** sample. As has been discussed in the preselection definition 7.1.1, the electron channel suffers from contamination of fake as well as non-prompt electrons. Since the relative magnitude of the non-prompt and fake components depends on the fraction of QCD multijet events with non-prompt electrons in the final state and on the details of electron misreconstruction effects that are impossible to model perfectly via simulation, it is not well known. Also, the ratio varies with the event kinematics, and thus the matrix method, which relies on a representative control region to measure the input values, is not well suited for the electron channel. Therefore, the template used for the fit of the QCD-multijet background is obtained using the jet-electron model. The method consists in choosing the E_T^{miss} distribution of a QCD enriched region orthogonal to the signal sample. This is done by selecting events for which all the criteria of the preselection are applied, but where the electron requirement is replaced by a jet requirement. This jet must have a $p_T > 25$ GeV, the same acceptance in η as the electron and $80 - 95\%$ of its energy should have been deposited in the electromagnetic section of the calorimeter. Additional requirements are that the jet must have been reconstructed from at least four tracks, in order to reduce contributions from converted photons. For top, W+jets, Z+jets and diboson processes, the templates have been obtained with the Monte Carlo samples.

The normalisation is determined by fitting the data in the low $E_T^{\text{miss}} < 25$ GeV region and then extrapolate to the signal region. The fit is performed after applying all selection cuts, including the triangular cut, but leaving out the cut on E_T^{miss}. The results of the fit on the E_T^{miss} distributions at pretag and then at tag level are shown on Fig. 7.2. An advantage of using a binned likelihood fit is that it directly provides an uncertainty on the result. The matrix method has also been applied in the electron channel as a cross-check and to estimate the systematic uncertainties.

The event yield of the QCD multijet events in both the electron and the muon channel is summarised in Tab. 7.4. There's a tendency for higher QCD fractions in the muon channel. A possible explanation is that the isolation requirement on the electron is already more efficient in removing QCD contributions than the isolation cut applied for the muon. This tendency is event stronger in the tag than in the pretag sample, since the b-tagging requirement enrichens the sample in events from $c\bar{c}$ and $b\bar{b}$ background contributions, where one jet has been identified as b and the other may have produced a reconstructed lepton.

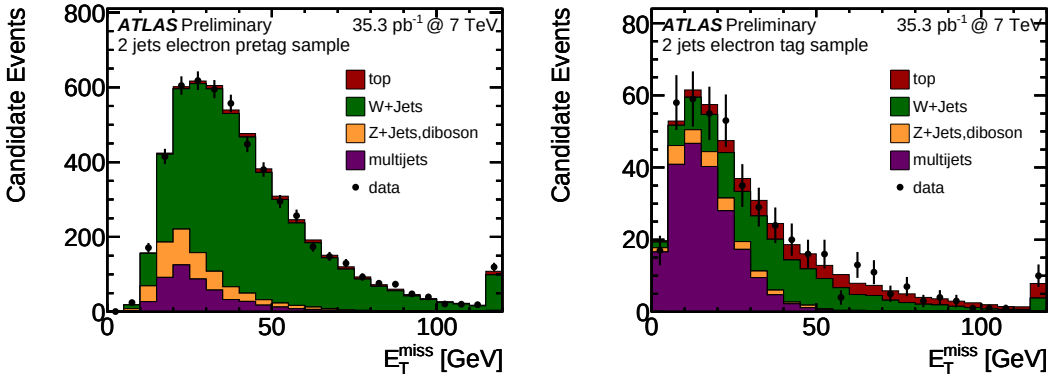

Figure 7.2: E_T^{miss} distribution for the electron two-jet pretag and tag data sets. A binned likelihood fit is performed to determine the fraction of QCD-multijet events and $W+2$ jets in the sample. Events with E_T^{miss} greater than 120 GeV are contained in the last bin.

Table 7.4: Summary of the QCD-multijet background in different jet bins of pretag and tagged events in the electron+jets and muon+jets data sets using the final uncertainty.

	Pretagged events		Tagged events	
Jet bin	e channel	μ channel	e channel	μ channel
1-jet	310 ± 310	580 ± 290	5 ± 5	22 ± 11
2-jet	260 ± 130	310 ± 160	6 ± 6	42 ± 21
3-jet	80 ± 80	150 ± 150	5 ± 5	22 ± 11
$\geq$4-jet	60 ± 30	70 ± 70	5 ± 5	13 ± 7

7.1.2.2 W+jets

The estimation of the W+jets background is relying on Monte Carlo samples for the shape of the distributions and the flavour composition and overall normalisation is derived from data. This scale factor is a product of a global W+jets normalisation times the flavour-specific scale factor. The total W+jets sample is normalised to the data in the pretag sample by event counting. The number of pretag W+jets events $N_{W+\text{jets}}^{\text{pretag}}$ is obtained by subtracting from the data count $N_{\text{data}}^{\text{pretag}}$ all other backgrounds $N_{\text{BKG}}^{\text{pretag}}$

$$N_{W+\text{jets}}^{\text{pretag}} = N_{\text{data}}^{\text{pretag}} - N_{\text{BKG}}^{\text{pretag}}, \tag{7.3}$$

where the background composition is given by the QCD multijet contribution $N_{\text{QCD}}^{\text{pretag}}$ determined just before in section 7.1.2.1 and the Z+jets, single top, $t\bar{t}$ and diboson processes given by the Monte Carlo samples $N_{\text{MC}}^{\text{pretag}}$

$$N_{\text{BKG}}^{\text{pretag}} = N_{\text{QCD}}^{\text{pretag}} + N_{\text{MC}}^{\text{pretag}}. \tag{7.4}$$

The resulting global scale factors are given in table 7.5. Since consistent results have been obtained in both channels, the combined result is used in the analysis.

Table 7.5: W+jets pretag scale factors obtained with the event counting method for the muon and electron samples and their combination. They are listed together with the uncertainty due to data statistics and systematics.

Pretag Sample	Data/MC		
	e channel	μ channel	Combined
W+1jet	1.04±0.01±0.21	1.02±0.01±0.22	1.03±0.01±0.22
W+2jet	1.00±0.02±0.32	0.98±0.02±0.33	0.99±0.01±0.32
W+3jet	0.98±0.04±0.48	0.90±0.03±0.47	0.93±0.02±0.46
W+4jet	0.91±0.10±0.74	0.92±0.08±0.78	0.92±0.06±0.74

As a cross-check of the obtained global W+jets scale factors, a second estimation is provided using the event ratio of positively and negatively charged leptons. Since the LHC is colliding protons, the u quark PDF is more important than that of the d quark. This results in a charge asymmetry in the produced W boson, whose measurement can be used to check the normalisation factors obtained earlier. The resulting scale factors for the electron channel are 0.92 ± 0.13 in the 2-jet bin and 1.07 ± 0.2 in the 3-jet bin. For the muon channel, the 2-jet bin scale factor is 0.98 ± 0.09, and 0.99 ± 0.16 for the 3-jet bin. These scale factors are consistent with those given by the event counting method.

Now that we have cross-checked global scale factors for W+jet production, we still need the individual flavour-dependent normalisation factors. Therefore, tagged control samples of the flavour contributions Wbb+Wcc, Wcj and Wjj are compared to the pretag sample. The fraction of each flavour contribution with respect to the total W+jets background are obtained by comparing the Monte Carlo samples to the data, where the other backgrounds (Z+jets, single top, $t\bar{t}$ and dibosons) have been subtracted. The comparison is done for the 1-jet pretag, 1-jet tag and 2-jet pretag events, and leads to a linear system of three equations, from which the three fractions can be extracted. The resulting scale factor for each flavour decomposition is given in Tab. 7.6.

Table 7.6: Scale factors SF for each W+jets flavour for the muon and electron samples combined, given with statistic and systematic uncertainties.

	$SF_{bb,cc}$	SF_{ljj}	SF_{cj}
W + 1jet	0.71±0.10±0.62	0.99±0.01±0.18	1.56±0.16±0.72
W + 2jet	0.68±0.09±0.64	0.95±0.02±0.25	1.50±0.16±0.66
W + 3jet	0.65±0.09±0.65	0.91±0.02±0.34	1.43±0.16±0.65
W + 4jet	0.65±0.09±0.76	0.90±0.04±0.53	1.43±0.17±0.78

7.1.2.3 Other background normalisation

Single top s- and t-channel, $t\bar{t}$ backgrounds and the contributions of the electroweak Z+jets and diboson productions WW, WZ and ZZ are simply normalised to the NLO theoretical cross sections given in Tab. 6.3 and the relevant scale factors for leptons

and b-jets are included. Additionally, the $t\bar{t}$ normalisation has been validated with a data-driven estimation.

7.1.2.4 Event yields

An event yield recapitulation of all signal and background processes after the preselection and the background estimations is given in App. E for the electron and the muon channel.

7.2 Cut-based analysis

7.2.1 Final selection

The final Wt selection selects a subset of each jet multiplicity bin, which has been defined previously in the preselection, by requiring only central jets, i.e. respecting $|\eta| < 2.5$. This tightened jet multiplicity is consistent with the preselection as it will only reject events in each jet multiplicity bin but not allow migration between multiplicities (i.e. a two jet event in the preselected sample remains a two jet event in the Wt tight selection). The data is splitted into three multiplicity bins, which are defined as

- **Two jets:** exactly 2 central jets with $p_T > 25$ GeV,
- **Three jets:** exactly 3 central jets with $p_T > 25$ GeV,
- **Four jets:** exactly 4 central jets with $p_T > 25$ GeV.

Further restrictions apply to the jets stemming from b quarks, which are identified by the `SV0` algorithm with a cut at 5.85 and are required to have a transverse momentum $p_T > 35$ GeV. We retain only events containing exactly one b-tagged jet, as this seems to be the most efficient discrimination against the $t\bar{t}$ background we can reasonably impose with the current amount of data. Further tightening of the b-tag p_T cut will augment the W+jets rejection but lower the overall signal as well as increase the relative $t\bar{t}$ background contribution. Further discrimination will have to be achieved with multivariate techniques, once more data becomes available for this to make sense.
As a first and simple approach to further reduce the background without removing too much of the signal, we choose to perform a cutbased analysis using a robust variable with some discriminating power against the $W+$ jets background: the difference in R between the first and the second jet $\Delta R(J_1, J_2)$. In order to ensure that the variable on which we will cut is well understood, data-background comparisons of those variables can be seen in Fig. 7.3.

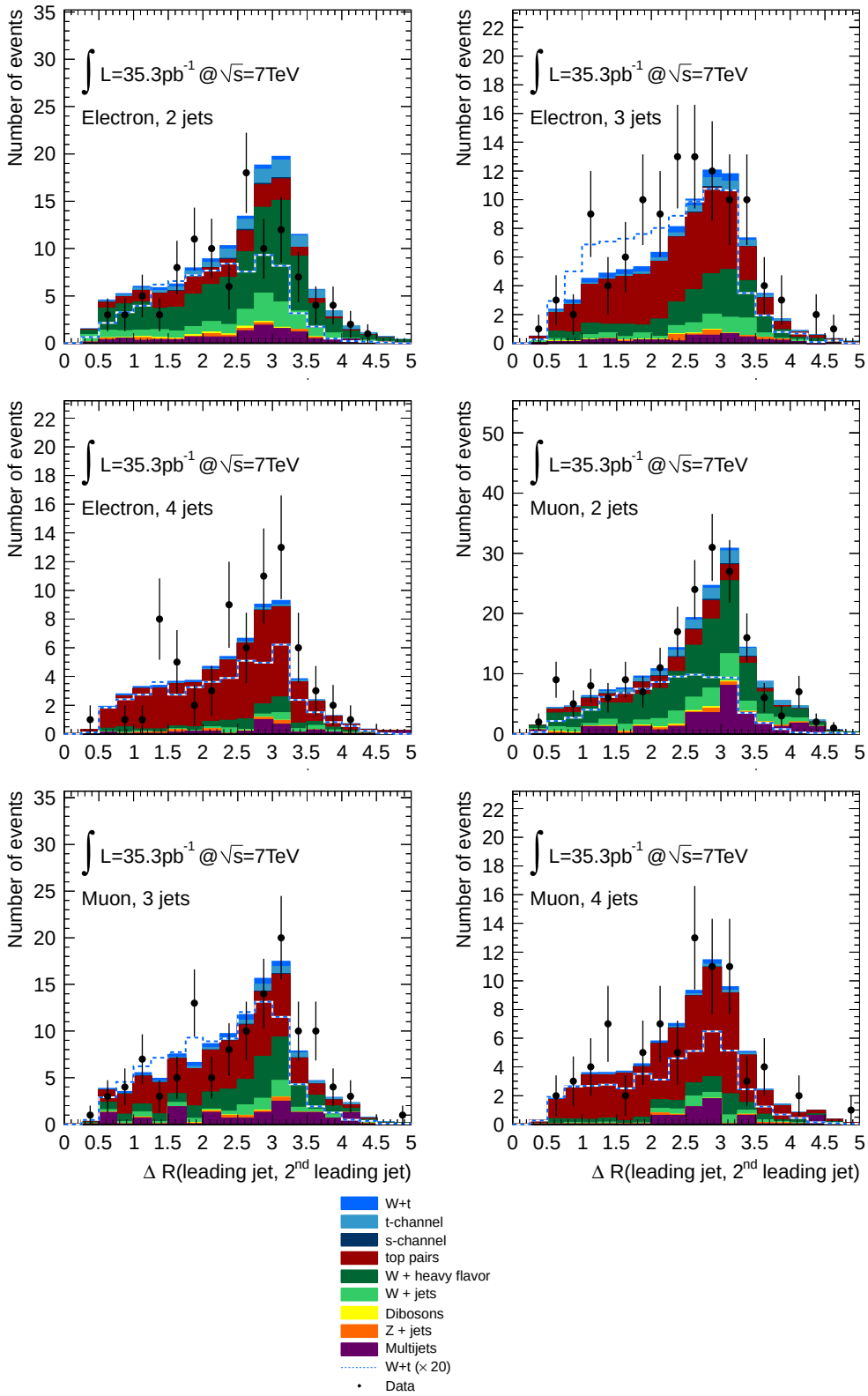

Figure 7.3: Distributions of $\Delta R(J_1, J_2)$ in the electron, rep. muon, 2-, 3- and 4-jet channel.

We retain the cut which optimises the signal over square root of background ratio $\frac{S}{\sqrt{B}}$.

7.2.2 Event yields

Optimised cut values and event yields after the cut-selection are summarised in Tab. 7.7, for which the last entry contains the sum over all systematic uncertainties squared $\Sigma^2 = \sum_i \mathrm{Syst}_i^2$,

Table 7.7: Event yields after cut on $\Delta R(J_1, J_2)$ at 2.5. Errors include all systematic effects detailed in section 7.3.

	Electron			Muon		
	2 jets	3 jets	4 jets	2 jets	3 jets	4 jets
Wt	2.3 ± 0.5	2.7 ± 0.4	1.2 ± 0.2	2.4 ± 0.5	2.8 ± 0.4	1.2 ± 0.2
Multijet	3.5 ± 3.5	1.2 ± 1.3	0.5 ± 0.5	5.7 ± 3.4	5.5 ± 3.3	1.2 ± 1.0
W+jets	7.5 ± 3.8	2.4 ± 1.5	0.8 ± 0.7	8.6 ± 4.0	2.5 ± 1.6	1.0 ± 0.9
Wc+jets	19.7 ± 10.3	4.8 ± 2.6	1.5 ± 0.9	22.8 ± 11.8	6.4 ± 3.5	1.7 ± 1.1
$Wc\bar{c}$+jets	2.1 ± 2.0	0.9 ± 1.0	0.2 ± 0.3	2.7 ± 2.6	1.3 ± 1.4	0.4 ± 0.5
$Wb\bar{b}$+jets	3.8 ± 3.6	1.2 ± 1.3	0.6 ± 0.8	4.7 ± 4.4	2.1 ± 2.1	0.8 ± 1.0
s, t-channel	3.7 ± 0.5	1.2 ± 0.2	0.3 ± 0.1	4.4 ± 0.6	1.3 ± 0.2	0.3 ± 0.1
$t\bar{t}$	11.4 ± 4.0	24.6 ± 5.3	23.2 ± 3.1	12.5 ± 4.1	27.5 ± 6.0	25.6 ± 3.8
VV	1.0 ± 0.2	0.4 ± 0.1	0.1 ± 0.0	1.2 ± 0.2	0.5 ± 0.1	0.1 ± 0.0
Z+jets	1.3 ± 1.3	0.5 ± 0.5	0.6 ± 0.6	1.2 ± 1.2	0.6 ± 0.6	0.2 ± 0.2
Background	54.0 ± 12.9	37.3 ± 6.5	27.7 ± 3.5	63.8 ± 14.6	47.7 ± 8.2	31.4 ± 4.4
Expected	56.3 ± 12.9	40.0 ± 6.5	29.0 ± 3.5	66.2 ± 14.6	50.5 ± 8.2	32.6 ± 4.4
Data	49	55	29	74	50	37
S/B	0.04	0.07	0.04	0.04	0.06	0.04
$S/\sqrt{B}$	0.31	0.44	0.23	0.30	0.41	0.21
$S/\sqrt{B+\Sigma^2}$	0.15	0.30	0.19	0.14	0.26	0.17

7.3 Systematic uncertainties

To complete the analysis of Wt production, we will investigate the systematic uncertainties which affect the cross section limit. These uncertainties are evaluated according to the common top group prescription and standard ATLAS procedures [156]. In this document, special emphasis is put on the PDF systematic uncertainty, since this was elaborated by our group.

7.3.1 The PDF systematic uncertainty

Parton distribution function (PDF) systematic uncertainties are computed following the PDF4LHC recommendation [157] which followed the interim report [158]. Its con-

crete form in the ATLAS framework [159] has already been used for the $t\bar{t}$ cross section measurement [52] and part of this computing effort can be taken over. We evaluate the systematic uncertainties within the context of the Wt analysis. Since we find that these uncertainties are small, we apply the uncertainties that we find to the not only the Wt analysis but also the single top t-channel analyses.

The Wt PDF systematic uncertainty is evaluated using as input reweighed events, which are obtained with new selection efficiencies. A new selection efficiency is evaluated for each error set, both for signal and background processes. Reweighed events have been calculated for the $t\bar{t}$ analysis and are accessible in ntuple form at [160]. These have to be retrieved and matched to the events before and after the selection cuts. The new weight w of an event which has been generated initially with PDF set f_0 for two incoming partons with momentum fraction x_a and x_b is given by

$$w_i = \frac{f_i(x_a)f_i(x_b)}{f_0(x_a)f_0(x_b)}, \tag{7.5}$$

where f_i stands for the i-est error set PDF. In this way, new event numbers before (tot) or after (sel) selection can be computed

$$N_i^{\mathrm{tot,sel}} = \sum_{\mathrm{tot,\ sel\ events}} w_i. \tag{7.6}$$

This has to be done for all error sets within a PDF collaboration, and repeated three times by selecting different PDF types: CTEQ 6.6, MSTW 2008 and NNPDF. An error band for each type is given by using the symmetric Hessian method for CTEQ 6.6, the asymmetric Hessian method for MSTW 2008 and the standard deviation for NNPDF, as discussed in Section 2.2.2. Input processes are split into four main categories: signal (Wt), background normalised on data (W/Z+jets), top background (single top s- and t-channel, $t\bar{t}$) and dibosons. As an example, we show results for events which contain three jets and an electron (EM3J channel) in Fig. 7.4. Reweighed events are plotted for each error set shift and the resulting error band for each type of PDF is also displayed.

We use the most conservative approach to give an overall uncertainty by selecting the envelope, i.e. the largest deviation from the central value, as the systematic uncertainty. Since the resulting errors are small, this is totally sufficient for the moment. The resulting uncertainty on the selection efficiencies for each process is given in Tab. 7.8.

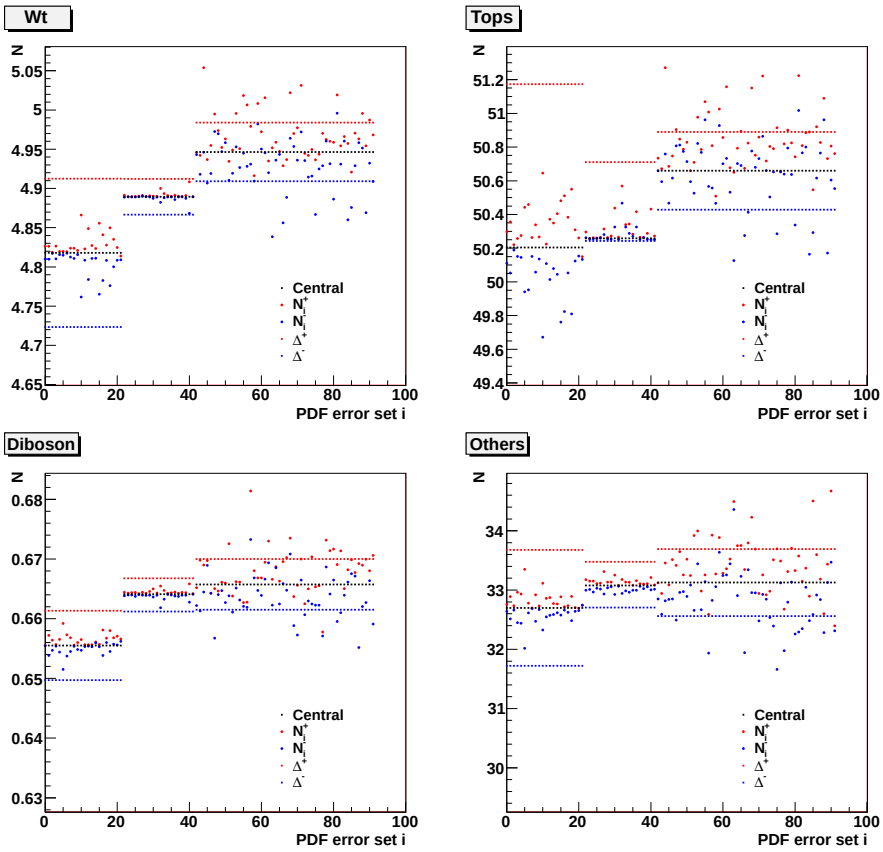

Figure 7.4: Examples of variations in the expected numbers of events for the EM3J channel, as a function of the error set PDF. The CTEQ 6.6 sets are shown for $i = 0$ to 21, MSTW2008 for $i = 22$ to 42 and NNPDF for $i = 43$ to 93.

Table 7.8: Selection efficiency uncertainties due to PDF variation in the Wt analysis.

	Electron			Muon		
	Two jets	Three jets	Four jets	Two jets	Three jets	Four jets
Wt						
$\Delta^+\epsilon/\epsilon$	3%	4%	3%	2%	2%	2%
$\Delta^-\epsilon/\epsilon$	-2%	-2%	-1%	-2%	-2%	-1%
$t\bar{t}$, s-, t-channel						
$\Delta^+\epsilon/\epsilon$	1%	1%	2%	1%	1%	1%
$\Delta^-\epsilon/\epsilon$	-1%	-2%	-2%	-1%	-2%	-2%
W, Z+jets						
$\Delta^+\epsilon/\epsilon$	3%	3%	4%	2%	1%	4%
$\Delta^-\epsilon/\epsilon$	-2%	-3%	-4%	-2%	-3%	-4%
Dibosons						
$\Delta^+\epsilon/\epsilon$	1%	1%	3%	2%	2%	2%
$\Delta^-\epsilon/\epsilon$	-1%	-1%	-1%	-1%	-1%	-1%

7.3.2 Other sources of systematic uncertainties

Since the analysis relies partly on Monte Carlo generated events, systematics related to the theoretical calculation and modelling have to be considered in addition to the PDF systematic uncertainty.

- **MC Generator and Parton shower modelling**
  A brief summary of the MC samples used to derive the systematic uncertainties due to the MC generator and the Parton shower model can be found in Tab. 7.9. They are listed with their corresponding cross section and the number of generated events N_{MC}. To assess the impact of Monte Carlo event generator modelling, $t\bar{t}$ event samples have been generated using MC@NLO as well as Powheg, associated with Herwig. This systematic uncertainty, given by the relative difference of events obtained with the two generators, is about 5 %. The same value is then taken over for the other single top samples. The parton shower effect can be studies by comparing Powheg samples showered with Herwig to those showered with Pythia. The effect is of the order of 2 % and is equally assigned to the other single top samples. Finally, the impact of initial state radiation (ISR) and final state radiation (FSR) can be studied with the dedicated ACERMC with Pythia samples, where various ISR/FSR tunes have been used. Variations are observed to be of the order of 2 %. These results are again taken over for all other MC generated processes.

Table 7.9: Top quark event Monte Carlo samples used for the determination of systematic uncertainties due to event generator and parton shower effects. The cross-section column includes K-factors and branching ratios.

	σ [pb]	Generator	N_{MC}
$t\bar{t}$ no fully hadronic	89.4	POWHEG+Herwig	200,000
$t\bar{t}$ no fully hadronic	89.4	POWHEG+Pythia	200,000
$t\bar{t}$ no fully hadronic ISR up	89.029	ACERMC+Pythia	200,000
$t\bar{t}$ no fully hadronic ISR down	89.029	ACERMC+Pythia	200,000
$t\bar{t}$ no fully hadronic FSR up	89.029	ACERMC+Pythia	200,000
$t\bar{t}$ no fully hadronic FSR down	89.029	ACERMC+Pythia	200,000

- **Theoretical cross section normalisation**
  Since the event yields from the $t\bar{t}$, Z+jets and diboson background processes are estimated using the acceptance from MC, we have to consider the uncertainty due to the theoretically predicted cross-sections. The cross section uncertainty on the $t\bar{t}$ cross section is (164.57-15.7+11.4) pb. An uncertainty of 5% is applied to the diboson background, and an uncertainty of 100% to the Z+jets background in all jet multiplicity bins.

- **MC statistics**
  The uncertainty due to the limited size of the Monte Carlo samples is taken into account by assuming a Poisson distribution.

There are also uncertainties coming from object modelling and reconstruction, as well as from the background estimation.

- **Lepton energy scale/resolution**
  The correspondence between the readout of the energy deposit from the EM calorimeter and the real energy of the lepton is subject to calibration and implies an uncertainty on the lepton energy scale. This uncertainty is evaluated by scaling the p_T of the lepton up or down by 1σ and re-applying the event selection. Following the prescriptions of the performance and the top group, the uncertainty due to the lepton energy resolution is evaluated by smearing the lepton energy in data. This has an effect of less than 1% on the signal and backgrounds.

- **Lepton ID and trigger efficiency scale factors**
  A scale factor is applied to the MC lepton trigger/ID efficiencies in order to reproduce the efficiencies seen in data and these scale factors have associated uncertainties. They are evaluated by recomputing the predicted MC event yields and signal acceptance using shifted scale factors. The resulting scale factor uncertainties are around 4%.

- **Jet energy scale**
  The jet energy scale is marred by an uncertainty of 3-5%, depending on the p_T and η of the reconstructed jet. The `JESUncertaintyProvider` tool can be used to scale the energy of each jet up or down by 1σ. This change is then propagated to the missing transverse energy calculation and the event selection is reapplied to assess the effect. The resulting alteration in event yield is between 10% and 30% for the signal and background samples.

- **B-tag heavy flavour and light flavour scale factor uncertainty**
  The uncertainty on the b-tagging data/MC scale factor is evaluated separately for heavy flavour (b, c quarks) and light flavour quark jets in the MC. The flavour-specific SF per jet are used to give a global SF per event. Since error contributions may come from tagging as well as mistagging, the two effects are varied separately and their effect combined quadratically.

- **QCD background normalisation**
  As described in Section 7.1.2.1, the QCD background is normalised to data through the fitting method in the electron channel and through the matrix method in the muon channel. The evaluation of the systematic uncertainty is based on the comparison with alternative QCD estimates and adds up to 100% in the electron channel and 50% in the muon channel.

- **W+jets background normalisation and flavour composition**
  The different W+jets flavour components are normalised to data samples which

are either orthogonal to the signal sample or a super-set of the signal sample with negligible signal. An uncertainty is due to limited data statistics in those normalisation samples. Also, the change in scale factors due to various systematic uncertainties is taken into account and propagated to the final analysis. The W+jets background normalisation uncertainty is the quadratic sum of the statistical and systematic uncertainties. The W+jets flavour uncertainties are treated as fully correlated between Wbb and Wcc and uncorrelated with Wcj and with Wjj.

- **W+jets shape uncertainty** The shape uncertainty of the W+jets background is obtained by varying several parameters in the generation of the W+jets samples. W+jet MC events are reweighed according to each of these parameters and the largest variation is taken as a systematic uncertainty. This amounts to 4%.

Additional sources of systematic uncertainties are

- **Pile-up**
  The pile-up uncertainty is evaluated by reweighing the MC primary vertex number distribution. The impact of the pile-up reweighing on the signal acceptance with respect to the nominal approach (no pile-up) is 2 % or less. Therefore, a 2% deviation is assigned to all MC signal and background sources.

- **Luminosity**
  The uncertainty on the integrated luminosity measurement is 3.4%. This value is applied to the MC-driven background estimates as well as the final cross-section measurement.

The exact values for all those systematic uncertainties in the different analysis channel are listed in appendix F.

7.4 Statistical analysis

In this section we concentrate on the statistical data analysis technique used to set a limit on the Wt cross section [161]. We must interpret the observed number of events by giving it a statistical significance. Usually this is done via a p-value. This is the probability, under assumption H, of finding data of equal or greater incompatibility with the predictions of hypothesis H. The hypothesis can be regarded as excluded if its p-value is below a certain threshold. In our analysis, as it is very common, we chose this threshold to be $p = 0.05$, thus giving a 95 % confidence level upper limit on the production cross section.

7.4.1 Semileptonic channels

One can establish limits on a new physics processes via a significance test using a profile likelihood ratio as test statistic. This is well-adapted to our purpose, since this

method takes into account the systematic uncertainties in form of nuisance parameters.

The measurement of the Wt channel cross-section is treated as a counting experiment modelled by the likelihood function

$$\mathcal{L}(\sigma_{sig}, \alpha_j) = \prod_{i \in \{\text{channel}\}} Pois\left(N_i^{obs} \mid N_{i,tot}^{exp}(\vec{\alpha})\right) \times \prod_{j \in \text{syst}} G(\alpha_j), \tag{7.7}$$

which is a product of i different analysis channels. For now, these are the electron an muon channels for the three jet multiplicities. Later on the product will also include the dilepton channels to give a combined result. For each channel, the likelihood includes a Poisson distribution $Pois$ in the observed number of events N^{obs}, the data, with expectation value $N_{i,tot}^{exp}$:

$$Pois\left(N_i^{obs} \mid N_{i,tot}^{exp}(\vec{\alpha})\right) = \frac{(N_i^{exp})^{N_i^{obs}} \exp(-N_i^{exp})}{N_i^{obs}}. \tag{7.8}$$

This is the sum of the expected contributions from signal and all MC- or data-driven backgrounds. Systematic uncertainties are grouped in uncorrelated sets and their effect is parametrised using a set of nuisance parameters α_j, which are supposed to have a Gaussian distribution centred at $\alpha_{0,j}$ and with standard deviation δ:

$$G(\alpha_j) = \frac{1}{\sqrt{2\pi}\delta} \exp(-\frac{(\alpha_j - \alpha_{0,j})^2}{2\delta^2}). \tag{7.9}$$

The great advantage of this method is that the correlation of each systematic between different sources and different analysis channels can be taken into account properly. To estimate the effect of these uncertainties, one computes, for each fluctuation of the nuisance parameters, the cross section which maximises the likelihood function.

The **profile likelihood ratio** λ is given by

$$\lambda(\sigma_{Wt}) = \mathcal{L}(\sigma_{Wt}, \hat{\hat{\alpha}}_j)/\mathcal{L}(\hat{\sigma_{sig}}, \hat{\alpha}_j), \tag{7.10}$$

where the double circumflex in the numerator refers to the values of the parameters which maximise the likelihood function $\mathcal{L}$ for a given value of the signal cross section σ_{Wt}. It is therefore called the conditional maximum-likelihood. On the denominator we find the maximal (unconditional) likelihood function, and parameters with a single circumflex are the maximum-likelihood estimators. The measured cross-section is then simply obtained by the maximum likelihood estimate. The presence of the nuisance parameters broadens the profile likelihood, reflecting the loss of information due to the statistical and systematic uncertainties.

From equation 7.10 we see that the limits of the profile likelihood are $0 \leq \lambda \leq 1$, and so a λ near unity implies good agreement between the data and the assumed SM cross section σ_{sig}. A useful test statistic is

$$t = -2 \ln \lambda(\sigma_{Wt}) \tag{7.11}$$

which, in the asymptotical limit, i.e. for large data samples, approaches a χ^2-distribution with one degree of freedom [162]. Since a p-value of 0.05 translates into 3.82 for the χ^2-distribution, the 95 % confidence level Wt cross section σ_{95} is given by

$$-\ln \lambda(\sigma_{95}) = 1.92. \tag{7.12}$$

The expected and observed profile likelihood distribution for the Wt analysis are shown in figure 7.5. The log-likelihood, displayed in red, takes into account only statistical fluctuations. As was just explained, the profile log-likelihood, displayed in blue, also incorporates systematic uncertainties. The expected curves are constructed by assuming that the measured number of events, i.e. cross section, is the SM value σ_{SM}. This is exactly the type of distribution people have been doing exclusively before there was any data. But fortunately, we can now move one step further and give the observed limit, because we have one realisation, namely the measured value N_{data} in the 2010 data. The intersection of the observed profile-log likelihood function with the line at 1.92 gives the desired cross section limit σ_{95}.

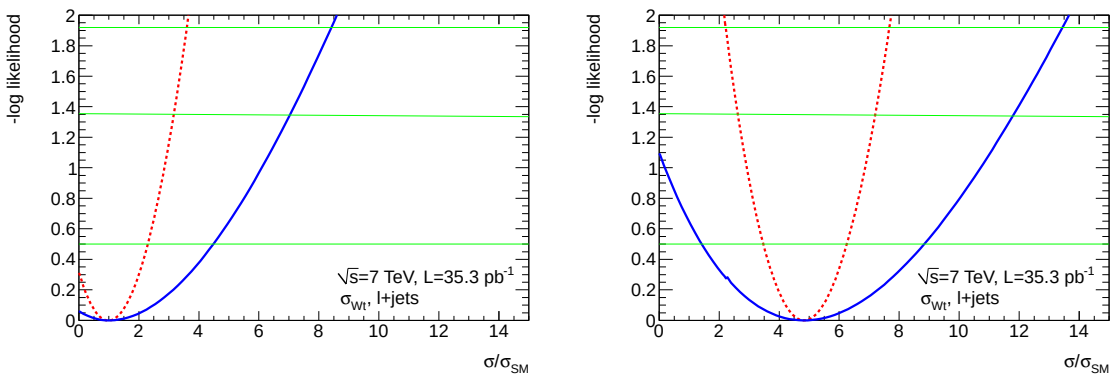

Figure 7.5: Log-likelihood ratio (dashed red) and profile log-likelihood ratio (plain blue) for the expected (left) and observed (right) limit in the Wt analysis as a function of the ratio $\sigma_{Wt}/\sigma_{Wt}^{SM}$. The green lines indicate the 68%, 90% and 95% confidence levels.

With the standard model cross-section of 14.58 pb, the 95% confidence level expected limit on the Wt cross section is $\sigma_{Wt} < 122.8$ pb. The fit for the observed value gives a cross section limit of σ_{Wt}<196.0 pb. The minimum of the observed likelihood is at almost five times the SM cross section value, which may seem quite high at a first glance. But considering the large uncertainty from statistical and systematic effects, this comes as no surprise. improving these uncertainties thus has to be one of the main objectives for future analyses.

These results have been cross-checked using a Bayesian method with full integration over the nuisance parameters, yielding extremely similar results, shown in Fig. 7.6.

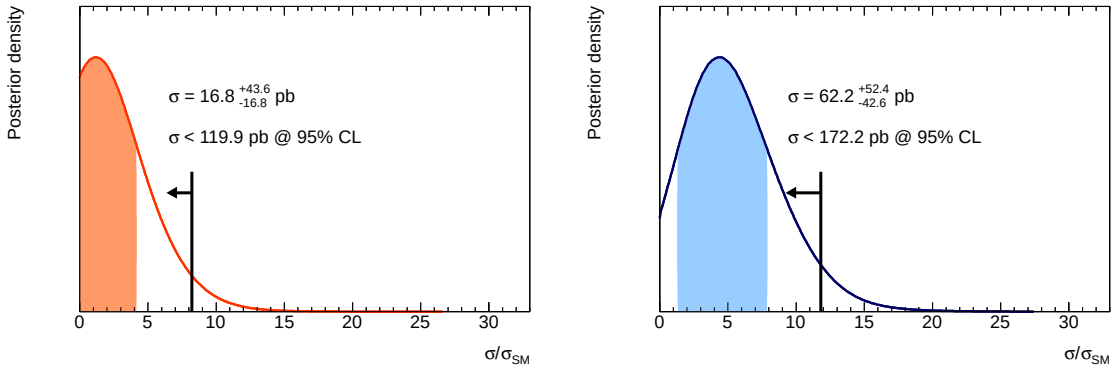

Figure 7.6: Bayes posterior density for the expected (left) and observed (right) in the Wt analysis. The coloured region corresponds to the 68% HPD interval, and the black line to the 95% CL limit.

7.4.2 Combination with the dileptonic channels

Wt production can best be seen at the LHC in the dileptonic channel, where both W bosons decay into either electrons or muons, giving three different analysis channels ee, $e\mu$ and $\mu\mu$. The analysis of the 2010 data is detailed in [163] and yields an upper bound on the Wt cross section of $\sigma_{Wt} < 110$ pb for the observed and $\sigma_{Wt} < 112$ pb for the expected value. The combination with the semileptonic channel has been done using the profile likelihood method by summing over all channels. The resulting 95 % confidence limit on the cross section is $\sigma_{Wt} < 158$ pb for the observed value and $\sigma_{Wt} < 94$ pb for the expected value. This is an amelioration of the semileptonic result, worsens however the observed value in the dilepton channel. But it ameliorates the expected value for both cases, giving hope that in the future combination will yield the most stringent limit.

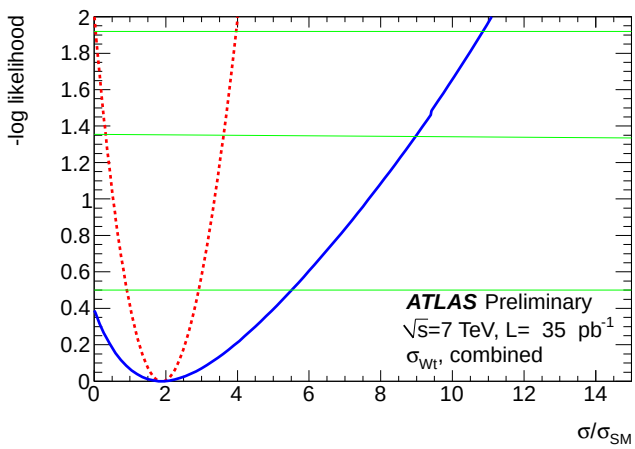

Figure 7.7: Observed likelihood ratio (red dashed) and profile likelihood ratio (blue solid) curves for the combined Wt-channel analysis. The horizontal green lines represent, from the top, the 95%, 90%, and 68% confidence intervals on the extracted cross-section.

7.5 Conclusion

The final result of this analysis has been approved by the ATLAS collaboration [164]. As was discussed in the previous section, a lot of effort will have to be put into reducing the uncertainties in the Wt analysis. In 2011, the LHC has already made a tremendous start, enabling ATLAS to collect almost 600 pb^{-1} in the first six months of operation, as shown on Fig. 7.8. Running with 1092 bunches per beam at the end of May, the machine already provides a third of its design luminosity. An exciting times lies ahead, with evidence and discovery of the electroweak single top production just within reach. At that point, a consistent $H^{\pm}t$ analysis will surely be in the starting blocks.

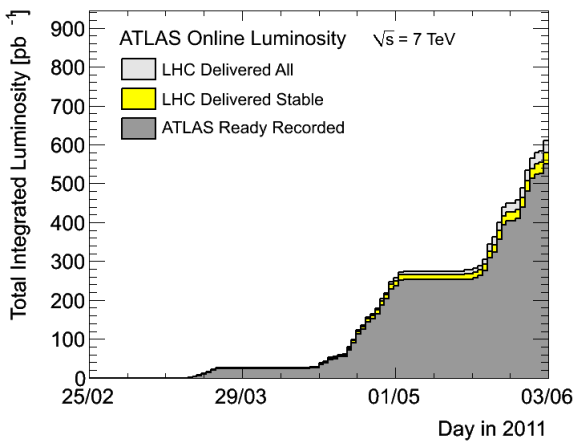

Figure 7.8: Integrated luminosity delivered by the LHC and recorded by the ATLAS detector in the first half of 2011.

Die Arbeit ist getan, das Buch ist fertig. Ob mir gelungen ist, was ich vorhatte, weiss ich nicht. Keiner, der eben das Wort Ende geschrieben hat, kann wissen, ob sein Plan gelang. Er steht noch zu dicht an dem Hause, das er erbaut hat. Ihm fehlt der Abstand. Und ob sich's in seinem Wortgebäude gut wird wohnen lassen, weiss er schon gar nicht.

Erich Kästner, *"Als ich ein kleiner Junge war"*

Conclusion

The Standard Model of particle physics encodes our current knowledge of the intimate structure of matter. The particle content has been established during the last century and all particles have been observed, but one. The Higgs boson is the last cornerstone of the Standard Model and, although precision measurements point to a relatively light mass, it continues to elude searches at colliders. Speculations have been ongoing as to the exact structure of the Standard Model scalar sector. In this context, the two Higgs doublet model provides a simple extension and gives rise to five physical Higgs bosons, out of which two are charged. Investigating the existence of these particles requires precise predictions as to the number of bosons being produced in hadron collisions, and kinematic distributions of simulated events from Monte Carlo event generators are to be studied.

In this thesis, I provide a detailed guide through the next-to-leading order (NLO) cross section calculation of charged Higgs boson production in association with a top quark. Although considered basic knowledge from specialists, the many aspects involved in the calculation are less known outside this restricted community. I therefore tried to insist on comments and examples concerning important concepts, as the renormalisation and factorisation scales, the matrix element calculations and parton showers, to name only a few. The NLO calculation of $H^{\pm}t$ has been performed using a method which permits the implementation of the process in Monte Carlo event generators. My independent NLO code provided useful checks on the process included in the MC@NLO generator and a dedicated paper has been published on this topic. I then turned to the actual implementation within the POWHEG event generator and this publication is in preparation. The availability of the NLO $H^{\pm}t$ process in two distinct generators is of great importance to the experimental community, since now a generator-related systematic uncertainty can be evaluated. The POWHEG implementation will also be useful for analyses at the Tevatron and the LHC, since positively weighted events can be used in multivariate techniques. I conclude this section with several studies of systematic uncertainties related to the theoretical prediction.

Then, I take off my theorist's hat an put a helmet on, since we will be following the protons from the duoplasmatron all the way through the Large Hadron Collider and the ATLAS detector, to the final histogram of an analysis plot. The LHC incident in 2008 resulted in a long shutdown, delaying the start of the machine and lowering the available energy from 14 to 7 TeV. This means that ultimately there was not enough

data to perform a charged Higgs boson analysis, which had been the original plan of this thesis. We therefore switched to background characterisation for $H^{\pm}t$ production by studying Wt-like events, which have a structure very similar to $H^{\pm}t$. In particular, the same methods are applied to separate the process from $t\bar{t}$ in the NLO generation step. We have been very fortunate to witness the start of the LHC, and thus this is one of the first thesis to contain a physics analysis on real collision data, after a long period of purely Monte Carlo events in Europe. It has been an extremely enriching experience to live the excitation of new achievements and Standard Model rediscovery practically on an every day basis. Since the Wt process has such a low production cross section at the Tevatron that it hasn't been observed yet, we were able to put a very first limit on its cross section, by using the amount of data collected with the ATLAS detector in 2010. With $\sigma < 158$ pb in the combined semileptonic and dileptonic analysis, this value is roughly ten times the one expected in the Standard Model. This result will surely quickly be improved with the 2011 LHC physics runs, due to the reduction of statistical uncertainties and systematic uncertainties. Especially in the dileptonic channel, observation of Wt will be within reach, reopening the way to $H^{\pm}t$ searches. Our Wt analysis has been approved by the ATLAS Collaboration. During the analysis phase, I also performed a regular service task, composed of two contributions. The first consisted in comparing the full simulation of events in the ATLAS framework to a CPU-optimised, faster version. The second constituent of the service task were run control shifts in the ATLAS control room. These tasks enabled me to gain improved knowledge on the simulation of events and the data taking process. This work has earned me the title of qualified author of ATLAS publications.

It has been interesting to experience the difference of operation in the two communities. On the one hand, the theorist, alone in his office, with pen and paper, books and Mathematica. On the other hand, the experimentalist, a tiny link in the long chain of the analysis, working as part of a physics group, depending on computing power to handle the enormous amount of data. Hence the change in pronoun in the previous paragraph... I hope I didn't loose too many people in this document, on my way from theory to experiment. And for those who stayed with me until the very end, I hope I could share how much of an amazing journey it has been.

A

Borel summation

The borel transform is a summation method for divergent series. It may be used to investigate the behaviour of perturbative expansions, as for example in mass definition issues tainted by renormalon contributions. If

$$y(z) = \sum_{k=0}^{\infty} y_k z^k \tag{A.1}$$

is a power series in z, then the Borel transform $\mathcal{B}[y]$ is given by

$$\mathcal{B}[y](t) = \sum_{k=0}^{\infty} \frac{y_k}{k!} t^k. \tag{A.2}$$

If the Borel transform converges to an analytic function near the origin which can be analytically continued along the real axis, then the Borel sum $\tilde{y}$ is given by

$$\tilde{y}(z) = \int_0^{\infty} \exp(-t)\mathcal{B}(tz)dt. \tag{A.3}$$

The following example shows how the Borel transform may be used to sum divergent asympotic expansions. Consider the series

$$y(z) = \sum_{k=0}^{\infty} (-1)^k k! z^k. \tag{A.4}$$

This series does not converge for $z \neq 0$. The Borel transform of the series is given by

$$\mathcal{B}[y](t) = \sum_{k=0}^{\infty} (-1)^k t^k = \frac{1}{1+t} \tag{A.5}$$

for $|t| < 1$. Now the Borel transform can even be analytically continuated to $t \geq 0$. Finally, the Borel sum is given by

$$\tilde{y}(z) = \int_0^\infty \frac{\exp(-t)}{1+zt} dt = \frac{\exp(1/z)}{z} \Gamma\Big(0, \frac{1}{z}\Big), \tag{A.6}$$

where Γ here is the incomplete Gamma function. We see that the integral is convergent for all $z \geq 0$ so the original divergent series is Borel summable for all $z \geq 0$. The function has an asymptotic expansion as $z \to 0$ which is given by the original divergent series.

B

Formulas for the Catani Seymour Dipole Subtraction

In this appendix we give additional details to the dipole calculation for the tH^- NLO cross section using the Catani Seymour formalism, as presented in Section 3.4.

B.1 Splitting functions for the real dipole contributions

The spin-averaged splitting functions, for initial state emitters with initial state spectators, are given by

- for process (a)
  - for gluon radiation of the quark ($a = q_b(p_2), b = g(p_1)$ and $i = g(k_3)$):

$$\langle s \mid \mathbf{V}^{qg,g} \mid s' \rangle = 8\pi\mu^{2\epsilon}\alpha_s C_F \Big[\frac{2}{1-x_{i,ab}} - (1+x_{i,ab})\Big]\delta_{ss'}, \tag{B.1}$$

  - for gluon radiation of the gluon ($a = g(p_1), b = q_b(p_2)$ and $i = g(k_3)$):

$$\begin{aligned}\langle \mu \mid \mathbf{V}^{gg,q} \mid \nu \rangle = 16\pi\mu^{2\epsilon}\alpha_s N_C \Big\{ -g^{\mu\nu}\Big[\frac{x_{i,ab}}{1-x_{i,ab}} + x_{i,ab}(1-x_{i,ab})\Big] \\ + \frac{1-x_{i,ab}}{x_{i,ab}} \frac{p_a p_b}{k_i p_a \; k_i p_b}\Big(k_i^\mu - \frac{k_i p_a}{p_b p_a} p_b^\mu\Big)\Big(k_i^\nu - \frac{k_i p_a}{p_b p_a} p_b^\nu\Big)\Big\},\end{aligned} \tag{B.2}$$

- for process (b) gluon radiation off the gluon ($a = g(p_1), b = g(p_2)$ and $i = g(k_3)$ and $a = g(p_2), b = g(p_1)$ and $i = g(k_3)$):

$$\langle s \mid \mathbf{V}^{g\bar{q},g} \mid s' \rangle = 8\pi\mu^{2\epsilon}\alpha_s T_R \Big[1 - 2x_{i,ab}(1 - x_{i,ab})\Big]\delta_{ss'}, \tag{B.3}$$

- and for process (c) ($a = q/\bar{q}(p_1), b = q_b(p_2)$ and $i = q/\bar{q}(k_3)$):

$$\langle \mu \mid \mathbf{V}^{qq,q} \mid \nu \rangle = 8\pi\mu^{2\epsilon}\alpha_s C_F \Big\{ -g^{\mu\nu} x_{i,ab} + 2\frac{1 - x_{i,ab}}{x_{i,ab}} \frac{p_a p_b}{k_i p_a \; k_i p_b} \Big(k_i^\mu - \frac{k_i p_a}{p_a p_b} p_b^\mu\Big)\Big(k_i^\nu - \frac{k_i p_a}{p_a p_b} p_b^\nu\Big)\Big\}. \tag{B.4}$$

The splitting functions $\mathbf{V}_t^{ai}$, for initial state emitters and the top as final state spectator, are

- for process (a)

$$\langle s \mid \mathbf{V}_t^{qg} \mid s' \rangle = 8\pi\mu^{2\epsilon}\alpha_s C_F \Big\{ \frac{2}{2 - x_{it,a} - \tilde{z}_t} - 1 - x_{it,a} \Big\}\delta_{ss'} \tag{B.5}$$

and

$$\langle \mu \mid \mathbf{V}_t^{gg} \mid \mu \rangle = \\ 16\pi\mu^{2\epsilon}\alpha_s N_C \Big\{ -g^{\mu\nu}\Big[\frac{1}{2 - x_{it,a} - \tilde{z}_t} - 1 + x_{it,a}(1 - x_{it,a})\Big] + \frac{1 - x_{it,a}}{x_{it,a}} \frac{\tilde{z}_i \tilde{z}_t}{k_i p_t} \Big(\frac{k_i^\mu}{\tilde{z}_i} - \frac{p_t^\mu}{\tilde{z}_t}\Big)\Big(\frac{k_i^\nu}{\tilde{z}_i} - \frac{p_t^\nu}{\tilde{z}_t}\Big)\Big\}, \tag{B.6}$$

- for process (b)

$$\langle \mu \mid \mathbf{V}_t^{g\bar{q}} \mid \nu \rangle = 8\pi\mu^{2\epsilon}\alpha_s T_R \Big[1 - 2x_{it,a}(1 - x_{it,a})\Big], \tag{B.7}$$

- and for process (c)

$$\langle \mu \mid \mathbf{V}_t^{qq} \mid \nu \rangle = 8\pi\mu^{2\epsilon}\alpha_s C_F \Big\{ -g^{\mu\nu} x_{it,a} + 2\frac{1 - x_{it,a}}{x_{it,a}} \frac{\tilde{z}_i \tilde{z}_t}{k_i p_t} \Big(\frac{k_i^\mu}{\tilde{z}_i} - \frac{p_t^\mu}{\tilde{z}_t}\Big)\Big(\frac{k_i^\nu}{\tilde{z}_i} - \frac{p_t^\nu}{\tilde{z}_t}\Big)\Big\}. \tag{B.8}$$

The splitting function $\mathbf{V}_{gt}^a$, for the top as final state emitter and initial state spectators, is given by

$$\langle s \mid \mathbf{V}_{gt}^a \mid s' \rangle = 8\pi\mu^{2\epsilon}\alpha_s C_F \Big\{ \frac{2}{2 - x_{it,a} - \tilde{z}_t} - 1 - \tilde{z}_t - \frac{m_t^2}{k_i p_t} \Big\}\delta_{ss'}. \tag{B.9}$$

B.2 P and K colour charge operators

B.2.1 General expressions

The most general P-term is given by

$$\mathbf{P}^{a,a'}\left(p_1,...,p_m;xp_a,p_b,x,\mu_F^2\right)=\frac{\alpha_s}{2\pi}P^{aa'}\left(x\right)\frac{1}{\mathbf{T}_{a'}^2}\left[\sum_j\mathbf{T}_j\cdot\mathbf{T}_{a'}\ln\frac{\mu_F^2}{2xp_a\cdot p_j}+\mathbf{T}_b\cdot\mathbf{T}_{a'}\ln\frac{\mu_F^2}{2xp_a\cdot p_b}\right], \tag{B.10}$$

in which $P^{aa'}(x)$ are the regularised Altarelli-Parisi probabilities

$$\begin{aligned}
P^{qg}(x) &= C_F\frac{1+(1-x)^2}{x}, && \text{(B.11)}\\
P^{gq}(x) &= T_R\left[x^2+(1-x)^2\right], && \text{(B.12)}\\
P^{qq}(x) &= C_F\left(\frac{1+x^2}{1-x}\right)_+, && \text{(B.13)}\\
P^{gg}(x) &= 2C_A\left[\left(\frac{1}{1-x}\right)_+ +\frac{1-x}{x}-1+x(1-x)\right]\\
&+ \delta(1-x)(\frac{11}{6}C_A-\frac{2}{3}N_fT_R), && \text{(B.14)}
\end{aligned}$$

where q can be replaced by $\bar{q}$ without any further change.

The general expression for the K-term is

$$\mathbf{K}_{m+b}^{a,a'}\left(x;\{k_i,m_i\},p_a,p_b\right)=$$
$$K_m^{a,a'}\left(x;\{k_i,m_i\},p_a\right)-\frac{\alpha_s}{2\pi}\mathbf{T}_b\cdot\mathbf{T}_{a'}\left\{\frac{1}{\mathbf{T}_{a'}^2}P_{reg}^{a,a'}(x)\ln(1-x)+\delta^{a,a'}\left[2\left(\frac{\ln(1-x)}{1-x}\right)_+-\frac{\pi^2}{3}\delta(1-x)\right]\right\}, \tag{B.15}$$

where

$$\begin{aligned}
&K_m^{a,a'}\left(x;\{k_i,m_i\},p_a\right)\\
&\quad=\frac{\alpha_s}{2\pi}\Big\{\bar{K}^{aa'}(x)-K_{FS}^{aa'}-\sum_j\mathbf{T}_j\cdot\mathbf{T}_{a'}\mathcal{K}_j^{a,a'}\left(x;s_{ja},m_j,\{m_F\}\right)\\
&\qquad-\frac{1}{\mathbf{T}_{a'}^2}\sum_j\mathbf{T}_j\cdot\mathbf{T}_{a'}\big[P_{reg}^{aa'}(x)\ln\frac{(1-x)s_{ja}}{(1-x)s_{ja}+m_j^2}\\
&\qquad+\gamma_a\delta^{aa'}\delta(1-x)\big(\ln\frac{s_{ja}-2m_j\sqrt{s_{ja}+m_j^2}+2m_j^2}{s_{ja}}+\frac{2m_j}{\sqrt{s_{ja}+m_j^2}+m_j}\big)\big]\Big\}. \qquad \text{(B.16)}
\end{aligned}$$

The regular parts of the auxilirary functions $P^{ab}_{reg}(x)$ in Eq. (B.15) and Eq. (B.16) are given by

$$P^{qq}_{reg}(x) = -C_F(1+x), \qquad P^{gq}_{reg}(x) = T_R\left[x^2 + (1-x)^2\right], \tag{B.17}$$

$$P^{qg}_{reg}(x) = C_F\frac{1+(1-x)^2}{x} \text{ and } \qquad P^{gg}_{reg}(x) = 2C_A\left[\frac{1-x}{x} - 1 + x(1-x)\right]. \tag{B.18}$$

The term $\bar{K}^{aa'}(x)$ in Eq. (B.16) is given by

$$\begin{aligned}\bar{K}^{aa'}(x) = P^{aa'}_{reg}(x)\ln\frac{1-x}{x} + \hat{P}^{aa'}(x)\\ + \delta^{aa'}\left[\mathbf{T}^2_a\left(\frac{2}{1-x}\ln\frac{1-x}{x}\right)_+ - \delta(1-x)\left(\gamma_a + K_a - \frac{5}{6}\pi^2\mathbf{T}^2_a\right)\right],\end{aligned} \tag{B.19}$$

where

$$\hat{P}^{qq}(x) = \hat{P}^{qg}(1-x) = C_F(1-x), \tag{B.20}$$

$$\hat{P}^{gq}(x) = 2T_R x(1-x) \text{ and} \tag{B.21}$$

$$\hat{P}^{gg}(x) = 0, \tag{B.22}$$

and

$$K_q = \left(\frac{7}{2} - \frac{\pi^2}{6}\right)C_F,\ K_g = \left(\frac{67}{18} - \frac{\pi^2}{6}\right)C_A - \frac{10}{9}T_R N_f \tag{B.23}$$

$$\gamma_q = \frac{3}{2}C_F,\ \gamma_g = \frac{11}{6}N_C - \frac{2}{3}T_R N_f. \tag{B.24}$$

Since we have only a quark in the Born final state, we list the relevant $\mathcal{K}$ terms in Eq. (B.16):

$$\mathcal{K}^{gq}_q(x; s_{ja}, m_j) = 0, \tag{B.25}$$

$$\begin{aligned}\mathcal{K}^{qq}_q(x; s_{ja}, m_j) = 2\left[\left(\frac{\ln(1-x)}{1-x}\right)_+ - \frac{\ln(2-x)}{1-x}\right] + \left[J^a_{gQ}\left(x, \frac{m_j}{\sqrt{s_{ja}}}\right)\right]_+\\ + 2\left(\frac{1}{1-x}\right)_+ \ln\frac{(2-x)s_{ja}}{(2-x)s_{ja} + m_j^2} + \delta(1-x)\left[\left(\frac{m_j^2}{s_{ja}} + \frac{1}{2}\right)\ln\frac{m_j^2}{s_{ja}+m_j^2} - \frac{\gamma_q}{C_F}\right],\end{aligned} \tag{B.26}$$

where $\left[J^a_{gQ}(x,\mu_Q)\right]_+$ stands for

$$\begin{aligned}\left[J^a_{gQ}(x,\mu_Q)\right]_+ = \left(\frac{1-x}{2(1-x+\mu_Q^2)^2} - \frac{2}{1-x}\left[1 + \ln(1-x+\mu_Q^2)\right]\right)_+\\ + \left(\frac{2}{1-x}\right)_+ \ln(2+\mu_Q^2 - x)\end{aligned} \tag{B.27}$$

with $\mu_Q = \frac{m_j}{\sqrt{s_{ja}}}$,

$$\mathcal{K}_q^{q,g}\left(x; s_{ja}, m_j\right) = 2\frac{C_F}{N_C}\frac{m_j^2}{x s_{ja}} \ln \frac{m_j^2}{(1-x)s_{ja} + m_j^2} \text{ and} \tag{B.28}$$

$$\mathcal{K}_q^{g,g}\left(x; s_{ja}, m_j\right) = \mathcal{K}_q^{q,q} + \frac{N_C}{C_F}\mathcal{K}_q^{q,g}. \tag{B.29}$$

B.2.2 tH^- specific expressions

Process (a) Concerning process (a), two possible configurations contribute: gluon radiation off the gluon: $a = g, a' = g$ and gluon radiation off the b quark: $a = q_b, a' = q_b$.

Thus the P-term is given by

$$\mathbf{P}_{2+q_b}^{gg} = \frac{\alpha_s}{2\pi} P^{gg}(x) \frac{1}{\mathbf{T}_{g'}^2} \left[\mathbf{T}_{g'} \cdot \mathbf{T}_{q_t} \ln \frac{\mu_F^2}{x(m_t^2 - t)} + \mathbf{T}_{g'} \cdot \mathbf{T}_{q_b} \ln \frac{\mu_F^2}{xs}\right] \tag{B.30}$$

and the K- term reads

$$\mathbf{K}_{2+q_b}^{gg} = \frac{\alpha_s}{2\pi}\left[\delta(1-x)\Delta\mathbf{K}^{gg} + \mathbf{K}_+^{gg} + \mathbf{K}^{gg}\right], \tag{B.31}$$

where

$$\begin{aligned}\Delta\mathbf{K}^{gg} = \frac{N_C}{2}\Big(-\frac{\pi^2}{3}\Big) - \Big[NC\Big(\frac{11}{6} + \frac{67}{18} - \pi^2\Big) - T_R N_f\Big(\frac{2}{3} + \frac{10}{9}\Big)\Big] \\ + \frac{N_C}{2}\Big[-\frac{3}{2} + \Big(\frac{1}{2} + \frac{m_t^2}{m_t^2 - t}\Big)\ln\frac{m_t^2}{2m_t^2 - t}\Big] \\ + \frac{1}{2}\Big(\frac{11}{6}N_C - \frac{2}{3}T_R N_f\Big)\Big(\ln\frac{m_t^2 - t - 2m_t\sqrt{2m_t^2 - t} + 2m_t^2}{m_t^2 - t} + \frac{2m_t}{\sqrt{2m_t^2 - t} + m_t}\Big),\end{aligned} \tag{B.32}$$

$$\begin{aligned}\mathbf{K}_+^{gg} = 2N_C\Big[\frac{\ln(1-x)}{1-x} + \frac{1}{1-x}\ln\frac{1-x}{x}\Big]_+ \\ + N_C\Big[\frac{1}{1-x}\Big]_+ \ln\frac{(2-x)(m_t^2 - t)}{(2-x)(m_t^2 - t) + m_t^2} \\ + \frac{N_C}{2}\Big[\Big(\frac{1-x}{2(1-x+\mu_Q^2)^2} - \frac{2}{1-x}\left[1 + \ln(1-x+\mu_Q^2)\right]\Big)_+ + \Big(\frac{2}{1-x}\Big)_+ \ln(2+\mu_Q^2 - x)\Big],\end{aligned} \tag{B.33}$$

with $\mu_Q = \frac{m_t}{\sqrt{m_t^2 - t}}$, and

$$\mathbf{K}^{gg} = 2N_C\Big[\frac{1-x}{x} - 1 + x(1-x)\Big]\Big[\frac{1}{2}\ln(1-x) + \frac{1}{2}\ln\frac{(1-x)(m_t^2-t)}{(1-x)(m_t^2-t)+m_t^2} + \ln\frac{1-x}{x}\Big]$$
$$+ N_C\Big[-\frac{\ln(2-x)}{1-x} + \frac{m_t^2}{x(m_t^2-t)}\ln\frac{m_t^2}{(1-x)(m_t^2-t)+m_t^2}\Big]. \quad \text{(B.34)}$$

For gluon radiation off the b-quark, the P-term reads

$$\mathbf{P}^{q_bq_b}_{2+g(k)} = \frac{\alpha_s}{2\pi}P^{qq}(x)\frac{1}{\mathbf{T}^2_{q_b}}\left[\mathbf{T}_{q_b}\cdot\mathbf{T}_{q_t}\ln\frac{\mu_F^2}{x(m_t^2-u)} + \mathbf{T}_{q_b}\cdot\mathbf{T}_g\ln\frac{\mu_F^2}{xs}\right], \quad \text{(B.35)}$$

while the K-term is given by

$$\mathbf{K}^{q_bq_b}_{2+g} = \frac{\alpha_s}{2\pi}\left[\delta(1-x)\Delta\mathbf{K}^{q_bq_b} + \mathbf{K}^{q_bq_b}_{+} + \mathbf{K}^{q_bq_b}\right], \quad \text{(B.36)}$$

where

$$\Delta\mathbf{K}^{q_bq_b} = \frac{N_C}{2}\Big(-\frac{\pi^2}{3}\Big) - \frac{1}{4}\Big(\ln\frac{m_t^2-u-2m_t\sqrt{2m_t^2-u}+2m_t^2}{m_t^2-u} + \frac{2m_t}{\sqrt{2m_t^2-u}+m_t^2}\Big)$$
$$- C_F(5-\pi^2) - \frac{1}{2N_C}\Big[\Big(\frac{1}{2}+\frac{m_t^2}{m_t^2-u}\Big)\ln\frac{m_t^2}{2m_t^2-u} - \frac{3}{2}\Big], \quad \text{(B.37)}$$

$$\mathbf{K}^{q_bq_b}_{+} = \Big(N_C\frac{\ln(1-x)}{1-x} + C_F\frac{2}{1-x}\ln\frac{1-x}{x}$$
$$- \frac{1}{2N_C}\Big(2\frac{\ln(1-x)}{1-x} + \frac{1-x}{2(1-x+\mu_Q^2)^2} - \frac{2}{1-x}(1+\ln(1-x+\mu_Q^2))\Big)\Big)_+$$
$$- \frac{1}{2N_C}\Big[2\Big(\frac{1}{1-x}\Big)_+\ln\frac{(2-x)(m_t^2-u)}{(2-x)(m_t^2-u)+m_t^2} + 2\Big(\frac{1}{1-x}\Big)_+\ln(2+\mu_Q^2-x)\Big] \quad \text{(B.38)}$$

and

$$\mathbf{K}^{q_bq_b} = -(1+x)\Big(\frac{N_C}{2}\ln(1-x) - \frac{1}{2N_C}\ln\frac{(1-x)(m_t^2-u)}{(1-x)(m_t^2-u)+m_t^2} + C_F\ln\frac{1-x}{x}\Big)$$
$$+ C_F(1-x) + \frac{1}{N_C}\frac{\ln(2-x)}{1-x}. \quad \text{(B.39)}$$

Process (b) For process (b), only one type of radiation is involved: gluon splitting into q_b and $\bar{q}_b$, so that this time $a = g, a' = q_b$ The P-term reads

$$P^{g,q_b}_{2+g(k)} = \frac{\alpha_s}{2\pi}P^{gq}(x)\frac{1}{\mathbf{T}^2_{q_b}}\left[\mathbf{T}_{q_t}\cdot\mathbf{T}_{q_b}\ln\frac{\mu_F^2}{x(m_t^2-t)} + \mathbf{T}_g\cdot\mathbf{T}_{q_b}\ln\frac{\mu_F^2}{xs}\right] \quad \text{(B.40)}$$

The K-term is given by

$$K_{2+g}^{gq} = \frac{\alpha_s}{2\pi}\Big\{P_{reg}^{gq}(x)\Big[\frac{N_C}{2C_F}\ln(1-x)+\ln\frac{1-x}{x}-\frac{1}{2C_F N_C}\ln\frac{(1-x)(m_t^2-u)}{(1-x)(m_t^2-u)+m_t^2}\Big]+2T_R x(1-x)\Big\} \tag{B.41}$$

Process (c) For process (c), the P- and K-terms are given by

$$P_{2+q}^{q/\bar{q}g} = \frac{\alpha_s}{2\pi}P^{q/\bar{q}g}(x)\frac{(-1)}{2}\Big(\ln\frac{\mu_F^2}{x(m_t^2-t)}+\ln\frac{\mu_F^2}{xs}\Big) \tag{B.42}$$

and

$$K_{2+q}^{q/\bar{q}g} = \frac{\alpha_s}{2\pi}\Big\{P_{reg}^{q/\bar{q}g}(x)\Big[\frac{1}{2}\ln(1-x)+\ln\frac{1-x}{x}+\frac{1}{2}\ln\frac{(1-x)(m_t^2-t)}{(1-x)(m_t^2-t)+m_t^2}\Big] + C_F x + C_F\frac{m_t^2}{x(m_t^2-t)}\ln\frac{m_t^2}{(1-x)(m_t^2-t)+m_t^2}\Big\} \tag{B.43}$$

C

Basic set of divergent scalar integrals

We list a set of useful scalar integrals needed in the tH^- NLO calculation. They are expressed using the Mandelstam variables defined in Section 3.1, and include Gamma functions and dilogarithms, as defined in Section 3.2. The relevant tadpole integral is

$$A_0(m^2) = \Big(\frac{\mu^2}{m^2}\Big)^\epsilon \frac{(4\pi)^\epsilon}{\Gamma(1-\epsilon)} m^2 \Big(\frac{1}{\epsilon} + 1\Big). \tag{C.1}$$

Several B functions are needed, which are

$$B_0(0;0,0) = \Big(\frac{\mu^2}{m^2}\Big)^\epsilon \frac{(4\pi)^\epsilon}{\Gamma(1-\epsilon)} \Big(\frac{1}{\epsilon} - \frac{1}{\epsilon}\Big), \tag{C.2}$$

$$B_0(0;m^2,m^2) = \Big(\frac{\mu^2}{m^2}\Big)^\epsilon \frac{(4\pi)^\epsilon}{\Gamma(1-\epsilon)} \frac{1}{\epsilon}, \tag{C.3}$$

$$B_0(m^2;0,m^2) = \Big(\frac{\mu^2}{m^2}\Big)^\epsilon \frac{(4\pi)^\epsilon}{\Gamma(1-\epsilon)} \Big(\frac{1}{\epsilon} + 2\Big), \tag{C.4}$$

$$B_0(s;0,0) = \Big(\frac{\mu^2}{m^2}\Big)^\epsilon \frac{(4\pi)^\epsilon}{\Gamma(1-\epsilon)} \Big(\frac{1}{\epsilon} + 2 - \log\frac{-s}{m^2}\Big), \tag{C.5}$$

and

$$B_0(s;0,m^2) = \Big(\frac{\mu^2}{m^2}\Big)^\epsilon \frac{(4\pi)^\epsilon}{\Gamma(1-\epsilon)} \Big(\frac{1}{\epsilon} + 2 + \frac{m^2-s}{s}\ln\frac{m^2-s}{m^2}\Big). \tag{C.6}$$

The relevant vertex functions are

$$C_0(0,0,s;0,0,0) = \Big(\frac{\mu^2}{m^2}\Big)^\epsilon \frac{(4\pi)^\epsilon}{\Gamma(1-\epsilon)} \frac{1}{s} \Big(\frac{1}{\epsilon^2} - \frac{1}{\epsilon}\log\frac{-s}{m^2} + \frac{1}{2}\log^2\frac{-s}{m^2}\Big), \tag{C.7}$$

$$C_0(0,p_2^2,p_3^2;0,0,m^2) = \\ \Big(\frac{\mu^2}{m^2}\Big)^\epsilon \frac{(4\pi)^\epsilon}{\Gamma(1-\epsilon)}\frac{1}{p_2^2-p_3^2}\Big(\frac{1}{\epsilon}\log\frac{m^2-p_3^2}{m^2-p_2^2}+Li_2\frac{p_2^2}{m^2}-Li_2\frac{p_3^2}{m^2}+\log^2\frac{m^2-p_2^2}{m^2}-\log^2\frac{m^2-p_3^2}{m^2}\Big), \tag{C.8}$$

and

$$C_0(0,p^2,m^2;0,0,m^2) = \\ \Big(\frac{\mu^2}{m^2}\Big)^\epsilon \frac{(4\pi)^\epsilon}{\Gamma(1-\epsilon)}\frac{1}{p^2-m^2}\Big(\frac{1}{2\epsilon^2}+\frac{1}{\epsilon}\log\frac{m^2}{m^2-p^2}+\frac{\pi^2}{12}-Li_2\frac{-p^2}{m^2-p^2}+\frac{1}{2}\log^2\frac{m^2}{m^2-p^2}\Big). \tag{C.9}$$

The two divergent box contributions are

$$D_0(0,0,m^2,p_4^2,s_{12},s_{23};0,0,0,m^2) = \\ \Big(\frac{\mu^2}{m^2}\Big)^\epsilon \frac{(4\pi)^\epsilon}{\Gamma(1-\epsilon)}\frac{1}{s_{12}(s_{23}-m^2)}\Big[\frac{3}{2}\frac{1}{\epsilon^2}-\frac{1}{\epsilon}\Big(2\log\frac{m^2-s_{23}}{m^2}+\log\frac{-s_{12}}{m^2}-\log\frac{m^2-p_4^2}{m^2}\Big) \\ -2Li_2\frac{s_{23}-p_4^2}{s_{23}-m^2}+2\log\frac{-s_{12}}{m^2}\log\frac{m^2-s_{23}}{m^2}-\log^2\frac{m^2-p_4^2}{m^2}-\frac{5\pi^2}{12}\Big] \tag{C.10}$$

and

$$D_0(0,m^2,0,p_4^2,s_{12},s_{23};0,0,m^2,m^2) = \\ \Big(\frac{\mu^2}{m^2}\Big)^\epsilon \frac{(4\pi)^\epsilon}{\Gamma(1-\epsilon)}\frac{1}{(s_{12}-m^2)(s_{23}-m^2)}\Big[\frac{1}{2\epsilon^2}-\frac{1}{\epsilon}\Big(\log\frac{m^2-s_{12}}{m^2}+\log\frac{m^2-s_{23}}{m^2}-\log\frac{m^2-p_4^2}{m^2}\Big) \\ +2\log\frac{m^2-s_{12}}{m^2}\log\frac{m^2-s_{23}}{m^2}-\log^2\frac{m^2-p_4^2}{m^2}-\frac{\pi^2}{12} \\ -2Li_2\big(1-\frac{m^2-p_4^2}{m^2}\big)-Li_2\big(1-\frac{m^2-p_4^2}{m^2-s_{12}}\big)-Li_2\big(1-\frac{m^2-p_4^2}{m^2-s_{23}}\big)\Big] \tag{C.11}$$

D

Combining W+jets samples by Heavy Flavour Overlap Removal

In this section, we give additional details as to how a global W+jets sample is fashionned out of several individually generated LO Alpgen samples. These samples are classified according to their heavy flavour quark content.

- The W+**light jets** are named $W \to l\nu + Np$. There are individual samples for $N = 0, 1, 2, 3, 4$ or 5 partons. These partons are hard jets (from gluons, u, d, s and c massless quarks) included in the ME. The b-quarks contained in those samples can only come from the PS and thus their p_T distribution peaks at low values (usually they have a $p_T < 15$ GeV). Samples with 0 to 4 partons are exclusive, i.e. contain events were exactly this number of partons has been generated in the ME. The 5 parton sample is inclusive, which means that it contains events with have been generated with 5 partons or more.

- The W+**heavy quarks+jets** are either $W \to l\nu + b\bar{b} + Np$ or $W \to l\nu + c\bar{c} + Np$ samples, where again those with 0 to 2 partons are exclusive, and the 3 parton sample is inclusive. Concerning the $W \to l\nu + c + Np$ samples, the ones with 0 to 3 partons are exclusive, the 4 parton sample is inclusive.

The simulation of the W+jets is far from trivial and its evaluation thus relies as much as possible on data. However, in several steps MC samples are needed and they are constructed as best as one can do at the moment.

The first approach has been to take only into account the W+light jets sample. In order to get a consistent sample, the different event multiplicities have to be added while carefully avoiding over-counting, since for example a process with N final state partons

may arise not only from the $2 \to N$ ME, but also from a $2 \to (N-1)$ ME where one additional jet is produced by the PS. In order to avoid double-counting these events, Alpgen incorporates a matching tool based on the MLM matching prescription [165]. In this algorithm, the final state light flavour parton multiplicity has to match the jet multiplicity after the PS (called exclusive matching), except in the highest multiplicity sample, where unmatched parton shower jets are allowed (called inclusive matching).

The next step consists in producing $Wb\bar{b}+Np$ samples, where this time the b jets have the correct kinematic behaviour since they are coming from the ME. Such an accurate description is mandatory since tagged jets are hard by definition of the tag. Again, the MLM matching procedure can be used to combine the different $Wb\bar{b}+Np$ samples with each other to give one $Wb\bar{b}+j$ sample, but the problem arises in combining it with the W+light jets sample. The overlap between events from the inclusive W+light jets and the $Wb\bar{b}$+ jets sample depends on the generator level cuts, and was evaluated in dedicated studies to be approximately 4 % [166]. The first attempt to reduce this overlap was based on a simple phase space cut between the b quark pair, where the cut values are identical to the MLM matching requirements: a b quark $p_T > 20$ GeV and $\Delta R(b\bar{b}) > 0.7$ allowed to minimise the amount of overlap between the samples. This is usually referred to as the MC08 method.

Since the major culprit of mistagging is the c quark, individual $W+c$+light jets and $Wc\bar{c}$ samples were generated to take into account this background properly. However, in presence of c-quark jets the overlap will be even larger since the $W+Np$ samples contain massless charm quarks already in the ME. To achieve combination of all those samples the Heavy Flavour Overlap Removal (HFOR) Tool has been elaborated. This alternative method is based on the distance separating two heavy flavour jets and it draws advantage of both the ME and PS respective strengths. For the following, keep in mind what we have seen in Chapters 3 and 4: the ME correctly describes events with large opening angles between the quarks, whereas the PS is adequately modelling collinear gluon splittings.
Remains the question if the matching procedure should be done according to the opening angle between the quarks or between the jets. Both approaches have been tested and will be detailed. It turns out that, when using the matching procedure on jets, it happens that some quarks are unmatched to any jet and these events are lost. This does not happen with the method based on quarks and thus this one is chosen for the final analysis.

The Jet-Based Overlap Removal

In this approach, heavy flavour quark pairs from ME generation are required to be matched to different reconstructed jets, whereas heavy flavour quark pairs from PS generation should lie in one reconstructed jet. If this is not the case, the event is thrown away. The actual matching of the different samples is done with a geometric cut ΔR on the distance between the jet axis and the b-quark in the (η, ϕ) plane. The chosen cut

value is the same as the jet cone size $R_0 = 0.4$ of the algorithm that has been used for the jet reconstruction. This leads to a choice of a subsample in each sample according to

- $W + Np$
  The tool removes all events where heavy flavour pairs have been produced with the ME. Now there can only be events where c and b quarks have been produced by the PS. Those are correctly described if they lie within one jet, thus the tool removes events for which this is not the case, i.e. where the heavy quark pairs are matched to two different jets.

- $W + c + Np$
  All events in which the heavy-flavour quark-pairs are not matched to one reconstructed jet are removed.

- $W + cc + Np$
  In this sample, both c quarks were given by the ME. Thus the tool removes all events, in which bb pairs are not matched to one reconstructed jet and all events, in which cc pairs are matched to one reconstructed jet.

- $W + b\bar{b} + Np$
  Events in which bb pairs are matched to one reconstructed jet are removed.

However, this algorithm experiences problems with events where some quarks are not matched to a jet. For example, in the inclusive and the Wbb sample, the fraction of b-quarks that lie within a jet cone of 0.4 is only about 50 %. To take these events into account in a correct fashion, another matching criterium has been chosen and the new algorithm works at quark-level and not at jet-level anymore.

The ΔR-Based Overlap Removal

The ΔR-, or Angular-Based Overlap Removal method performs the matching of the different samples according to the distance in R which separates two heavy flavour quarks. Again, the matching distance has been chosen equal to the jet cone distance $R_0 = 0.4$. This means that events where $\Delta R < R_0$ are taken into account if both heavy quarks have been generated by the parton shower. Events where $\Delta R > R_0$ should have heavy quarks described by the ME. This definition allows for migration of events, because events originally generated in the lighter quark sample can be reclassified in the heavy quark sample. The resulting distributions of the merging procedure for the cc and bb quark pairs are shown in Fig. D.1. These distributions, which are normalised to the standard model predictions, show a smooth transition between the part taken from the PS and the one from the ME.

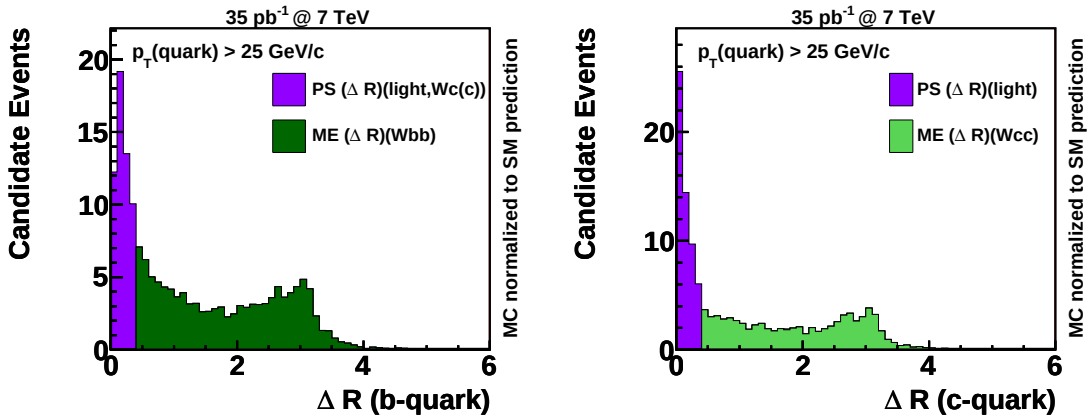

(a) (b)

Figure D.1: The ΔR distributions between $b\bar{b}$ (a) or $c\bar{c}$ (b) quark pairs for the matched sample obtained with the ΔR-based overlap removal method. The distributions are normalised to the number of expected events where the transverse momentum of the heavy quark is $p_{\mathrm{T}} > 25$ GeV.

In Fig. D.2 we show the conceptual difference between the matching procedure based on the MLM algorithm (figure (a)) and the two alternative schemes based on the angular distance between two heavy quarks or jets (figure (b)).

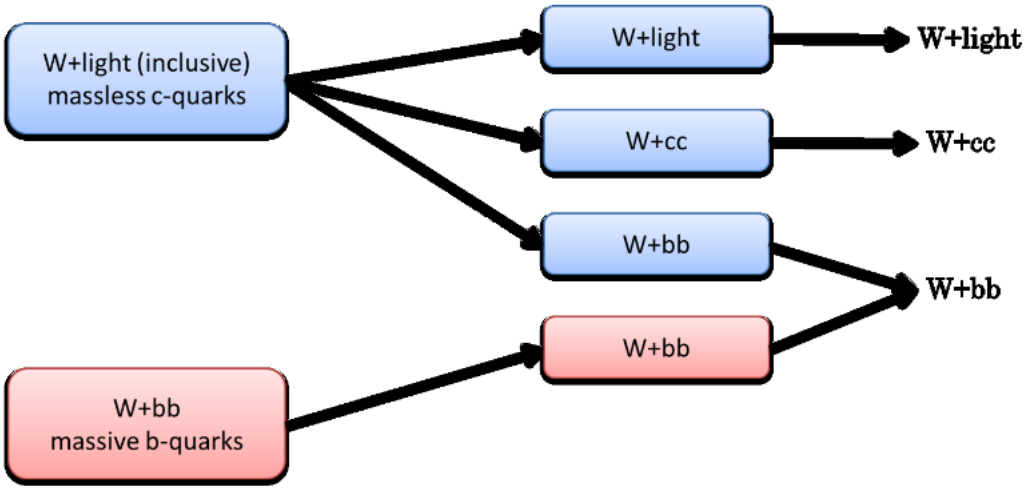

(a)

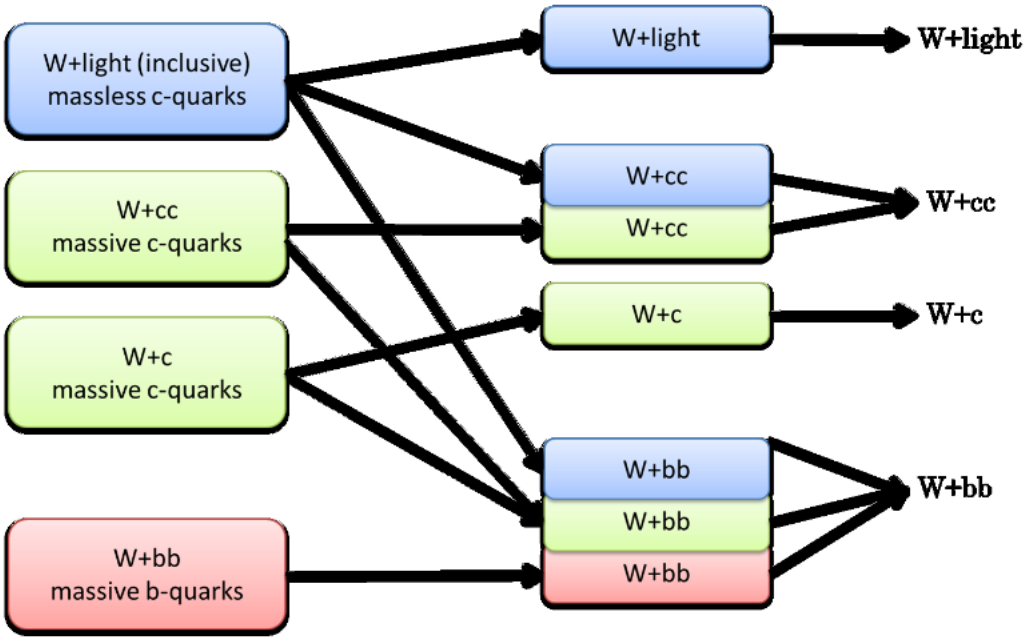

(b)

Figure D.2: Schematic illustration of how the different final W+jet samples (in plain text) are build from the Alpgen samples (boxes on the left) so as to avoid over-counting as much as possible [159]. Figure (a) shows the early attempts to match the W+light jets with the $Wb\bar{b}$+jets samples a simple phase space cut, based on the MLM procedure. In figure (b), the more complicated jet or angular based removal scheme is applied to take into account the c jets contribution. Overlapping boxes indicate that some events may have been removed.

We conclude this section with a general comment on the heavy flavour composition of the MC samples. At a first glance, one may wonder at the absence of a $W + b$+jets sample as an analogue of the $W + c$+jets. Since the production mechanism is different between $W + b$+jets and $W + c$+jets, which can be obtained via $s \to Wc$, it turns out that this process cannot be produced within Alpgen at the moment. While this was not the case for the Tevatron, $W + bj + X$ production is the dominant production process compared to $W + bb + X$ at the LHC [167]. The predicted cross section of $W + bj + X$ is actually twice the cross section of the $W + bb + X$ process. These comments and this whole section show that, in order to understand the W+jets background as best as we can, there is still some work to do and combined input form both the theoretical and experimental community is mandatory.

E

Preselection event yield

In this appendix, we list the event yields after the preselection and background estimations, detailed in Section 7.1.1, for the pretag sample in the electron channel in Tab. E.1 and for the muon channel in Tab. E.3, and for the tag sample in the electron channel in Tab. E.2 and for the muon channel in Tab. E.4.

Table E.1: Event yield for the electron channel after the preselection and background estimations in the pretag sample. All W+jets samples are scaled by the factors determined from data. The QCD fake event estimation is from the fitting method. All the other expectations are derived using theoretical cross sections and their uncertainties are also theoretical.

	Electron pretag sample			
	1-jet	2-jets	3-jets	$\geq$4-jets
Wt	3.9±0.4	11.5±1.2	13.6±1.4	12.0±1.2
s-channel	1.3±0.1	2.5±0.3	1.1±0.1	0.4±0.1
t-channel	19.8±2.0	45.6±4.6	17.3±1.7	6.2±0.6
$t\bar{t}$	9.1±0.7	53.2±4.4	123±10.1	260±21.3
W+jets	10636±1987	2635±708	598±224	183±107
Wc+jets	1746±826	619±278	158±74	50±28
$Wb\bar{b}$+jets	88±78	60±56	24±24	12±14
$Wc\bar{c}$+jets	276±245	156±147	56±56	25±29
Diboson	43.1±2.2	43.7±2.2	14.9±0.7	4.9±0.2
Z+jets	210.1±105.1	187.9±94.0	86.7±43.3	50.4±25.2
Multijets	310±310	260±130	80±80	60±30
TOTAL Exp	13343±2192	4074±793	1173±260	664±123
DATA	13566	4112	1212	667

Table E.2: Event yield for the electron channel after the preselection and background estimations in the tag sample.

	Electron tag sample			
	1-jet	2-jets	3-jets	≥4-jets
Wt	1.1±0.1	4.5±0.5	6.0±0.6	5.6±0.6
s-channel	0.5±0.1	1.2±0.1	0.6±0.1	0.2±0.1
t-channel	5.2±0.5	19.7±2.0	8.0±0.8	2.9±0.3
$t\bar{t}$	3.3±0.3	23.5±1.9	58±4.8	125±10.3
W+jets	32±5.9	19±5	8±3	4±2
Wc+jets	113±54	55±25	17±8	6±3
$Wb\bar{b}$+jets	11±10	15±14	7±7	4±5
$Wc\bar{c}$+jets	7±6	10.4±9.8	5±5	3±4
Diboson	1.2±0.1	2.2±0.1	0.9±0.1	0.4±0.1
Z+jets	0.8±0.4	3.0±1.5	1.9±1.0	2.9±1.5
Multijets	5±5	6±6	5±5	5±5
TOTAL Exp	180±55	159±31	116±14	159±14
DATA	185	163	141	179

Table E.3: Event yield for the muon channel after the preselection and background estimations in the pretag sample. All W+jets samples are scaled by the factors determined from data. The QCD fake event estimation is given by the matrix method. All the other expectations are derived using theoretical cross sections and their uncertainties are also theoretical.

	Muon pretag sample			
	1-jet	2-jets	3-jets	≥4-jets
Wt	4.5±0.5	12.9±1.3	15.3±1.5	12.6±1.3
s-channel	1.8±0.2	3.5±0.3	1.5±0.2	0.6±0.1
t-channel	25.9±2.6	57.3±5.7	21.6±2.2	7.4±0.7
$t\bar{t}$	10.5±0.9	60.8±5.0	142±11.6	302±24.8
W+jets	15403±2878	3795±1020	829±310	260±152
Wc+jets	2413±1142	795±358	203±95	63±35
$Wb\bar{b}$+jets	129±115	81±76	32±32	16±18
$Wc\bar{c}$+jets	401±356	223±210	74±74	31±37
Diboson	57.8±2.9	58.9±2.9	18.5±0.9	5.7±0.3
Z+jets	665.6±332.8	222.9±111.5	71.2±35.6	27.7±13.8
Multijets	580±290	310±160	150±150	70±70
TOTAL Exp	19692±3150	5621±1121	1558±369	795±178
DATA	19508	5591	1521	820

Table E.4: Event yield for the muon channel after the preselection and background estimations in the tag sample.

	Muon tag sample			
	1-jet	2-jets	3-jets	$\geq$4-jets
Wt	1.3±0.1	4.9±0.5	6.7±0.7	5.8±0.6
s-channel	0.7±0.1	1.7±0.2	0.7±0.1	0.3±0.1
t-channel	7±0.7	24.6±2.5	10.0±1.0	3.4±0.3
$t\bar{t}$	3.9±0.3	26.8±2.2	66±5.4	145±11.9
W+jets	38±7	27±7	9±3	5±3
Wc+jets	152±72	68±31	22±10	8±4
$Wb\bar{b}$+jets	16±14	20±19	10±10	6±7
$Wc\bar{c}$+jets	9±8	12±11	6±6	4±5
Diboson	1.5±0.1	2.7±0.1	1.2±0.1	0.4±0.1
Z+jets	4.3±2.2	5.0±2.5	2.0±1.0	1.5±0.7
Multijets	22±11	42±21	22±11	13±7
TOTAL Exp	256±77	235±44	155±20	192±17
DATA	251	265	170	203

F

Tables of systematic uncertainties

This section contains details about the systematic uncertainties for the t-channel and Wt analysis. We quote relative uncertainties for the signal, as well as for the different backgrounds:

- **Tops**, which includes $t\bar{t}$, t-channel and s-channel,
- **VV**, standing for diboson production,
- **W+jets**, summed over all flavours and
- **QCD**.

Tables F.1 to F.6 show the systematic uncertainties after the Wt analysis cuts. All values quoted as relative errors.

Table F.1: Relative systematic uncertainties (in %) in the electron 2-jets channel.

	Wt	s,t	$t\bar{t}$	VV	W+jets	Multijet
Jet Energy Scale	-17.7	-1.9	-24.0	$+2.9$	$+1.6$	–
	$+13.1$	$+0.1$	$+26.1$	-2.7	-1.6	
Jet Energy Resolution	±0.4	±0.3	±0.3	±1.0	–	–
Jet Reconstruction	±7.8	±1.5	±14.3	±2.1	–	–
B-tagging	±12.4	±8.6	±9.1	±17.3	±18.1	–
Mistag	< 0.1	±0.1	±0.1	±1.6	±3.7	–
Lepton Scale Factor	±3.9	±4.1	±3.9	±4.1	–	–
Lepton Resolution	< 1.0	< 1.0	< 1.0	< 1.0	–	–
PDF	$+3.0$	$+1.0$	$+1.0$	$+1.0$	–	–
	-2.0	-1.0	-1.0	-1.0		
ISR/FSR	±3.0	±3.0	±11.0	–	–	–
MC Generator	±3.0	±3.0	±5.0	–	±4.0	–
Parton Shower Modeling	±2.0	±2.0	±8.0	–	–	–
Pile-Up	±2.0	±2.0	±2.0	–	–	–
Normalization to data	–	–	–	–	±54.4	±100.0
Normalization to theory	–	±10.0	±8.2	–	–	–
Luminosity	–	±3.2	±3.2	±3.2	–	–
MC/Data statistics	±3.0	±3.7	±2.1	±4.3	±6.3	±11.6

Table F.2: Relative systematic uncertainties (in %) in the muon 2-jets channel.

	Wt	s,t	$t\bar{t}$	VV	W+jets	Multijet
Jet Energy Scale	-15.9	-1.8	-21.1	$+1.3$	$+3.4$	–
	$+13.5$	-1.8	$+29.7$	-1.8	-3.4	
Jet Energy Resolution	±0.3	±0.7	±1.8	±1.1	–	–
Jet Reconstruction	±2.3	∓2.0	±10.5	±1.9	–	–
B-tagging	±11.9	±8.0	±8.6	±16.2	±17.7	–
Mistag	< 0.1	< 0.1	< 0.1	±1.8	±3.1	–
Lepton Scale Factor	±1.2	±1.2	±1.2	±1.2	–	–
Lepton Resolution	< 1.0	< 1.0	< 1.0	< 1.0	–	–
PDF	$+2.0$	$+1.0$	$+1.0$	$+2.0$	–	–
	-2.0	-1.0	-1.0	-1.0		
ISR/FSR	±3.0	±3.0	±13.0	–	–	–
MC Generator	±3.0	±3.0	±2.0	–	±4.0	–
Parton Shower Modeling	±2.0	±2.1	±3.0	–	–	–
Pile-Up	±2.0	±2.0	±2.0	–	–	–
Normalization to data	–	–	–	–	±54.2	±50.0
Normalization to theory	–	±10.0	±8.2	–	–	–
Luminosity	–	±3.2	±3.2	±3.2	–	–
MC/Data statistics	±2.8	±3.4	±2.0	±3.9	±5.8	±31.6

Table F.3: Relative systematic uncertainties (in %) in the electron 3-jets channel.

	Wt	s,t	$t\bar{t}$	VV	W+jets	Multijet
Jet Energy Scale	-0.5	$+10.5$	-11.9	$+5.8$	$+4.4$	–
	-2.4	-15.5	$+11.7$	-17.5	-4.4	
Jet Energy Resolution	±1.1	±4.4	±0.1	±1.8	–	–
Jet Reconstruction	±2.7	∓3.4	±1.3	±3.2	–	–
B-tagging	±10.7	±5.9	±5.2	±17.5	±16.6	–
Mistag	< 0.1	∓0.1	< 0.1	±1.4	±4.1	–
Lepton Scale Factor	±4.0	±4.0	±4.0	±3.9	–	–
Lepton Resolution	< 1.0	< 1.0	< 1.0	< 1.0	–	–
PDF	$+4.0$	$+1.0$	$+1.0$	$+1.0$	–	–
	-2.0	-2.0	-2.0	-1.0		
ISR/FSR	±3.0	±3.0	±14.0	–	–	–
MC Generator	±3.0	±3.0	±3.0	–	±4.0	–
Parton Shower Modeling	±2.0	±2.2	±2.0	–	–	–
Pile-Up	±2.0	±2.0	±2.0	–	–	–
Normalization to data	–	–	–	–	±63.1	±100.0
Normalization to theory	–	±10.0	±8.2	–	–	–
Luminosity	–	±3.2	±3.2	±3.2	–	–
MC/Data statistics	±2.8	±6.3	±1.4	±7.0	±11.8	±18.0

Table F.4: Relative systematic uncertainties (in %) in the muon 3-jets channel.

	Wt	s,t	$t\bar{t}$	VV	W+jets	Multijet
Jet Energy Scale	-3.2	$+8.4$	-15.8	$+9.0$	$+2.6$	–
	-0.8	-9.5	$+12.4$	-18.4	-2.6	
Jet Energy Resolution	±0.5	±2.3	±0.2	±5.8	–	–
Jet Reconstruction	±1.2	∓4.8	±1.6	±5.6	–	–
B-tagging	±10.6	±5.7	±5.1	±15.9	±17.3	–
Mistag	±0.1	±0.1	< 0.1	±2.3	±3.2	–
Lepton Scale Factor	±1.2	±1.3	±1.2	±1.1	–	–
Lepton Resolution	< 1.0	< 1.0	< 1.0	< 1.0	–	–
PDF	$+2.0$	$+1.0$	$+1.0$	$+2.0$	–	–
	-2.0	-2.0	-2.0	-1.0		
ISR/FSR	±3.0	±3.0	±12.0	–	–	–
MC Generator	±3.0	±3.0	±1.0	–	±4.0	–
Parton Shower Modeling	±2.0	±2.0	±4.0	–	–	–
Pile-Up	±2.0	±2.0	±2.0	–	–	–
Normalization to data	–	–	–	–	±64.6	±50.0
Normalization to theory	–	±10.0	±8.2	–	–	–
Luminosity	–	±3.2	±3.2	±3.2	–	–
MC/Data statistics	±2.7	±6.1	±1.4	±6.2	±10.0	±33.3

Table F.5: Relative systematic uncertainties (in %) in the electron 4-jets channel.

	Wt	s,t	$t\bar{t}$	VV	W+jets	Multijet
Jet Energy Scale	$^{+13.0}_{-13.9}$	$^{+28.7}_{-11.2}$	$^{-0.5}_{-4.6}$	$^{+46.1}_{-11.3}$	$^{+4.1}_{-4.1}$	–
Jet Energy Resolution	±2.9	±9.5	±1.9	±21.8	–	–
Jet Reconstruction	±4.4	∓6.6	±2.8	±6.3	–	–
B-tagging	±8.0	±3.8	±2.8	±14.9	±16.8	–
Mistag	< 0.1	∓0.3	∓0.1	±2.7	±2.8	–
Lepton Scale Factor	±4.0	±4.0	±4.0	±3.8	–	–
Lepton Resolution	< 1.0	< 1.0	< 1.0	< 1.0	–	–
PDF	$^{+3.0}_{-1.0}$	$^{+2.0}_{-2.0}$	$^{+2.0}_{-2.0}$	$^{+3.0}_{-1.0}$	–	–
ISR/FSR	±7.0	±7.0	±7.0	–	–	–
MC Generator	±0.5	±0.5	±0.5	–	±4.0	–
Parton Shower Modeling	±2.0	±2.0	±2.0	–	–	–
Pile-Up	±2.0	±2.0	±2.0	–	–	–
Normalization to data	–	–	–	–	±80.4	±100.0
Normalization to theory	–	±10.0	±8.2	–	–	–
Luminosity	–	±3.2	±3.2	±3.2	–	–
MC/Data statistics	±4.2	±13.0	±1.5	±15.3	±20.0	±40.8

Table F.6: Relative systematic uncertainties (in %) in the muon 4-jets channel.

	Wt	s,t	$t\bar{t}$	VV	W+jets	Multijet
Jet Energy Scale	$^{+3.7}_{-12.6}$	$^{+24.7}_{-17.5}$	$^{-1.3}_{-2.9}$	$^{+27.9}_{-24.1}$	$^{-6.2}_{+6.2}$	–
Jet Energy Resolution	±1.1	±5.3	±0.5	±6.1	–	–
Jet Reconstruction	±4.7	∓6.8	±3.3	±2.2	–	–
B-tagging	±8.2	±4.3	±3.0	±14.8	±16.3	–
Mistag	< 0.1	∓0.2	∓0.1	±3.8	±3.4	–
Lepton Scale Factor	±1.2	±1.1	±1.2	±1.3	–	–
Lepton Resolution	< 1.0	< 1.0	< 1.0	< 1.0	–	–
PDF	$^{+2.0}_{-1.0}$	$^{+1.0}_{-2.0}$	$^{+1.0}_{-2.0}$	$^{+2.0}_{-1.0}$	–	–
ISR/FSR	±10.0	±10.0	±10.0	–	–	–
MC Generator	±3.0	±3.0	±3.0	–	±4.0	–
Parton Shower Modeling	±3.0	±3.0	±3.0	–	–	–
Pile-Up	±2.0	±2.0	±2.0	–	–	–
Normalization to data	–	–	–	–	±82.8	±50.0
Normalization to theory	–	±10.0	±8.2	–	–	–
Luminosity	–	±3.2	±3.2	±3.2	–	–
MC/Data statistics	±4.2	±12.4	±1.4	±13.9	±18.0	±70.7

Bibliography

[1] S. Frixione and B.R. Webber. Matching NLO QCD computations and parton shower simulations. *JHEP*, 0206:029, 2002.

[2] S. Frixione, P. Nason, and C. Oleari. Matching NLO QCD computations with Parton Shower simulations: the POWHEG method. *JHEP*, 0711:070, 2007.

[3] The ATLAS Collaboration. The ATLAS HLT, DAQ and DCS Technical Design Report. 2003. ATLAS TDR-016.

[4] S. Catani and M. H. Seymour. The dipole formalism for the calculation of QCD jet cross sections at next-to-leading order. *Phys. Lett.*, B 378:287–301, 1996.

[5] S. Catani, S. Dittmaier, M. H. Seymour, and Z. Trocsanyi. The Dipole Formalism for Next-to-Leading Order QCD Calculations with Massive Partons. *Nucl. Phys.*, B 627:189–265, 2002.

[6] The Athena framework. `https://indico.cern.ch/conferenceDisplay.py?confId=a05403#s2`.

[7] E. Zeidler. *Quantum Field Theory II: Quantum Electrodynamics. A Bridge between Mathematicians and Physicists.* Springer, 2009.

[8] K. Nakamura *et al.* The Review of Particle Physics. *J. Phys.*, G 37:075021, 2010.

[9] R.K. Ellis, W.J. Stirling, and B.R. Webber. *QCD and Collider Physics.* Cambridge University Press, 1996.

[10] C.H. Llewellyn Smith. High energy behaviour and gauge symmetry. *Phys. Lett.*, B46:233–236, 1973.

[11] J.M. Cornwall, D.M. Levin, and G. Tiktopoulos. Derivation of gauge-invariance from high-energy unitarity bounds on the S-matrix. *Phys. Rev.*, D10:1145–1167, 1974.

[12] F. Englert and R. Brout. Broken Symmetry and the Mass of Gauge Vector Mesons. *Phys. Rev. Lett.*, 13:321–323, 1964.

[13] P. W. Higgs. Broken Symmetries and the Masses of Gauge Bosons. *Phys. Rev. Lett.*, 13:508–509, 1964.

[14] N. Arkani-Hamed, A. G. Cohen, E. Katz, and A. E. Nelson. The Littlest Higgs. *JHEP*, 0207:034, 2002.

[15] R. Contino, Y. Nomura, and A. Pomarol. Higgs as a Holographic Pseudo-Goldstone Boson. *Nucl. Phys.*, B 671:148, 2003.

[16] C. Csaki, C. Grojean, H. Murayama, L. Pilo, and J. Terning. Gauge Theories on an Interval: Unitarity without a Higgs. *Phys. Rev.*, D 69:055006, 2004.

[17] S. P. Martin. A Supersymmtery Primer. 2008. arXiv:hep-ph/9709356v5.

[18] S. R. Coleman and J. Mandula. All possible symmetries of the S matrix. *Phys. Rev.*, 159:1251–1256, 1967.

[19] R. Haag, J. T. Lopuszanski, and M. Sohnius. All possible generators of Supersymmetries of the S matrix. *Nucl. Phys.*, B 88:257, 1975.

[20] J.L. Diaz-Cruz, A. Diaz-Furlong, and J.H. Montes de Oca. The general 2HDM extensions of the SM. 2010. arXiv:1010.0950[hep-ph].

[21] J.F. Gunion and H.E. Haber. CP-conserving two-Higgs-doublet model: The approach to the decoupling limit. *Phys. Rev.*, D 67:075019, 2003.

[22] A. Djouadi. The Anatomy of Electro-Weak Symmetry Breaking. II: The Higgs bosons in the Minimal Supersymmetric Model. *Phys. Rept.*, 459:1–241, 2008.

[23] A. Djouadi, J. Kalinowski, and M. Spira. HDECAY: a Program for Higgs Boson Decays in the Standard Model and its Supersymmetric Extension. *Comput. Phys. Commun.*, 108:56–74, 1998.

[24] V. M. Abazov *et al.* (The D0 Collaboration). Combination of $t\bar{t}$ cross section measurements and constraints on the mass of the top quark and its decays into charged Higgs bosons. *Phys. Rev.*, D 80:071102(R), 2009.

[25] V. M. Abazov *et al.* (The D0 Collaboration). Search for charged Higgs bosons in top quark decays. *Phys. Lett.*, B 682:278, 2009.

[26] V. M. Abazov *et al.* (The D0 Collaboration). Search for Charged Higgs Bosons Decaying into Top and Bottom Quarks in $p\bar{p}$ Collisions. *Phys. Rev. Lett.*, 102:191802, 2009.

[27] A. Abulencia *et al.* (The CDF Collaboration). Search for Charged Higgs Bosons in Decays of Top Quarks in $p\bar{p}$ Collisions at $\sqrt{s} = 1.96$ TeV. *Phys. Rev. Lett.*, 103:101803, 2009.

[28] Heavy Flavour Averaging Group. `http://www.slac.stanford.edu/xorg/hfag/`.

[29] H. Flaecher, M. Goebel, J. Haller, A. Hoecker, K. Moenig, and J. Stelzer. Revisiting the Global Electroweak Fit of the Standard Model and Beyond with Gfitter. *Eur.Phys.*, C 60:543–583, 2009.

[30] S.W. Herb *et al.* Observation of a Dimuon Resonance at 9.5 GeV in 400 GeV Proton-Nucleus Collisions. *Phys. Rev. Lett.*, 39:252, 1977.

[31] S.L. Glashow, J. Iliopoulos, and L. Maiani. Weak Interactions with Lepton-Hadron Symmetry. *Phys. Rev.*, D 2:1285, 1970.

[32] The JADE Collaboration. A measurement of the electroweak induced charge asymmetry in $e^+e^- \to b\bar{b}$. *Phys. Lett.*, B 146:437–442, 1984.

[33] F. Abe *et al.* (The CDF Collaboration). Evidence for Top Quark Production in $\bar{p}p$ Collisions at $\sqrt{s} = 1.8$ TeV. *Phys. Rev. Lett.*, 73:225–231, 1994.

[34] F. Abe *et al.* (The CDF Collaboration). Observation of Top Quark Production in pp Collisions with the Collider Detector at Fermilab. *Phys. Rev. Lett.*, 74:2626–2631, 1995.

[35] S. Abachi *et al.* (The D0 Collaboration). Search for High Mass Top Quark Production in $\bar{p}p$ Collisions at $\sqrt{s} = 1.8$ TeV. *Phys. Rev. Lett.*, 74:2422–2426, 1995.

[36] V. M. Abazov *et al.* (The D0 Collaboration). Observation of Single Top Quark Production. *Phys. Rev. Lett.*, 103:092001, 2009.

[37] T. Aaltonen *et al.* (The CDF Collaboration). First Observation of Electroweak Single Top Quark Production. *Phys. Rev. Lett.*, 103:092002, 2009.

[38] A. Quadt. Top quark physics at hadron colliders. *Eur. Phys. J.*, C 48:835–1000, 2006.

[39] $t\bar{t}$ production cross sections. `https://twiki.cern.ch/twiki/bin/view/AtlasProtected/TopMC2009#Reference_cross_section`.

[40] Top production Feynman diagrams. `http://www-d0.fnal.gov/Run2Physics/top/top_public_web_pages/top_feynman_diagrams.html`.

[41] Single top production cross sections with the ATLAS detector. `https://twiki.cern.ch/twiki/bin/view/AtlasProtected/SingleTopGroup#Expected_Single_top_Cross_section`.

[42] T. Aaltonen *et al.* (The CDF Collaboration). Combined template-based Top Quark Mass Measurement in the Lepton+Jets and Dileptons Channels Using 4.8 fb^1 of data. *CDF Note*, (10033), 2010.

[43] V. M. Abazov *et al.* (The D0 Collaboration). Measurement of the Top Quark Mass in the Lepton+Jets Channel Using the Matrix Element Method on 3.6 fb^1 of D0 Run II Data. *D0 Note*, (D0–CONF–5877), 2009.

[44] T. Aaltonen *et al.* (The CDF Collaboration). Top Mass Measurement in the Lepton + Jets Channel Using a Matrix Element Method with Quasi-Monte Carlo Integration and in situ Jet Calibration with 4.8 fb^1. 2010. arXiv:1010.4582v1 [hep-ex].

[45] The CDF and D0 collaborations. Combination of CDF and D0 Results on the Mass of the Top Quark. arXiv:1007.3178[hep-ex].

[46] V. M. Abazov *et al.* (The D0 Collaboration). Direct Measurement of the Mass Difference between Top and Antitop Quarks. *Phys. Rev. Lett.*, 103:132001, 2009.

[47] T. Aaltonen *et al.* (The CDF Collaboration). A Measurement of Top Quark Width using Template Method in Lepton+Jets Channel with 4.3 fb^1. *CDF Note*, (10035), 2010.

[48] V. M. Abazov *et al.* (The D0 Collaboration). Experimental Discrimination between Charge 2e/3 Top Quark and Charge 4e/3 Exotic Quark Production Scenarios. *Phys. Rev. Lett.*, 98:041801, 2007.

[49] T. Aaltonen *et al.* (The CDF Collaboration). Measurements of the top-quark mass using charged particle tracking. *Phys. Rev.*, D 81:032002, 2010.

[50] V. M. Abazov *et al.* (The D0 Collaboration). Measurement of spin correlation in ttbar production using dilepton final states. 2011. arXiv:1103.1871 [hep-ph].

[51] T. Aaltonen *et al.* (The CDF Collaboration). Measurement of ttbar Spin Correlations Coefficient in 2.8 fb-1 Dilepton Candidates. *CDF Note*, (9824), 2009.

[52] The ATLAS Collaboration. Measurement of the top quark-pair production cross section with ATLAS in *pp* collisions at $\sqrt{s} = 7$TeV. *submitted to EPJC*, 2010. arXiv:1012.1792v2 [hep-ex].

[53] The ATLAS Collaboration. Measurement of the top quark pair production cross-section using a statistical combination of dilepton and semileptonic final states. *ATLAS Note*, (ATL-COM-PHYS-2011-186), 2011.

[54] The ATLAS Collaboration. Top charge measurement at ATLAS detector. *ATLAS Note*, ATLAS Note PHYS-2003-35, 2003.

[55] F. Hubaut, E. Monnier, P. Pralavorio, K. Smolek, and V. Simak. ATLAS sensitivity to top quark and W boson polarization in *tt* events. *Eur. Phys. J.*, C 44S2:13, 2005.

[56] J. A. Aguilar-Saavedra, J. Carvalho, N. Castro, A. Onofre, and F. Veloso. ATLAS sensitivity to Wtb anomalous couplings in top quark decays. *ATLAS Note*, (SN-ATLAS-2007-064), 2007.

[57] J. Carvalho, N. Castro, L. Chikovani, T. Djobava, J. Dodd, S. McGrath, A. Onofre, J. Parsons, and F. Veloso. Study of ATLAS sensitivity to FCNC top decays. *Eur. Phys. J.*, C 52:999–1019, 2007.

[58] E. Cogneras and D. Pallin. Generic tt resonance search with the ATLAS detector. *ATLAS Note*, (ATL-PHYS-PUB-2006-033), 2006.

[59] S. Bethke. The 2009 World average of α_S. *Eur. Phys. J.*, C 64:689–703, 2009.

[60] S.D. Drell and T.M. Yan. Partons and their applications at high energies. *Ann. Phys.*, 66:578, 1971.

[61] V.N. Gribov and L. N. Lipatov. Deep inelastic ep scattering in perturbation theory. *Sov. J. Nucl. Phys.*, 15:438, 1972.

[62] G. Altarelli and G. Parisi. Asymptotic freedom in parton language. *Nucl. Phys.*, B 126:298, 1977.

[63] Yu. L. Dokshitzer. Calculation of the Structure Functions for Deep Inelastic Scattering and e+ e- Annihilation by Perturbation Theory in Quantum Chromodynamics. . *Sov.Phys. JETP*, 46:641, 1977.

[64] Handbook of perturbative QCD. `http://www.phys.psu.edu/~cteq/#Handbook`.

[65] EW Physics inclusive processes from H1 and ZEUS. `https://www.desy.de/h1zeus/combined_results/index.php`.

[66] The ATLAS Collaboration. Parton densities at the LHC. *ATLAS Note*, (ATL-PHYS-CONF-2008-011), 2008.

[67] A.D.Martin, W.J.Stirling, R.S.Thorne, and G.Watt. Parton distributions for the LHC. *Eur. Phys. J.*, C 63:189–285, 2009.

[68] J. Pumplin, D.R. Stump, J. Huston, H.L. Lai, P. Nadolsky, and W.K. Tung. New Generation of Parton Distributions with Uncertainties from Global QCD Analysis. *JHEP*, 0207:012, 2002.

[69] R. D. Ball, L. Del Debbio, S. Forte, A. Guffanti, J. I. Latorre, J. Rojo, and M. Ubiali. A first unbiased global NLO determination of parton distributions and their uncertainties. 2010. arXiv:1002.4407 [hep-ph].

[70] R. D. Ball, V. Bertone, F. Cerutti, L. Del Debbio, S. Forte, A. Guffanti, J. I. Latorre, J. Rojo, and M. Ubiali. Impact of Heavy Quark Masses on Parton Distributions and LHC Phenomenology. 2011. arXiv:1101.1300 [hep-ph].

[71] L3 Collaboration OPAL Collaboration the LEP Electroweak Working Group The LEP Collaborations: ALEPH Collaboration, DELPHI Collaboration. Precision Electroweak Measurements and Constraints on the Standard Model. *CERN-PH-EP/2007-039*, arXiv:0712.0929v2 [hep-ex], 2007.

[72] I.I. Bigi, M.A. Shifman, N.G. Uraltsev, and A.I. Vainshtein. The pole mass of the heavy quark. Perturbation theory and beyond. 1994. arXiv:hep-ph/9402360.

[73] M. Beneke and V.M. Braun. Heavy quark effective theory beyond perturbation theory: renormalons, the pole mass and the reidual term. 1994. arXiv:hep-ph/9402364.

[74] A. H. Hoang, M. C. Smith, T. Stelzer, and S. Willenbrock. Quarkonia and the Pole Mass. *Phys. Rev.*, D 59:114014, 1999.

[75] A. H. Hoang, A. Jain, I. Scimemi, and I. W. Stewart. Infrared Renormalization Group Flow for Heavy Quark Masses. *Phys. Rev. Lett.*, 101:151602, 2008.

[76] G. Corcella. Theoretical issues on the top mass reconstruction at hadron colliders. 2010. arXiv:1008.4498[hep-ph].

[77] S. Fleming, A. H. Hoang, S. Mantry, and I. W. Stewar. Top Jets in the Peak Region: Factorization Analysis with NLL Resummation. *Phys. Rev.*, D 77:114003, 2008.

[78] S. Biswas, K. Melnikov, and M. Schulze. Next-to-leading order QCD effects and the top quark mass measurements at the LHC. *JHEP*, 1008:048, 2010.

[79] S. H. Zhu. Complete next-to-leading order QCD corrections to charged Higgs boson associated production with top quark at the CERN Large Hadron Collider. *Phys. Rev.*, D 67:075006, 2003.

[80] T. Plehn. Charged higgs boson production in bottom gluon fusion. *Phys. Rev.*, D 67:014018, 2003.

[81] J.M. Jauch and F. Rohrlich. *The theory of photons and electrons.* Addison-Wesley, 1955.

[82] W. Pauli and F. Villars. On the Invariant Regularization in Relativistic Quantum Theory. *Rev. Mod. Phys.*, 21:434, 1949.

[83] E.R. Speer. Analytic Renormalization. *J. Math. Phys.*, 9:1404, 1968.

[84] R. K. Ellis and G. Zanderighi. Scalar one-loop integrals for QCD. *JHEP*, 0802:002, 2008.

[85] T. Muta. *Foundations of Quantum Chromodynamics.* World Scientific, 1998.

[86] J. C. Collins, F. Wilczek, and A. Zee. Low-Energy Manifestations Of Heavy Particles: Application To The Neutral Current. *Phys. Rev. D*, 18:242, 1978.

[87] T. Kinoshita. Mass Singularities of Feynman Amplitudes. *J. Math. Phys.*, 3:650, 1962.

[88] T. D. Lee and M. Nauenberg. Degenerate Systems and Mass Singularities. *Phys. Rev.*, 133:B1549–B1562, 1964.

[89] N. Nakanishi. General Theory of Infrared Divergence. *Progr. Theor. Phys.*, 19:159, 1958.

[90] W.B. Kilgore and W.T. Giele. Next-to-leading order gluonic three-jet production at hadron colliders, journal = Phys. Rev., volume = D 55, year = 1997, pages = 7183.

[91] W.T. Giele *et al.* *Nucl. Phys.*, B403:633, 1993.

[92] S. Keller and E. Laenen. Next-to-leading order cross sections for tagged reactions. *Phys. Rev.*, D 59:114004, 1999.

[93] S. Catani and M.H. Seymour. A general algorithm for calculating jet cross sections in NLO QCD. *Nucl. Phys.*, B 485:291, 1997.

[94] S. Frixione, Z. Kunszt, and A. Signer. Three-jet cross sections to next-to-leading order. *Nucl. Phys.*, B 467:399, 1996.

[95] L. Phaf and S. Weinzierl. Dipole formalism with heavy fermions. *JHEP*, 0104:006, 2001.

[96] S. Frixione, E. Laenen, P. Motylinski, B. R. Webber, and C. D. White. Single-top hadroproduction in association with a W boson. *JHEP*, 07:029, 2008.

[97] I. I. Balitsky and L. N. Lipatov. The Pomeranchuk singularity in quantum Chromodynamics. *Sov. J. Nucl. Phys.*, 28:822–829, 1978.

[98] G. Marchesini. QCD coherence in the structure function and associated distributions at small x. *Nucl. Phys.*, B445:49–80, 1995.

[99] R. D. Field and S. Wolfram. A QCD model for e^+e^- annihilation . *Nucl. Phys.*, B 213:65, 1983.

[100] M.A. Dobbs *et al.* Les Houches Guidebook to Monte Carlo Generators for Hadron Collider Physics. 2004. arXiv:hep-ph/0403045.

[101] T. Sjoestrand. High-Energy-Physics Event Generation with PYTHIA 6.1. *Comput. Phys. Commun.*, 135:238, 2001.

[102] T. Sjoestrand, S. Mrenna, and P. Skands. PYTHIA 6.4 Physics and Manual. 2006. arXiv: hep-ph/0603175.

[103] Corcella *et al.* HERWIG 6: an event generator for hadron emission reactions with interfering gluons (including supersymmetric processes). *JHEP*, 0101:010, 2001.

[104] T. Gleisberg, S. Hoche, F. Krauss, M. Schonherr, S. Schumann, F Siegert, and J. Winter. Event generation with Sherpa 1.1. *JHEP*, 02:007, 2009.

[105] B. P. Kersevan and E. Richter-Was. The Monte Carlo Event Generator AcerMC version 3.5 with interfaces to PYTHIA 6.4, HERWIG 6.5 and ARIADNE 4.1. 2004. arXiv: hep-ph/0405247.

[106] M.L. Mangano, M. Moretti, F. Piccinini, R. Pittau, and A. Polosa. ALPGEN, a generator for hard multiparton processes in hadronic collisions. *JHEP*, 0307:001, 2003.

[107] J.M. Butterworth, J. R. Forshaw, and M. H. Seymour. Multiparton Interactions in Photoproduction at HERA. *Z. Phys.*, C 72:637, 1996.

[108] J. M. Campbell, R. K. Ellis, and C. Williams. MCFM. `http://mcfm.fnal.gov/mcfm.pdf`.

[109] J. M. Campbell and R. K. Ellis. MCFM for the Tevatron and the LHC. *Nucl. Phys. Proc. Suppl.*, 205–206:10–15, 2010.

[110] E. Boos *et al.* CompHEP 4.4 - Automatic Computations from Lagrangians to Events. *Nucl. Instrum. Meth.*, A 534:250–25, 2004.

[111] J. Alwall *et al.* MadGraph/MadEvent v4: the new web generation. *JHEP*, 09:028, 2007.

[112] O. Stal. `http://www.grid.tsl.uu.se/chargedhiggs2010/`.

[113] T. Hahn, S. Heinemeyer, W. Hollik, and G. Weiglein. Precision Higgs Masses with FeynHiggs 2.2. 2005. arXiv: hep-ph/0507009.

[114] D. Eriksson, J. Rathsman, and O. Stal. 2HDMC - Two-Higgs-Doublet Model Calculator. *Comput. Phys. Commun.*, 181:189–205, 2010.

[115] F.N. Mahmoudi. SuperIso. `http://superiso.in2p3.fr/`.

[116] P. Bechtle, O. Brein, S. Heinemeyer, G. Weiglein, and K. E. Williams. HiggsBounds: Confronting Arbitrary Higgs Sectors with Exclusion Bounds from LEP and the Tevatron. *Comput. Phys. Commun.*, 181:138–167, 2010.

[117] J. Alwall. MATCHIG: A program for matching charged Higgs boson production at hadron colliders. arXiv:hep-ph/0503124.

[118] C. Weydert *et al.* Charged Higgs boson production in association with a top quark in MC@NLO. *Eur. Phys. J.*, C 67:617–636, 2010.

[119] T. Plehn and C. Weydert. Charged Higgs production with a top in MC@NLO. 2010. arXiv:1012.3761 [hep-ph].

[120] S. Dittmaier, M. Krämer, M. Spira, and M. Walser. Charged-Higgs-boson production at the LHC: NLO supersymmetric QCD corrections. *Phys. Rev.*, D 83:055005, 2011.

[121] LHC Higgs Cross Section Working Group. Handbook of LHC Higgs Cross Sections: 1. Inclusive Observables. arXiv:1101.0593 [hep-ph].

[122] S. Alioli, P. Nason, C. Oleari, and E. Re. A general framework for implementing NLO calculations in shower Monte Carlo programs: the POWHEG BOX. 2010. arXiv:1002.2581 [hep-ph].

[123] C. Oleari. The POWHEG-BOX. *Nucl. Phys. Proc. Suppl.*, 205–206:36–41, 2010.

[124] M. Klasen, K. Kovarik, P. Nason, and C. Weydert. Associated production of charged Higgs bosons and top quarks with POWHEG. *In preparation.*

[125] Karol Kovarik. Private code.

[126] G. Unal, S. Laplace, and J. Vivie. La physique au LHC. `http://ecole-de-gif.in2p3.fr/Passed/gif_cours.deGif`.

[127] Interim summary report on the analysis of the 19 September 2008 incident at the LHC. *CERN-ATL-PhL*, EDMS(973073).

[128] The ATLAS Collaboration. Letter of intent for a general purpose *pp* experiment at the Large Hadron Collider at CERN. 1992. CERN/LHCC/92-4.

[129] The ATLAS Collaboration. ATLAS Technical Proposal for a general purpose *pp* experiment at the Large Hadron Collider at CERN. 1994. CERN/LHCC/94-43.

[130] The ATLAS Collaboration. Detector and Physics Performance Technical Design Report Volume I. 1999. CERN/LHCC/99-14.

[131] The ATLAS Collaboration. The ATLAS Experiment at the CERN Large Hadron Collider. *JINST*, 3:S08003, 2008.

[132] Run Control Shifter training. `https://atlasop.cern.ch/twiki/bin/view/Main/RCShifterTraining`.

[133] The ATLAS Collaboration. Data streaming in ATLAS. *ATLAS Note*, (ATL-GEN-INT-2007-002), 2008.

[134] 2010 trigger menu. `https://twiki.cern.ch/twiki/bin/viewauth/Atlas/TriggerPhysicsMenu`.

[135] The ATLAS Collaboration. ATLAS Computing Technical Design Report. *ATLAS TDR*, (CERN-LHCC-2005-02), 2005.

[136] M. Dührssen. The fast calorimeter simulation FastCaloSim. *ATLAS Note*, (ATL-PHYS-INT-2008-043), 2008.

[137] A. Salzburger *et al.* The Fast ATLAS Track Simulation (FATRAS). *ATLAS Note*, (ATL-SOFT-PUB-2008-001), 2008.

[138] 2010 data taking periods. `https://twiki.cern.ch/twiki/bin/view/AtlasProtected/DataPeriods`.

[139] The ATLAS Collaboration. Lepton trigger and identification for the Winter 2011 top quark analyses. *ATLAS Note*, (ATL-COM-PHYS-2011-123), 2011.

[140] The ATLAS Collaboration. Expected electron performance in the ATLAS experiment. *ATLAS Note*, (ATL-PHYS-INT-2010-126), 2010.

[141] Electron calibration and resolution. `https://twiki.cern.ch/twiki/bin/view/AtlasProtected/EnergyScaleResolutionRecommendations`.

[142] The ATLAS collaboration. ATLAS Muon Momentum Resolution in the First Pass Reconstruction of the 2010 *pp* Collision Data at $\sqrt{s} = 7$ TeV. *ATLAS Note*, (ATLAS-CONF-2011-046), 2011.

[143] G. P. Salam and G. Soyez. A Practical Seedless Infra-red Safe Cone jet algorithm. *JHEP*, 05:086, 2007.

[144] The ATLAS Collaboration. In-situ jet energy scale and jet shape corrections for multiple interactions in the first ATLAS data at the LHC. *ATLAS Note*, (ATLAS-CONF-2011-030), 2011.

[145] The ATLAS Collaboration. Validation of the ATLAS jet energy scale uncertainties using tracks in proton-proton collisions at $\sqrt{s}$=7 TeV. *ATLAS Note*, (ATLAS-CONF-2011-067), 2011.

[146] The ATLAS Collaboration. Close-by Jet Effects on Jet Energy Scale Calibration in pp Collisions at $\sqrt{s} = 7$ TeV with the ATLAS Detector. *ATLAS Note*, (ATLAS-CONF-2011-062), 2011.

[147] The ATLAS Collaboration. Jet energy scale and its systematic uncertainty in proton-proton collisions at $\sqrt{s} = 7$ TeV in ATLAS 2010 data. *ATLAS Note*, (ATLAS-CONF-2011-032), 2011.

[148] The ATLAS Collaboration. Calibrating the b-Tag Efficiency and Mistag Rate of the SV0 b-Tagging Algorithm in 3 pb^1 of Data with the ATLAS Detector. *ATLAS Note*, (ATLAS-CONF-2010-099), 2010.

[149] The ATLAS Collaboration. Expected Performance of the ATLAS experiment-detector, trigger and physics. 2008. CERN-OPEN-2008-020.

[150] The ATLAS Collaboration. Performance of the ATLAS secondary vertex b-tagging algorithm in 7 TeV collision data. *ATLAS Note*, (ATL-COM-PHYS-2010-274), 2010.

[151] The ATLAS Top Group. b-jet tagging for top physics: performance studies, calibrations and heavy flavor fractions. *ATLAS Note*, (ATL-COM-PHYS-2011-124), 2011.

[152] The ATLAS Collaboration. Single Boson and Diboson Production Cross Sections in pp Collisions at $\sqrt{s} = 7$ TeV. *ATLAS Note*, (ATLAS-COM-PHYS-2010-695), 2010.

[153] A. Shibata *et al.* Monte Carlo samples used for top physics. *ATLAS Note*, (ATL-PHYS-INT-2010-132), 2010.

[154] Allwood-Spires *et al.* Understanding Monte Carlo Generators for Top Physics. *ATLAS Note*, (ATL-COM-PHYS-2009-334), 2009.

[155] The ATLAS Collaboration. Measurement of Single Top-Quark Production in the Lepton+Jets Channel in pp Collisions at $\sqrt{s} = 7$ TeV. *ATLAS Note*, (ATL-COM-PHYS-2011-058), 2011.

[156] Top systematic uncertainties. `https://twiki.cern.ch/twiki/bin/view/AtlasProtected/TopSystematicUncertainties`.

[157] M. Botje *et al.* The PDF4LHC Working Group Interim Recommendations. 2011. arXiv:1101.0538 [hep-ph].

[158] S. Alekhin *et al.* The PDF4LHC Working Group Interim Report. 2011. arXiv:1101.0536 [hep-ph].

[159] The ATLAS Collaboration. Monte Carlo samples for top physics. *ATLAS Note*, (ATL-PHYS-INT-2010-132), 2010.

[160] Top PDF uncertainty. `https://twiki.cern.ch/twiki/bin/view/AtlasProtected/TopPdfUncertainty`.

[161] G. Cowan, K. Cranmer, E. Gross, and O. Vitells. Asymptotic formulae for likelihood-based tests of new physics. 2010. arXiv:1007.1727 [data-an].

[162] S.S. Wilks. The large sample distribution of the likelihood ratio for testing composite hypotheses. *Ann. Math. Stat.*, 9:60–2, 1938.

[163] The ATLAS Collaboration. Search for W-associated single top quark production in dilepton final states at $\sqrt{s} = 7$ TeV with 35.3 pb^1. *ATLAS Note*, (ATL-COM-PHYS-2011-059), 2010.

[164] The ATLAS Collaboration. Searches for Single Top-Quark Production with the ATLAS Detector in pp collisions at $\sqrt{s} = 7$ TeV. *ATLAS Note*, (ATLAS-CONF-2011-027), 2011.

[165] M.L. Mangano. MLM matching. `http://mlm.web.cern.ch/mlm/talks/lund-alpgen.pdf`.

[166] The ATLAS Collaboration. Understanding Monte Carlo Generators for top physics. *ATLAS Note*, (ATL-COM-PHYS-2009-334), 2010.

[167] J. Campbell, R.K. Ellis, F. Maltoni, and S. Willenbrock. Production of a W boson and two jets with one b-quark tag. *Phys.Rev.*, D 75:054015, 2007.